DYNAMICS AND CONTROL OF ORBITING FLEXIBLE SYSTEMS: A FORMULATION WITH APPLICATIONS

CHUN–KI ALFRED NG

B.A.Sc., University of British Columbia, 1984
M.A.Sc., University of British Columbia, 1987

A THESIS SUBMITTED IN PARTIAL FULFILMENT OF
THE REQUIREMENTS FOR THE DEGREE OF

DOCTOR OF PHILOSOPHY

in

The Faculty of Graduate Studies
Department of Mechanical Engineering

We accept this thesis as conforming
to the required standard

. . . . . .

. . . . . .

THE UNIVERSITY OF BRITISH COLUMBIA

April 1992

In presenting this thesis in partial fulfilment of the requirements for an advanced degree at the University of British Columbia, I agree that the Library shall make it freely available for reference and study. I further agree that permission for extensive copying of this thesis for scholarly purposes may be granted by the head of my department or by his or her representatives. It is understood that copying or publication of this thesis for financial gain shall not be allowed without my written permission.

Department of Mechanical Engineering
The University of British Columbia
Vancouver, B.C. CANADA

Date: April 1992

ABSTRACT

A relatively general formulation for studying the nonlinear dynamics and control of spacecraft with interconnected flexible members in a tree-type topology is developed. The distinctive features of the formulation include the following:

(i) It is applicable to a large class of present and future spacecraft with flexible beam and plate type appendages, arbitrary in number and orientation.

(ii) The members are free to undergo predefined slewing maneuvers to facilitate modelling of sun tracking solar panels and large angle maneuvers of space based robots.

(iii) Solar radiation induced thermal deformations of flexible members are incorporated in the study.

(iv) The governing equations of motion are highly nonlinear, nonautonomous and coupled. They are programmed in a modular fashion to help isolate the effects of flexibility, librational motion, thermal deformations, slewing maneuvers, shifting center of mass, higher modes, initial conditions, etc.

The first chapter of the thesis presents a general background to the subject and a brief review of the relevant literature on multibody dynamics. This is followed by the kinematics and kinetics of the problem leading to the Lagrangian equations of motion. The third chapter focuses on methodology and development of the computer code suitable for parametric dynamical study and control.

Next, versatility of the general formulation is illustrated through the analysis of five spacecraft configurations of contemporary interest: the next generation of multi-purpose communications spacecraft represented by the INdian SATellite II (IN-

SAT II); the First Element Launch (FEL) and the Permanently Manned Configuration (PMC) of the proposed Space Station *Freedom*; the Mobile Servicing System (MSS) to be developed by Canada for operation on the Space Station; and the Space Flyer Unit (SFU) to be launched by Japan in mid-nineties. In the FEL study, the attention is directed towards interactions between the librational and vibrational dynamics. During the PMC investigation, effects of the thermal deformation and orbital eccentricity are introduced and the microgravity environment around the station center of mass explored. The MSS study assesses pointing errors arising from inplane and out-of-plane maneuvers of the robotic arms. The SFU represents a challenging configuration to assess deployment and retrieval dynamics associated with a solar array. Parameters considered here include symmetry, orientation and duration of the deployment/retrieval maneuvers.

Results of the dynamical study clearly shows that, under critical combinations of parameters, the systems can become unstable. Obviously, the next logical step is to explore control strategies to restore equilibrium. To that end, feasibility of the nonlinear control based on the Feedback Linearization Technique (FLT) is explored with reference to the INSAT II and the MSS. Results show the procedure to be quite promising in controlling the INSAT II over a range of disturbances, including the thermal effects. Application of the control to the MSS reduced the pointing error induced by robotic arm maneuvers significantly.

The amount of information obtained through a planned parametric analysis of the system dynamics and control is indeed enormous. More significant results are summarized in the concluding chapter together with a few recommendations for future study.

TABLE OF CONTENTS

LIST OF SYMBOLS

a_b	beam radius
a_c^y, a_c^z	power boom accelerations in Y_c and Z_c directions, respectively; Eq. (4.3)
a_1, a_2, a_3	constants written in terms of ρ, ω, and i; Eq. (2.4)
b_b	beam wall thickness
b_1, b_2, b_3	components of $\hat{u}$ along X_o, Y_o, and Z_o axes, respectively; Eq. (2.3)
$\bar{d}_i, \bar{d}_{i,j}$	position vectors from O_c to O_i and O_i to $O_{i,j}$, respectively; Fig. 2-2
dm_c, dm_i, $dm_{i,j}$	elemental mass in body B_c, B_i, and $B_{i,j}$, respectively
f_c, f_i, $f_{i,j}$	fundamental frequency of bodies B_c, B_i, and $B_{i,j}$, respectively
h	angular momentum per unit mass of spacecraft
i	orbit inclination with respect to the ecliptic plane; Fig. 2-3
$\hat{i}_k, \hat{j}_k, \hat{k}_k$	unit vectors in the directions of X_k, Y_k, and Z_k axes, respectively; $k = p$, c, i or i, j
k_b	thermal conductivity of an appendage
$\bar{l}$	direction cosines of $\bar{R}_{cm}$ with respect to X_p,Y_p,Z_p axes; Eq. (2.39)
l_b, l_p	beam and plate lengths, respectively
l_b^*, l_p^*	thermal reference lengths of the beam and plate, respectively; Eqs. (2.16) and (2.19)

l_c, l_i, $l_{i,j}$	length of bodies B_c, B_i, and $B_{i,j}$, respectively
m_b	beam mass per unit length
$m_c, m_i, m_{i,j}$	mass of the bodies B_c, B_i, and $B_{i,j}$, respectively
m_p	mass per unit area of the plate
n_i	number of $B_{i,j}$ bodies attached to body B_i
$\bar{q}_f$, $\bar{q}_r$	vector representing flexible and rigid generalized coordinates
$(\bar{q}_r)_d$	vector representing the desired rigid generalized coordinates
q_s	solar radiation intensity; W/m^2
t	time
t_c	plate thickness
$\hat{u}$	unit vector representing direction of the solar radiation; Eq. (2.3)
$\bar{u}_k$	unit vectors $\{\hat{\imath}_k, \hat{\jmath}_k, \hat{k}_k\}^T$; $k = c, i$ or i, j
v^b, w^b	transverse vibration of a beam in its Y and Z directions, respectively
w^p	transverse vibration of the plate in its Z direction
x_k, y_k, z_k	coordinates of a point along X_k,Y_k,Z_k directions, respectively; $k = c, i$, or i, j
$\mathbf{C}^c_i, \mathbf{C}^c_{i,j}$	transformation matrices defining orientation of F_i and $F_{i,j}$ relative to F_c, respectively
$\bar{C}_{cm}$	$\bar{C}^f_{cm} + \bar{C}^i_{cm}$
$\bar{C}^f_{cm}$	position vector from C^i to the instantaneous centre of mass of spacecraft; Eq. (2.12b)
$\bar{C}^i_{cm}$	position vector from O_c to the centre of mass of undeformed

	spacecraft; Eq. (2.12a)
C^i, C^f	centres of mass of the undeformed and deformed configurations of spacecraft, respectively
D	flexural rigidity of the plate
$EI_{b,yy}, EI_{b,zz}$	flexural rigidity of a beam about its Y and Z axes, respectively
F_k	reference frame for coordinate axes X_k,Y_k,Z_k; $k = o, c, i$ or i, j
$H_k^{s,t}$	generalized coordinate associated with the s^{th} and t^{th} modes in its X and Y directions, respectively, for a plate undergoing transverse vibrations; $k = c, i$, or i, j
$\underline{H}_k^{s,t}$	dimensionless generalized coordinate; $\underline{H}_k^{s,t} = H_k^{s,t}/l_k$
$\bar{H}_{sys}$	angular momentum of spacecraft with respect to X_c,Y_c,Z_c axes; Eq. (2.36)
$\mathbf{I}_{sys}$	inertia matrix of spacecraft with respect to the X_c,Y_c,Z_c axes; Eq. (2.37)
$(I_{xx})_k$, $(I_{yy})_k$, $(I_{zz})_k$	principal inertia of Body B_k about X_k, Y_k, and Z_k axes, respectively; $k = c$, i, or i, j
$\mathbf{K_p}$, $\mathbf{K_v}$	displacement and velocity gain matrices, Eq. (5.5)
M	total mass of spacecraft
N, N_j	total number of B_i and $B_{i,j}$ bodies, respectively
$O_c, O_i, O_{i,j}$	origins of the coordinate axes for bodies B_c, B_i, and $B_{i,j}$, respectively
P_k^r, Q_k^r	generalized coordinates associated with the r^{th} transverse vi-

	bration mode of a beam in its Y and Z directions, respectively; $k = c, i$ or i, j
$\underline{P}_k^r$, $\underline{Q}_k^r$	dimensionless generalized coordinates; $\underline{P}_k^r = P_k^r/l_k$, $\underline{Q}_k^r = Q_k^r/l_k$
$\bar{Q}_f$, $\bar{Q}_r$	control effort vectors for flexible and rigid coordinates, respectively; Eq. (5.6)
Q_ψ, Q_ϕ, Q_l	control effort for pitch, roll and yaw degrees of freedom, respectively
$\bar{R}_{cm}$	position vector from the centre of force to the instantaneous centre of mass of spacecraft; Figure 2-2
$\bar{R}_c, \bar{R}_i, \bar{R}_{i,j}$	position vectors of the mass elements dm_c, dm_i, and $dm_{i,j}$, respectively as measured from the centre of force; Eq. (2.9)
$R_{cm}, R_c, R_i, R_{i,j}$	magnitudes of $\bar{R}_{cm}$, $\bar{R}_c$, $\bar{R}_i$, and $\bar{R}_{i,j}$, respectively
S_x, S_y, S_z	pointing errors of the manipulator in the orbit normal, local vertical, and local horizontal directions, respectively; Eq. (4.5)
S_{tot}	$\sqrt{S_x^2 + S_y^2 + S_z^2}$
T	total kinetic energy of spacecraft
T_{sys}	system kinetic energy due to various coupling effects; Eq. (2.35)
U	potential energy of spacecraft; $U_e + U_g$
$\mathbf{U}$	unit matrix
U_e	strain energy of spacecraft; Eq. (2.40)
U_g	gravitational potential energy of the spacecraft; Eq. (2.38)
X_k,Y_k,Z_k	body coordinate axes associated with B_c, B_i, and $B_{i,j}$, re-

	spectively; $k = c$, i, or i, j
X_o,Y_o,Z_o	inertial coordinate system located at the earth's center
X_p,Y_p,Z_p	coordinate axes with origin at C^f and parallel to x_c,y_c,z_c, respectively
X_s,Y_s,Z_s	orbital frame with X_s in the direction of the orbit-normal, Y_s along the local vertical, and Z_s towards the local horizontal; Figure 2-4
α_s, α_t	absorptivity and coefficient of thermal expansion of the appendage material, respectively
α_{sl}, α_m	slewed angle and maximum slew angle; Eq. (4.4)
$\bar{\delta}_c, \bar{\delta}_i, \bar{\delta}_{i,j}$	vectors representing transverse vibration of dm_c, dm_i, and $dm_{i,j}$, respectively; Figure 2-2
α_x, α_y, α_z	angular accelerations of the system about X_c, Y_c and Z_c axes, respectively
δ_k^y, δ_k^z	tip deflection of a beam element in the Y_k and Z_k directions, respectively; $k = c$, i, or i, j; Eq. (4.1)
ϵ	eccentricity
ϵ_k^x, ϵ_k^y	end deflection of a plate centerline in X_k and Y_k directions, respectively; $k = c$, i, or i, j; Eq. (4.2)
ϕ	rotation about the local horizontal axis, Z_1, of the intermediate frame X_1,Y_1,Z_1; Figure 2-4
$\phi_k^x, \phi_k^y, \phi_k^z$	solar radiation incidence angles measured with respect to X_k, Y_k, and Z_k axes, respectively; $k = c$, i or i, j
$\bar{\phi}_k$	column matrix representation of the direction cosines of solar

	radiation incidence angles; $\{\cos\phi_k^x, \cos\phi_k^y, \cos\phi_k^z\}^T$; $k = c$, i or i, j;
λ	rotation about the local vertical axis, Y_2, of the intermediate frame X_2,Y_2,Z_2; Figure 2-4
μ_e	gravitational constant
$\mu_{i,j}$	matrix representing slewing motion of body $B_{i,j}$
θ	true anomaly
ρ	longitude of the ascending node; Figure 2-3
$\bar{\rho}_c, \bar{\rho}_i, \bar{\rho}_{i,j}$	vectors denoting positions of dm_c, dm_i, and $dm_{i,j}$, respectively, in the undeformed configuration of the spacecraft; Figure 2-2
σ_t	Stefan-Boltzman constant
τ_{sl}	slewing period; Eq. (4.4)
$\bar{\tau}_c, \bar{\tau}_i, \bar{\tau}_{i,j}$	vectors denoting thermal deformations of dm_c, dm_i, and $dm_{i,j}$, respectively; Figure 2-2
ω	argument of the perigee point; Figure 2-3
$\bar{\omega}$	librational velocity vector with respect to X_p,Y_p,Z_p axes; Eq. (2.2)
ψ	rotation about the orbit normal, X_s; Figure 2-4

ABBREVIATIONS

c.m.	center of mass
p-p	peak-to-peak
DOF	Degrees Of Freedom

FEL	First Element Launch
FEM	Finite Element Method
FLT	Feedback Linearization Technique
IP	InPlane
INSAT II	INdian SATellite II
MSS	Mobile Servicing System
OP	Out-of-Plane
PMC	Permanently Manned Configuration
PV	PhotoVoltaic
QCLC	Quasi-Closed-Loop Control
QOLC	Quasi-Open-Loop Control
SAP	Solar Array Pedal
SFU	Space Flyer Unit
SSM	Substructure Synthesis Method

Dot ($\dot{}$) and prime ($'$) represent differentiations with respect to time t and true anomaly θ, respectively. Subscripts o and e indicate initial and equilibrium conditions, respectively. Unless stated otherwise, overbar ($\bar{}$) represents a vector; **boldfaced** symbol, a matrix; and underbar ($\underline{}$) refers to a dimensionless quantity.

LIST OF FIGURES

LIST OF TABLES

ACKNOWLEDGEMENTS

I would like to thank Prof. V.J. Modi for his guidance throughout the preparation of the thesis.

The thesis has benefited from discussions and consultation among colleagues. In particular, I would like to express my gratitude to Mr. J. Chan, Mr. H. Mah, and Mr. A. Suleman for exchange of ideas. Also, Dr. Karray has provided useful tutorial into the nonlinear control study. His help is deeply appreciated.

During the course of my Ph.D. study, program execution went through a transition from the mainframe to decentralized workstation. This was facilitated through the technical advice offered by Mr. A. Steeves. Special thanks to Prof. D. Cherchas for the use of VaxStation 3200.

The research project is supported by the Natural Sciences and Engineering Research Council of Canada, Grant No. A–2181 and the Center of Excellence Program, Grant No. IRIS/C–8, 5–55380, both held by Prof. Modi.

1. INTRODUCTION

1.1 Preliminary Remarks

Ever since the launching of the first satellite Sputnik in 1957, there is a general trend towards larger and more complex spacecraft designs. This is as a consequence of the ever increasing demand on spacecraft capabilities in telecommunications, weather forecasting, surveillance, remote sensing and others. Most of the designs can be identified as consisting of a main body with appendages attached to it. The main body can be rigid or flexible whereas the appendages in the form of solar arrays, antennas, robotic arms, etc. are usually flexible. The following few examples of contemporary spacecraft illustrate this point:

(i) The European Space Agency's L–SAT (Large SATellite system, Olympus, Figure 1-1), launched in 1989, represents a new generation of communications satellite. It has two solar panels, each 25 m in length, connected to a central body.

(ii) To better understand the behaviour of flexible structures in space and their control, the NASA's Langley Research Centre once designed an Orbiter based experiment called COFS (Control Of Flexible Structures). Its first phase, called SCOLE (Structural COntrol Laboratory Experiment, [1]), involved laboratory simulation of a flexible configuration as shown in Figure 1-2 followed by flight verification on board the Shuttle. The experimental setup consists of a mast around 40 m in length, with its one end attached to the shuttle. At the other end, there is an asymmetrically mounted reflector plate-type antenna, 22.8 m in diameter.

(iii) The U.S. led Space Station *Freedom*, scheduled to be completed around 1998,

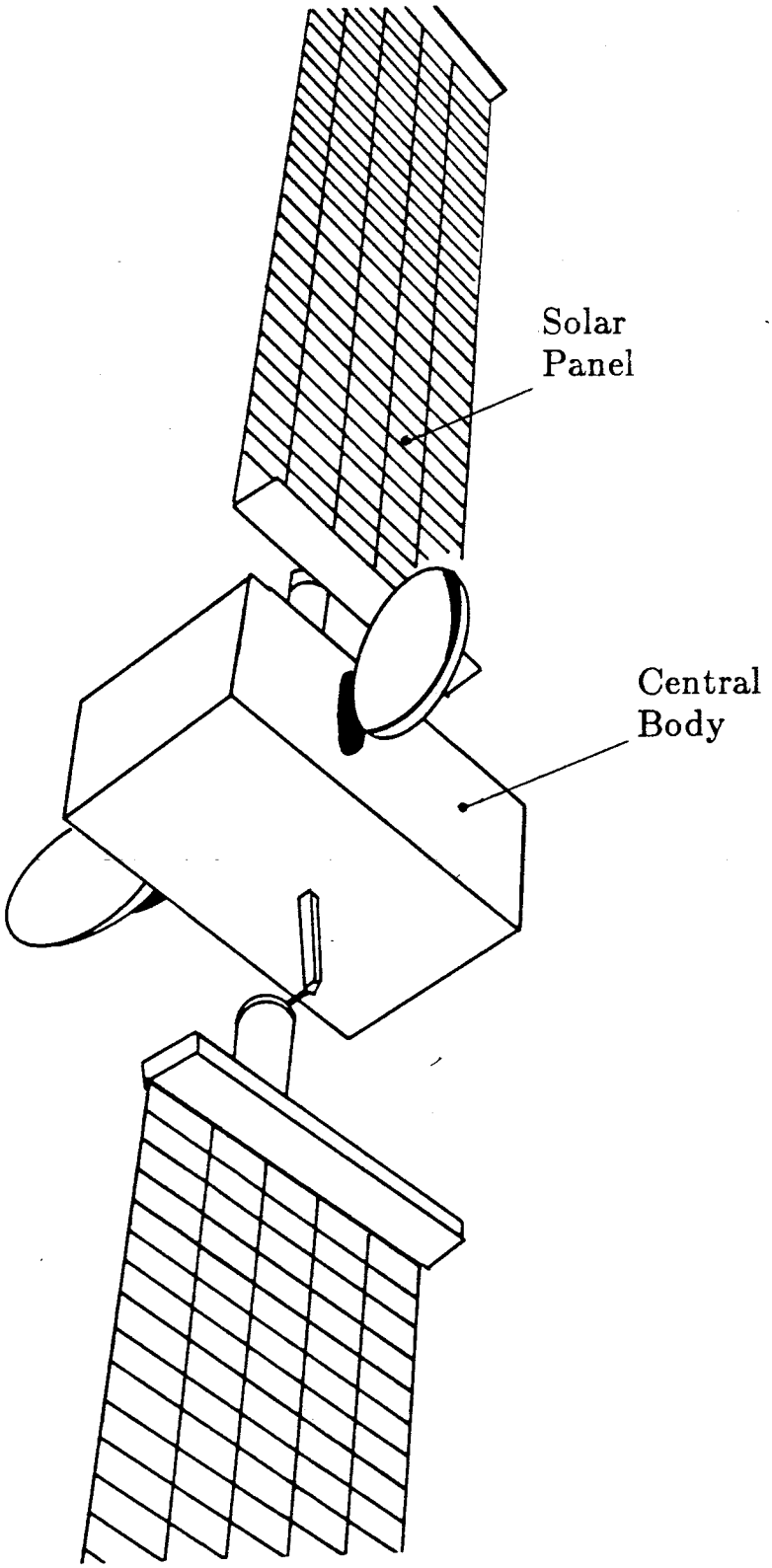

Figure 1-1 The European Space Agency's L–SAT (Olympus) launched in 1989.

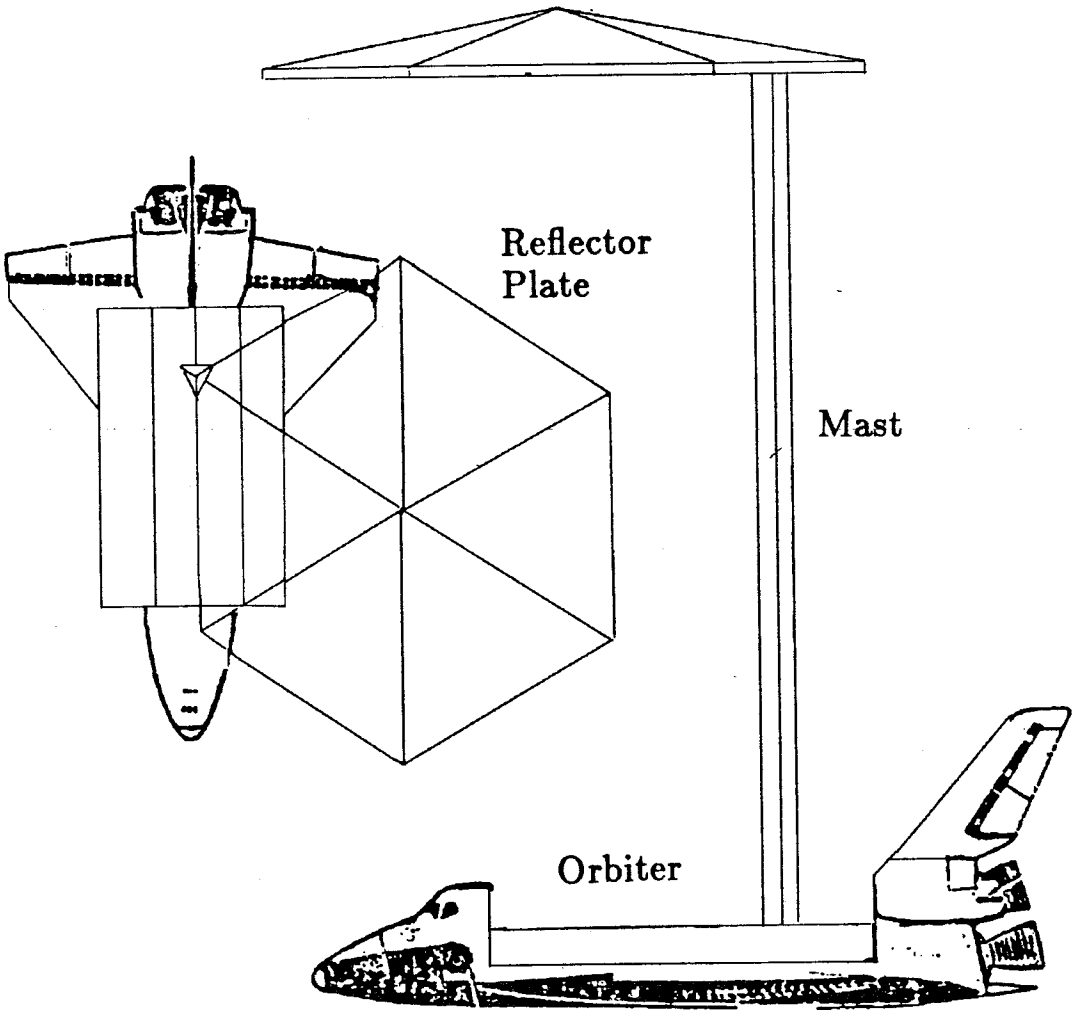

Figure 1-2 SCOLE configuration showing the main components: shuttle, mast, and plate-type reflector antenna.

will have a main truss of 155 m in length. Equipment attached to the truss includes habitat, command and other modules, power generation equipment and system control assembly, stinger and resistojet, photovoltaic (PV) arrays, PV array and station radiators, etc. (Figure 1-3).

The space dynamicists have traditionally relied mostly on mathematical tools to design spacecraft. Ground based experiments have been of limited value due to practical difficulty in simulating environmental forces (gravity gradient, magnetic, free molecular, solar radiation, etc.) and structural flexibility. This has led to increasing dependence on numerical methods, particularly with larger and more complex spacecraft configurations. A general formulation applicable to a large class of systems is always attractive although it usually demands more time and effort. On the other hand, once the governing equations are established and the associated integration program is operational, it becomes a powerful versatile tool. Several, relatively general, approaches for multibody dynamics simulation have been developed. In general, they treat systems of interconnected rigid/flexible bodies of tree-type topology. As can be expected, each approach has its own special features. Some of them are touched upon below:

(i) Treetops, developed by Singh et al. [2], is based on Kane's method in formulating the equations of motion. Deformations are described by a modal set which satisfies the kinematic boundary conditions. It has the capability to carry out numerical linearization and control simulation.

(ii) ALLFLEX, designed by Ho et al. [3,4], formulates the equations of motion using Ho's direct path method [5] in conjunction with the Lagrangian or Newtonian approach. Substructure modal data are obtained through a finite element program. Besides control simulation capability, the program has

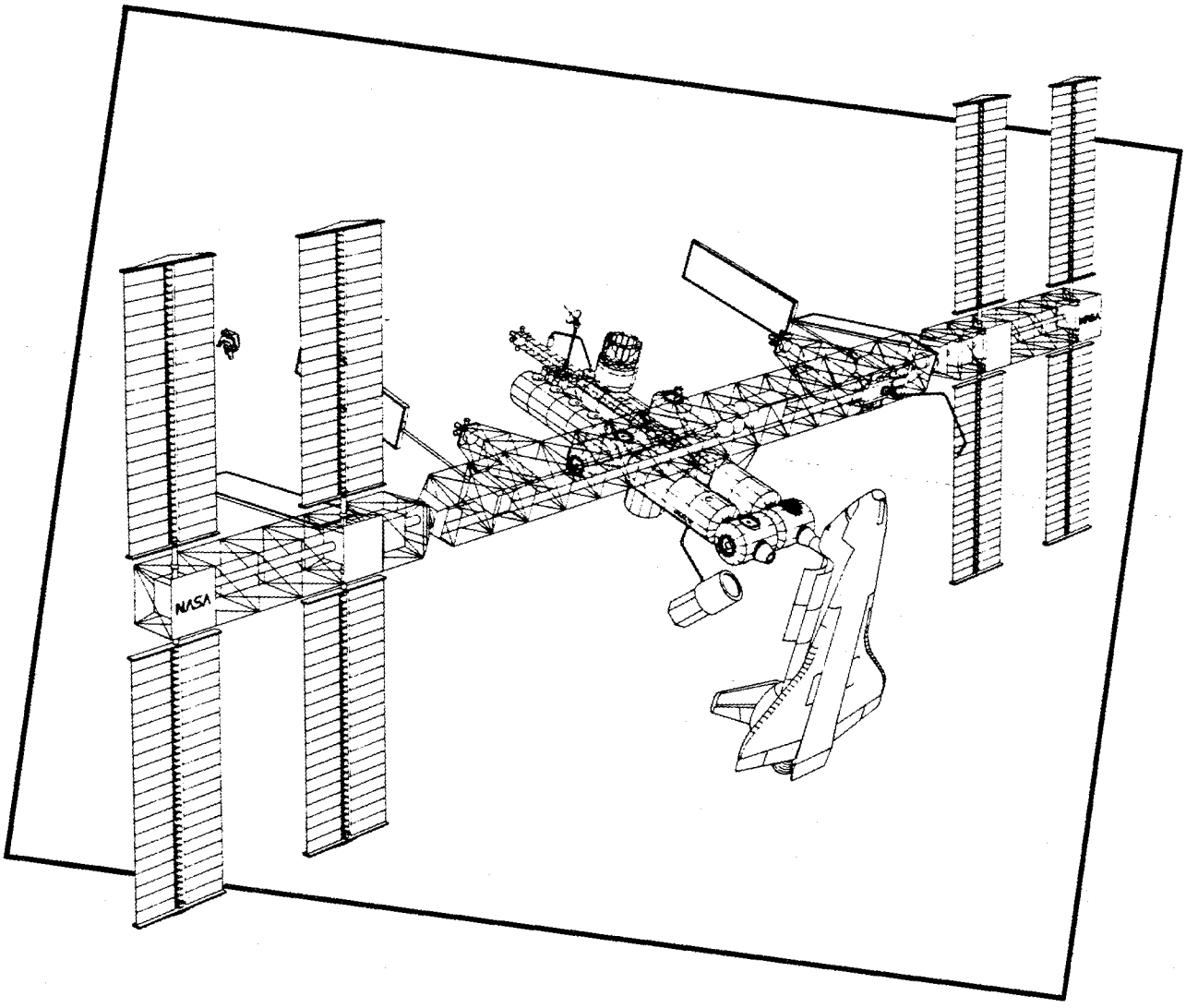

Figure 1-3 The proposed Space Station *Freedom* configuration as of 1988.

a provision to accept subroutines accounting for the environmental disturbances.

(iii) DISCOS (Dynamic Interaction Simulation of COntrols and Structures) is an industry standard software for multibody dynamics simulations. The equations of motion are derived using Lagrange's approach. The program has several features of both the Treetops and ALLFLEX.

A measure of the program efficiency is the order of the algorithm, n^x, where n is the number of degrees of freedom and x is the index of the order. Physically, the order relates to the computational time. As the number of degrees of freedom doubles, the execution time is expected to increase by 2^x times. Obviously, a small index is desirable. The order of the Treetops is not revealed in literature whereas ALLFLEX and DISCOS have orders of n^2 and n^3. Recent developments in DISCOS have reduced the order to n for some special cases [6].

These three programs are described as easy to use and portable among computers. A number of users would not agree with this assertion. Experience suggests that making a program operational and applicable to a problem in hand often involves enormous time and effort. Perhaps the major limitation is their 'black-box' character which makes any enlighten variations virtually impossible. Thus one is left with a feeling of a bystander pulling levers and collecting massive output of numbers rather than actively participating in the investigation. There are two other aspects to consider:

(i) Besides portability of the program, its size is a critical factor in determining whether the program can be executed on a new machine. The limitation on size is particularly important in time-sharing computer systems.

(ii) To take advantage of the feature that allows user-supplied subroutines, one

has to have a thorough understanding of the formulation procedures and program architecture. Unfortunately, this information is not provided because of the proprietary considerations. Even when available, their thorough understanding would entail substantial effort and time.

This being the case, considerable interest exists in the community of space dynamicists and control engineers to develop efficient, relatively general formulations, applicable to a class of systems of contemporary interest, and associated algorithms that are user-friendly. The present thesis takes a small step in that direction.

1.2 A Brief Review of the Relevant Literature

Over the past thirty years, the amount of literature accumulated on the subject of spacecraft dynamics is literally enormous. It can be classified into four broad categories: formulation; dynamics and control; environmental effects; and experimental validation. The thesis is primarily concerned with the first three aspects: formulation, dynamics and environmental effects (thermal); hence, the focus of the review is in these areas. Likins [7], Modi et al. [8−10], Roberson [11], and Markland [12] have provided excellent overview of the subject. Theses by Lips [13], Ibrahim [14], Chan [15] and others have also reviewed relevant aspects at great lengths to acquaint an interested researcher with the status of the field.

Perhaps year 1965 marked the beginning of interest in the multibody formulation methodology. Early literature was limited to rigid spacecraft with hinged joints. Hooker and Margulies [16] derived the attitude equations for n rigid bodies interconnected to form a topological tree configuration. The formulation was based on the Newton-Euler approach and accounted for dissipative and elastic joints. This problem was also studied by Roberson and Wittenburg [17] who introduced the idea of system-graph, which made the implementation of the equations on a digital computer

easier.

Roberson [18] later extended the study to interconnected nonrigid bodies where translational motion between the members was allowed. Ho [5] considered a tree-type topological configuration with the end bodies flexible. He selected the direct path method and derived the equations using both the Newton-Euler as well as Lagrangian procedures. The latter formulation was found to be faster from the mathematical point of view as the lengthy procedure to eliminate the constraint forces and torques was not necessary. To overcome this drawback of Newton-Euler method, Hooker [19] has shown that it is possible to use Ho's method together with Newton-Euler approach to derive equations of motion in which constraint forces and torques do not appear explicitly.

By introducing path and reference matrices that describe the topology of n-body configurations, Jerkovsky [20] presented the equations of motion for both tree-type and closed-loop configurations. A comparison with the multibody formulations by Roberson and Witterburg [17], Hooker [21], Ho [5], and several others was also given.

Hughes [22] derived the equations of motion for a chain of flexible bodies with terminal members rigid. The Newton-Euler approach was used and the resulting equations were linear in the angular rates as well as elastic deformations. The equations were tailored for control system design.

Kane and Levinson [23] compared the pros and cons of different formulation techniques such as Newton-Euler method, D'Alemberts' principle, Hamilton's canonical equations and Lagrangian procedure. They then introduced what is referenced as "Kane's method" using two classes of quantities known as "partial angular velocities" and "partial velocities." The authors have concluded that "Kane's method" leads to the simplest equations.

Using the Lagrangian procedure, Modi and Ibrahim [24] presented the general equations of motion for studying librational and vibrational dynamics of a large class of spacecraft during deployment of flexible members. The equations accounted for the gravitational effects, shifting center of mass, changing rigid body inertia, appendage offset and transverse oscillation. Appendages with variable mass density, flexural rigidity, and cross-sectional area along its length can also be accommodated.

For a maneuvring spacecraft, the general equations of motion were obtained by Meirovitch and Quinn [25] using the Lagrangian approach in conjunction with the component mode synthesis. In order to improve computational efficiency, a perturbation approach was then applied. This resulted in a set of equations governing the rigid-body motion (unperturbed system), and a system of time-varying linear equations for small elastic motions as well as deviations from the prescribed rigid-body maneuver (perturbed system).

Vu-Quoc and Simo [26] studied the dynamics of satellites with flexible components by referring the motion directly to the inertial frame. In order to avoid numerical problems associated with ill-conditioned matrices, the dynamics of far field (attitude motion) and near field (elastic deformations) were treated separately through introduction of a rotationally-fixed floating frame.

Recent contributions in multibody formulation include studies by Keat [27] using the velocity transform method, Huston [28] employing Kane's method, and Kurdila [29] relying on Maggi's approach. Unlike the earlier studies, the emphasis here is on the numerical efficiency rather than methodology.

The literature on spacecraft control is primarily concerned with two aspects: attitude control and vibration control. Contributions in the attitude control field have been reviewed by Roberson [11] whereas Balas [30], and Meirovitch and Öz [31] have

provided overviews of the vibration control problems. A few studies aimed at control algorithms for flexible spacecraft are briefly touched upon here.

Flexible spacecraft, being a distributed parameter system, needs to be discretized to study the associated dynamics and its control. The discrete system can be transformed further into the modal-space using modal matrices. Meirovitch and Öz [32] have found that the control as applied to the transformed system (modal-space control) is more efficient than that applied to the discrete system ("actual space" control). Subsequent contributions by the same authors [33–35] study application of the modal-space control to different spacecraft configurations.

Balas [36] examined the undesirable effects of applying control to a flexible structure discretized by a limited number of modes. This effect, known as spillover, results in the excitation of unmodeled modes. Using modal-space control, the author [37, 38] has derived the conditions under which spillover effect can be eliminated. The idea was later extended to attitude stabilization of flexible spacecraft [39]. Balas has also discussed advantages of the Direct Velocity FeedBack (DVFB) procedure [40]; however, implementation of the DVFB was found to be quite involved.

Wie and Bryson [41] modeled flexible space structures using single-input single-output transcendental transfer functions. The models were simple enough for poles and zeroes to be determined analytically. The results were then used in the preliminary controller design. Wie [42] applied this approach to Control of Flexible Structures (COFS–I) mast flight system . Chu et al. [43] employed the same idea in modeling and designing the Space Station attitude controller. Using multi-input multi-output transfer functions and numerical algorithms, Kida et al. [44] designed the controller of flexible spacecraft with constrained and unconstrained modes.

Goh and Caughey [45] explored the idea of stiffness modification in vibration

suppression of flexible structures. The control scheme guaranteed global stability by virtue of the positive definite rate of energy decay. The implementation required not the conventional actuators but rather transducers which converted strain into control signals and then into electronic damping. This was considered to be a favourable feature.

In understanding the problem at a fundamental level and progressively making it more complicated to approach a real-life situation, the study by Reddy et al. [46] concerning attitude and vibration control of plate-like platform is particularly useful. Equally informative are the contributions by Yedavalli [47] and Sundarnarayan et al. [48] on the robustness of controllers for Large Space Structures (LSS) applications.

In general, the studies pertaining to environmental influence on spacecraft dynamics and control are relatively few; however, contributions on solar radiation effects are not lacking. Among them, research by Modi et al. [49–54], Beletsky and Starostin [55], Goldman [56], Yu [57], Frisch [58,59], Tsuchiya [60,61], and Bainum et al. [62–66] are worth-mentioning.

Modi and Brereton [49] studied the planar librational stability of a slender flexible satellite under the influence of solar heating. Using the quasi-static solutions describing a thermally flexed configuration and the concept of integral manifold, the authors developed charts as functions of initial conditions and eccentricity showing limiting stability of the satellite. In general, thermal heating was found to decrease the size of the stability region.

A similar approach was adopted by Modi and Flanagan [50–52] to study the influence of solar radiation pressure on gravity oriented satellites at different altitudes. It was observed that the solar radiation was a significant disturbance except at low altitudes (less than 1000 km) where aerodynamic drag became dominant. Introduc-

ing the solar parameter proportional to the satellite length, the difference between material reflectivity and transmissivity, offset of the center of pressure, etc., stability charts were obtained which clearly indicated the effect of solar radiation. The significance of the solar parameter was two-fold. On the one hand, the stability region decreased as the parameter value increased. On the other hand, for a given initial condition, there existed a value of the solar parameter for which librational motion was minimum. By a judicious choice of the solar parameter, the authors [53] showed that solar radiation can be utilized to damp the librational motion effectively.

Modi and Kumar [54] studied the solar heating effect on gravity oriented satellites with flexible plate-type appendages. Employing the integral manifold concept, stability charts were obtained. Appendage flexibility was found to cause a substantial reduction in the size of the stability region. The destabilizing influence was particularly severe in presence of the solar radiation pressure and orbit eccentricity. Similar problem was also studied by Beletsky and Starostin [55]. The emphasis was on the existence and stability of symmetrical and nonsymmetrical periodic solutions. The problem was solved by both the analytical (Volosov-Morgunov averaging method) and numerical means.

Using a quasi-static approach, Goldman [56] studied the influence of solar heating on the dynamic stability of a satellite. Equilibrium position of the booms in the presence of differential heating was determined without consideration of the transverse deformations. The simulation results helped to confirm that solar heating contributed to the anomalous behavior of the Naval Research Laboratory's Gravity Gradient Satellite 164.

Yu [57] investigated thermally induced vibration of spacecraft booms with a tip mass. The problem was formulated using Hamilton's principle. In absence of damp-

ing, the motion of the boom was found to be stable if pointed away from the sun. Viscous-fluid damper incorporated into the tip mass also proved to be effective in suppressing thermal flutter. However, the results are controversial: using other approaches, Jordan [67] and Augusti [68] concluded that the boom motion was stable only when pointed towards the sun.

Frisch [58] studied coupled nonplanar transverse and torsional vibration of booms. Numerical simulation results helped to explain the anomalous behaviour of several three-axis-stabilized satellites with long extendable booms. The results showed that thermally induced vibration can be eliminated by increasing torsional rigidity of the boom. The author also presented approaches based on finite element and finite difference methods to include thermal effect in multibody formulations [59].

Tsuchiya analyzed the effect of thermally induced appendage vibration on a spinning satellite [60], and a satellite with a rotor [61]. The criteria for appendage resonance were derived. Amplitudes of the vibrational and nutational motions were determined by the method of averaging. Numerical simulation of the system near the resonance was also presented.

Krishna and Bainum examined the effects of solar radiation pressure on the rigid and flexible modes of a beam [62] and a square plate [63]. The dynamical response indicated that induced rigid body response was more significant than the flexible motion. Control laws based on linear quadratic Gaussian technique were found to be effective in providing both shape and orientation control. The authors [64–66] later extended the study to include thermal deformation of the structure. In general, the effect of solar radiation pressure acting on structures undergoing thermal deformations was found to be relatively more important.

Sikka et al. [69] studied the static problem of thermal deformation. The tem-

perature distribution and curvature produced in long, solid circular and rectangular cross-section cylinders were obtained using approximate analytical methods such as the least-square fitting. Modeling a lattice-type space structures using finite element method, Lutz et al. [70] carried out a thermoelastic analysis of the structural members. Although thermal moments were found to be very small, thermal axial forces induced significant mechanical bending in the structure.

1.3 Scope of the Present Investigation

With this as background, this thesis presents a relatively general formulation particularly suitable for studying dynamics of evolving structures such as the Space Station. In essence, it is a Lagrangian formulation based on the direct path method. The emphasis is on the applicability of the formulation to study complex dynamics of large space structures using relatively simple mathematical models to gain better physical understanding of interactions between librational dynamics and flexibility. The formulation has the following distinctive features:

(i) It is applicable to an arbitrary number of lumped masses, beam and plate type structural members, in any desired orbit, interconnected to form a tree-type topology.

(ii) It takes into account slewing of solar panels and transverse vibrations of the bodies. Thus, it is possible to study the complex system dynamics due to interactions between librational motion, transverse vibration, and slewing maneuvers.

(iii) The shift in the centre of mass due to transverse vibrations and slewing maneuvers is incorporated in the formulation.

(iv) The formulation accounts for the thermal deformation of both beam and plate

type appendages explicitly. Effect of the free molecular environment can be introduced quite readily through generalized forces.

(v) The governing nonlinear, nonautonomous and coupled equations are programmed in such a way that the effects of flexibility, librational motion, thermal deformation, slewing maneuvers, shifting c.m., higher modes, initial conditions, etc. can be isolated easily.

The thesis can be divided into four parts: relatively general formulation of the problem; program implementation; numerical simulation; and control study.

The problem formulation begins with the study of kinematics of a spacecraft with interconnected flexible bodies. The discretization of elastic deflection and evaluation of the thermal deformation are discussed next, leading to the expressions for kinetic and potential energies. Using the Lagrangian procedure, general equations of motion, applicable to a large class of systems, are obtained.

The second part discusses implementation of the equations of motion into computer codes. It briefly describes transformation of the equations into a form suitable for numerical analysis and develops associated algorithm. The emphasis is on the methodology that results in algorithms which are both easy to program and debug. Validity of the program is first established through comparison of dynamical simulation results, for two particular configurations, obtained by Ng [71] and Chan [15]. The convergence of the numerical solution is also demonstrated.

In the third part, response simulation of four distinctively different spacecraft configurations of contemporary interests is carried out. The objective here is to study complex interactions between librational and vibrational dynamics, flexibility and initial disturbances. Effects of thermal deformations are also discussed. The amount of information obtained is literally enormous; however, for brevity, only some

typical results useful in establishing trends are presented here.

The next logical step is to explore effectiveness of a control strategy applicable to such a formidable class of problems. The last part studies the control using the feedback linearization approach to selected spacecraft models.

The concluding chapter summarizes more important results and presents recommendations for future studies. An overview of the thesis layout is shown in Figure 1-4

.

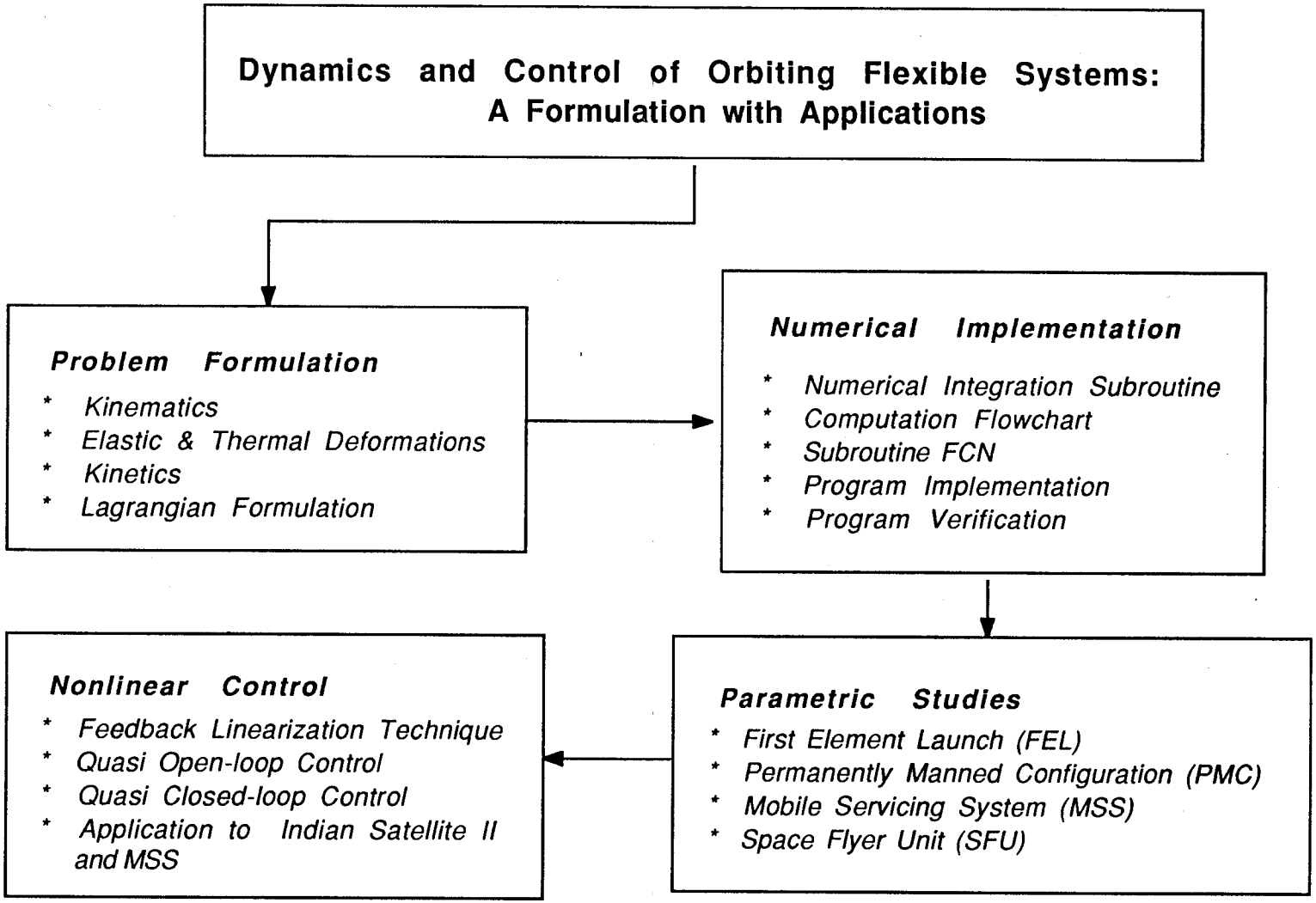

Figure 1-4 The layout of the thesis showing the four major parts of the present study.

2. FORMULATION OF THE PROBLEM

2.1 Preliminary Remarks

From the literature review, it is apparent that the the Newton-Euler method and the Lagrangian approach are more commonly used procedures in the dynamical formulation of multibody systems. The Newton-Euler method is based on the principle of angular momentum whereas the Lagrangian approach relies on the system energy. Attractive features of the Newton-Euler method include relatively less time and effort as well as more compact form of the governing equations. This also makes the Newton-Euler method computationally more attractive. However, the method has two major drawbacks:

(i) It requires the introduction and subsequent elimination of the constraint forces.

(ii) The principle of angular momentum has to be applied at the centre of mass of the system; hence, for a system with shifting center of mass, its application can lead to inaccuracies.

In the present study, due to the complex character of the system, the elimination of constraint forces is indeed quite involved. Also, due to the thermal deformations and transverse vibrations of the appendages, the centre of mass is shifting. Application of the Newton-Euler method is, therefore, not particularly attractive. On the other hand, Lagrangian approach does not suffer from these limitations. Furthermore, Silver [72] has shown that, at least for ground based robot manipulators, the Lagrangian formulation with a proper choice of generalized coordinates can be numerically as efficient as the Newton-Euler approach. However, the Lagrangian procedure has its own undesirable features –it involves enormous amount of algebra leading to

lengthy equations of motion. This is especially true in the case of multibody systems where position vectors are represented as a product of a matrix (e.g. $\mathbf{A}$) and a vector (say, $\bar{U}$). Differentiation of either $\mathbf{A}$ or $\bar{U}$ is not difficult to handle; however, differentiation of the product of $\mathbf{A}\bar{U}$ would involve enormous amount of algebra, especially when second derivative is required. Fortunately, with the advent of computers and refined softwares, the problem is manageable. The user supplies the derivatives of $\mathbf{A}$ and $\bar{U}$ and let the computer evaluate the derivatives of products by numerical means. This approach is appealing in cases where closed-form solution to the problem does not exist and a numerical simulation is the only alternative. In the present case, the governing equations of motion are expected to be highly nonlinear, nonautonomous, and coupled; hence, closed-form solution is not expected to exist. The Lagrangian procedure is therefore selected to assure accuracy of the governing equations.

This chapter can be divided into four sections: kinematics, substructure deformations, kinetics, and the Lagrangian formulation. The kinematics begin with a discussion of the system geometry and reference coordinate systems used to identify the deformed configuration. The spatial orientation of the system as described by a set of orbital elements and modified Eulerian rotations is presented next, together with the solar radiation incidence angles. Finally, the shift in the center of mass due to deformations, and associated rotation matrices, are discussed. In the following section, determination of thermal and elastic deformations of substructures are explained and application of the assumed mode method to represent elastic deformations examined. The kinetics of the problem deals with evaluation of the kinetic and potential energies. Using the Lagrangian procedure, the governing equations of motion are finally derived.

2.2 Kinematics of the Problem

2.2.1 Configuration selection

The system model selected for study consists of flexible bodies connected to form a branched geometry: central body B_c is connected to bodies B_i $(B_1, \ldots, B_N)$. In turn, each B_i is connected to $B_{i,j}$ bodies $(B_{i,1}, \ldots, B_{i,n_i})$ as shown in Figure 2-1. Altogether, there are N_j $(= \sum_{i=1}^{N} n_i)$ $B_{i,j}$ bodies. The number and locations of bodies are kept arbitrary so that the configuration can be used to study a large class of present and future spacecraft. For instance, to simulate the European Space Agency's Olympus (L–SAT, Figure 1-1), the satellite's central rigid body and two solar panels are represented by bodies B_c and B_i, respectively. As for the SCOLE configuration mentioned earlier, the dynamic simulation may be performed treating the Orbiter, mast and reflector antenna as bodies B_c, B_i, and $B_{i,j}$, respectively. When applied to the proposed Space Station *Freedom*, the central body B_c may simulate the main truss of the Space Station with the modules, power generation equipment and system control assembly treated as lumped masses. The stinger, station radiators, PV arrays and radiators are represented by bodies B_i.

2.2.2 Coordinate system

Consider the spacecraft model in Figure 2-2 . The centres of mass of the undeformed and deformed configurations of the system are located at C^i and C^f, respectively. Let X_o,Y_o,Z_o be the inertial coordinate system located at the earth's centre. Attached to each member of the model is a body coordinate system helpful in defining relative motion between the members. Thus reference frame F_c is attached to body B_c at an arbitrary point O_c. Frame F_i, with origin at O_i, is attached to body B_i at the joint between body B_i and B_c. In addition, for defining attitude and solar radi-

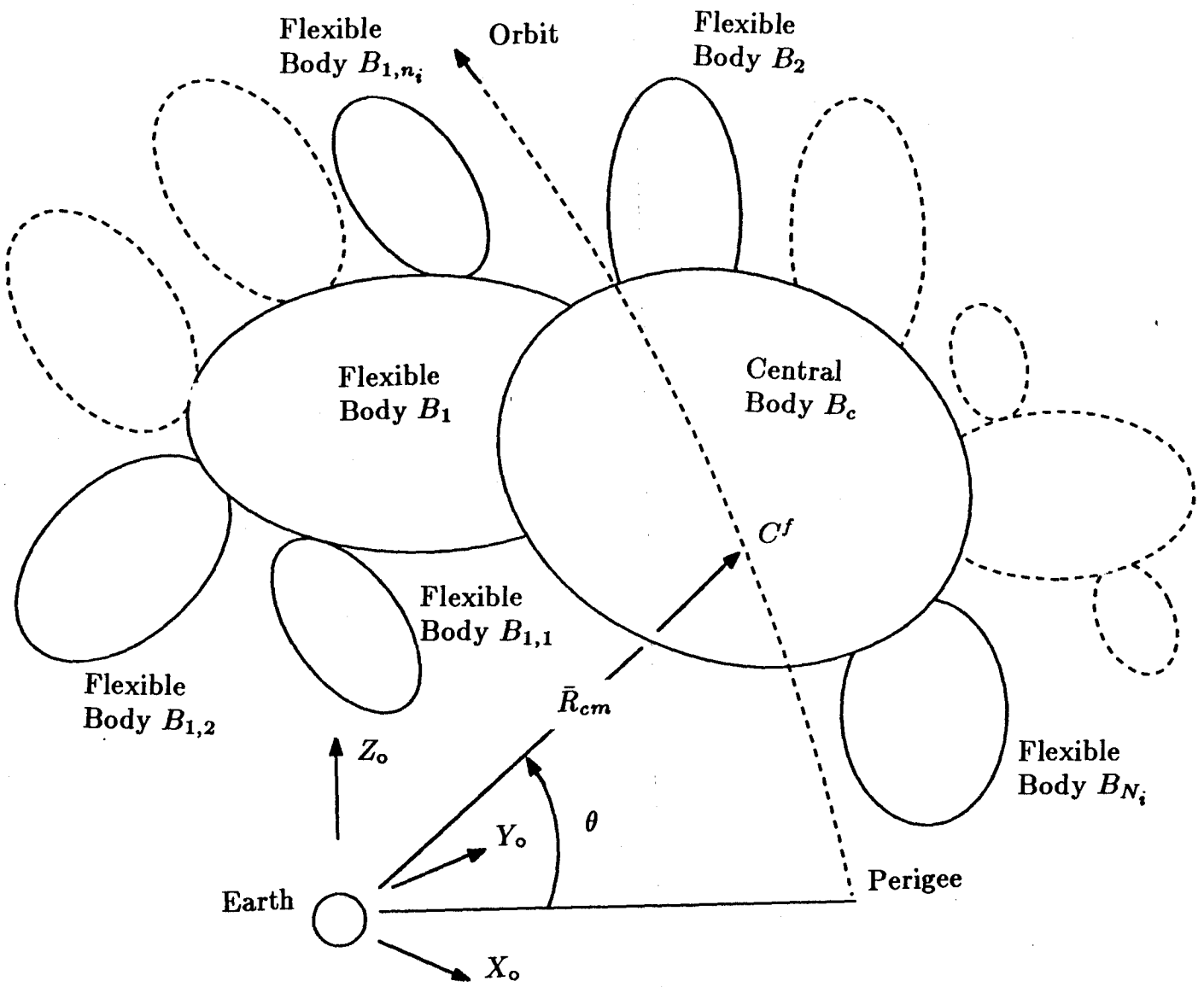

Figure 2-1 A schematic diagram of the spacecraft model.

ation incidence angles, a reference frame is located at C^f such that the axes X_p, Y_p, and Z_p are parallel to X_c, Y_c, and Z_c, respectively. Note, an arbitrary mass element dm_i on body B_i can be reached through a direct path from O_c via O_i. O_c, in turn, is located with respect to the instantaneous center of mass C^f and the inertial reference frame, F_o. Thus motion of dm_i caused by librational and vibrational motions of B_c and B_i can be expressed in terms of the inertial coordinate system. Similarly, frame $F_{i,j}$ is attached to body $B_{i,j}$ and has its origin $(O_{i,j})$ at the joint between B_i and $B_{i,j}$. The relative position of O_i with respect to O_c is denoted by the vector $\bar{d}_i$ whereby $\bar{d}_{i,j}$ defines the position of $O_{i,j}$ relative to O_i.

The location of the elemental mass of the central body, dm_c, relative to O_c is defined by a series of vectors. $\bar{\rho}_c$ indicates the undeformed position of the element. Thermal deformation of the element is represented by $\bar{\tau}_c$. Finally, the transverse vibration of the element, $\bar{\delta}_c$, shifts the element to the end position. Similarly, $\bar{\rho}_i$, $\bar{\tau}_i$, and $\bar{\delta}_i$ define the location of the elemental mass dm_i, in body B_i, relative to O_i. For the elemental mass $dm_{i,j}$ of body $B_{i,j}$, its position relative to $O_{i,j}$ is defined by $\bar{\rho}_{i,j}$, $\bar{\tau}_{i,j}$, and $\bar{\delta}_{i,j}$.

Orientation of the coordinate axes X_i,Y_i,Z_i and $X_{i,j}$,$Y_{i,j}$,$Z_{i,j}$ relative to X_c,Y_c,Z_c is defined by the matrices $\mathbf{C_i^c}$ and $\mathbf{C_{i,j}^c}\mu_{\mathbf{i,j}}$, respectively such that

$$\bar{u}_p = \bar{u}_c = \mathbf{C_i^c}\bar{u}_i = (\mathbf{C_{i,j}^c}\mu_{\mathbf{i,j}})\bar{u}_{i,j}\,, \tag{2.1}$$

where $\mu_{\mathbf{i,j}}$ is the matrix denoting the motion of body $B_{i,j}$ relative to body B_i. $\bar{u}_k$ $(k = p,\ c,\ i,\ \text{or}\ i,j)$ is the column vector representing the unit vectors in the corresponding coordinate axes; for instance, $\bar{u}_c = \{\hat{\imath}_c, \hat{\jmath}_c, \hat{k}_c\}^T$. It should be noted that the thermal deformation and transverse vibration of B_c and B_i result in the time-varying characteristics of $\mathbf{C_i^c}$ and $\mathbf{C_{i,j}^c}$, respectively.

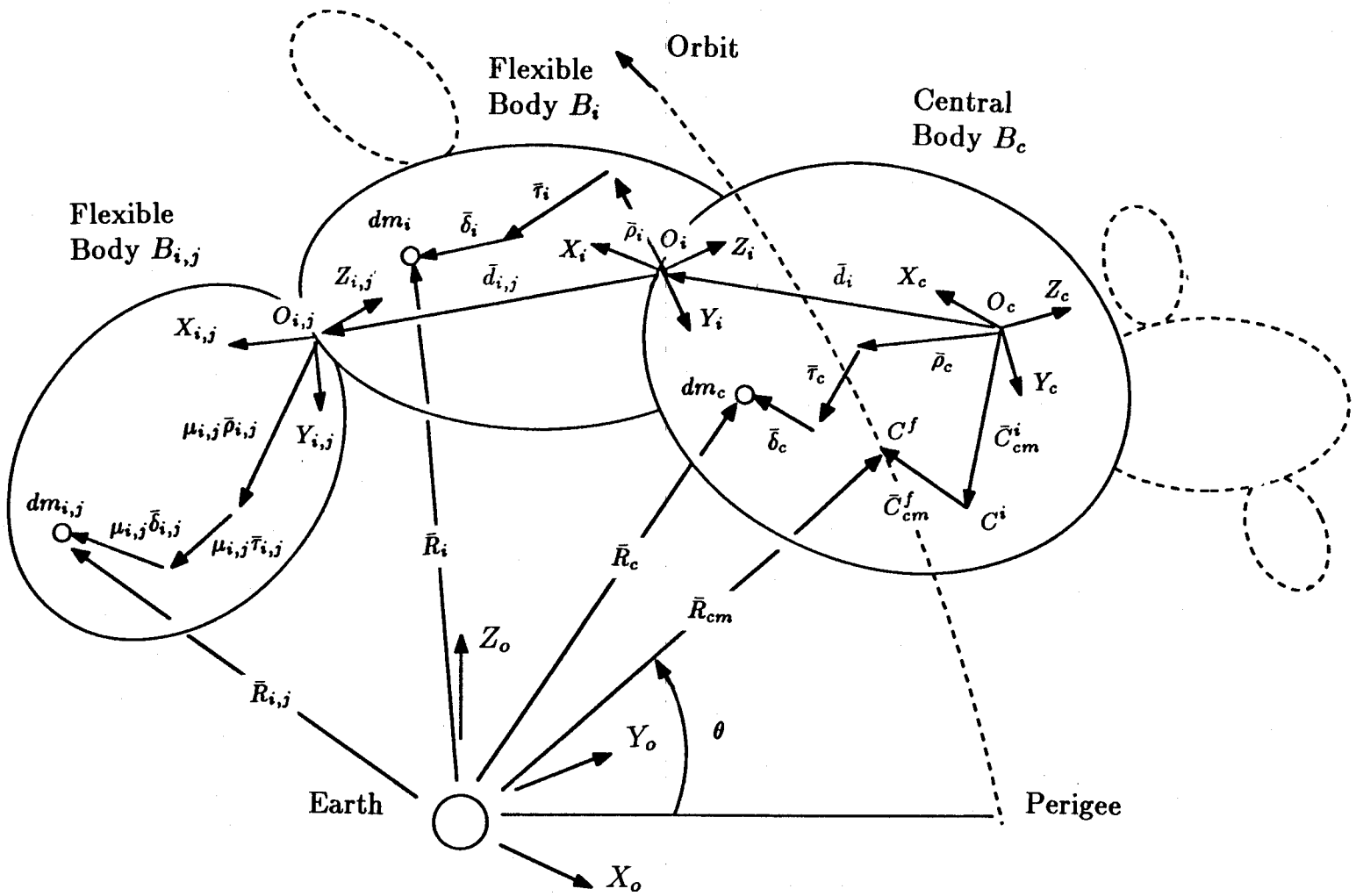

Figure 2-2 The system of coordinates used in the formulation.

2.2.3 Position of spacecraft in space

Consider a spacecraft with its instantaneous centre of mass at C^f negotiating an arbitrary trajectory about the centre of force coinciding with the homogeneous, spherical earth's centre. At any instant, the position of C^f is determined by the orbital elements ρ, i, ω, ϵ, R_{cm}, and θ. Here, ρ is the longitude of the ascending node; i, the inclination of the orbit with respect to the ecliptic plane; ω, the argument of the perigee point; ϵ, the eccentricity of the orbit; R_{cm}, the distance from the center of the earth to C^f; and θ, the true anomaly of the orbit. In general, ρ, i, ω, and ϵ, are fixed while R_{cm} and θ are functions of time (Figure 2-3).

As the spacecraft has finite dimensions, i.e. it has mass as well as inertia, in addition to negotiating the trajectory, it is free to undergo librational motion about its center of mass. Let X_s, Y_s, Z_s represent moving coordinates along the orbit normal, local vertical, and local horizontal, respectively. Any spatial orientation of X_p,Y_p,Z_p with respect to X_s,Y_s,Z_s can be described by three modified Eulerian rotations in the following sequence: a pitch motion, ψ, about the X_s-axis giving rise to the first set of intermediate axes X_1,Y_1,Z_1; a roll motion ϕ about the Z_1-axis generating the intermediate axes X_2,Y_2,Z_2; and finally, a yaw motion, λ, about the Y_2-axis yielding X_p,Y_p,Z_p (Figure 2-4). From the figure, it can be seen that the librational velocity vector, $\bar{\omega}$, is given by,

$$\begin{aligned}\bar{\omega} = &\left[-\dot{\phi}\sin\lambda + (\dot{\theta}+\dot{\psi})\cos\phi\cos\lambda\right]\hat{\imath}_p + \left[\dot{\lambda} - (\dot{\theta}+\dot{\psi})\sin\phi\right]\hat{\jmath}_p \\ &+ \left[\dot{\phi}\cos\lambda + (\dot{\theta}+\dot{\psi})\cos\phi\sin\lambda\right]\hat{k}_p\,, \end{aligned} \tag{2.2}$$

where $\dot{\theta}$ represents the orbital rate of the spacecraft.

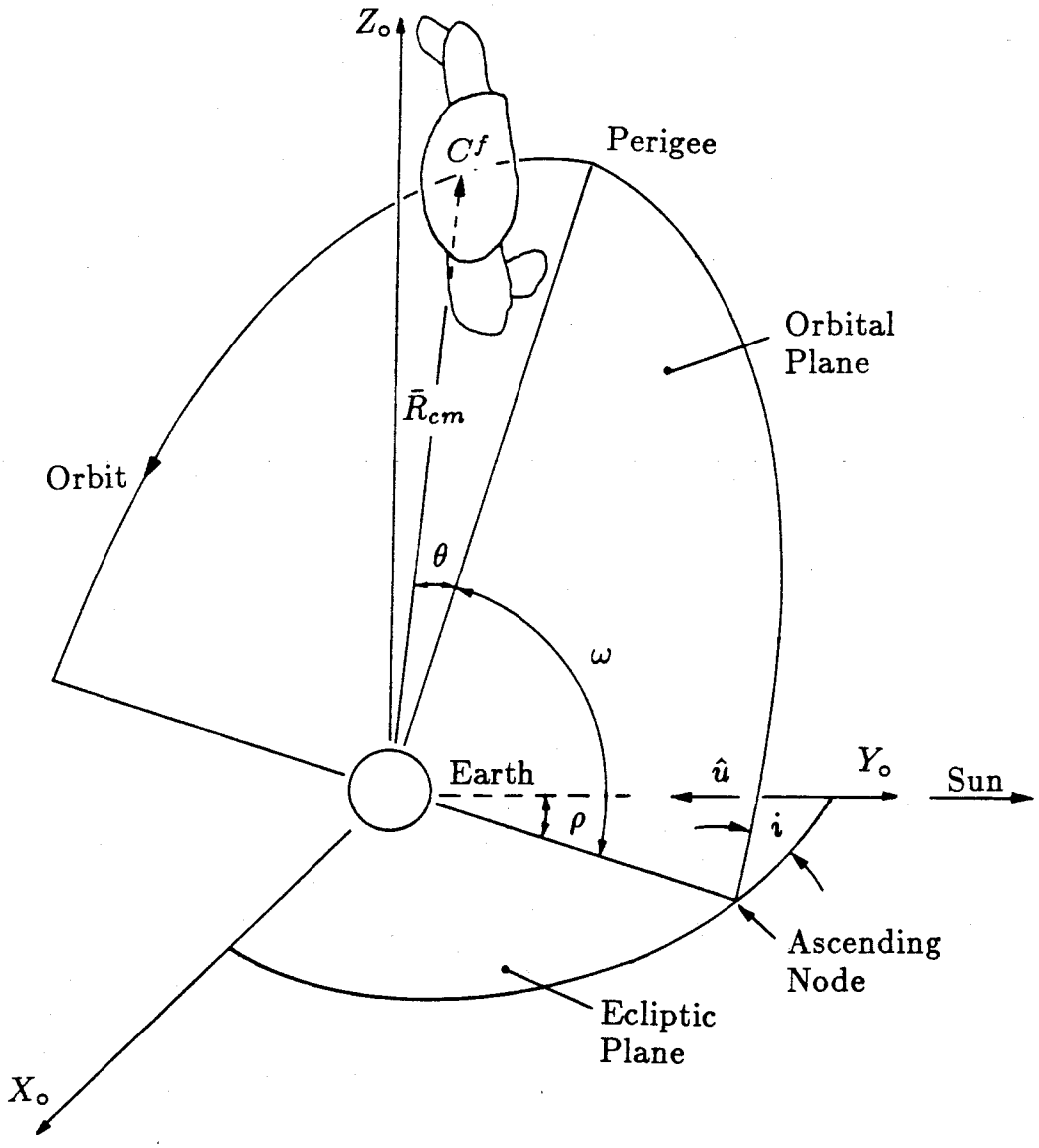

Figure 2-3 Orbital elements defining position of the center of mass of spacecraft.

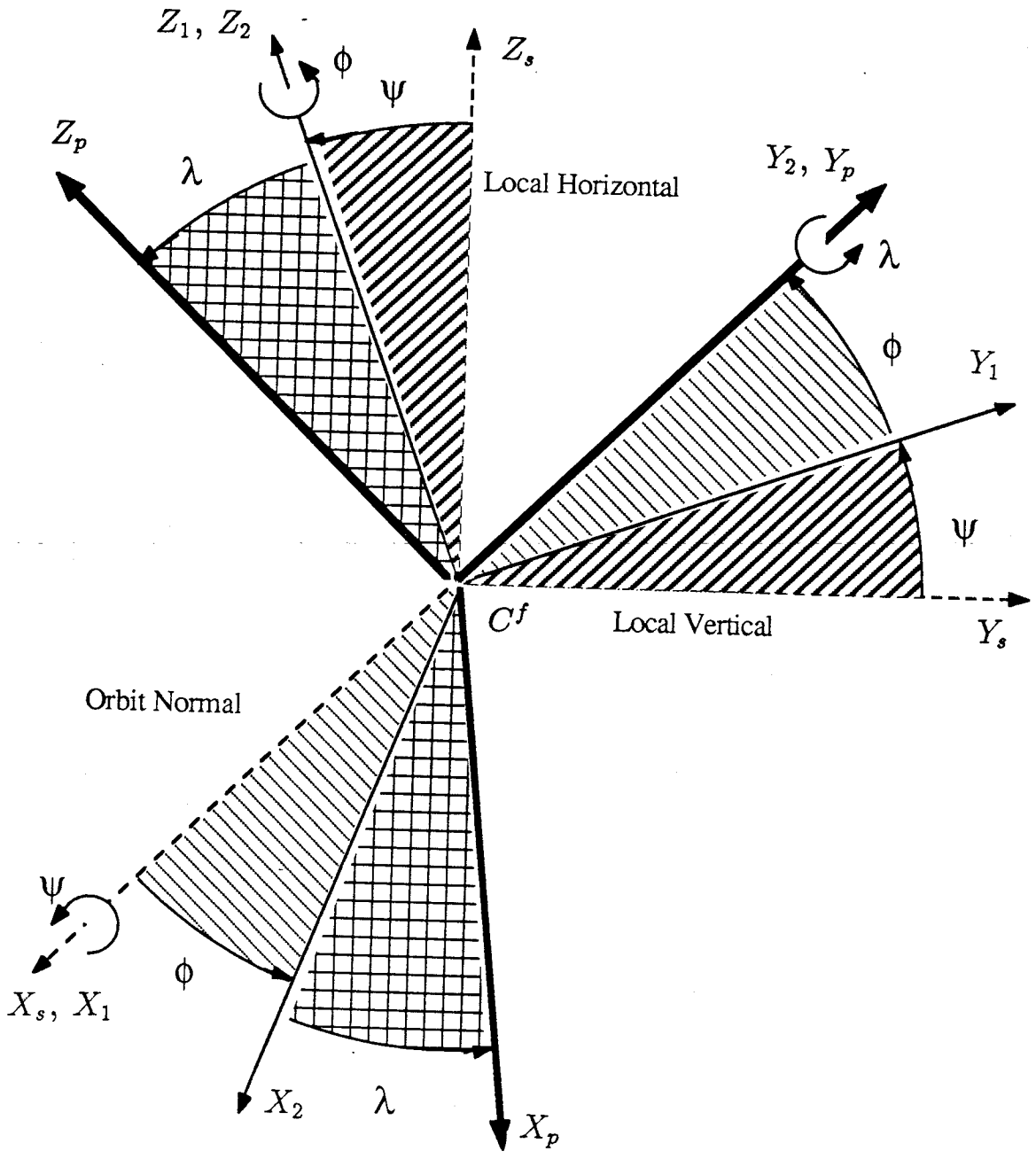

Figure 2-4 Modified Eulerian rotations ψ, ϕ, and λ defining an arbitrary spatial orientation of spacecraft.

2.2.4 Solar radiation incidence angles

Position of the spacecraft with respect to the sun is defined by the solar radiation incidence angles, ϕ_p^x, ϕ_p^y, and ϕ_p^z. They are defined as angles between the unit vector, $\hat{u}$, representing the direction of solar radiation, and the X_p, Y_p, and Z_p axes, respectively (Figure 2-5).

With reference to the moving coordinate system X_s, Y_s, Z_s, the unit vector $\hat{u}$ can be written as

$$\begin{aligned}\hat{u} &= a_3\hat{\imath}_s + \left[-a_1\cos\theta + a_2\sin\theta\right]\hat{\jmath}_s + \left[a_1\sin\theta + a_2\cos\theta\right]\hat{k}_s \\ &= b_1\hat{\imath}_s + b_2\hat{\jmath}_s + b_3\hat{k}_s, \end{aligned} \tag{2.3}$$

where:

$$\begin{aligned} a_1 &= \cos\rho\cos\omega + \sin\phi\cos i\sin\omega\ ; \\ a_2 &= \cos\rho\sin\omega - \sin\rho\cos i\cos\omega\ ; \\ a_3 &= \sin\rho\sin i\ . \end{aligned} \tag{2.4}$$

Now, in terms of the coordinates X_p,Y_p,Z_p:

$$\begin{aligned} \hat{\imath}_s &= -\sin\phi\hat{\imath}_p + \cos\phi\sin\lambda\hat{\jmath}_p + \cos\phi\cos\lambda\hat{k}_p\ ; \\ \hat{\jmath}_s &= (\cos\psi\cos\phi)\hat{\imath}_p + (\cos\psi\sin\phi\sin\lambda - \sin\psi\cos\lambda)\hat{\jmath}_p \\ &\qquad + (\cos\psi\sin\phi\cos\lambda + \sin\psi\sin\lambda)\hat{k}_p\ ; \\ \hat{k}_s &= (\sin\psi\cos\phi)\hat{\imath}_p + (\sin\psi\sin\phi\sin\lambda + \cos\psi\cos\lambda)\hat{\jmath}_p \\ &\qquad + (\sin\psi\sin\phi\cos\lambda - \cos\psi\sin\lambda)\hat{k}_p\ . \end{aligned} \tag{2.5}$$

Hence, substituting from Eq. (2.5) into Eq. (2.3), $\hat{u}$ can be rewritten as

$$\begin{aligned}\hat{u} &= \cos\phi_p^x\hat{\imath}_p + \cos\phi_p^y\hat{\jmath}_p + \cos\phi_p^z\hat{k}_p \\ &= \bar{\phi}_p^T\bar{u}_p\ , \end{aligned} \tag{2.6}$$

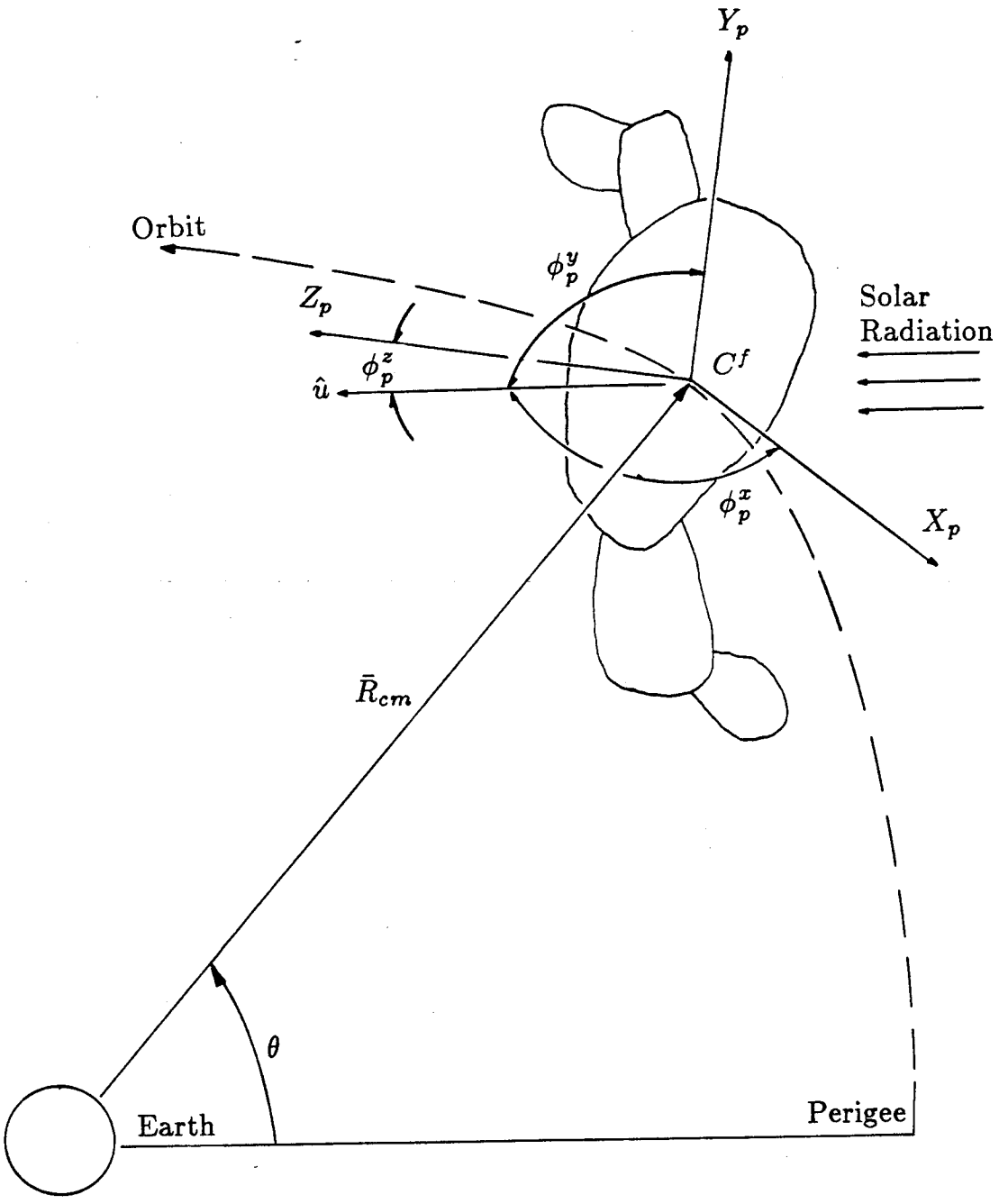

Figure 2-5 Solar radiation incidence angles ϕ_p^x, ϕ_p^y, and ϕ_p^z.

where:

$$\bar{\phi}_p^T = \left\{\cos\phi_p^x, \cos\phi_p^y, \cos\phi_p^z\right\};$$

$$\begin{aligned}
\cos\phi_p^x &= b_1(\cos\psi\sin\phi\cos\lambda + \sin\psi\sin\lambda) + b_2(\sin\psi\sin\phi\cos\lambda - \cos\psi\sin\lambda) \\
&\quad + b_3\cos\phi\cos\lambda\,; \\
\cos\phi_p^y &= b_1\cos\psi\cos\phi + b_2\sin\psi\cos\phi - b_3\sin\phi\,; \\
\cos\phi_p^z &= b_1(\cos\psi\sin\phi\sin\lambda - \sin\psi\cos\lambda) + b_2(\sin\psi\sin\phi\sin\lambda + \cos\psi\cos\lambda) \\
&\quad + b_3\cos\phi\sin\lambda\,. \qquad (2.7)
\end{aligned}$$

It can be seen that the angles are functions of both the orbital elements (ρ, i, ω) and the libration angles (ψ, ϕ, λ). Using Eq. (2.1), the solar radiation incidence angles with respect to coordinate frames attached to B_c, B_i and $B_{i,j}$ bodies can be obtained:

$$\bar{\phi}_c = \bar{\phi}_p\,; \qquad (2.8a)$$

$$\bar{\phi}_i = (\mathbf{C}_\mathbf{i}^\mathbf{c})^T\bar{\phi}_p\,; \qquad (2.8b)$$

$$\bar{\phi}_{i,j} = (\mathbf{C}_{\mathbf{i,j}}^\mathbf{c})^T\bar{\phi}_p\,; \qquad (2.8c)$$

where $\bar{\phi}_c$, $\bar{\phi}_i$ and $\bar{\phi}_{i,j}$ are defined similar to $\bar{\phi}_p$ as above.

2.2.5 Shift in the center of mass

The centre of mass of the spacecraft is the reference point to describe the spacecraft libration and orbital motion. For a rigid system, where the centre of mass remains stationary, it can be determined easily; however, this is no longer true for a flexible system. The general expression describing a shift in the centre of mass is derived below.

Consider the spacecraft in Figure 2-2. Here, C^i and C^f represent the centres of mass of the undeformed and deformed configurations of the system, respectively. The

vector $\bar{C}^f_{cm}$, which denotes the position of C^f relative to C^i, represents the shift in the instantaneous centre of mass of the spacecraft due to its deformation. This vector will be necessary in evaluation of the kinetic and potential energies of the system.

From the figure, with reference to X_p,Y_p,Z_p axes, the vectors from the center of the earth to elemental mass dm_c, dm_i, and $dm_{i,j}$ represented by $\bar{R}_c$, $\bar{R}_i$, and $\bar{R}_{i,j}$, respectively, can be written as:

$$\begin{aligned}
\bar{R}_c &= \bar{R}_{cm} - \bar{C}^f_{cm} - \bar{C}^i_{cm} + \bar{\rho}_c + \bar{\tau}_c + \bar{\delta}_c \,; \\
\bar{R}_i &= \bar{R}_{cm} - \bar{C}^f_{cm} - \bar{C}^i_{cm} + \bar{d}_i + \mathbf{C^c_i}(\bar{\rho}_i + \bar{\tau}_i + \bar{\delta}_i) \,; \\
\bar{R}_{i,j} &= \bar{R}_{cm} - \bar{C}^f_{cm} - \bar{C}^i_{cm} + \bar{d}_i + \mathbf{C^c_i}\bar{d}_{i,j} + \mathbf{C^c_{i,j}}\mu_{\mathbf{i,j}}(\bar{\rho}_{i,j} + \bar{\tau}_{i,j} + \bar{\delta}_{i,j}) \,. \qquad (2.9)
\end{aligned}$$

Taking moment about the centre of force gives

$$\bar{R}_{cm} = \frac{1}{M}\left\{\int_{m_c} \bar{R}_c \, dm_c + \sum_{i=1}^{N}\left[\int_{m_i} \bar{R}_i \, dm_i + \sum_{j=1}^{n_i}\int_{m_{i,j}} \bar{R}_{i,j} \, dm_{i,j}\right]\right\}, \qquad (2.10)$$

where M is the mass of the spacecraft. Substituting Eq. (2.9) into Eq. (2.10) yields

$$\begin{aligned}
\bar{C}_{cm} = \frac{1}{M}\Bigg\{ & \int_{m_c}\left\{\bar{\rho}_c + \bar{\tau}_c + \bar{\delta}_c\right\} dm_c + \sum_{i=1}^{N}\Bigg[\int_{m_i}\left\{\bar{d}_i + \mathbf{C^c_i}[\bar{\rho}_i + \bar{\tau}_i + \bar{\delta}_i]\right\} dm_i \\
& + \sum_{j=1}^{n_i}\int_{m_{i,j}}\left\{\bar{d}_i + \mathbf{C^c_i}\bar{d}_{i,j} + \mathbf{C^c_{i,j}}\mu_{\mathbf{i,j}}[\bar{\rho}_{i,j} + \bar{\tau}_{i,j} + \bar{\delta}_{i,j}]\right\} dm_{i,j}\Bigg]\Bigg\}, \qquad (2.11)
\end{aligned}$$

where:

$\bar{C}_{cm}$ =$\bar{C}^f_{cm} + \bar{C}^i_{cm}$;

$\bar{C}^i_{cm}$ =position vector of C^i, the centre of mass of the undeformed spacecraft, relative to O_c;

$\bar{C}^f_{cm}$ =position vector of C^f relative to C^i;

n_i =number of $B_{i,j}$ bodies attached to body B_i;

N =number of B_i bodies;

M =total mass of the spacecraft; $\quad m_c + \sum_{i=1}^{N}\left[m_i + \sum_{j=1}^{n_i} m_{i,j}\right]$.

Since

$$\bar{C}^i_{cm} = \frac{1}{M}\left\{\int_{m_c} \bar{\rho}_c \, dm_c + \sum_{i=1}^{N}\left[\left\{m_i \bar{\rho}_c(O_i) + \int_{m_i} \mathbf{C^c_i}\,\bar{\rho}_i \, dm_i\right\} + \sum_{j=1}^{n_i}\left\{m_{i,j}[\bar{\rho}_c(O_i) + \mathbf{C^c_i}\,\bar{\rho}_i(O_{i,j})] + \int_{m_{i,j}} \mathbf{C^c_{i,j}}\,\bar{\rho}_{i,j} \, dm_{i,j}\right\}\right]\right\}, \tag{2.12a}$$

$\bar{C}^f_{cm}$ can be simplified as

$$\begin{aligned}\bar{C}^f_{cm} = \frac{1}{M}\Bigg\{&\int_{m_c}\left\{\bar{\tau}_c + \bar{\delta}_c\right\} dm_c \\ &+ \sum_{i=1}^{N}\Bigg[\left\{m_i[\bar{\tau}_c(O_i) + \bar{\delta}_c(O_i)] + \int_{m_i} \mathbf{C^c_i}[\bar{\tau}_i + \bar{\delta}_i]\, dm_i\right\} \\ &+ \sum_{j=1}^{n_i}\Big\{m_{i,j}[\bar{\tau}_c(O_i) + \bar{\delta}_c(O_i) + \mathbf{C^c_i}(\bar{\tau}_i(O_{i,j}) + \bar{\delta}_i(O_{i,j}))] \\ &+ \int_{m_{i,j}} \mathbf{C^c_{i,j}}[(\mu_{\mathbf{i,j}} - \mathbf{U})\bar{\rho}_{i,j} + \mu_{\mathbf{i,j}}\bar{\tau}_{i,j} + \mu_{\mathbf{i,j}}\bar{\delta}_{i,j}]\, dm_{i,j}\Big\}\Bigg]\Bigg\}, \end{aligned} \tag{2.12b}$$

where $\bar{\tau}_k(O_l)$ and $\bar{\delta}_k(O_l)$ $(k = c, i;\ l = i \text{ or } i, j)$ represent $\bar{\tau}_k$ and $\bar{\delta}_k$, respectively, evaluated at the coordinates of O_l; and $\mathbf{U}$ is the unit matrix. Equation (2.11) is the general expression valid for both rigid as well as flexible systems; however, for a rigid system, Eq. (2.12a) is adequate.

2.3 Elastic and Thermal Deformations

2.3.1 Background

Evaluation of the kinetic and potential energies requires expressions for the system deformation. In the past, considerable effort has been directed to this end; hence, it would be appropriate to briefly review the relevant literature.

For a multibody system, two distinct approaches have been popular to estimate elastic deformations: the Finite Element Method (FEM) and Substructure Synthesis Method (SSM). In the FEM, the system is first subdivided into finite elements with degrees of freedom at the nodes. Using the local degrees of freedom as generalized coordinates, the mass and stiffness matrices of the element can be derived readily. Applying the boundary conditions for the system and compatibility requirements between adjacent elements, the system mass and stiffness matrices can be assembled from the corresponding matrices of the elements. The system modes can then be evaluated numerically using finite element subroutines such as NASTRAN.

In the SSM, the system's flexural motion is represented in terms of the components' dynamics. The first step is to obtain the series of admissible functions, by solving the eigenvalue problem for each component, representing its elastic deformation. These functions are referred to as "component modes" by Hurty [73], who pioneered the SSM approach. It should be pointed out that the FEM can be used in deriving the component modes. Compared to the FEM, the subsubstructure eigenvalue problem can represent a tremendous saving in the computational effort. This is especially true when the components are geometrically similar or uniform elements. In the latter category, analytical solutions for beam and plate type elements are available. The second step is to assemble the component admissible functions in such a way that each component does not vibrate as an independent body but rather as a part of the system. Hurty [73] implemented this idea by enforcing geometric compatibility between adjacent elements at pre-selected points. Subsequent research in the SSM is aimed at selection of the substructure modes and improvements in geometric compatibility at internal boundaries.

Craig and Bampton [74] used the FEM to obtain the component shape functions.

Geometric compatibility between elements can be satisfied easily by selecting appropriate boundary conditions for components. Benfield and Hruda [75] derived the component admissible functions based on free boundaries. Geometric compatibility is then enforced by applying inertial and stiffness loadings at internal boundaries. MacNeal [76] selects hybrid modes to represent component elastic motions, i.e. the modes are evaluated by assuming the boundaries to be free, fixed, or free in one part and fixed in the rest. The advantage of this approach is the generality of the boundary conditions under which the component modes are calculated. Using the same approach, Rubin [77] includes the contribution of residual modes to improve accuracy of the system elastic deformation.

Hughes [78] suggested another approach in obtaining the component modes. He distinguished two kinds of component modes: "unconstrained" and "constrained." In the former category, the component mode of a substructure is calculated without imposing any restriction on the adjacent body. The component modes obtained by Hurty [73], Craig and Bampton [74], Benfield and Hruda [75], MacNeal [76], and Rubin [77] belong to "unconstrained" category. In contrast, "constrained" modes of a component are derived by holding the adjacent body stationary. Hughes [79] pointed out that "unconstrained" modes are commonly used in the study of flexible aircraft whereas "constrained" modes are often used for flexible spacecraft. Defining "modal identities " which are integrals of mode shapes relating to linear and angular momentum, Hughes [79] has shown the existence of relations between these integrals of "constrained" and "unconstrained" modes. These identities can be used to assess the influence of each substructure on the system. Using a spacecraft with a rigid central body and flexible appendages, Hablani [80] studied the convergence of both "constrained" and "unconstrained" modes. He concluded that as the rigid portion increases, the convergence of "constrained" and "unconstrained" modes improves.

For "constrained" modes, the contribution to system dynamics comes from the first few modes whereas the importance of "unconstrained" modes is usually not ordered by frequency.

The next question confronting space dynamicists is the number of modes required. Traditionally, high frequency modes are dropped; however, Hablani [80] and Hughes [81] have pointed out that frequency alone is not a sufficient condition in modal truncation unless the modes are "constrained". Hughes [81] recommended using "modal identities" of linear and angular momentum as criteria. Similarly, Hughes and Skelton [82] studied, besides frequency consideration, completeness of inertial indices, controllability and observability of component modes in modal truncation. Another approach, adopted by Gregory [83], is the application of Moore's [84] internal balancing theory. The objective here is to transform the state-space form of the system's equations of motion into the balanced form such that the controllability and observability grammians are equal and diagonal. Generalized coordinates which have small diagonal elements are least controllable or observable; hence, they can be discarded. Using the same idea, Spanos and Tsuha [85] reduced the model order obtained by Hurty et al. [73–77]. The effectiveness of the approach was illustrated through the dynamical study of the Galileo spacecraft.

The SSM discussed so far, though computationally less intensive than the FEM, still involves considerable effort. It stems from the three steps required: component modes derivation, geometric compatibility satisfaction, and model order reduction. Visualizing the SSM from another perspective, Meirovitch and Hale [86,87] simplified the procedure further. The SSM can be regarded as a Rayleigh-Ritz procedure applied to the "intermediate" substructure. The difference between an actual and "intermediate" substructure lies in geometric compatibility: the former is geomet-

rically compatible along the boundaries with the adjacent elements; whereas the latter satisfies geometric compatibility at a limited number of points on the internal boundaries. The convergence of the intermediate substructure to the actual one is guaranteed by the Rayleigh-Ritz method provided the admissible functions form a complete set. The convergence can be achieved by: (i) increasing the number of admissible functions; (ii) confirming to the requirement of geometric compatibility; and (iii) implementing both (i) and (ii) simultaneously. This point of view suggests that it is theoretically correct to use any admissible functions, such as polynomials, provided they satisfy the kinematic boundary conditions and constitute a complete set. Considering a plate-type problem, Meirovitch and Hale [86,87] illustrated the idea by showing the convergence of eigenvalues using low-order polynomials as admissible functions. The results agree with those obtained using 36 terms of the transcendental functions as admissible functions. The same idea was applied to a truss-like structure by Meirovitch and Kwak [88]. Here, the authors pointed out an inconsistency in the Rayleigh-Ritz theory: individual admissible function has to satisfy all the boundary conditions although the solution is based on the linear combination of the admissible functions. Using this argument, the authors presented a method to select the admissible functions. These are called "quasi-comparison functions" which differ from the admissible functions in that the former satisfy only some of the natural boundary conditions. However, when synthesized they result in a faster convergence.

2.3.2 Substructure equations of motion

Yu [57] has shown that the equation for transverse vibration of a thermally flexed appendage is given by

$$EI_b \frac{\partial^4 w^b}{\partial x^4} + \frac{\partial^2 M_t^b}{\partial x^2} + m_b \frac{\partial^2 w^b}{\partial t^2} = 0\,, \tag{2.13}$$

with the appropriate boundary conditions. For instance, for a beam cantilevered at $x = 0$ and free at $x = l_b$, the boundary conditions are:

$$w^b = \frac{\partial w^b}{\partial x} = 0 \qquad \text{at} \quad x = 0\,;$$
$$EI_b \frac{\partial^2 w^b}{\partial x^2} + M_t^b = EI_b \frac{\partial^3 w^b}{\partial x^3} + \frac{\partial M_t^b}{\partial x} = 0 \qquad \text{at} \quad x = l_b\,.$$

Here EI_b is the bending stiffness of the beam; m_b, the mass per unit length of the beam; and M_t^b, the thermal bending moment given by

$$M_t^b = \int_{Area} E\alpha_t T(x,y,z) z \, dA\,,$$

where $T(x,y,z)$ is the difference between the ambient temperature and the temperature at a point on the appendage with coordinates (x,y,z); and α_t is the thermal expansion coefficient of the beam material. The integral is over the cross sectional area of the appendage. For a thermally deformed plate, Johns [89] has shown that the equation of motion is given by

$$D\nabla^4 w^p + \frac{1}{1-\nu}\nabla^2 M_t^p + m_p \frac{\partial^2 w^p}{\partial t^2} = 0\,, \tag{2.14}$$

where ∇ is the Laplacian; m_p, the plate mass per unit length; D and ν are the flexural rigidity and Poisson's ratio, respectively; and M_t^p, the thermal bending moment of the plate defined similar to M_t^b. For a cantilevered plate with the built-in edge at $x = 0$ and free edges at $x = l_p$, $y = \pm w_p/2$, the boundary conditions are given by:

$$w^p = \frac{\partial w^p}{\partial x} = 0 \qquad \text{at } x = 0\,;$$
$$M_x = 0, \quad \frac{\partial M_x}{\partial x} - 2\frac{\partial M_{xy}}{\partial y} = 0, \quad (M_{xy})_1 - (M_{xy})_2 = 0 \qquad \text{at } x = l_p\,;$$
$$M_y = 0, \quad \frac{\partial M_y}{\partial y} - 2\frac{\partial M_{xy}}{\partial x} = 0, \quad (M_{xy})_1 - (M_{xy})_2 = 0 \qquad \text{at } y = \pm w_p/2\,;$$

where subscripts 1 and 2 refer to values of the twisting moment, M_{xy}, on the sides

forming the corner.

The analytical solution for Eqs. (2.13) and (2.14) is difficult to obtain even when possible. The problem is overcome by first assuming that the thermal and elastic deformation are independent, i.e. the solution for thermal deformation can be obtained independent of the elastic displacement, and vice versa. The thermal deformation function is obtained as a solution of the heat balance equation, for a beam or a plate, with the assumption that the element is not undergoing any transverse vibration. Similarly, elastic deformation is represented by admissible functions obtained from the beam or plate equation without thermal deformation.

It should be pointed out that the longitudinal vibrations, torsional oscillations and foreshortening effects are purposely not considered in the formulation. This does not imply that they are difficult to incorporate or negligible. The formulation even without these effects is indeed quite challenging. The main objective is to assess the influence of thermal deformations which is anticipated to be dominant compared to the parameters mentioned above. Further complication of the problem, it is felt, will only mask appreciation of interactions between librational dynamics, flexibility, thermal effects and initial conditions.

2.3.3 Thermal deformations

Modi and Brereton [49] obtained the heat balance equation of an appendage under the influence of the solar radiation. The time constant of the equation was found to be very small for most appendage materials; hence at each orientation, the appendage was assumed to attain the steady state instantaneously. The steady state solution showed that the shape of the centreline of a thermally flexed appendage is given by:

$$\frac{\delta_y}{l_b^*} = -\ln\left[\cos\left(\frac{\eta}{l_b^*}\right)\right]\cos\phi^y\,;$$

$$\frac{\delta_z}{l_b^*} = -\ln\left[\cos\left(\frac{\eta}{l_b^*}\right)\right]\cos\phi^z\,; \tag{2.15}$$

where

$$l_b^* = \frac{2a_b}{\alpha_s\alpha_t q_s}\left[\frac{k_b b_b}{a_b^2} + 4\epsilon_b\sigma_t\left(\frac{q_s\alpha_s}{\pi\epsilon_b\sigma_t}\right)^{3/4}\left(\frac{8-\epsilon_b}{4-\epsilon_b}\right)\right]. \tag{2.16}$$

Here δ_y, δ_z represent deflections in the Y and Z directions, respectively; ϕ^y and ϕ^z are solar radiation incidence angles in the appendage reference Y and Z directions, respectively; η is the distance along the appendage axis from the centre point; and l_b^*, the thermal reference length of the appendage, is a function of the solar radiation intensity (q_s), Stefan-Boltzman constant (σ_t), appendage dimension (a_b, b_b), and appendage physical properties (α_s, α_t, ϵ_b, k_b). For common appendage materials such as steel or beryllium copper, l_b^* is found to be over 100 m.

Evaluation of the kinetic and potential energies involves integration of Eq. (2.15). However, the transcendental character of the equation makes the integration difficult. Ng and Modi [90] showed that the solution to Eq. (2.15) can be approximated to a parabolic form as follows:

$$\begin{aligned}\frac{\delta_y}{l_b^*} &= \frac{1}{2}\left(\frac{\eta}{l_b^*}\right)^2\cos\phi^y\,;\\ \frac{\delta_z}{l_b^*} &= \frac{1}{2}\left(\frac{\eta}{l_b^*}\right)^2\cos\phi^z\,.\end{aligned} \tag{2.17}$$

The difference between Eqs. (2.15) and (2.17) is found to be negligible ($\approx 3\%$) for $\eta/l_b^* < 0.6$, which corresponds to an appendage of up to 60 m in length. Thus, in a number of situations, Eq. (2.17) can be used without incurring significant error.

Similar to Eq. (2.17), Krishna and Bainum [66] used an approximate parabolic solution to describe the deflection of a thermally flexed plate,

$$\frac{\delta_z}{l_p^*} = \frac{1}{2}\left(\frac{\eta}{l_p^*}\right)^2\cos\phi^z\,, \tag{2.18}$$

where

$$l_p^* = \frac{t_c}{\alpha_t \Delta T} \,. \tag{2.19}$$

Here δ_z is the deflection of the plate; l_p^*, the thermal reference length of the plate; t_c, the thickness of the plate; and ΔT $(= T_1 - T_2)$, the temperature difference between the top (T_1) and bottom (T_2) of the plate, is obtained by solving numerically the heat balance equations:

$$\epsilon_b \sigma_t (T_1^4 + T_2^4) = \alpha_s q_s \,;$$
$$\epsilon_b \sigma_t T_2^4 = \frac{k_b}{t_c}(T_1 - T_2) \,.$$

Equations (2.17) and (2.18) are used in the formulation to represent thermal deformations of beams and plates, respectively. For instance, the thermal deformation of body B_i (say, a beam), $\bar{\tau}_i$, and of body $B_{i,j}$ (say, a plate), $\bar{\tau}_{i,j}$, are given by,

$$\bar{\tau}_i = \left\{0 \,, \quad \frac{l_i^*}{2}\left(\frac{x_i}{l_i^*}\right)^2 \cos\phi_i^y \,, \quad \frac{l_i^*}{2}\left(\frac{x_i}{l_i^*}\right)^2 \cos\phi_i^z\right\}^T \,;$$
$$\bar{\tau}_{i,j} = \left\{0 \,, \quad 0 \,, \quad \frac{l_{i,j}^*}{2}\left(\frac{x_{i,j}}{l_{i,j}^*}\right)^2 \cos\phi_{i,j}^z\right\}^T \,. \tag{2.20}$$

2.3.4 Transverse vibrations

The transverse vibration of the substructures can be obtained by the SSM. However, as pointed out by Meirovitch et al. [86–88], convergence of any set of admissible functions to the actual solution is guaranteed by Rayleigh-Ritz procedure provided the admissible functions satisfy the kinematic boundary conditions and form a complete set. With this in mind, the vibrational displacements of beam-type elements are represented in terms of modes of the Euler-Bernoulli beams. For body B_c, the admissible functions used are similar to those of a free-free beam [91],

$$\psi^r(x) = \cosh(\beta^r \frac{x}{l_b}) + \cos(\beta^r \frac{x}{l_b}) - \gamma^r \left[\sinh(\beta^r \frac{x}{l_b}) + \sin(\beta^r \frac{x}{l_b})\right] \,,$$

$$r = 1, 2, \ldots \qquad (2.21)$$

where $\beta^r l_b$ is the solution of the equation

$$\cosh(\beta^r)\cos(\beta^r) - 1 = 0\,,$$

and γ^r is given by

$$\gamma^r = \frac{\sin(\beta^r) + \sinh(\beta^r)}{-\cos(\beta^r) + \cosh(\beta^r)}\,.$$

For B_i and $B_{i,j}$, cantilevered modes are selected,

$$\psi^r(x) = \cosh(\beta^r \frac{x}{l_b}) - \cos(\beta^r \frac{x}{l_b}) - \gamma^r \left[\sinh(\beta^r \frac{x}{l_b}) - \sin(\beta^r \frac{x}{l_b})\right], \qquad r = 1, 2, \ldots \qquad (2.22)$$

where β^r is the solution of the equation

$$\cosh(\beta^r)\cos(\beta^r) + 1 = 0\,,$$

and γ^r is given by

$$\gamma^r = \frac{\sin(\beta^r) - \sinh(\beta^r)}{\cos(\beta^r) - \cosh(\beta^r)}\,.$$

Using Eqs. (2.21) and (2.22), the transverse vibrations of a beam-type substructure in its reference Y and Z directions, v^b and w^b, respectively, can be written as:

$$v^b = \sum_{r=1}^{n} P^r(t)\psi^r(x)\,;$$
$$w^b = \sum_{r=1}^{n} Q^r(t)\psi^r(x)\,; \qquad (2.23)$$

where $P^r(t)$ and $Q^r(t)$ are the generalized coordinates associated with vibrations in the Y and Z directions, respectively; and $\psi^r(x)$ is the admissible function.

The equation of motion for a plate of length l_p and width w_p (aspect ratio $\alpha_r =$

l_p/w_p) undergoing transverse vibration is given by [92]

$$\frac{\partial^4 w}{\partial x^4} + 2\frac{\partial^4 w}{\partial x^2 \partial y^2} + \frac{\partial^4 w}{\partial y^4} + D\frac{\partial^2 w}{\partial t^2} = 0, \tag{2.24}$$

where $D = Eh^3/12(1-\nu^2)$. The boundary conditions are given by:

(i) Simply supported along edge $x = l_p$

$$w(x,y) = \frac{\partial^2 w(x,y)}{\partial x^2} = 0 \qquad \text{at} \qquad x = l_p\,;$$

(ii) Clamped along edge $x = l_p$

$$w(x,y) = \frac{\partial w(x,y)}{\partial x} = 0 \qquad \text{at} \qquad x = l_p\,;$$

(iii) Free along edge $x = l_p$

$$\frac{\partial^2 w(x,y)}{\partial x^2} + \nu\frac{\partial^2 w(x,y)}{\partial y^2} = 0 \qquad \text{at} \qquad x = l_p\,.$$

Except for plates with at least two opposite edges simply supported, the solution to Eq. (2.24) is difficult to obtain, even when possible. Approximate solutions have been reported by numerous researchers and reviewed by Leissa [93]. In general, the approximate solution does not satisfy completely either the boundary conditions or the governing differential equation.

Warburton [94] put forward an approximate solution by assuming the displacement to be,

$$w^p(x,y) = \sum_{s=1}^{m}\sum_{t=1}^{n} H^{s,t}(t)\phi^s(x)\psi^t(y)\,. \tag{2.25}$$

The shape functions for opposite edges that are fixed-free and free-free are given by:

(i) Fixed at $x = 0$ and free at $x = l_p$

$$\phi^s(x) = \cos(\beta^s\frac{x}{l_p}) - \cosh(\beta^s\frac{x}{l_p}) + \gamma^s\Big[\sin\beta^s(\frac{x}{l_p}) - \sinh(\beta^s\frac{x}{l_p})\Big]$$

$$s = 1, 2, 3, \ldots \qquad (2.26)$$

where $\gamma^s = \dfrac{\sin\beta^s - \sinh\beta^s}{\cos\beta^s - \cosh\beta^s}$ and $\cos\beta^s \cosh\beta^s = -1\,.$

(ii) Free at $x = 0$ and free at $x = l_p$

$$\phi^s(x) = \sin\Big[\beta^s(\frac{x}{l_p} - \frac{1}{2})\Big] + \gamma^s \sinh\Big[\beta^s(\frac{x}{l_p} - \frac{1}{2})\Big]$$

$$s = 1, 3, 5, \ldots \qquad (2.27a)$$

where $\gamma^s = \dfrac{\sin\frac{1}{2}\beta^s}{\sinh\frac{1}{2}\beta^s}$ and $\tan\frac{1}{2}\beta^s - \tanh\frac{1}{2}\beta^s = 0\,;$

and $\phi^s(x) = \cos\Big[\beta^s(\frac{x}{l_p} - \frac{1}{2})\Big] + \gamma^s \cosh\Big[\beta^s(\frac{x}{l_p} - \frac{1}{2})\Big]$

$$s = 2, 4, 6, \ldots \qquad (2.27b)$$

with $\gamma^s = \dfrac{-\sin\frac{1}{2}\beta^s}{\sinh\frac{1}{2}\beta^s}$ and $\tan\frac{1}{2}\beta^s + \tanh\frac{1}{2}\beta^s = 0\,.$

Note that rigid body rotation of the plate is not considered in (ii). It should be pointed out that the shape functions of (i) satisfy the boundary conditions completely whereas those of (ii) are only approximate.

In order to overcome the shortcoming of the approximate solution. Gorman [95] introduced the method of superposition to solve the plate equation. The idea is similar to the SSM. The original plate problem is treated as a combination of building blocks. Each building block is a plate problem where the solution is readily available. The solutions of these building blocks are then synthesized. Finally, the constants in the individual building block solutions are constrained so as to satisfy the boundary conditions of the original plate problem. This results in a set of algebraic equations where the nontrivial solution gives the natural frequencies and mode shapes desired. Gorman [96] tabulated the results for different boundary conditions. For a cantilever

plate, for instance, the shape functions are found by three building blocks such that:

$$w(x,y) = w_1(x,y) + w_2(x,y) + w_3(x,y)\,; \tag{2.28}$$

where

$$w_1(x,y) = \sum_{m=1,3,5}^{k_m^*} \frac{E_m}{\theta_{a,m}}(\cosh\beta_m\frac{x}{l_p} + \theta_{b,m}\cos\gamma_m\frac{x}{l_p})\sin\frac{m\pi}{2}\frac{y}{w_p}$$
$$+ \sum_{m=k_m^*+2}^{\infty} \frac{E_m}{\theta_{c,m}}(\cosh\beta_m\frac{x}{l_p} + \theta_{d,m}\cosh\gamma_m\frac{x}{l_p})\sin\frac{m\pi}{2}\frac{y}{w_p}\,;$$

with $\theta_{a,m} = \left[\nu\alpha_r^2(m\pi/2)^2 - \beta_m^2\right]\cosh\beta_m + \theta_{b,m}\left[\nu\alpha_r^2(m\pi/2)^2 + \gamma^2\right]\cos\gamma_m\,;$

$$\theta_{b,m} = \frac{\beta_m\left[(1-\nu)\alpha_r^2(m\pi/2)^2 - \beta_m^2\right]\sinh\beta_m}{\gamma_m\left[(1-\nu)\alpha_r^2(m\pi/2)^2 + \gamma_m^2\right]\sin\gamma_m}\,;$$

$$\theta_{c,m} = \left[\nu\alpha_r^2(m\pi/2)^2 - \beta_m^2\right]\cosh\beta_m + \theta_{d,m}\left[\nu\alpha_r^2(m\pi/2)^2 + \gamma^2\right]\cosh\gamma_m\,;$$

$$\theta_{d,m} = \frac{\beta_m\left[(1-\nu)\alpha_r^2(m\pi/2)^2 - \beta_m^2\right]\sinh\beta_m}{\gamma_m\left[-(1-\nu)\alpha_r^2(m\pi/2)^2 + \gamma_m^2\right]\sinh\gamma_m}\,;$$

$$\beta_m = \alpha_r\sqrt{\lambda_e^2 + (m\pi/2)^2}\,;$$

$$\gamma_m = \alpha_r\sqrt{\lambda_e^2 - (m\pi/2)^2} \qquad \text{or} \qquad \alpha_r\sqrt{(m\pi/2)^2 - \lambda_e^2}\,;$$

$$w_2(x,y) = \sum_{n=0,1}^{k_n^*} \frac{E_n}{\theta_{a,n}}(\sinh\beta_n\frac{x}{l_p} + \theta_{b,n}\sin\gamma_n\frac{x}{l_p})\cos n\pi\frac{y}{w_p}$$
$$+ \sum_{n=k_n^*+1}^{\infty} \frac{E_n}{\theta_{c,n}}(\sinh\beta_n\frac{x}{l_p} + \theta_{d,n}\sinh\gamma_n\frac{x}{l_p})\cos n\pi\frac{y}{w_p}\,;$$

with $\theta_{a,n} = \left[\nu\alpha_r^2(n\pi)^2 - \beta_n^2\right]\sinh\beta_n + \theta_{b,n}\left[\nu\alpha_r^2(n\pi)^2 + \gamma^2\right]\sin\gamma_n\,;$

$$\theta_{b,n} = \frac{\beta_n\left[-(1-\nu)\alpha_r^2(n\pi)^2 + \beta_n^2\right]\cosh\beta_n}{\gamma_n\left[(1-\nu)\alpha_r^2(n\pi)^2 + \gamma_n^2\right]\cos\gamma_n}\,;$$

$$\theta_{c,n} = \left[\nu\alpha_r^2(n\pi)^2 - \beta_n^2\right]\sinh\beta_n - \theta_{d,n}\left[-\nu\alpha_r^2(n\pi)^2 + \gamma^2\right]\sinh\gamma_n\,;$$

$$\theta_{d,n} = \frac{\beta_n\left[-(1-\nu)\alpha_r^2(n\pi)^2 + \beta_n^2\right]\cosh\beta_n}{\gamma_n\left[-(1-\nu)\alpha_r^2(n\pi)^2 + \gamma_n^2\right]\cosh\gamma_n}\,;$$

$$\beta_n = (1/\alpha_r)\sqrt{(\alpha_r\lambda_e)^2 + (n\pi)^2}\,;$$

$$\gamma_n = (1/\alpha_r)\sqrt{(\alpha_r\lambda_e)^2 - (n\pi)^2} \qquad \text{or} \qquad (1/\alpha_r)\sqrt{(n\pi)^2 - (\alpha_r\lambda_e)^2}\,;$$

$$\begin{aligned} w_3(x,y) = \sum_{p=0}^{k_p^*} \frac{E_p}{(\gamma_p^2 + \beta_p^2)\cos\gamma_p}\Big[\cos\gamma_p(1-\frac{x}{l_p}) \\ - \frac{\cos\gamma_p}{\cosh\beta_p}\cosh\beta_p(1-\frac{x}{l_p})\Big]\cos p\pi\frac{y}{w_p} \\ + \sum_{p=k_p^*+1}^{\infty} \frac{-E_p}{(\gamma_p^2 - \beta_p^2)\cosh\gamma_p}\Big[\cosh\gamma_p(1-\frac{x}{l_p}) \\ - \frac{\cosh\gamma_p}{\cosh\beta_p}\cosh\beta_p(1-\frac{x}{l_p})\Big]\cos p\pi\frac{y}{w_p}\,; \end{aligned}$$

with $\beta_p = (1/\alpha_r)\sqrt{(\alpha_r\lambda_e)^2 + (p\pi)^2}\,;$

$$\gamma_p = (1/\alpha_r)\sqrt{(\alpha_r\lambda_e)^2 - (p\pi)^2} \qquad \text{or} \qquad (1/\alpha_r)\sqrt{(p\pi)^2 - (\alpha_r\lambda_e)^2}\,.$$

Here, λ_e represents the eigenvalues of the plate. The values of k_i^* $(i = m,\ n,\ p)$ are the maximum integral values of i such that $[\lambda_e^2 - (m\pi)^2]$, $[(\alpha_r\lambda_e)^2 - (n\pi)^2]$, and $[(\alpha_r\lambda_e)^2 - (p\pi)^2]$ are positive. The general solution of Eq. (2.28) satisfies some of the boundary conditions already. However, there are three additional boundary conditions to be satisfied: (i) zero bending moment at $y = w_p$; (ii) zero slope at $x = 0$; and (iii) zero bending moment at $x = l_p$. The Fourier coefficients E_m, E_n, and E_p are determined by constraining the overall solution to satisfy these three boundary conditions simultaneously. It is achieved in the following manner. First, the number of terms (say k) in w_1, w_2 and w_3 are selected. Using the boundary conditions, three equations with $3k$ unknowns are obtained. Since E_m, E_n, and E_p are Fourier coefficients, one can make use of the orthogonality conditions to obtain $3k - 3$ equations. Let Eq. (2.28) be rewritten in a form

$$w(x,y) = \sum_{m=1,3,5}^{\infty} E_m f_m(\beta_m,\gamma_m)\sin\frac{m\pi}{2}\frac{y}{w} + \sum_{n=0,1}^{\infty} E_n f_n(\beta_n,\gamma_n)\cos n\pi\frac{y}{w}$$

$$+\sum_{p=0}^{\infty} E_p f_p(\beta_p, \gamma_p) \cos p\pi \frac{y}{w} .$$

Multiplying the equation by $\sin \pi y/2w$ and integrating over 0 to 1 would eliminate E_m for $m \neq 1$. This procedure can be repeated $3k$ times to obtain $3k$ equations. Finally, the coefficient matrix of dimension $3k \times 3k$ in terms of E_m, E_n, and E_p is obtained. The matrix equation can then be solved to determine the eigenvalues and eigenvectors. Note, since the method gives a solution that satisfies the plate differential equation and all the boundary conditions, it can be regarded as exact.

The next question is the accuracy of the approximate solution. Leissa [93] studied the convergence of eigenvalues obtained by different researchers using Rayleigh-Ritz method and concluded that in general the accuracy deteriorates as the number of free edges increases. Also, accuracy is further affected by the existence of a diagonal symmetry such as in the case of square free-free plate. These observations are verified in Table 2-1 . Here, a comparison is made between the first five eigenvalues obtained by Warburton (approximate) and Gorman (exact) for cantilever and free-free plates. It can be seen that the approximate solution predicts the eigenvalues with good accuracy for the cantilever plate; however, this is no longer true for free-free plates.

Despite the accuracy of Gorman's solution, it is not readily available. Considerable amount of numerical work, as outlined above, has to be performed first. Also, complexity of the solution makes programming task much more difficult. In view of this, Warburton's approximate shape functions are adopted in the formulation. It should be pointed out that, if higher accuracy in admissible functions is desired, Gorman's solution can always be accommodated in the general formulation at the expense of programming effort and computing cost.

Using Eqs. (2.23) and (2.25), $\bar{\delta}_i$ and $\bar{\delta}_{i,j}$ (say, for a beam and a plate, respectively)

Table 2-1 A comparison between Warburton [94] approximate and Gorman [96] exact eigenvalues of cantilever and free-free plates.

CANTILEVER PLATE							
Mode		$l/w = 1$		$l/w = 1.5$		$l/w = 2$	
1st	W	3.52	(S)	3.52	(S)	3.52	(S)
	G	3.46	(S)	3.44	(S)	3.42	(S)
2nd	W	9.32	(A)	13.41	(A)	17.61	(A)
	G	8.36	(A)	11.43	(A)	14.50	(A)
3rd	W	22.03	(S)	22.03	(S)	22.03	(S)
	G	21.09	(S)	21.32	(S)	21.28	(S)
4th	W	28.52	(S)	40.65	(A)	50.60	(A)
	G	27.06	(S)	38.70	(A)	47.32	(A)
5th	W	31.69	(A)	56.78	(S)	61.69	(S)
	G	30.55	(A)	53.06	(S)	59.76	(S)

FREE-FREE PLATE							
Mode		$l/w = 1$		$l/w = 1.5$		$l/w = 2$	
1st	W	13.86	(A)	20.79	(A)	22.38	(S)
	G	3.29	(A)	4.91	(A)	5.31	(S)
2nd	W	19.36	(S)	22.38	(S)	27.72	(A)
	G	4.81	(S)	5.29	(S)	6.49	(A)
3rd	W	24.73	(S)	47.80	(S/A)	60.59	(S/A)
	G	6.11	(S)	11.38	(S/A)	14.34	(S/A)
4th	W	35.97	(S/A)	50.37	(S)	61.69	(S/A)
	G	8.56	(S/A)	12.45	(S)	21.92	(S)
5th	W	61.69	(S/A)	61.69	(S/A)	89.54	(S)
	G	15.23	(S/A)	21.17	(A)	24.98	(A)

W: Warburton's results
G: Gorman's results
(S) Symmetric mode
(A) Antisymmetric mode
(S/A) Symmetric-Antisymmetric mode

can be written as,

$$\bar{\delta}_i = \left\{0\,,\quad \sum_{r=1}^{n} P_i^r(t)\psi_i^r(x_i)\,,\quad \sum_{r=1}^{n} Q_i^r(t)\psi_i^r(x_i)\right\}^T;$$

$$\bar{\delta}_{i,j} = \{0\,, \quad 0\,, \quad \sum_{s=1}^{m}\sum_{t=1}^{n} H_{i,j}^{s,t}(t)\psi_{i,j}^{s}(x_{i,j})\phi_{i,j}^{t}(y_{i,j})\}^{T}\,. \tag{2.29}$$

2.4 Kinetics

2.4.1 Rotation matrices

Matrix $\mathbf{C_i^c}$ as defined in Eq. (2.1) denotes orientation of the frame F_i relative to the frame F_c. Two rotation sequences are needed to determine $\mathbf{C_i^c}$: the first one, $\mathbf{C_i^{c,r}}$, defines the rigid body orientation of F_i with respect to F_c whereas the second one, $\mathbf{C_i^{c,f}}$, defines the rotation of frame F_i relative to F_c due to elastic and thermal deformations of the body B_c. A modified Eulerian rotation of the following sequence is selected: a rotation $\theta_{x_c}^r$ about X_c-axis, followed by $\theta_{y_c}^r$ about Y_c-axis, and finally $\theta_{z_c}^r$ about Z_c-axis, i.e.,

$$\begin{aligned}
\mathbf{C_i^{c,r}} &= \begin{bmatrix} \cos\theta_{z_c}^r & -\sin\theta_{z_c}^r & 0 \\ \sin\theta_{z_c}^r & \cos\theta_{z_c}^r & 0 \\ 0 & 0 & 1 \end{bmatrix} \begin{bmatrix} \cos\theta_{y_c}^r & 0 & \sin\theta_{y_c}^r \\ 0 & 1 & 0 \\ -\sin\theta_{y_c}^r & 0 & \cos\theta_{y_c}^r \end{bmatrix} \\
&\quad \times \begin{bmatrix} 1 & 0 & 0 \\ 0 & \cos\theta_{x_c}^r & -\sin\theta_{x_c}^r \\ 0 & \sin\theta_{x_c}^r & \cos\theta_{x_c}^r \end{bmatrix} \\
&= \begin{bmatrix} \cos\theta_{y_c}^r\cos\theta_{z_c}^r & \sin\theta_{x_c}^r\sin\theta_{y_c}^r\cos\theta_{z_c}^r - \cos\theta_{x_c}^r\sin\theta_{z_c}^r & \cos\theta_{x_c}^r\sin\theta_{y_c}^r\cos\theta_{z_c}^r + \sin\theta_{x_c}^r\sin\theta_{z_c}^r \\ \cos\theta_{y_c}^r\sin\theta_{z_c}^r & \sin\theta_{x_c}^r\sin\theta_{y_c}^r\sin\theta_{z_c}^r + \cos\theta_{x_c}^r\cos\theta_{z_c}^r & \cos\theta_{x_c}^r\sin\theta_{y_c}^r\sin\theta_{z_c}^r - \sin\theta_{x_c}^r\cos\theta_{z_c}^r \\ -\sin\theta_{y_c}^r & \sin\theta_{x_c}^r\cos\theta_{y_c}^r & \cos\theta_{x_c}^r\cos\theta_{y_c}^r \end{bmatrix}.
\end{aligned} \tag{2.30a}$$

Similarly,

$$\mathbf{C_i c, f} = \begin{bmatrix} \cos\theta_{y_c}^f\cos\theta_{z_c}^f & \sin\theta_{x_c}^f\sin\theta_{y_c}^f\cos\theta_{z_c}^f - \cos\theta_{x_c}^f\sin\theta_{z_c}^f & \cos\theta_{x_c}^f\sin\theta_{y_c}^f\cos\theta_{z_c}^f + \sin\theta_{x_c}^f\sin\theta_{z_c}^f \\ \cos\theta_{y_c}^f\sin\theta_{z_c}^f & \sin\theta_{x_c}^f\sin\theta_{y_c}^f\sin\theta_{z_c}^f + \cos\theta_{x_c}^f\cos\theta_{z_c}^f & \cos\theta_{x_c}^f\sin\theta_{y_c}^f\sin\theta_{z_c}^f - \sin\theta_{x_c}^f\cos\theta_{z_c}^f \\ -\sin\theta_{y_c}^f & \sin\theta_{x_c}^f\cos\theta_{y_c}^f & \cos\theta_{x_c}^f\cos\theta_{y_c}^f \end{bmatrix}$$

$$\begin{matrix} \cos\theta^f_{x_c}\sin\theta^f_{y_c}\cos\theta^f_{z_c}+\sin\theta^f_{x_c}\sin\theta^f_{z_c} \\ \cos\theta^f_{x_c}\sin\theta^f_{y_c}\sin\theta^f_{z_c}-\sin\theta^f_{x_c}\cos\theta^f_{z_c} \\ \cos\theta^f_{x_c}\cos\theta^f_{y_c} \end{matrix}\Bigg] \quad . \qquad (2.30b)$$

and

$$\mathbf{C_i^c = C_i^{c,f} \times C_i^{c,r}}$$

The choice of the rotation sequence is somewhat arbitrary because the multiplication of rotation matrices is commutative for small rotations; however, as pointed out by Hughes [97], the concern is the location of the singularity. For the sequence selected, the singularity is located at $\theta^r_{y_c} = \pi/2$ or $\theta^f_{y_c} = \pi/2$. If this leads to a problem, it is easy to select another rotation sequence with minor changes to the computer program. Note that $\theta^f_{x_c}$, $\theta^f_{y_c}$, and $\theta^f_{z_c}$ are functions of the thermal and elastic deformations of B_c. Consider the spacecraft model in Figure 2-6 with a beam type central body attached to another body at coordinates (d_{x_c}, d_{y_c}, d_{z_c}). Initially, in absence of any deformations:

$$\begin{aligned} \theta^r_{x_c} &= \frac{\pi}{2}\,; \\ \theta^r_{y_c} &= 0\,; \\ \theta^r_{z_c} &= 0\,. \end{aligned} \qquad (2.31a)$$

With the inclusion of thermal and elastic deformations, $\theta^f_{x_c}$, $\theta^f_{y_c}$, and $\theta^f_{z_c}$ can be evaluated using Eqs. (2.20) and (2.29):

$$\begin{aligned} \theta^f_{x_c} &= \frac{\pi}{2}\,; \\ \theta^f_{y_c} &= -\sum_{r=1}^{n} \frac{Q^r_c(t)}{l_c}\frac{d\psi^r_c}{dx_c}\Big|_{x_c=d_{x_c}} - \frac{d_{x_c}}{l^*_c}\cos\phi^z_c\,; \\ \theta^f_{z_c} &= \sum_{r=1}^{n} \frac{P^r_c(t)}{l_c}\frac{d\psi^r_c}{dx_c}\Big|_{x_c=d_{x_c}} + \frac{d_{x_c}}{l^*_c}\cos\phi^y_c\,. \end{aligned} \qquad (2.31b)$$

If B_c is a free plate, then the appropriate expressions would be:

$$\theta^f_{x_c} = \frac{\pi}{2} + \sum_{s=1}^{m}\sum_{t=1}^{n} \frac{H_c^{s,t}(t)}{l_c}\psi_c^s(d_{x_c})\frac{d\phi_c^t}{dy_c}|_{y_c=d_{y_c}} - \frac{d_{x_c}}{l_c^*}\cos\phi_c^z\,;$$

$$\theta^f_{y_c} = -\sum_{s=1}^{m}\sum_{t=1}^{n} \frac{H_c^{s,t}(t)}{l_c}\frac{d\psi_c^s}{dx_c}|_{x_c=d_{x_c}}\phi_c^t(d_{y_c}) + \frac{d_{x_c}}{l_c^*}\cos\phi_c^y\,;$$

$$\theta^f_{z_c} = 0\,. \tag{2.31c}$$

As for $\mathbf{C^c_{i,j}}$, which is the orientation matrix of frame $F_{i,j}$ relative to F_c, it is expressed as the product of $\mathbf{C^c_i}$ and $\mathbf{C^c_{i,j}}$, i.e.

$$\mathbf{C^c_{i,j}} = \mathbf{C^c_i}\cdot\mathbf{C^i_{i,j}}\,, \tag{2.32}$$

where $\mathbf{C^i_{i,j}}$ is defined similar to $\mathbf{C^c_i}$ in Eq. (2.12) with subscripts x_c, y_c, z_c replaced by x_i, y_i, and z_i, respectively.

2.4.2 Kinetic energy

The kinetic energy, T, of the spacecraft is given by

$$T = \frac{1}{2}\left\{\int_{m_c}\dot{\bar{R}}_c\cdot\dot{\bar{R}}_c\,dm_c + \sum_{i=1}^{N}\left[\int_{m_i}\dot{\bar{R}}_i\cdot\dot{\bar{R}}_i\,dm_i + \sum_{j=1}^{n_i}\int_{m_{i,j}}\dot{\bar{R}}_{i,j}\cdot\dot{\bar{R}}_{i,j}\,dm_{i,j}\right]\right\}, \tag{2.33}$$

where $\dot{\bar{R}}_c$, $\dot{\bar{R}}_i$, and $\dot{\bar{R}}_{i,j}$ are obtained by differentiating Eq. (2.9) with respect to time:

$$\begin{aligned}
\dot{\bar{R}}_c &= \dot{\bar{R}}_{cm} - \dot{\bar{C}}^f_{cm} - \dot{\bar{C}}^i_{cm} + \dot{\bar{\tau}}_c + \dot{\bar{\delta}}_c + \bar{\omega}\times\left[-\bar{C}^f_{cm} - \bar{C}^i_{cm} + \bar{\rho}_c + \bar{\tau}_c + \bar{\delta}_c\right];\\
\dot{\bar{R}}_i &= \dot{\bar{R}}_{cm} - \dot{\bar{C}}^f_{cm} - \dot{\bar{C}}^i_{cm} + \dot{\bar{d}}_i + \mathbf{\dot{C}^c_i}(\bar{\tau}_i + \bar{\delta}_i) + \mathbf{C^c_i}(\dot{\bar{\tau}}_i + \dot{\bar{\delta}}_i)\\
&\quad + \bar{\omega}\times\left[-\bar{C}^f_{cm} - \bar{C}^i_{cm} + \bar{d}_i + \mathbf{C^c_i}(\bar{\rho}_i + \bar{\tau}_i + \bar{\delta}_i)\right];\\
\dot{\bar{R}}_{i,j} &= \dot{\bar{R}}_{cm} - \dot{\bar{C}}^f_{cm} - \dot{\bar{C}}^i_{cm} + \dot{\bar{d}}_i + \mathbf{C^c_i}\dot{\bar{d}}_{i,j}\\
&\quad + (\mathbf{\dot{C}^c_{i,j}}\mu_{\mathbf{i,j}} + \mathbf{C^c_{i,j}}\dot{\mu}_{\mathbf{i,j}})(\bar{\rho}_{i,j} + \bar{\tau}_{i,j} + \bar{\delta}_{i,j}) + \mathbf{C^c_{i,j}}\mu_{\mathbf{i,j}}(\dot{\bar{\tau}}_{i,j} + \dot{\bar{\delta}}_{i,j})\\
&\quad + \bar{\omega}\times\left[-\bar{C}^f_{cm} - \bar{C}^i_{cm} + \bar{d}_i + \mathbf{C^c_i}\bar{d}_{i,j}\right.\\
&\quad \left. + \mathbf{C^c_{i,j}}\mu_{\mathbf{i,j}}(\bar{\rho}_{i,j} + \bar{\tau}_{i,j} + \bar{\delta}_{i,j})\right].
\end{aligned} \tag{2.34}$$

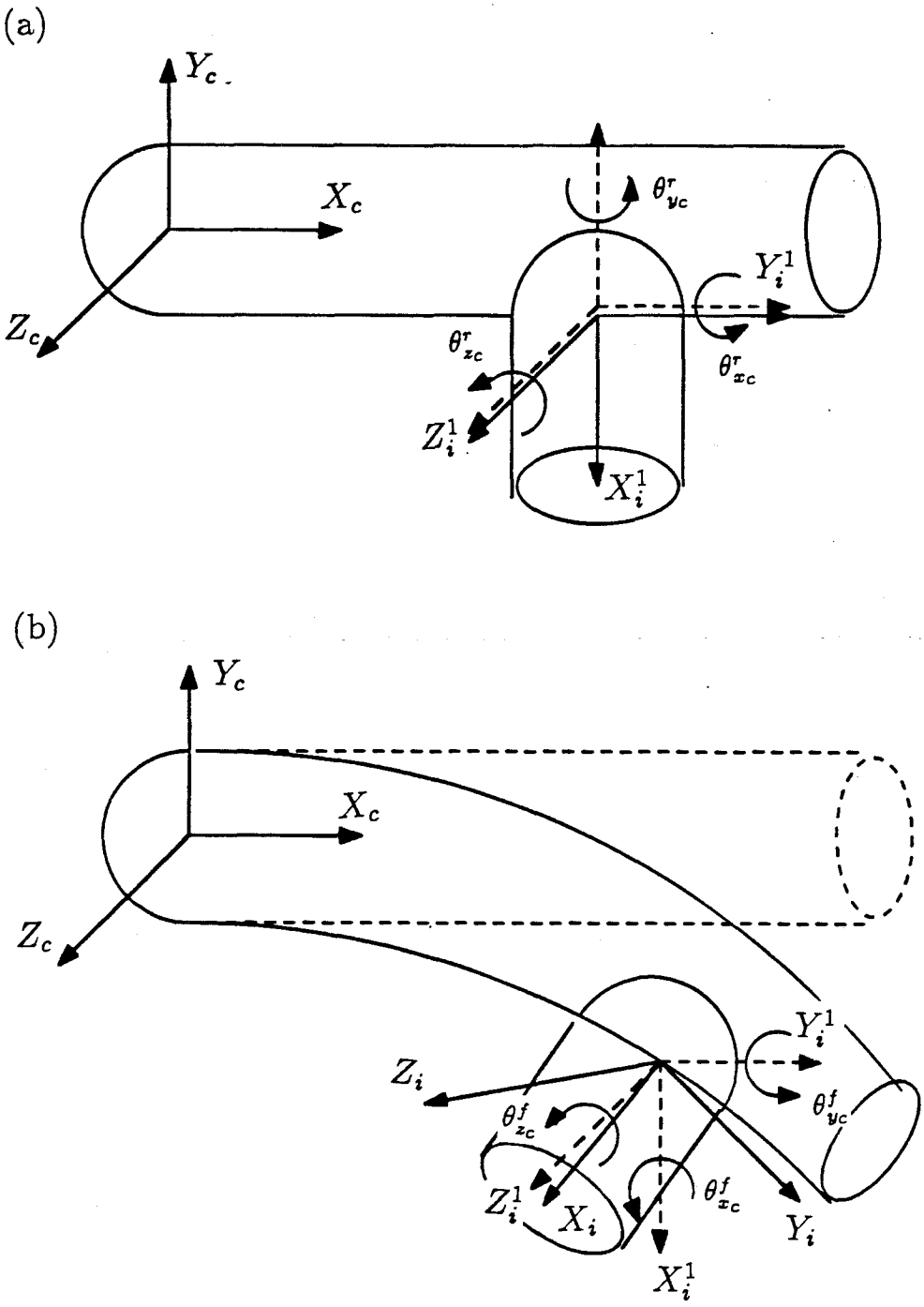

Figure 2-6 An illustration of the Eulerian rotation.

Substituting Eq. (2.34) into (2.33), the kinetic energy expression can be written in the form

$$\begin{aligned} T &= T_{orb} + T_{cm} + T_h + T_{jr} + T_t + T_v + T_{h,jr} + T_{h,t} + T_{h,v} + T_{jr,t} + T_{jr,v} + T_{t,v} \\ &\quad + \frac{1}{2}\bar{\omega}^T \mathbf{I}_{sys}\, \bar{\omega} + \bar{\omega}^T \bar{H}_{sys}\,, \\ &= T_{orb} + T_{sys} + \frac{1}{2}\bar{\omega}^T \mathbf{I}_{sys}\, \bar{\omega} + \bar{\omega}^T \bar{H}_{sys}\,, \end{aligned} \tag{2.35}$$

where $\bar{\omega}$ is the libration velocity vector; $\mathbf{I}_{sys}$, the inertia matrix; $\bar{H}_{sys}$, the angular momentum with respect to the F_c frame; $\frac{1}{2}\bar{\omega}^T \mathbf{I}_{sys}\bar{\omega}$, the kinetic energy due to pure rotation; and $\bar{\omega}^T \bar{H}_{sys}$, the kinetic energy due to coupling between rotational motion, transverse vibration, and thermal deformation. T_{sys} represents the kinetic energy contributions due to various effects with the subscripts involved defined below:

orb	orbital motion;
cm	centre of mass motion;
h	hinge position between body B_c and B_i or between body B_i and $B_{i,j}$;
jr	joint rotation due to elastic and thermal deformation;
t	thermal deformation;
v	transverse vibration.

For instance, $T_{t,v}$ refers to the contribution of kinetic energy due to the rate of thermal deformation and transverse vibration velocity. Details of the kinetic energy expression are given in Appendix I. The evaluation of the integrals require *a priori* knowledge of $\bar{\rho}_k$, $\bar{\tau}_k$, $\bar{\delta}_k$, and $\bar{d}_k$ ($k = c, i,$ or i, j); hence, the configuration and location of each body must be specified before the evaluation can proceed. The matrix $\mathbf{I}_{sys}$, which represents inertia of the system, is time-dependent and consists of several components,

$$\begin{aligned} \mathbf{I}_{sys} &= \mathbf{I}_{cm} + \mathbf{I}_h + \mathbf{I}_r + \mathbf{I}_t + \mathbf{I}_v \\ &\quad + \mathbf{I}_{h,r} + \mathbf{I}_{h,t} + \mathbf{I}_{h,v} + \mathbf{I}_{r,t} + \mathbf{I}_{r,v} + \mathbf{I}_{t,v}\,, \end{aligned} \tag{2.36}$$

where the subscripts cm, h, t, and v have the same meaning as before. Subscript r denotes contribution from the rigid body component. For example, $\mathbf{I}_{r,t}$ represents contribution to the inertia by the rigid component and thermal deformation.

The angular momentum vector, $\bar{H}_{sys}$, can be written as

$$\begin{aligned}\bar{H}_{sys} = \bar{H}_{cm} + \bar{H}_h + \bar{H}_{jr} + \bar{H}_t + \bar{H}_v + \bar{H}_{h,jr} + \bar{H}_{h,r} \\ + \bar{H}_{h,t} + \bar{H}_{h,v} + \bar{H}_{r,t} + \bar{H}_{r,v} + \bar{H}_{t,v}\,,\end{aligned} \tag{2.37}$$

with the subscripts defined as before. Similar to $\mathbf{I}_{sys}$, $\bar{H}_{sys}$ is a time-dependent quantity. The details of $\mathbf{I}_{sys}$ and $\bar{H}_{sys}$ are given in Appendix I.

2.4.3 Potential energy

The potential energy, U, of the spacecraft has contribution from two sources: gravitational potential energy, U_g, and strain energy due to transverse vibration and thermal deformation, U_e,

$$U = U_e + U_g.$$

The potential energy due to gravity gradient is given by

$$U_g = \mu_e \left\{ \int_{m_c} \frac{dm_c}{R_c} + \sum_{i=1}^{N} \left[\int_{m_i} \frac{dm_i}{R_i} + \sum_{j=1}^{n_i} \int_{m_{i,j}} \frac{dm_{i,j}}{R_{i,j}} \right] \right\}.$$

Substituting the expressions for R_c, R_i, and $R_{i,j}$ from Eq. (2.9), and ignoring the terms of order $1/R_{cm}^4$ and higher, U_g can be written as

$$U_g = -\frac{\mu_e M}{R_{cm}} - \frac{\mu_e}{2R_{cm}^3} \mathrm{tr}\left[\mathbf{I}_{sys}\right] + \frac{3\mu_e}{2R_{cm}^3} \bar{l}^T \mathbf{I}_{sys}\, \bar{l}\,, \tag{2.38}$$

where μ_e is the gravitational constant and $\bar{l}$ represents the direction cosine vector of $\bar{R}_{cm}$ with reference to X_p,Y_p,Z_p axes. From Figure 2-4, $\bar{l}$ is given by

$$\bar{l} = (\cos\psi \sin\phi \cos\lambda + \sin\psi \sin\lambda)\hat{\imath}_c + \cos\psi \cos\phi \hat{\jmath}_c$$

$$+ (\cos\psi \sin\phi \sin\lambda - \sin\psi \cos\lambda)\hat{k}_c \,. \tag{2.39}$$

The strain energy expression for a beam and a plate are [24]:

$$\begin{aligned} U_{e,plate} &= \frac{D}{2}\int_{A_p}\left\{\left(\frac{\partial^2 w^p}{\partial x^2}\right)^2 + 2\nu\left(\frac{\partial^2 w^p}{\partial x^2}\right)\left(\frac{\partial^2 w^p}{\partial y^2}\right) + \left(\frac{\partial^2 w^p}{\partial y^2}\right)^2 \right. \\ &\qquad \left. + 2(1-\nu)\left(\frac{\partial^2 w^p}{\partial x \partial y}\right)^2\right\} dA_p \,; \\ U_{e,beam} &= \frac{1}{2}\int_{l_b}\left\{EI_{yy}\left(\frac{\partial^2 w^b}{\partial x^2}\right)^2 + EI_{zz}\left(\frac{\partial^2 v^b}{\partial x^2}\right)^2\right\} dl_b \,; \end{aligned} \tag{2.40}$$

where D and ν are the flexural rigidity and Poisson's ratio of the plate, respectively; and EI_{yy} and EI_{zz} are the bending stiffness of the beam about Y and Z axes, respectively. By specifying the configuration of each body constituting the system, the strain energy can be evaluated. For instance, a system with bodies B_c, B_i beams and $B_{i,j}$ plates, the strain energy expression can be written as

$$\begin{aligned} U_e = \frac{1}{2}\int_{l_c}&\left\{EI_{c,yy}\left[\frac{\partial^2}{\partial x_c^2}\left((\tau_c)_z + (\delta_c)_z\right)\right]^2 + EI_{c,zz}\left[\frac{\partial^2}{\partial x_c^2}\left((\tau_c)_y + (\delta_c)_y\right)\right]^2\right\} dl_c \\ &+ \sum_{i=1}^{N}\left[\frac{1}{2}\int_{l_i}\left\{EI_{i,yy}\left[\frac{\partial^2}{\partial x_i^2}\left((\tau_i)_z + (\delta_i)_z\right)\right]^2 + EI_{i,zz}\left[\frac{\partial^2}{\partial x_i^2}\left((\tau_i)_y + (\delta_i)_y\right)\right]^2\right\} dl_i \right. \\ &+ \sum_{j=1}^{n_i}\frac{D_{i,j}}{2}\int_{A_{i,j}}\left\{\left[\frac{\partial^2}{\partial x_{i,j}^2}\left((\tau_{i,j})_z + (\delta_{i,j})_z\right)\right]^2 \right. \\ &+ 2\nu_{i,j}\left[\frac{\partial^2}{\partial x_{i,j}^2}\left((\tau_{i,j})_z + (\delta_{i,j})_z\right)\right]\left[\frac{\partial^2}{\partial y_{i,j}^2}\left((\tau_{i,j})_z + (\delta_{i,j})_z\right)\right] \\ &+ \left[\frac{\partial^2}{\partial y_{i,j}^2}\left((\tau_{i,j})_z + (\delta_{i,j})_z\right)\right]^2 \\ &\left.\left. + 2(1-\nu_{i,j})\left[\frac{\partial^2}{\partial x_{i,j}\partial y_{i,j}}\left((\tau_{i,j})_z + (\delta_{i,j})_z\right)\right]^2\right\} dA_{i,j}\right] , \end{aligned}$$

where $(\tau_k)_y + (\delta_k)_y$ and $(\tau_k)_z + (\delta_k)_z$ ($k = c$, i, or i,j) are the Y and Z components of $\bar{\tau}_k + \bar{\delta}_k$, respectively.

2.5 Lagrangian Formulation

Using the Lagrangian procedure, the governing equations of motion can be obtained from

$$\frac{d}{dt}\left(\frac{\partial T}{\partial \dot{q}}\right) - \frac{\partial T}{\partial q} + \frac{\partial U}{\partial q} = F_q \,,$$

where q and F_q are the generalized coordinate and generalized force, respectively. The number of generalized coordinates depends on the system configuration, i.e., the degrees of freedom involved. For instance, consider a central beam-type body B_c, undergoing general librational motion, with N beams (body B_i) attached to it. In turn, let each B_i body be attached to n_i plates ($B_{i,j}$ bodies). Then q will be

$$q = R_{cm},\ \theta,\ \psi,\ \phi,\ \lambda,\ P_c^{r_c},\ Q_c^{r_c},\ P_i^{r_i},\ Q_i^{r_i},\ H_{i,j}^{s,t} \,,$$

with:

$$r_c = 1, \ldots, n_{r_c} \,;$$

$$r_i = 1, \ldots, n_{r_i} \,;$$

$$s = 1, \ldots, n_s \,;$$

$$t = 1, \ldots, n_t \,;$$

where n_{r_c} and n_{r_i} denote the number of modes used to represent the transverse vibration of B_c and B_i, respectively; and n_s and n_t represent the number of modes of transverse vibration of $B_{i,j}$ in the plate reference X and Y directions, respectively. The total number of generalized coordinates is now given as

$$N_q = 5 + 2 \times n_{r_c} + 2 \times (N \times n_{r_i}) + (N_j \times n_s \times n_t) \,,$$

where

$$N_j = \sum_{i=1}^{N} n_i \,.$$

In general, the effect of librational and vibrational motion on the orbital motion is small unless the system dimension is comparable to R_{cm} [98,99]. Hence, the orbit

can be represented by the classical Keplerian relations:

$$R_{cm} = \frac{h^2}{\mu_e(1+\epsilon\cos\theta)} ;$$
$$R_{cm}^2\dot{\theta} = h ; \tag{2.41}$$

where h is the angular momentum per unit mass of the system, μ_e is the gravitational constant, and ϵ is the eccentricity of the orbit. Therefore, q and N_q would reduce to:

$$q = \psi,\ \phi,\ \lambda,\ \underline{P}_c^{rc},\ \underline{Q}_c^{rc},\ \underline{P}_i^{ri},\ \underline{Q}_i^{ri},\ \underline{H}_{i,j}^{s,t} ;$$
$$N_q = 3 + 2 \times n_{rc} + 2 \times (N \times n_{r_i}) + (N_j \times n_s \times n_t) .$$

Here $\underline{P}_c^{rc}$, $\underline{Q}_c^{r,c}$, $\underline{P}_i^{ri}$, $\underline{Q}_i^{ri}$, and $\underline{H}_{i,j}^{s,t}$ are the nondimensional values P_c^{rc}/l_c, Q_c^{rc}/l_c, P_i^{ri}/l_i, Q_i^{ri}/l_i, and $H_{i,j}^{s,t}/l_{i,j}$, respectively. In parametric studies of spacecraft dynamics, dimensionless parameters and independent variable are desirable. For instance, simulation results using time as the independent variable from $t = T_{initial}$ to $t = T_{final}$ are applicable for a particular orbit only. In contrast, using true anomaly as the independent variable, simulations for $\theta = \theta_{initial}$ to $\theta = \theta_{final}$ are valid for similar orbits at different altitudes. In the present study, all masses and lengths are nondimensionalized by the characteristic mass and length, respectively. As the simulation results are independent of the characteristic mass and length, their choice is arbitrary. Variables with a dimension of time, such as frequencies, are nondimensionalized by the orbital rate at the perigee point, $\dot{\theta}_p$. As for the time derivatives, their true anomaly counterparts are obtained using the following relations:

$$\frac{d}{dt} = \dot{\theta}\frac{d}{d\theta} ; \tag{2.42a}$$
$$\frac{d^2}{dt^2} = \dot{\theta}^2\left(\frac{d^2}{d\theta^2} - \frac{2\epsilon\sin\theta}{1+\epsilon\cos\theta}\frac{d}{d\theta}\right) ; \tag{2.42b}$$

where Eq. (2.42b) is derived from Eqs. (2.41) and (2.42a).

The general equations of motion can now be written as:

$$\begin{bmatrix} \mathbf{M}_{lib} & \vdots & \mathbf{M}_{lib,vib} \\ \cdots\cdots & \cdots & \cdots\cdots \\ \mathbf{M}_{lib,vib}^T & \vdots & \mathbf{M}_{vib} \end{bmatrix} \begin{Bmatrix} \psi'' \\ \phi'' \\ \lambda'' \\ \cdots \\ q_1'' \\ \vdots \\ q_{n_v}'' \end{Bmatrix} + \begin{Bmatrix} C_\psi \\ C_\phi \\ C_\lambda \\ \cdots \\ C_{q_1} \\ \vdots \\ C_{q_{n_v}} \end{Bmatrix} + \begin{Bmatrix} K_\psi \\ K_\phi \\ K_\lambda \\ \cdots \\ K_{q_1} \\ \vdots \\ K_{q_{n_v}} \end{Bmatrix} = \begin{Bmatrix} Q_\psi \\ Q_\phi \\ Q_\lambda \\ \cdots \\ Q_{q_1} \\ \vdots \\ Q_{q_{n_v}} \end{Bmatrix};$$

$$\text{or} \qquad \mathbf{M}(q)\bar{q}'' + \bar{C}(q, q', \theta) + \bar{K}(q, \theta) = \bar{Q}(\theta)\,; \tag{2.43}$$

where primes denote differentiation with respect to the true anomaly; n_v is the total number of vibrational degrees of freedom such that $N_q = 3 + n_v$. Here $\mathbf{M}$ is a non-singular symmetric matrix of dimension $N_q \times N_q$. The entries in $\mathbf{M}$ come from second order terms of $d/d\theta(\partial T/\partial q')$. $\bar{C}$ is a $N_q \times 1$ vector representing the gyroscopic terms of the system. They come from two sources: from the Coriolis terms of $d/d\theta(\partial T/\partial q')$ and from $\partial T/\partial q$. $\bar{K}$, also a $N_q \times 1$ vector, denotes the stiffness of the system. Its sole contribution is from $(\partial U/\partial q)$. $\bar{Q}$, the generalized force vector of dimension $N_q \times 1$, is evaluated using the virtual work principle. Note, nonlinear entries in $\mathbf{M}$ together with nonlinear and time varying components of $\bar{C}$, $\bar{K}$, and $\bar{Q}$ result in a set of coupled, nonlinear, and nonautonomous equations of motion.

3. NUMERICAL IMPLEMENTATION

3.1 Preliminary Remarks

The computer code required to simulate a general system of interconnected flexible bodies is expected to be complicated and lengthy. In implementing such a computer program, the following points must be taken into consideration:

(i) Each computer has a constraint on the acceptable program size beyond which its execution is at a suboptimal speed. This limit on size is especially stringent in time-sharing systems.

(ii) The numerical integration subroutine determines, to a certain extent, the speed of execution and accuracy of the numerical solution. The ideal fast, higher-order subroutine is based on the multi-value method.

(iii) The architecture of the code is critical in program management and debugging. A computer code with simple and easy to follow algorithm is always desirable.

With the advances in computer technology, the importance of the first point has diminished; however, the other two aspects remain critical for the success of a multibody simulation program.

The chapter begins with a discussion of the numerical integration subroutine and program flowchart. This is followed by details of the program and subroutine structures. The emphasis is on the effort required by the user, the architecture and algorithm of the computer code that facilitates simulations of a large class of spacecraft.

3.2 Numerical Integration Subroutine

In order to solve the equations of motion numerically, they have to be first rearranged into a set of first order ordinary differential equations. Consider Eq. (2.43), a set of N second order differential equations, which can be rewritten as

$$\begin{aligned} \bar{q}'' &= \mathbf{M}^{-1}(q)\Big\{\bar{Q}(\theta) - \bar{C}(q, q', \theta) - \bar{K}(q, \theta)\Big\} \\ &= \bar{F}(q, q', \theta)\,. \end{aligned} \tag{3.1}$$

Now let

$$\bar{y} = \left\{ \begin{array}{c} \bar{q} \\ \bar{q}' \end{array} \right\},$$

then

$$\bar{y}' = \left\{ \begin{array}{c} \bar{q}' \\ \bar{F}(q, q', \theta) \end{array} \right\}, \tag{3.2}$$

which represents a set of $2N$ first order differential equations to be integrated numerically.

The subroutine IMSL:DGEAR is chosen to perform the numerical integration of the equations of motion. The advantages of this subroutine include: (a) automatic adjustments of the iteration step-size and order of the iteration formulae; (b) user-supplied or numerical evaluation of the system Jacobian matrix; and (c) user selected integration methods (Adams or Gear method). The latter feature is particularly appealing as the two methods complement each other. Adams method is particularly suitable for non-stiff equations whereas Gear method handles stiff systems efficiently [100,101].

In order to understand the program architecture, a little background on the methodology of numerical integration is appropriate. Consider Eq. (3.2) with $\bar{y}_n$ as the solution at the nth integration interval (τ), such that $\theta = n\tau$. Two methods, one-value or multi-value, can be used to obtain $\bar{y}_n$. The former uses only $\bar{y}_{n-1}$ while

the latter uses k previous values $\bar{y}_{n-1}, \ldots, \bar{y}_{n-k}$. The advantage of the multi-value method over the one-value approach is in the accuracy and reliability of the solution; however, the multi-value method has a disadvantage in the execution speed.

The multi-value method consists of three stages: prediction, error test and correction. Given $\bar{y}_{n-1}, \ldots, \bar{y}_{n-k}$, the predicted value of $\bar{y}_n$, denoted by $\bar{y}_{n,0}$, is obtained by a linear interpolation method. An error test is then performed on $\bar{y}_{n,0}$ to determine whether the error is within the user-specified tolerance. A negative result of the test prompts the corrector formula to determine a refined value $\bar{y}_{n,1}$ which is subjected to the error test again. The error test and correction procedures are repeated m times until $\bar{y}_{n,m}$ satisfies the tolerance giving $\bar{y}_n = \bar{y}_{n,m}$.

3.3 Computational Flowchart

The flowchart showing computational steps involved for multibody simulation is presented in Figure 3-1 . The input phase requires the user to supply the following information:

(i) orbital elements ρ, i, ω (used for the determination of solar radiation incidence angles), and eccentricity, ϵ;

(ii) simulation period and IMSL: DGEAR parameters such as tolerance, method, initial step size, etc.;

(iii) inclusion/exclusion of thermal deformation effects;

(iv) initial conditions representing disturbances.

This is followed by the calling of the subroutines MODEL and MODE which are briefly explained below.

Subroutine MODEL

The subroutine reads in the data relating to the system configuration. The data

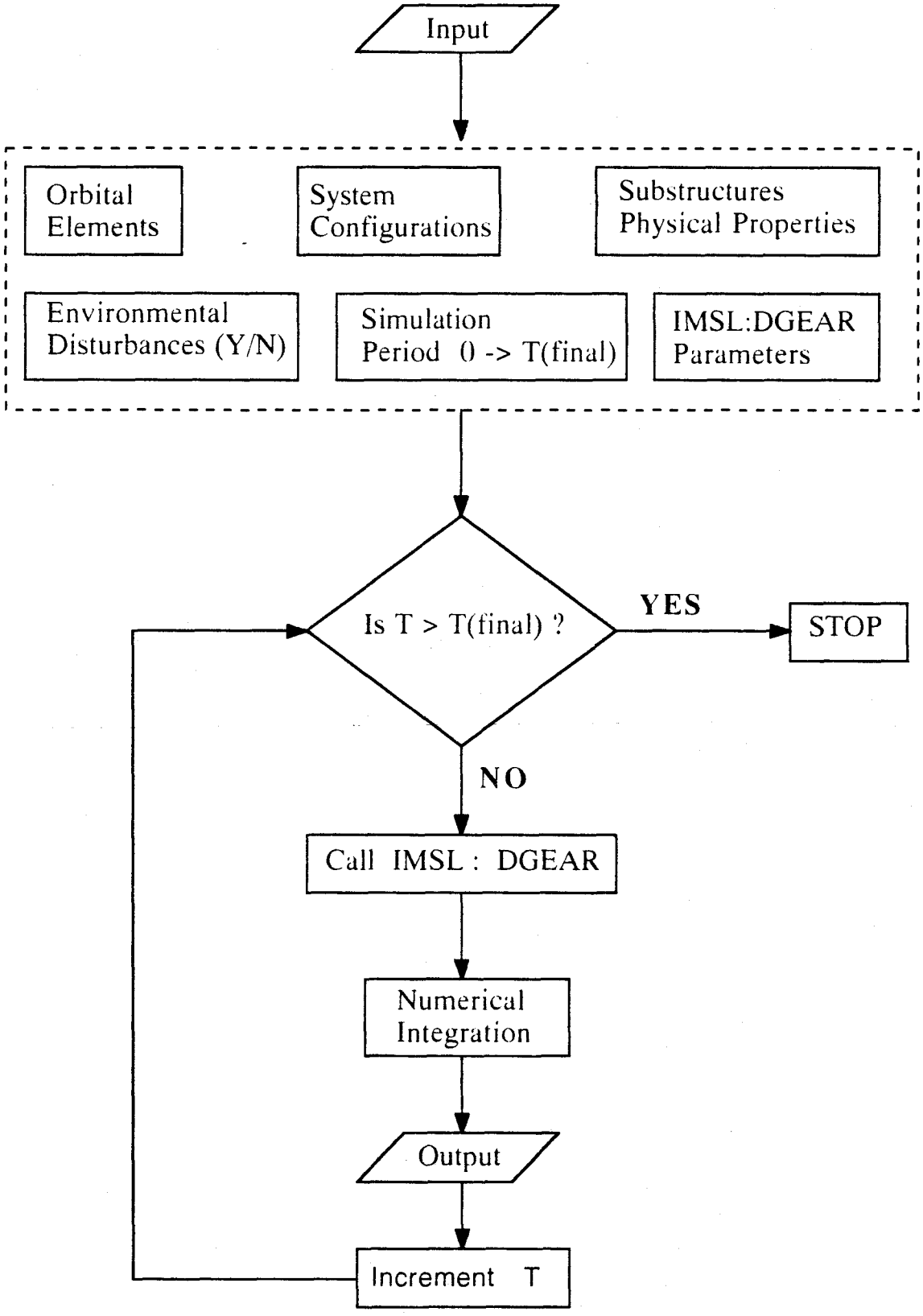

Figure 3-1 Flowchart showing numerical approach to multibody dynamics simulation.

include:

(i) number of B_i and $B_{i,j}$ bodies;

(ii) number of modes for beam and plate shape functions;

(iii) geometry of each body: rigid body, flexible beam or plate-type appendage;

(iv) for body B_k: mass (m_k), length (l_k), length/width ratio (r_k), thermal length ratio (L_k^*), and stiffness (ω_k);

(v) principal and cross-product of inertias of body B_k: $(I_{xx})_k$, $(I_{yy})_k$, $(I_{zz})_k$, $(I_{xy})_k$, $(I_{xz})_k$, and $(I_{yz})_k$;

(vi) orientation of F_c with respect to the orbital axes, of F_i w.r.t. F_c, and $F_{i,j}$ w.r.t. F_i;

(vii) location of O_i relative to O_c, and of $O_{i,j}$ relative to O_i.

Note that B_c can be either a rigid body, free-free beam or completely free plate whereas B_i and $B_{i,j}$ can be rigid bodies, cantilevered beams, cantilevered plates or combinations of them. For a parametric study, all quantities in (iv) and (v) are introduced in dimensionless forms.

Subroutine MODE

Once the geometry of each body is known, the modal integrals for each body can be determined. These integrals, which are used in the evaluation of kinetic and potential energies, include:

$$\Phi_1^r = \int_{-\zeta_l}^{\zeta_u} \phi^r(\zeta)\, d\zeta\,; \qquad \Phi_5^r = \int_{-\zeta_l}^{\zeta_u} \frac{d^2\phi^r(\zeta)}{d\zeta^2}\, d\zeta\,;$$

$$\Phi_2^r = \int_{-\zeta_l}^{\zeta_u} (\phi^r(\zeta))^2\, d\zeta\,; \qquad \Phi_6^{r,s} = \int_{-\zeta_l}^{\zeta_u} \phi^r(\zeta)\frac{d^2\phi^s(\zeta)}{d\zeta^2}\, d\zeta\,;$$

$$\Phi_3^r = \int_{-\zeta_l}^{\zeta_u} \zeta \phi^r(\zeta)\, d\zeta \; ; \qquad \Phi_7^{r,s} = \int_{-\zeta_l}^{\zeta_u} \frac{d\phi^r(\zeta)}{d\zeta} \frac{d\phi^s(\zeta)}{d\zeta}\, d\zeta \; .$$

$$\Phi_4^r = \int_{-\zeta_l}^{\zeta_u} \zeta^2 \phi^r(\zeta)\, d\zeta \; ;$$

The limits of the integrals are either $(-0.5 < \zeta < 0.5)$ for free-free shape functions or $(0 < \zeta < 1)$ for the cantilevered case. The first four integrals (Φ_1^r, Φ_2^r, Φ_3^r, and Φ_4^r) are used in the evaluation of the kinetic energy expressions. For instance, using Eq. (2.20) and (2.29) to evaluate $T_{t,v}$ in Eq. (2.35), Φ_4^r would be required. The last three integrals are used in the evaluation of strain energies as can be seen from Eq. (2.40). For plate type appendages, the integrals for shape functions in both X and Y directions are evaluated.

After executing the subroutines MODEL and MODE, the program begins the numerical integration of the equations of motion which are coded in the subroutine FCN. At the completion of each integration step, the program can evaluate the energies of the system if such information is desired. Let the solution $\bar{y}_{n-1}$ at $\theta = (n-1)\tau$ be known. The determination of $\bar{y}_n$ can proceed as indicated in Figure 3-2 . The importance of the subroutine FCN is now apparent; it is required at every prediction or correction step. Hence, it would be useful to understand in greater details the architecture of FCN.

3.4 Subroutine FCN

3.4.1 Background

In general, evaluation of the kinetic and potential energies is straightforward; however, determination of their derivatives is not necessarily so. For instance,

$$T_v = \frac{1}{2} \int_{m_c} \bar{\delta}_c' \cdot \bar{\delta}_c'\, dm_c + \frac{1}{2} \sum_{i=1}^{N} \left[\int_{m_i} (\mathbf{C}_\mathbf{i}^\mathbf{c} \bar{\delta}_i') \cdot (\mathbf{C}_\mathbf{i}^\mathbf{c} \bar{\delta}_i')\, dm_i \right.$$

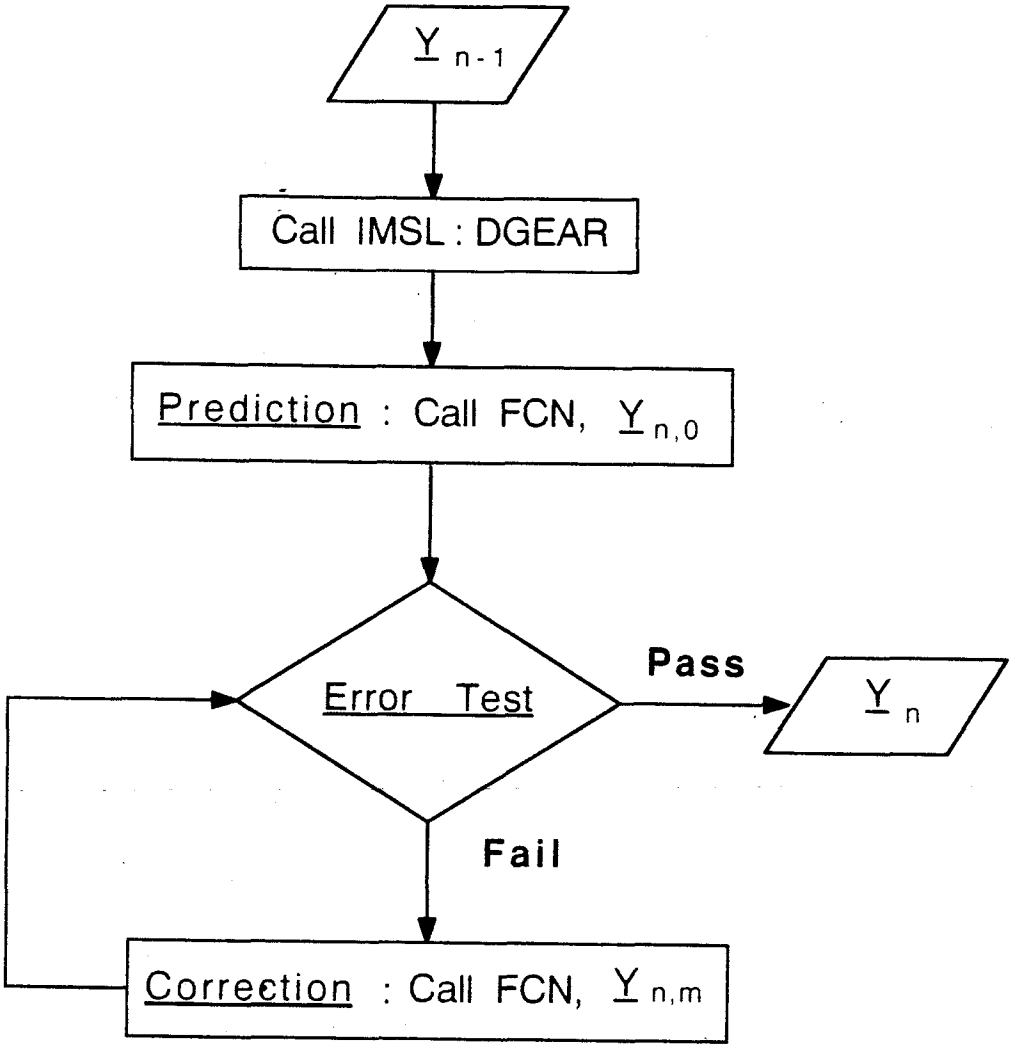

Figure 3-2 Flowchart of a numerical integration subroutine.

$$+\sum_{j=1}^{n_i}\int_{m_{i,j}}(\mathbf{C}^{\mathbf{c}}_{\mathbf{i,j}}\mu_{\mathbf{i,j}}\bar{\delta}'_{ij})\cdot(\mathbf{C}^{\mathbf{c}}_{\mathbf{i,j}}\mu_{\mathbf{i,j}}\bar{\delta}'_{ij})\,dm_{i,j}\Bigg]; \tag{3.3a}$$

$$\frac{d}{d\theta}\frac{\partial T_v}{\partial q'}=\int_{m_c}\left\{\frac{d\bar{\delta}'_c}{d\theta}\cdot\frac{\partial\bar{\delta}'_c}{\partial q'}+\bar{\delta}'_c\cdot\frac{d}{d\theta}\frac{\partial\bar{\delta}'_c}{\partial q'}\right\}dm_c$$

$$+\sum_{i=1}^{N}\left[\int_{m_i}\left\{(\mathbf{C}^{\mathbf{c}\prime}_{\mathbf{i}}\bar{\delta}'_i+\mathbf{C}^{\mathbf{c}}_{\mathbf{i}}\bar{\delta}''_i)\cdot\frac{\partial(\mathbf{C}^{\mathbf{c}}_{\mathbf{i}}\bar{\delta}'_i)}{\partial q'}+(\mathbf{C}^{\mathbf{c}}_{\mathbf{i}}\bar{\delta}'_i)\cdot\frac{d}{d\theta}\frac{\partial(\mathbf{C}^{\mathbf{c}}_{\mathbf{i}}\bar{\delta}'_i)}{\partial q'}\right\}dm_i\right.$$

$$+\sum_{j=1}^{n_i}\int_{m_{i,j}}\Big\{(\mathbf{C}^{\mathbf{c}\,\prime}_{\mathbf{ij}}\mu_{\mathbf{ij}}\bar{\delta}'_{ij}+\mathbf{C}^{\mathbf{c}}_{\mathbf{ij}}\mu'_{\mathbf{ij}}\bar{\delta}'_{ij}+\mathbf{C}^{\mathbf{c}}_{\mathbf{i,j}}\mu_{\mathbf{i,j}}\bar{\delta}''_{ij})\cdot\frac{\partial(\mathbf{C}^{\mathbf{c}}_{\mathbf{i,j}}\mu_{\mathbf{i,j}}\bar{\delta}'_{ij})}{\partial q'}$$

$$+(\mathbf{C}^{\mathbf{c}}_{\mathbf{i,j}}\mu_{\mathbf{i,j}}\bar{\delta}'_{ij})\cdot\frac{d}{d\theta}\frac{\partial(\mathbf{C}^{\mathbf{c}}_{\mathbf{i,j}}\mu_{\mathbf{i,j}}\bar{\delta}'_{ij})}{\partial q'}\Big\}\,dm_{i,j}\Big]\,. \tag{3.3b}$$

At first glance, numerical evaluation of Eq. (3.3b) does not seem to be much more difficult than that of Eq. (3.3a). Only the number of terms has increased from 3 to 9. The problem lies in a dramatic increase in vector dot products, multiplications between matrices and between matrices and vectors. In evaluating T_v according to Eq. (3.3a), 3 dot products, 1 product of matrices and 2 multiplications between a matrix and a vector are required. The respective numbers of operations in Eq. (3.3b) for evaluating $d/d\theta(\partial T_v/\partial q')$ are 6, 7, and 13. Obviously, the increase in the effort required for the operations is phenomenal. Although the operations can be executed manually, the resulting computer codes for Eq. (3.3b) are lengthy and hence demand considerable effort to manage and debug. An effective way to evaluate derivatives of T_{sys}, $\mathbf{I}_{sys}$ and $\bar{H}_{sys}$ is therefore necessary. One such approach is presented next. The idea is to assemble terms in Eq. (3.3b) in stages, each according to a simple algorithm. The significant advantage of this approach is that the user is only required to perform simple differentiation and supply this information to the program.

3.4.2 Definitions of new operators

Consider matrices $\mathbf{A}$, $\mathbf{B}$ and vectors $\bar{C}$, $\bar{D}$ such that

$$\mathbf{A}=\begin{bmatrix}a_{11}&a_{12}&a_{13}\\a_{21}&a_{22}&a_{23}\\a_{31}&a_{32}&a_{33}\end{bmatrix}=[a_{kl}]\,;\qquad \mathbf{B}=\begin{bmatrix}b_{11}&b_{12}&b_{13}\\b_{21}&b_{22}&b_{23}\\b_{31}&b_{32}&b_{33}\end{bmatrix}=[b_{kl}]\,;$$

$$\bar{C}=\begin{Bmatrix}c_1\\c_2\\c_3\end{Bmatrix}\,;\qquad \bar{D}=\begin{Bmatrix}d_1\\d_2\\d_3\end{Bmatrix}\,;$$

Four operations on these matrices and vectors are defined:

$$\Upsilon(\mathbf{A},\mathbf{B}) = \begin{bmatrix} (a_{11}b_{11}+a_{21}b_{21}+a_{31}b_{31}) \\ (a_{12}b_{11}+a_{22}b_{21}+a_{32}b_{31}) \\ (a_{13}b_{11}+a_{23}b_{21}+a_{33}b_{31}) \\ (a_{11}b_{12}+a_{21}b_{22}+a_{31}b_{32}) \\ (a_{12}b_{12}+a_{22}b_{22}+a_{32}b_{32}) \\ (a_{13}b_{12}+a_{23}b_{22}+a_{33}b_{32}) \\ (a_{11}b_{13}+a_{21}b_{23}+a_{31}b_{33}) \\ (a_{12}b_{13}+a_{22}b_{23}+a_{32}b_{33}) \\ (a_{13}b_{13}+a_{23}b_{23}+a_{33}b_{33}) \end{bmatrix}$$

$$= [\upsilon_m], \qquad m = 1,\ldots,9; \tag{3.4a}$$

$$\Gamma(\mathbf{A},\mathbf{B}) = \begin{bmatrix} a_{11}[b_{kl}] & a_{12}[b_{kl}] & a_{13}[b_{kl}] \\ a_{21}[b_{kl}] & a_{22}[b_{kl}] & a_{23}[b_{kl}] \\ a_{31}[b_{kl}] & a_{32}[b_{kl}] & a_{33}[b_{kl}] \end{bmatrix}$$

$$= [\gamma_{mn}], \qquad m = 1,\ldots,9;\ n = 1,\ldots,9; \tag{3.4b}$$

$$\Lambda(\mathbf{A},\mathbf{B}) = \begin{bmatrix} (b_{21}a_{31}-b_{31}a_{21}) & (b_{31}a_{11}-b_{11}a_{31}) & (b_{11}a_{21}-b_{21}a_{11}) \\ (b_{21}a_{32}-b_{31}a_{22}) & (b_{31}a_{12}-b_{11}a_{32}) & (b_{11}a_{22}-b_{21}a_{12}) \\ (b_{21}a_{33}-b_{31}a_{23}) & (b_{31}a_{13}-b_{11}a_{33}) & (b_{11}a_{23}-b_{21}a_{13}) \\ (b_{22}a_{31}-b_{32}a_{21}) & (b_{32}a_{11}-b_{12}a_{31}) & (b_{12}a_{21}-b_{22}a_{11}) \\ (b_{22}a_{32}-b_{32}a_{22}) & (b_{32}a_{12}-b_{12}a_{32}) & (b_{12}a_{22}-b_{22}a_{12}) \\ (b_{22}a_{33}-b_{32}a_{23}) & (b_{32}a_{13}-b_{12}a_{33}) & (b_{12}a_{23}-b_{22}a_{13}) \\ (b_{23}a_{31}-b_{33}a_{21}) & (b_{33}a_{11}-b_{13}a_{31}) & (b_{13}a_{21}-b_{23}a_{11}) \\ (b_{23}a_{32}-b_{33}a_{22}) & (b_{33}a_{12}-b_{13}a_{32}) & (b_{13}a_{22}-b_{23}a_{12}) \\ (b_{23}a_{33}-b_{33}a_{23}) & (b_{33}a_{13}-b_{13}a_{33}) & (b_{13}a_{23}-b_{23}a_{13}) \end{bmatrix}$$

$$= [\lambda_{mn}], \qquad m = 1,\ldots,9;\ n = 1,\ldots,3; \tag{3.4c}$$

$$\Theta(\bar{C},\bar{D}) = \begin{bmatrix} c_1d_1 \\ c_1d_2 \\ c_1d_3 \\ c_2d_1 \\ c_2d_2 \\ c_2d_3 \\ c_3d_1 \\ c_3d_2 \\ c_3d_3 \end{bmatrix}$$

$$= [\theta_m] , \qquad m = 1, \ldots, 9; \tag{3.4d}$$

where Υ, Γ, Λ, and Θ have the dimensions of 9×1, 9×9, 9×3 and 9×1, respectively. The next step is to operate Γ, Λ, and Υ with Θ giving:

$$\Upsilon(\mathbf{A},\, \mathbf{B}) \circ \Theta(\bar{C},\, \bar{D}) = \sum_{k=1}^{9} \upsilon_k \theta_k \, ; \tag{3.5a}$$

$$\Gamma(\mathbf{A},\, \mathbf{B}) \circ \Theta(\bar{C},\, \bar{D}) = \begin{bmatrix} \sum_{k=1}^{9} \gamma_{1k}\theta_k & \sum_{k=1}^{9} \gamma_{2k}\theta_k & \sum_{k=1}^{9} \gamma_{3k}\theta_k \\ \sum_{k=1}^{9} \gamma_{4k}\theta_k & \sum_{k=1}^{9} \gamma_{5k}\theta_k & \sum_{k=1}^{9} \gamma_{6k}\theta_k \\ \sum_{k=1}^{9} \gamma_{7k}\theta_k & \sum_{k=1}^{9} \gamma_{8k}\theta_k & \sum_{k=1}^{9} \gamma_{9k}\theta_k \end{bmatrix} \, ; \tag{3.5b}$$

$$\Lambda(\mathbf{A},\, \mathbf{B}) \circ \Theta(\bar{C},\, \bar{D}) = \begin{Bmatrix} \sum_{k=1}^{9} \lambda_{k1}\theta_k \\ \sum_{k=1}^{9} \lambda_{k2}\theta_k \\ \sum_{k=1}^{9} \lambda_{k3}\theta_k \end{Bmatrix} . \tag{3.5c}$$

Using these operators, $T_{t,v}$, $\mathbf{I}_{t,v}$, and $\bar{H}_{t,v}$ can be written as:

$$\begin{aligned}
T_{t,v} = & \int_{m_c} \Upsilon(\mathbf{U}, \mathbf{U}) \circ \Theta(\bar{\tau}_c', \bar{\delta}_c')\, dm_c \\
& + \sum_{i=1}^{N} \Bigg[\int_{m_i} \Upsilon(\mathbf{C_i^c}, \mathbf{C_i^c}) \circ \Theta(\bar{\tau}_i', \bar{\delta}_i')\, dm_i \\
& + \sum_{j=1}^{n_i} \int_{m_{i,j}} \Upsilon(\mathbf{C_{i,j}^c}\mu_{\mathbf{i,j}}, \mathbf{C_{i,j}^c}\mu_{\mathbf{i,j}}) \circ \Theta(\bar{\tau}_{ij}', \bar{\delta}_{ij}')\, dm_{i,j} \Bigg] \, ; \\
\mathbf{I}_{t,v} = & \int_{m_c} \Big\{ 2\Upsilon(\mathbf{U}, \mathbf{U}) \circ \Theta(\bar{\tau}_c, \bar{\delta}_c)\mathbf{U} \\
& - \Gamma(\mathbf{U}, \mathbf{U}) \circ \Big[\Theta(\bar{\tau}_c, \bar{\delta}_c) + \Theta(\bar{\delta}_c, \bar{\tau}_c) \Big] \Big\}\, dm_c \\
& + \sum_{i=1}^{N} \Bigg[\int_{m_i} \Big\{ 2\Upsilon(\mathbf{C_i^c}, \mathbf{C_i^c}) \circ \Theta(\bar{\tau}_i, \bar{\delta}_i)\mathbf{U} \\
& - \Gamma(\mathbf{C_i^c}, \mathbf{C_i^c}) \circ \Big[\Theta(\bar{\tau}_i, \bar{\delta}_i) + \Theta(\bar{\delta}_i, \bar{\tau}_i) \Big] \Big\}\, dm_i \\
& + \sum_{j=1}^{n_i} \Bigg[\int_{m_{i,j}} \Big\{ 2\Upsilon(\mathbf{C_{i,j}^c}\mu_{\mathbf{i,j}}, \mathbf{C_{i,j}^c}\mu_{\mathbf{i,j}}) \circ \Theta(\bar{\tau}_{ij}, \bar{\delta}_{ij})\mathbf{U} \\
& - \Gamma(\mathbf{C_{i,j}^c}\mu_{\mathbf{i,j}}, \mathbf{C_{i,j}^c}\mu_{\mathbf{i,j}}) \circ \Big[\Theta(\bar{\tau}_{ij}, \bar{\delta}_{ij}) + \Theta(\bar{\delta}_{ij}, \bar{\tau}_{ij}) \Big] \Big\}\, dm_{i,j} \Bigg] \, ;
\end{aligned}$$

$$\bar{H}_{t,v} = \int_{m_c} \left\{ \Lambda(\mathbf{U},\mathbf{U}) \circ \left[\Theta(\bar{\tau}_c, \bar{\delta}'_c) + \Theta(\bar{\delta}_c, \bar{\tau}'_c) \right] \right\} dm_c$$
$$+ \sum_{i=1}^{N} \left[\int_{m_i} \left\{ \Lambda(\mathbf{C}^{\mathbf{c}}_{\mathbf{i}}, \mathbf{C}^{\mathbf{c}}_{\mathbf{i}}) \circ \left[\Theta(\bar{\tau}_i, \bar{\delta}'_i) + \Theta(\bar{\delta}_i, \bar{\tau}'_i) \right] \right\} dm_i \right.$$
$$\left. + \sum_{j=1}^{n_i} \int_{m_{i,j}} \left\{ \Lambda(\mathbf{C}^{\mathbf{c}}_{\mathbf{i,j}}\mu_{\mathbf{i,j}}, \mathbf{C}^{\mathbf{c}}_{\mathbf{i,j}}\mu_{\mathbf{i,j}}) \circ \left[\Theta(\bar{\tau}_{ij}, \bar{\delta}'_{ij}) + \Theta(\bar{\delta}_{ij}, \bar{\tau}'_{ij}) \right] \right\} dm_{i,j} \right] .$$

The expressions appearing in Eqs. (I–1), (I–2), and (I–3) are rewritten in terms of the new operators in Appendix II. For example, consider Eq. (3.3b), which can be expressed as:

$$\frac{d}{d\theta}\frac{\partial T_v}{\partial q'} = \int_{m_c} \left\{ \Upsilon(\mathbf{U},\mathbf{U}) \circ \frac{d}{d\theta}\frac{\partial}{\partial q'}\Theta(\bar{\delta}'_c, \bar{\delta}'_c) \right\} dm_c$$
$$+ \sum_{i=1}^{N} \left[\int_{m_i} \left\{ \frac{d}{d\theta}\Upsilon(\mathbf{C}^{\mathbf{c}}_{\mathbf{i}}, \mathbf{C}^{\mathbf{c}}_{\mathbf{i}}) \circ \frac{\partial}{\partial q'}\Theta(\bar{\delta}'_i, \bar{\delta}'_i) \right.\right.$$
$$\left. + \Upsilon(\mathbf{C}^{\mathbf{c}}_{\mathbf{i}}, \mathbf{C}^{\mathbf{c}}_{\mathbf{i}}) \circ \frac{d}{d\theta}\frac{\partial}{\partial q'}\Theta(\bar{\delta}'_i, \bar{\delta}'_i) \right\} dm_i$$
$$+ \sum_{j=1}^{n_i} \int_{m_{i,j}} \left\{ \frac{d}{d\theta}\Upsilon(\mathbf{C}^{\mathbf{c}}_{\mathbf{i,j}}\mu_{\mathbf{i,j}}, \mathbf{C}^{\mathbf{c}}_{\mathbf{i,j}}\mu_{\mathbf{i,j}}) \circ \frac{\partial}{\partial q'}\Theta(\bar{\delta}'_{ij}, \bar{\delta}'_{ij}) \right.$$
$$\left. + \Upsilon(\mathbf{C}^{\mathbf{c}}_{\mathbf{i,j}}\mu_{\mathbf{i,j}}, \mathbf{C}^{\mathbf{c}}_{\mathbf{i,j}}\mu_{\mathbf{i,j}}) \circ \frac{d}{d\theta}\frac{\partial}{\partial q'}\Theta(\bar{\delta}'_{ij}, \bar{\delta}'_{ij}) \right\} dm_{i,j} . \qquad (3.6)$$

Merit of the new operators is not quite apparent through a direct comparison of Eqs. (3.3b) and (3.6); however, there are two subtle advantages. First, once rotational matrices $\mathbf{C}^{\mathbf{c}}_{\mathbf{i}}$ and $\mathbf{C}^{\mathbf{c}}_{\mathbf{i,j}}\mu_{\mathbf{i,j}}$ are determined, all the required Υ, Γ, and Λ operations can be easily programmed using simple algorithms. Similarly, all the required Θ operations can be coded once the position vectors are determined. The evaluations of T_{sys}, $\mathbf{I}_{sys}$, $\bar{H}_{sys}$ and their derivatives is just a matter of assembling the appropriate Υ, Γ or Λ with the suitable Θ. The second advantage is best illustrated using the expressions of $\mathbf{I}_r$, $\mathbf{I}_t$, and $\mathbf{I}_v$:

$$\mathbf{I}_r = \int_{m_c} \left\{ \Upsilon(\mathbf{U},\mathbf{U}) \circ \Theta(\bar{\rho}_c, \bar{\rho}_c)\mathbf{U} - \Gamma(\mathbf{U},\mathbf{U}) \circ \Theta(\bar{\rho}_c, \bar{\rho}_c) \right\} dm_c$$

$$
\begin{aligned}
&+\sum_{i=1}^{N}\Bigg[\int_{m_i}\Big\{\Upsilon(\mathbf{C_i^c},\mathbf{C_i^c})\circ\Theta(\bar{\rho}_i,\bar{\rho}_i)\mathbf{U}-\Gamma(\mathbf{C_i^c},\mathbf{C_i^c})\circ\Theta(\bar{\rho}_i,\bar{\rho}_i)\Big\}\,dm_i\\
&+\sum_{j=1}^{n_i}\int_{m_{i,j}}\Big\{\Upsilon(\mathbf{C_{i,j}^c}\mu_{\mathbf{i,j}},\mathbf{C_{i,j}^c}\mu_{\mathbf{i,j}})\circ\Theta(\bar{\rho}_{ij},\bar{\rho}_{ij})\mathbf{U}\\
&-\Gamma(\mathbf{C_{i,j}^c}\mu_{\mathbf{i,j}},\mathbf{C_{i,j}^c}\mu_{\mathbf{i,j}})\circ\Theta(\bar{\rho}_{ij},\bar{\rho}_{ij})\Big\}\,dm_{i,j}\Bigg];\\
\mathbf{I}_t=&\int_{m_c}\Big\{\Upsilon(\mathbf{U},\mathbf{U})\circ\Theta(\bar{\tau}_c,\bar{\tau}_c)\mathbf{U}-\Gamma(\mathbf{U},\mathbf{U})\circ\Theta(\bar{\tau}_c,\bar{\tau}_c)\Big\}\,dm_c\\
&+\sum_{i=1}^{N}\Bigg[\int_{m_i}\Big\{\Upsilon(\mathbf{C_i^c},\mathbf{C_i^c})\circ\Theta(\bar{\tau}_i,\bar{\tau}_i)\mathbf{U}-\Gamma(\mathbf{C_i^c},\mathbf{C_i^c})\circ\Theta(\bar{\tau}_i,\bar{\tau}_i)\Big\}\,dm_i\\
&+\sum_{j=1}^{n_i}\int_{m_{i,j}}\Big\{\Upsilon(\mathbf{C_{i,j}^c}\mu_{\mathbf{i,j}},\mathbf{C_{i,j}^c}\mu_{\mathbf{i,j}})\circ\Theta(\bar{\tau}_{ij},\bar{\tau}_{ij})\mathbf{U}\\
&-\Gamma(\mathbf{C_{i,j}^c}\mu_{\mathbf{i,j}},\mathbf{C_{i,j}^c}\mu_{\mathbf{i,j}})\circ\Theta(\bar{\tau}_{ij},\bar{\tau}_{ij})\Big\}\,dm_{i,j}\Bigg];\\
\mathbf{I}_v=&\int_{m_c}\Big\{\Upsilon(\mathbf{U},\mathbf{U})\circ\Theta(\bar{\delta}_c,\bar{\delta}_c)\mathbf{U}-\Gamma(\mathbf{U},\mathbf{U})\circ\Theta(\bar{\delta}_c,\bar{\delta}_c)\Big\}\,dm_c\\
&+\sum_{i=1}^{N}\Bigg[\int_{m_i}\Big\{\Upsilon(\mathbf{C_i^c},\mathbf{C_i^c})\circ\Theta(\bar{\delta}_i,\bar{\delta}_i)\mathbf{U}-\Gamma(\mathbf{C_i^c},\mathbf{C_i^c})\circ\Theta(\bar{\delta}_i,\bar{\delta}_i)\Big\}\,dm_i\\
&+\sum_{j=1}^{n_i}\int_{m_{i,j}}\Big\{\Upsilon(\mathbf{C_{i,j}^c}\mu_{\mathbf{i,j}},\mathbf{C_{i,j}^c}\mu_{\mathbf{i,j}})\circ\Theta(\bar{\delta}_{ij},\bar{\delta}_{ij})\mathbf{U}\\
&-\Gamma(\mathbf{C_{i,j}^c}\mu_{\mathbf{i,j}},\mathbf{C_{i,j}^c}\mu_{\mathbf{i,j}})\circ\Theta(\bar{\delta}_{ij},\bar{\delta}_{ij})\Big\}\,dm_{i,j}\Bigg].
\end{aligned}
\tag{3.7}
$$

Note, the same Υ and Γ operations are used in each expression. This results in a significant saving of the computational effort.

3.4.3 Subprograms in FCN

Figure 3-3 shows the flowchart for subroutine FCN. Contributions of the various subprograms are briefly explained below.

Subprogram DIRANG

The subroutine evaluates the angular velocities $\bar{\omega}$ of Eq. (2.2), direction cosines

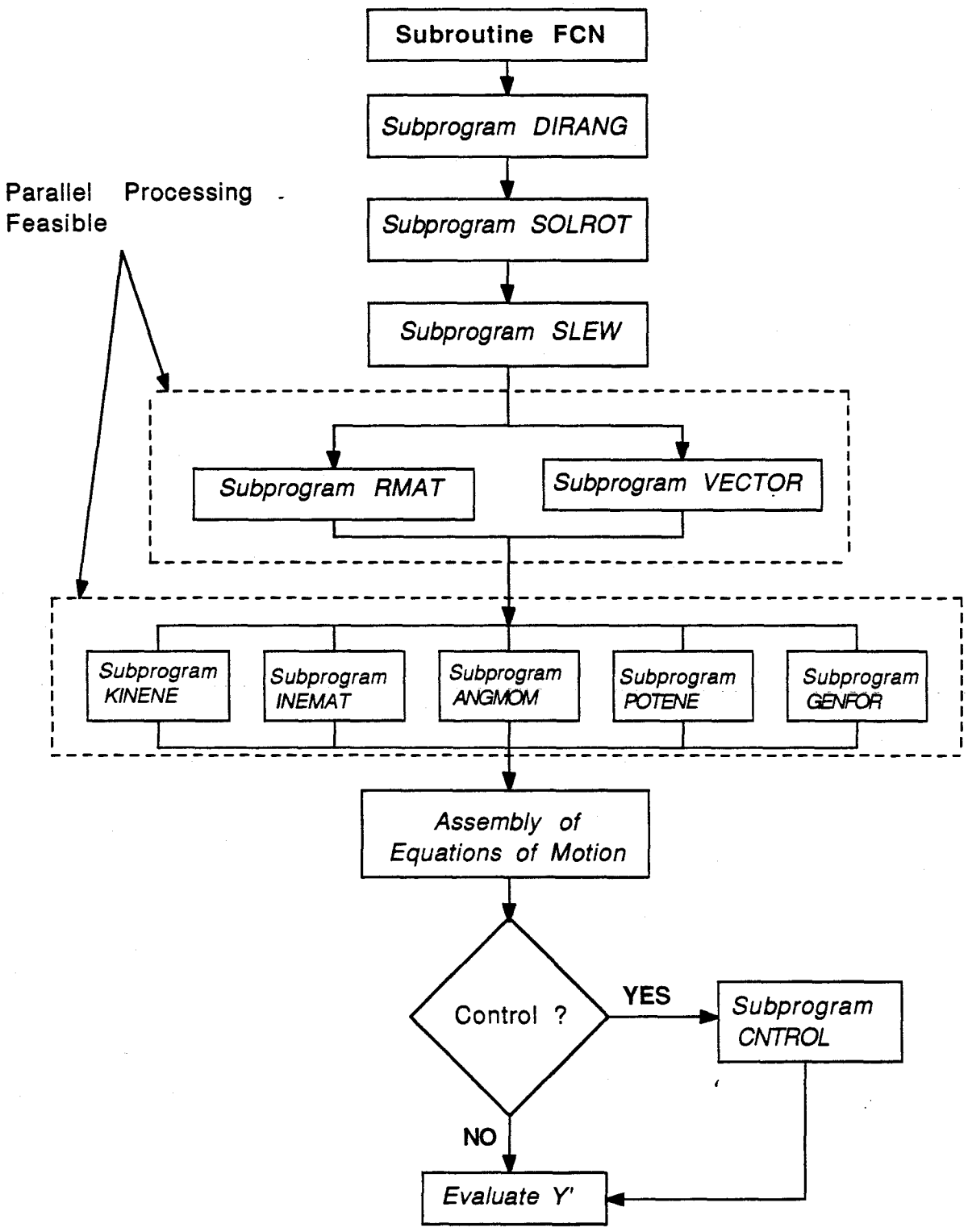

Figure 3-3 Flowchart of the subroutine FCN.

$\bar{l}$ of Eq. (2.39), and their derivatives. These include $\partial\bar{\omega}/\partial q$, $\partial\bar{\omega}/\partial q'$, $d/d\theta(\partial\bar{\omega}/\partial q')$, and $d\bar{\omega}/d\theta$ ($q = \psi, \phi$, and λ). These derivatives are evaluated manually and then programmed into the subroutine. In evaluating $d\bar{\omega}/d\theta$, it is further separated into two parts: one contains ψ'', ϕ'', and λ'' while the other contains the coupling among ψ', ϕ', and λ'. This procedure is necessary in the assembly of the system mass matrix.

Subprogram SOLROT

The objective of the subroutine is to evaluate the solar radiation incidence angles ($\bar{\phi}_c$, $\bar{\phi}_i$, and $\bar{\phi}_{i,j}$), the rotation matrices ($\mathbf{C^c_i}$ and $\mathbf{C^c_{i,j}}$) and their derivatives. To illustrate, the procedure for evaluation of $\bar{\phi}_c$ and $\mathbf{C^c_i}$ is explained below:

(i) Using the orbital elements and libration angles as input, $\bar{\phi}_c$ as given by Eq. (2.7) is calculated. The derivatives ($\partial\bar{\phi}_c/\partial q$, $\bar{\phi}'_c$, $d/d\theta(\partial\bar{\phi}_c/\partial q')$, and $\bar{\phi}''_c$) are evaluated based on the explicit coded expressions.

(ii) θ_{x_c}, θ_{y_c}, and θ_{z_c} are evaluated using Eq. (2.31). Note that depending on the configuration of B_c, the subroutine selects the correct expression from Eqs. (2.31a), (2.31b), and (2.31c).

(iii) The rotation matrix $\mathbf{C^c_i}$ as given by Eq. (2.30) and its derivatives are determined next. Again, explicit expressions for the derivatives are coded for this purpose.

The same procedure is repeated for $\bar{\phi}_i$ and $\mathbf{C^i_{i,j}}$ using Eq. (2.8a) and (2.30), respectively. Finally $\mathbf{C^c_{i,j}}$ is determined from Eq. (2.32) and substituted into Eq. (2.8b) to give the required $\bar{\phi}_{i,j}$.

Subprogram SLEW

In this subroutine, $\mu_{\mathbf{i,j}}$, $\mu'_{\mathbf{i,j}}$, and $\mu''_{\mathbf{i,j}}$ are coded explicitly. Using $\mathbf{C^c_{i,j}}$ and its derivatives from subroutine SOLROT, the subprogram then evaluates $\mathbf{C^c_{i,j}}\mu_{\mathbf{i,j}}$ and

the associated derivatives.

Subprogram RMAT

The subprogram evaluates all the necessary Υ, Γ, and Λ matrices given by Eq. (3.4a), (3.4b) and (3.4c), respectively. These matrices are shown in Table 3-1 . The alphanumeric name in the first column identifies the array in the computer program; and its location in the array is denoted by the subscript of Υ, Γ, or Λ. For instance, $\Lambda(\mathbf{U}, \mathbf{C_i^{c\prime}})$ is represented by $R93i(4)$ in the program. The required derivatives for each operation are:

$$\begin{aligned}
\Upsilon &: \frac{\partial \Upsilon}{\partial q}, \quad \frac{\partial \Upsilon}{\partial q'}, \quad \frac{d}{d\theta}\frac{\partial \Upsilon}{\partial q'}, \quad \frac{d\Upsilon}{d\theta}; \\
\Gamma &: \frac{\partial \Gamma}{\partial q}, \quad \frac{d\Gamma}{d\theta}; \\
\Lambda &: \frac{\partial \Lambda}{\partial q}, \quad \frac{\partial \Lambda}{\partial q'}, \quad \frac{d}{d\theta}\frac{\partial \Lambda}{\partial q'}, \quad \frac{d\Lambda}{d\theta}.
\end{aligned}$$

Although there are a number of operations involved, they all can be executed using similar algorithms. Besides, the derivatives of the operators do not require any manual effort. For instance,

$$\frac{\partial \Lambda(\mathbf{C_i^c}, \mathbf{C_i^c})}{\partial q} = \Lambda(\frac{\partial \mathbf{C_i^c}}{\partial q}, \mathbf{C_i^c}) + \Lambda(\mathbf{C_i^c}, \frac{\partial \mathbf{C_i^c}}{\partial q}),$$

with $\partial \mathbf{C_i^c}/\partial q$ provided by the subroutine SOLROT.

Subprogram VECTOR

The subroutine evaluates all the required Θ column matrices as given by Eq. (3.4d). Table 3-2 represents their complete list. Each Θ column matrix occupies a unique position in the program which is indicated by its array name in the first column and its array position in the subscript of Θ. For instance, $DDij(3)$ refers to $\Theta(\bar{d}_i, \bar{d}'_{i,j})$.

Table 3-1 List of Υ, Λ, and Γ operations executed in subroutine RMAT

$R91c$	$\Upsilon_1(\mathbf{U},\mathbf{U})$		
$R91i$	$\Upsilon_1(\mathbf{C_i^{c\prime}},\mathbf{C_i^{c\prime}})$	$\Upsilon_2(\mathbf{C_i^{c\prime}},\mathbf{C_i^{c}})$	$\Upsilon_3(\mathbf{U},\mathbf{C_i^{c\prime}})$
	$\Upsilon_4(\mathbf{C_i^{c}},\mathbf{C_i^{c}})$	$\Upsilon_5(\mathbf{U},\mathbf{C_i^{c}})$	
$R91ij$	$\Upsilon_1(\mathbf{C_i^{c\prime}},(\mathbf{C_{i,j}^{c}}\mu_{\mathbf{i,j}})')$	$\Upsilon_2(\mathbf{C_i^{c\prime}},\mathbf{C_{i,j}^{c}}\mu_{\mathbf{i,j}})$	$\Upsilon_3(\mathbf{C_i^{c}},(\mathbf{C_{i,j}^{c}}\mu_{\mathbf{i,j}})')$
	$\Upsilon_4(\mathbf{C_i^{c}},\mathbf{C_{i,j}^{c}}\mu_{\mathbf{i,j}})$		
$R91j$	$\Upsilon_1((\mathbf{C_{i,j}^{c}}\mu_{\mathbf{i,j}})',(\mathbf{C_{i,j}^{c}}\mu_{\mathbf{i,j}})')$	$\Upsilon_2((\mathbf{C_{i,j}^{c}}\mu_{\mathbf{i,j}})',\mathbf{C_{i,j}^{c}}\mu_{\mathbf{i,j}})$	$\Upsilon_3(\mathbf{U},(\mathbf{C_{i,j}^{c}}\mu_{\mathbf{i,j}})')$
	$\Upsilon_4(\mathbf{C_{i,j}^{c}}\mu_{\mathbf{i,j}},\mathbf{C_{i,j}^{c}}\mu_{\mathbf{i,j}})$	$\Upsilon_5(\mathbf{U},\mathbf{C_{i,j}^{c}}\mu_{\mathbf{i,j}})$	
$R99c$	$\Gamma_1(\mathbf{U},\mathbf{U})$		
$R99i$	$\Gamma_1(\mathbf{C_i^{c}},\mathbf{C_i^{c}})$	$\Gamma_2(\mathbf{U},\mathbf{C_i^{c}})$	
$R99ij$	$\Gamma_1(\mathbf{C_i^{c}},\mathbf{C_{i,j}^{c}}\mu_{\mathbf{i,j}})$		
$R99j$	$\Gamma_1(\mathbf{C_{i,j}^{c}}\mu_{\mathbf{i,j}},\mathbf{C_{i,j}^{c}}\mu_{\mathbf{i,j}})$	$\Gamma_2(\mathbf{U},\mathbf{C_{i,j}^{c}}\mu_{\mathbf{i,j}})$	
$R93c$	$\Lambda_1(\mathbf{U},\mathbf{U})$		
$R93i$	$\Lambda_1(\mathbf{C_i^{c\prime}},\mathbf{C_i^{c\prime}})$	$\Lambda_2(\mathbf{C_i^{c\prime}},\mathbf{C_i^{c}})$	$\Lambda_3(\mathbf{U},\mathbf{C_i^{c\prime}})$
	$\Lambda_4(\mathbf{C_i^{c}},\mathbf{C_i^{c}})$	$\Lambda_5(\mathbf{U},\mathbf{C_i^{c}})$	
$R93ij$	$\Lambda_1(\mathbf{C_i^{c\prime}},(\mathbf{C_{i,j}^{c}}\mu_{\mathbf{i,j}})')$	$\Lambda_2(\mathbf{C_i^{c\prime}},\mathbf{C_{i,j}^{c}}\mu_{\mathbf{i,j}})$	$\Lambda_3(\mathbf{C_i^{c}},(\mathbf{C_{i,j}^{c}}\mu_{\mathbf{i,j}})')$
	$\Lambda_4(\mathbf{C_i^{c}},\mathbf{C_{i,j}^{c}}\mu_{\mathbf{i,j}})$		
$R93j$	$\Lambda_1((\mathbf{C_{i,j}^{c}}\mu_{\mathbf{i,j}})',(\mathbf{C_{i,j}^{c}}\mu_{\mathbf{i,j}})')$	$\Lambda_2((\mathbf{C_{i,j}^{c}}\mu_{\mathbf{i,j}})',\mathbf{C_{i,j}^{c}}\mu_{\mathbf{i,j}})$	$\Lambda_3(\mathbf{U},(\mathbf{C_{i,j}^{c}}\mu_{\mathbf{i,j}})')$
	$\Lambda_4(\mathbf{C_{i,j}^{c}}\mu_{\mathbf{i,j}},\mathbf{C_{i,j}^{c}}\mu_{\mathbf{i,j}})$	$\Lambda_5(\mathbf{U},\mathbf{C_{i,j}^{c}}\mu_{\mathbf{i,j}})$	

$\bar{f}_k$, $\bar{g}_k$, and $\bar{h}_k$ are defined as follows:

$$\bar{f}_k = \frac{1}{m_k}\int_{m_k} \bar{\rho}_k \, dm_k \, ;$$

$$\bar{g}_k = \frac{1}{m_k}\int_{m_k} \bar{\tau}_k \, dm_k \, ;$$

$$\bar{h}_k = \frac{1}{m_k}\int_{m_k} \bar{\delta}_k \, dm_k \, ;$$

where $k = c, i,$ or i,j. The required derivatives include $\partial\Theta/\partial q$, $\partial\Theta/\partial q'$, $d/d\theta(\partial\Theta/\partial q')$, and $d\Theta/d\theta$. Only the derivatives of $\bar{d}_k$, $\bar{g}_k$, $\bar{h}_k$, $\bar{\tau}_k$, and $\bar{\delta}_k$ ($k = c$, i, or i,j) are calculated beforehand and coded. Using this information, the subroutine is able to evaluate

Table 3-2 List of all the Θ operations executed in subroutine VECTOR

CMc	$\Theta_1(\bar{C}'_{cm}, \bar{C}'_{cm})$	$\Theta_2(\bar{C}'_{cm}, \bar{C}_{cm})$	$\Theta_3(\bar{C}_{cm}, \bar{C}'_{cm})$	$\Theta_4(\bar{C}_{cm}, \bar{C}_{cm})$
DDi	$\Theta_1(\bar{d}'_i, \bar{d}'_i)$	$\Theta_2(\bar{d}'_i, \bar{d}_i)$	$\Theta_3(\bar{d}_i, \bar{d}'_i)$	$\Theta_4(\bar{d}_i, \bar{d}_i)$
$DDij$	$\Theta_1(\bar{d}'_i, \bar{d}'_{i,j})$	$\Theta_2(\bar{d}'_i, \bar{d}_{i,j})$	$\Theta_3(\bar{d}_i, \bar{d}'_{i,j})$	$\Theta_4(\bar{d}_i, \bar{d}_{i,j})$
DDj	$\Theta_1(\bar{d}'_{i,j}, \bar{d}'_{i,j})$	$\Theta_2(\bar{d}'_{i,j}, \bar{d}_{i,j})$	$\Theta_3(\bar{d}_{i,j}, \bar{d}'_{i,j})$	$\Theta_4(\bar{d}_{i,j}, \bar{d}_{i,j})$
DFi	$\Theta_1(\bar{d}'_i, \bar{f}_i)$	$\Theta_2(\bar{d}_i, \bar{f}_i)$		
$DFij$	$\Theta_1(\bar{d}'_i, \bar{f}_{i,j})$	$\Theta_2(\bar{d}_i, \bar{f}_{i,j})$		
DFj	$\Theta_1(\bar{d}'_{i,j}, \bar{f}_{i,j})$	$\Theta_2(\bar{d}_{i,j}, \bar{f}_{i,j})$		
DGi	$\Theta_1(\bar{d}'_i, \bar{g}'_i)$	$\Theta_2(\bar{d}'_i, \bar{g}_i)$	$\Theta_3(\bar{d}_i, \bar{g}'_i)$	$\Theta_4(\bar{d}_i, \bar{g}_i)$
$DGij$	$\Theta_1(\bar{d}'_i, \bar{g}'_{i,j})$	$\Theta_2(\bar{d}'_i, \bar{g}_{i,j})$	$\Theta_3(\bar{d}_i, \bar{g}'_{i,j})$	$\Theta_4(\bar{d}_i, \bar{g}_{i,j})$
DGj	$\Theta_1(\bar{d}'_{i,j}, \bar{g}'_{i,j})$	$\Theta_2(\bar{d}'_{i,j}, \bar{g}_{i,j})$	$\Theta_3(\bar{d}_{i,j}, \bar{g}'_{i,j})$	$\Theta_4(\bar{d}_{i,j}, \bar{g}_{i,j})$
DHi	$\Theta_1(\bar{d}'_i, \bar{h}'_i)$	$\Theta_2(\bar{d}'_i, \bar{h}_i)$	$\Theta_3(\bar{d}_i, \bar{h}'_i)$	$\Theta_4(\bar{d}_i, \bar{h}_i)$
$DHij$	$\Theta_1(\bar{d}'_i, \bar{h}'_{i,j})$	$\Theta_2(\bar{d}'_i, \bar{h}_{i,j})$	$\Theta_3(\bar{d}_i, \bar{h}'_{i,j})$	$\Theta_4(\bar{d}_i, \bar{h}_{i,j})$
DHj	$\Theta_1(\bar{d}'_{i,j}, \bar{h}'_{i,j})$	$\Theta_2(\bar{d}'_{i,j}, \bar{h}_{i,j})$	$\Theta_3(\bar{d}_{i,j}, \bar{h}'_{i,j})$	$\Theta_4(\bar{d}_{i,j}, \bar{h}_{i,j})$
RRc	$\Theta_1(\bar{\rho}_c, \bar{\rho}_c)$			
RRi	$\Theta_1(\bar{\rho}_i, \bar{\rho}_i)$			
RRj	$\Theta_1(\bar{\rho}_{i,j}, \bar{\rho}_{i,j})$			
RTc	$\Theta_1(\bar{\rho}_c, \bar{\tau}'_c)$	$\Theta_2(\bar{\tau}'_c, \bar{\rho}_c)$	$\Theta_3(\bar{\rho}_c, \bar{\tau}_c)$	
RTi	$\Theta_1(\bar{\rho}_i, \bar{\tau}'_i)$	$\Theta_2(\bar{\tau}'_i, \bar{\rho}_i)$	$\Theta_3(\bar{\rho}_i, \bar{\tau}_i)$	
RTj	$\Theta_1(\bar{\rho}_{i,j}, \bar{\tau}'_{i,j})$	$\Theta_2(\bar{\tau}'_{i,j}, \bar{\rho}_{i,j})$	$\Theta_3(\bar{\rho}_{i,j}, \bar{\tau}_{i,j})$	
RVc	$\Theta_1(\bar{\rho}_c, \bar{\delta}'_c)$	$\Theta_2(\bar{\delta}'_c, \bar{\rho}_c)$	$\Theta_3(\bar{\rho}_c, \bar{\delta}_c)$	
RVi	$\Theta_1(\bar{\rho}_i, \bar{\delta}'_i)$	$\Theta_2(\bar{\delta}'_i, \bar{\rho}_i)$	$\Theta_3(\bar{\rho}_i, \bar{\delta}_i)$	
RVj	$\Theta_1(\bar{\rho}_{i,j}, \bar{\delta}'_{i,j})$	$\Theta_2(\bar{\delta}'_{i,j}, \bar{\rho}_{i,j})$	$\Theta_3(\bar{\rho}_{i,j}, \bar{\delta}_{i,j})$	
TTc	$\Theta_1(\bar{\tau}'_c, \bar{\tau}'_c)$	$\Theta_2(\bar{\tau}'_c, \bar{\tau}_c)$	$\Theta_3(\bar{\tau}_c, \bar{\tau}'_c)$	$\Theta_4(\bar{\tau}_c, \bar{\tau}_c)$
TTi	$\Theta_1(\bar{\tau}'_i, \bar{\tau}'_i)$	$\Theta_2(\bar{\tau}'_i, \bar{\tau}_i)$	$\Theta_3(\bar{\tau}_i, \bar{\tau}'_i)$	$\Theta_4(\bar{\tau}_i, \bar{\tau}_i)$
TTj	$\Theta_1(\bar{\tau}'_{i,j}, \bar{\tau}'_{i,j})$	$\Theta_2(\bar{\tau}'_{i,j}, \bar{\tau}_{i,j})$	$\Theta_3(\bar{\tau}_{i,j}, \bar{\tau}'_{i,j})$	$\Theta_4(\bar{\tau}_{i,j}, \bar{\tau}_{i,j})$
TVc	$\Theta_1(\bar{\tau}'_c, \bar{\delta}'_c)$	$\Theta_2(\bar{\tau}'_c, \bar{\delta}_c)$	$\Theta_3(\bar{\tau}_c, \bar{\delta}'_c)$	$\Theta_4(\bar{\tau}_c, \bar{\delta}_c)$
TVi	$\Theta_1(\bar{\tau}'_i, \bar{\delta}'_i)$	$\Theta_2(\bar{\tau}'_i, \bar{\delta}_i)$	$\Theta_3(\bar{\tau}_i, \bar{\delta}'_i)$	$\Theta_4(\bar{\tau}_i, \bar{\delta}_i)$
TVj	$\Theta_1(\bar{\tau}'_{i,j}, \bar{\delta}'_{i,j})$	$\Theta_2(\bar{\tau}'_{i,j}, \bar{\delta}_{i,j})$	$\Theta_3(\bar{\tau}_{i,j}, \bar{\delta}'_{i,j})$	$\Theta_4(\bar{\tau}_{i,j}, \bar{\delta}_{i,j})$
VVc	$\Theta_1(\bar{\delta}'_c, \bar{\delta}'_c)$	$\Theta_2(\bar{\delta}'_c, \bar{\delta}_c)$	$\Theta_3(\bar{\delta}_c, \bar{\delta}'_c)$	$\Theta_4(\bar{\delta}_c, \bar{\delta}_c)$
VVi	$\Theta_1(\bar{\delta}'_i, \bar{\delta}'_i)$	$\Theta_2(\bar{\delta}'_i, \bar{\delta}_i)$	$\Theta_3(\bar{\delta}_i, \bar{\delta}'_i)$	$\Theta_4(\bar{\delta}_i, \bar{\delta}_i)$
VVj	$\Theta_1(\bar{\delta}'_{i,j}, \bar{\delta}'_{i,j})$	$\Theta_2(\bar{\delta}'_{i,j}, \bar{\delta}_{i,j})$	$\Theta_3(\bar{\delta}_{i,j}, \bar{\delta}'_{i,j})$	$\Theta_4(\bar{\delta}_{i,j}, \bar{\delta}_{i,j})$

all the required derivatives. Take $\partial(\bar{d}_i, \bar{d}_{i,j})/\partial q$ as an example, it can be evaluated as:

$$\frac{\partial\Theta(\bar{d}_i, \bar{d}_{i,j})}{\partial q}) = \Theta(\frac{\partial\bar{d}_i}{\partial q}, \bar{d}_{i,j}) + \Theta(\bar{d}_i, \frac{\partial\bar{d}_{i,j}}{\partial q}) .$$

The Θ vector for the shift in the centre of mass is evaluated in two stages. First, $\bar{C}^i_{cm}$, $\bar{C}^f_{cm}$ and their derivatives are determined using Eq. (2.12). Now, the procedure as explained earlier is used to evaluate Θ.

Subprogram KINENE

The evaluation of $\partial T_{sys}/\partial q$ and $d/d\theta(\partial T_{sys}/\partial q')$, where T_{sys} is given by Eq. (2.35), is the objective of this subroutine. In order to facilitate the assembly of system mass matrix, $d/d\theta(\partial T_{sys}/\partial q')$ is separated into components of double derivative and coupling among velocities (Coriolis effect). The evaluation is done using Υ and Θ operations as given in Eq. (3.5a). A portion of the computer program for the assembly of $\partial T_{sys}/\partial q$ is presented in Appendix II.

Subprogram INEMAT

Here, the mass inertia matrix $\mathbf{I}_{sys}$ of the system, as given by Eq. (2.36), is assembled using the operation between Γ and Θ in Eq. (3.5b). In addition, the two derivatives, $\partial\mathbf{I}_{sys}/\partial q$ and $d\mathbf{I}_{sys}/d\theta$, are also evaluated. Appendix II shows the source code for the assembly of $\mathbf{I}_{sys}$.

Subprogram ANGMOM

This subroutine evaluates angular momentum $\bar{H}_{sys}$ given by Eq. (2.37) and the related derivatives including $\partial\bar{H}_{sys}/\partial q$, $\partial\bar{H}_{sys}/\partial q'$, $d/d\theta(\partial\bar{H}_{sys}/\partial q')$, and $d\bar{H}_{sys}/d\theta$. Similar to $d\bar{\omega}/d\theta$, $d\bar{H}_{sys}/d\theta$ is separated into two parts with one consisting of the double derivative terms and the other the Coriolis terms. The evaluation is just a matter of assembly of Λ and Θ operations in Eq. (3.5c). The source code for

calculation of $\bar{H}_{sys}$ is listed in Appendix II.

Subprogram POTENE

The subroutine calculates the $\partial U/\partial q$ term in Lagrange's equation. Here U represents sum of the gravitational potential energy and the strain energy. The former is evaluated using Eq. (2.38) while the latter with Eq. (2.40). Depending on the beam or plate type appendage, the subroutine selects the correct expression for calculating the strain energy derivative.

Subprogram GENFOR

This subroutine calculates the generalized force based on user-supplied explicit expressions. For instance, the generalized force for the Space Station can be the actuator output, solar pressure disturbance, aerodynamic drag, astronaut motion, etc.

Subprogram CNTROL

If a control study is undertaken, this subprogram would calculate the desired controlled states and control effort using the Feedback Linearization Technique.

Assembly of equations of motion

After the execution of the aforementioned subprograms, the next step is to assemble the equations of motion in the form of Eq. (3.2). From Eq. (2.35), the kinetic energy of the system, T, is given by

$$T = T_{orb} + T_{sys} + \frac{1}{2}\bar{\omega}^T \mathbf{I}_{sys}\bar{\omega} + \bar{\omega}^T \bar{H}_{sys} \,. \tag{2.35}$$

Taking the derivative with respect to q and q' gives:

$$\frac{\partial T}{\partial q} = \frac{\partial T_{sys}}{\partial q} + \frac{\partial \bar{\omega}^T}{\partial q}\Big[\mathbf{I}_{sys}\bar{\omega} + \bar{H}_{sys}\Big] + \bar{\omega}^T\Big[\frac{\partial T_{sys}}{\partial q}\bar{\omega} + \frac{\partial \bar{H}_{sys}}{\partial q}\Big] \,; \tag{3.8}$$

$$\frac{\partial T}{\partial q'} = \frac{\partial T_{sys}}{\partial q'} + \frac{\partial \bar{\omega}^T}{\partial q'}\Big[\mathbf{I}_{sys}\bar{\omega} + \bar{H}_{sys}\Big] + \bar{\omega}^T \frac{\partial \bar{H}_{sys}}{\partial q'} \,. \tag{3.9}$$

Note since the Keplerian relations (Eq. 2.41) are assumed to be valid, T_{orb} does not contribute to the equations of motion; hence, it is discarded in the differentiation. Differentiating Eq. (3.9) with respect to θ gives

$$\begin{aligned}\frac{d}{d\theta}\frac{\partial T}{\partial q'} = {} & \frac{d}{d\theta}\frac{\partial T_{sys}}{\partial q'} + \frac{d}{d\theta}\frac{\partial \bar{\omega}^T}{\partial q'}\Big[\mathbf{I}_{sys}\bar{\omega} + \bar{H}_{sys}\Big] \\ & + \frac{\partial \bar{\omega}^T}{\partial q'}\Big[\frac{d\mathbf{I}_{sys}}{d\theta}\bar{\omega} + \mathbf{I}_{sys}\frac{d\bar{\omega}}{d\theta} + \frac{d\bar{H}_{sys}}{d\theta}\Big] + \frac{d\bar{\omega}^T}{d\theta}\frac{\partial \bar{H}_{sys}}{\partial q'} + \bar{\omega}^T \frac{d}{d\theta}\frac{\partial \bar{H}_{sys}}{\partial q'} \,,\end{aligned}$$

which can be separated into the first and second order components:

$$\begin{aligned}O_1\Big(\frac{d}{d\theta}\frac{\partial T}{\partial q'}\Big) = {} & O_1\Big(\frac{d}{d\theta}\frac{\partial T_{sys}}{\partial q'}\Big) + \frac{d}{d\theta}\frac{\partial \bar{\omega}^T}{\partial q'}\Big[\mathbf{I}_{sys}\bar{\omega} + \bar{H}_{sys}\Big] \\ & + \frac{\partial \bar{\omega}^T}{\partial q'}\Big[\frac{d\mathbf{I}_{sys}}{d\theta}\bar{\omega} + \mathbf{I}_{sys}O_1\Big(\frac{d\bar{\omega}}{d\theta}\Big) + O_1\Big(\frac{d\bar{H}_{sys}}{d\theta}\Big)\Big] \\ & + O_1\Big(\frac{d\bar{\omega}^T}{d\theta}\Big)\frac{\partial \bar{H}_{sys}}{\partial q'} + \bar{\omega}^T\frac{d}{d\theta}\frac{\partial \bar{H}_{sys}}{\partial q'} \,; \end{aligned} \tag{3.10a}$$

$$\begin{aligned}O_2\Big(\frac{d}{d\theta}\frac{\partial T}{\partial q'}\Big) = {} & O_2\Big(\frac{d}{d\theta}\frac{\partial T_{sys}}{\partial q'}\Big) + \frac{\partial \bar{\omega}^T}{\partial q'}\Big[\mathbf{I}_{sys}O_2\Big(\frac{d\bar{\omega}}{d\theta}\Big) + O_2\Big(\frac{d\bar{H}_{sys}}{d\theta}\Big)\Big] \\ & + O_2\Big(\frac{d\bar{\omega}^T}{d\theta}\Big)\frac{\partial \bar{H}_{sys}}{\partial q'} \,. \end{aligned} \tag{3.10b}$$

Here O_1 and O_2 represent the first and second order components of the function in parenthesis. Equation (3.1) can now be assembled with ease. $\mathbf{M}$ is given by Eq. (3.10b) and $\bar{Q}$ by the subroutine GENFOR. $\bar{C}$ is the sum of Eqs. (3.8) and (3.10a), and $\bar{K}$ is given by $\partial U/\partial q$ of the subroutine POTENE. Using a suitable matrix inversion subroutine, $\mathbf{M^{-1}}$ can be calculated; hence, $\bar{q}''$ can be obtained. It is then rearranged in the form of Eq. (3.2) and ready for the numerical integration.

Finally, a few general comments concerning implementation of the computer program are appropriate.

(i) To help assess validity of the computer code, the program checks for the

symmetric character of **M** at every integration step. Any indication of non-symmetric entries in **M** would halt further execution.

(ii) The program requires minimal effort in terms of explicit differentiation by the user. Only subroutines DIRANG, SOLROT, and VECTOR require the user to supply explicit expressions of differentiation which, in general, are simple. In evaluating the potential and kinetic energies, no further differentiation effort is required from the user.

(iii) Each subroutine is programmed with simple and repetitive algorithm. This feature greatly aids in the debugging process of the program.

(iv) The modification of the program can be undertaken quite easily due to its modular architecture. This is particularly useful if other shape functions are desired. One just has to replace the subroutine MODE with the new shape functions, while the rest of the program remains intact.

(v) Although the source code is being programmed for sequential execution purpose, the code can always be modified for parallel execution if it is supported by the hardware. This would result in a potential saving in execution time. The possibility of parallel execution exists at two places. First, it can be implemented in processing RMAT and VECTOR subroutines. Second, the subroutines KINENE, INEMAT, and ANGMOM can be executed simultaneously.

3.5 Program Functions

The usefulness of the computer program is not limited to simulating runs for any initial conditions; the program also serves as a powerful tool to study the effect of flexibility, librational motion, thermal deformation, shift in c.m., slewing maneuvers,

etc. For instance, in order to investigate the thermal effect, one has to supply the appropriate index for the thermal parameter in the input of the main program: '0' for exclusion and '1' for inclusion of the thermal effect. If '0' is assumed, the program would essentially set all components of T_{sys}, $\mathbf{I}_{sys}$, and $\bar{H}_{sys}$ associated with the thermal effect to zero, i.e.

$$
\begin{aligned}
T_{sys} &= T_{orb} + T_{cm} + T_h + T_{jr} + T_v + T_{h,jr} + T_{h,v} + T_{jr,v} \; ; \\
\mathbf{I}_{sys} &= \mathbf{I}_{cm} + \mathbf{I}_h + \mathbf{I}_r + \mathbf{I}_v + \mathbf{I}_{h,r} + \mathbf{I}_{h,v} + \mathbf{I}_{r,v} \; ; \\
\bar{H}_{sys} &= \bar{H}_{cm} + \bar{H}_h + \bar{H}_{jr} + \bar{H}_v + \bar{H}_{h,jr} + \bar{H}_{h,r} + \bar{H}_{h,v} + \bar{H}_{r,v} \; .
\end{aligned}
$$

A second run is then made with index '1' which can be compared with the previous result to reveal the effect of thermal deformations. Similar procedure can be used to study the effect of shifting c.m. and slewing maneuvers.

The effect of flexibility and higher modes is assessed by manipulating input to the subroutine MODEL. In order to study the effect of flexibility, one first needs to obtain simulation results for the rigid body case. This can be achieved easily by putting flexible degrees of freedom for each body to be zero. The higher mode effects can be studied by carrying out simulation runs with an increasing number of assumed modes. Once again, this number is supplied at the subroutine MODEL input phase.

The program can also be used to study gyroscopic effect and the influence of the choice of shape functions. Unlike the aforementioned cases, these studies require minor modifications to the program. To isolate the gyroscopic effect, $\bar{C}$ in Eq. (3.1) is set to zero; whereas to study the choice of shape functions, one has to replace subroutine MODE with a new set of admissible functions.

3.6 Program Verification

In modelling a system of such complexity, an obvious question concerning its validity arises. In absence of similar equations obtained independently by others, two avenues are available:

(i) check energy and angular momentum functions;

(ii) comparison with particular cases if reported in literature.

Both methods are pursued here. A check on the energy variation is performed first. An arbitrary rigid satellite with the following nondimensional inertia diadic is chosen:

$$\mathbf{I}_{sys} = \begin{bmatrix} 2719.8 & 0 & 0 \\ 0 & 10.53 & -13.14 \\ 0 & -13.14 & 2717.2 \end{bmatrix} .$$

The satellite is aligned in the gravity gradient stabilized orientation, i.e. the maximum inertia, I_{xx}, is about the orbit normal. Assuming the nondimensional gravitational potential energy at $\theta = 0$ and $\theta = \theta_f$ be denoted by U_0 and U_f, respectively, $\delta U = U_f - U_0$. Similarly, $\delta T = T_f - T_0$ is the difference in the nondimensional kinetic energy of the satellite at $\theta = 0$ and $\theta = \theta_f$. The variation of δU and δT for the satellite subjected to three different librational disturbances is shown in Figures 3-4 to 3-6. Two simulation runs were carried out for each initial condition. In the first case, denoted by the solid line in each plot, $\dot{\theta} \neq 0$ and $\bar{\omega}$ as given by Eq. (2.2) is used. In contrast, the second case, represented by the dotted line, is a fictitious physical situation with the orbital rate assumed to be zero, i.e., the orbital frame is stationary ($\dot{\theta} = 0$). With this assumption,

$$\begin{aligned} \bar{\omega} = &\left[-\phi' \sin\lambda + \psi' \cos\phi \cos\lambda\right]\hat{\imath}_p + \left[\lambda' - \psi' \sin\phi\right]\hat{\jmath}_p \\ &+ \left[\phi' \cos\lambda + \psi' \cos\phi \sin\lambda\right]\hat{k}_p \, . \end{aligned} \tag{3.11}$$

Figure 3-4 shows the system response and energy variation for an initial pitch displacement of 1° (Figure 3-4a) and pitch velocity disturbance of 0.03 (Figure 3-4b). The figure shows that although there is no visible difference in the librational response for both the cases, the energy variation is different. Note that, the magnitude of δT and δU are immaterial, instead, it is the trend that is useful. In $\dot{\theta} = 0$ case, the system is conservative as $\delta T + \delta U$ is zero; however, this is not true for $\dot{\theta} \neq 0$ case. It can be regarded as only quasi-conservative.

For an initial condition in the roll degree of freedom ($\phi_o = 1°$ in Figure 3-5 a and $\phi'_o = 0.2$ in Figure 3-5b), Figure 3-5 shows that the two cases have different librational responses as well as energy variations. Once again, only the fictitious system is conservative. Similar observation can be made for the response associated with an initial yaw displacement of 1° (Figure 3-6 a) and yaw rate of 0.02 (Figure 3-6b).

In theory, both the cases should be conservative. The lack of conservation of energy for $\dot{\theta} \neq 0$ case is attributed to the assumption that the Keplerian relations, Eq. (2.41), are valid. For a rigid satellite, the total energy of the system as given by Eqs. (2.34) and (2.35) is:

$$T + U = \frac{1}{2} M \bar{R}'_{cm} \cdot \bar{R}'_{cm} - \frac{\mu_e M}{R_{cm}} - \frac{\mu_e}{2R^3_{cm}} \mathrm{tr}\,[\mathbf{I}_{sys}] + \frac{1}{2} \bar{\omega}^T \mathbf{I}_{sys}\, \bar{\omega} + \frac{3\mu_e}{2R^3_{cm}} \bar{l}^T \mathbf{I}_{sys}\, \bar{l}\,, \tag{3.12}$$

and

$$\delta T + \delta U = \frac{1}{2}\left(\bar{\omega}_f^T \mathbf{I}_{sys}\, \omega_f - \bar{\omega}_o \mathbf{I}_{sys}\, \bar{\omega}_o\right) + \frac{3\mu_e}{2R^3_{cm}}\left(\bar{l}_f^T \mathbf{I}_{sys}\, \bar{l}_f - \bar{l}_o^T \mathbf{I}_{sys}\, \bar{l}_o\right). \tag{3.13}$$

In the $\dot{\theta} \neq 0$ case, the first three terms of Eq. (3.12) are forced to be constants by the assumption of the Keplerian relations; hence, it is not surprising that the change in

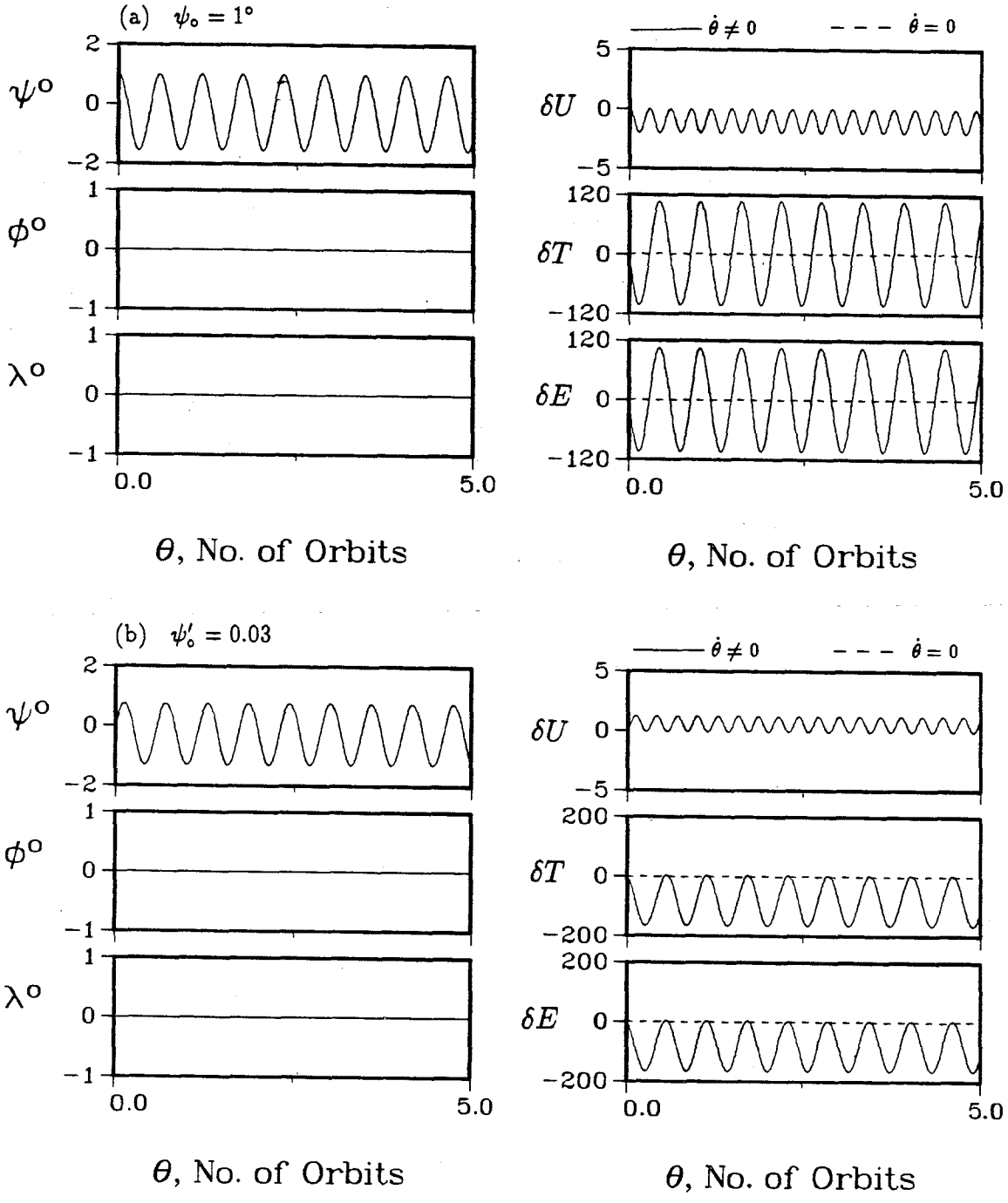

Figure 3-4 Librational response and energy variation of a rigid satellite subjected to an initial pitch disturbance: (a) $\psi_o = 1°$; (b) $\psi'_o = 0.03$.

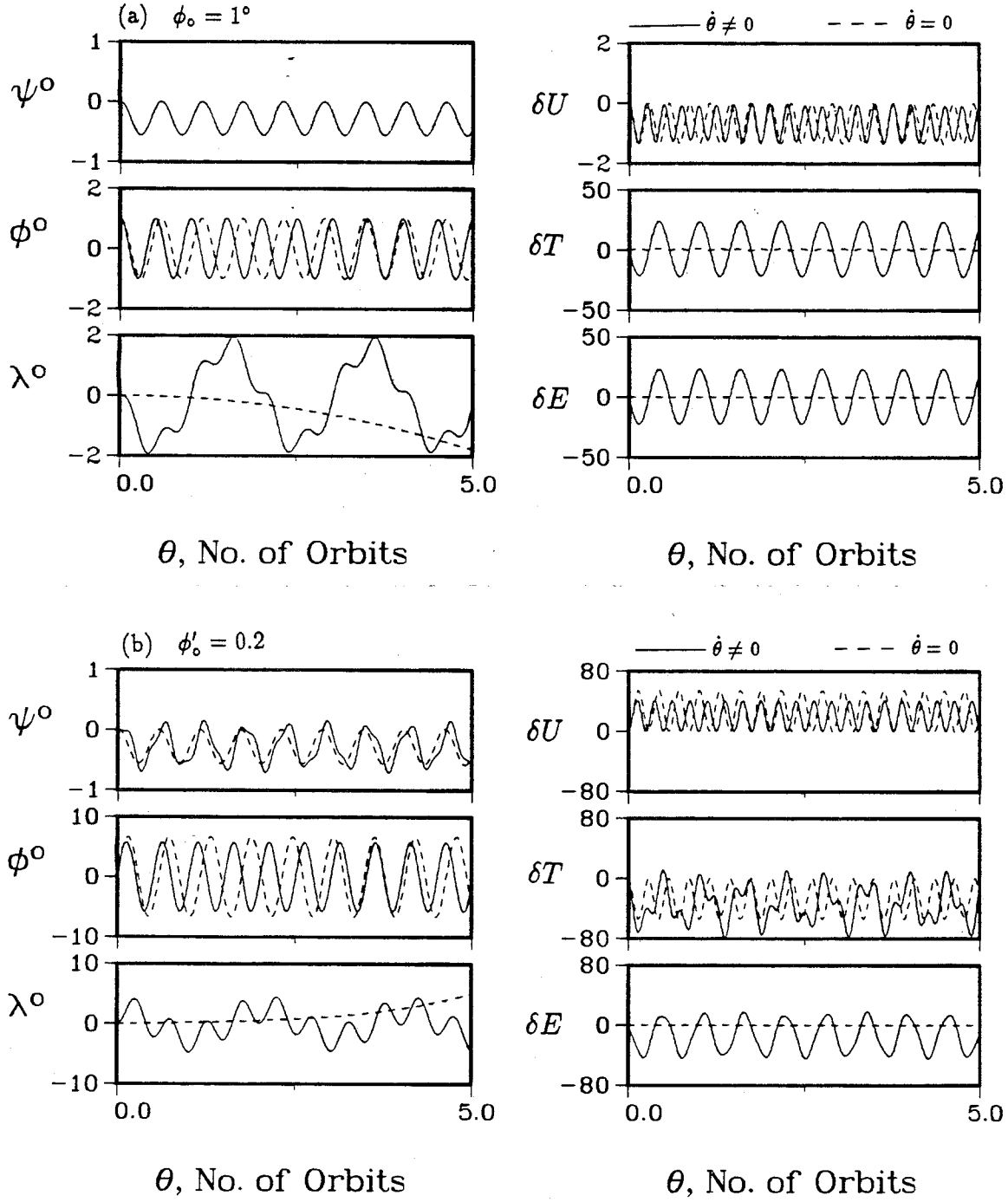

Figure 3-5 The effect of roll disturbance on a rigid satellite libration and energy variation: (a) $\phi_0 = 1°$; (b) $\phi_0' = 0.2$.

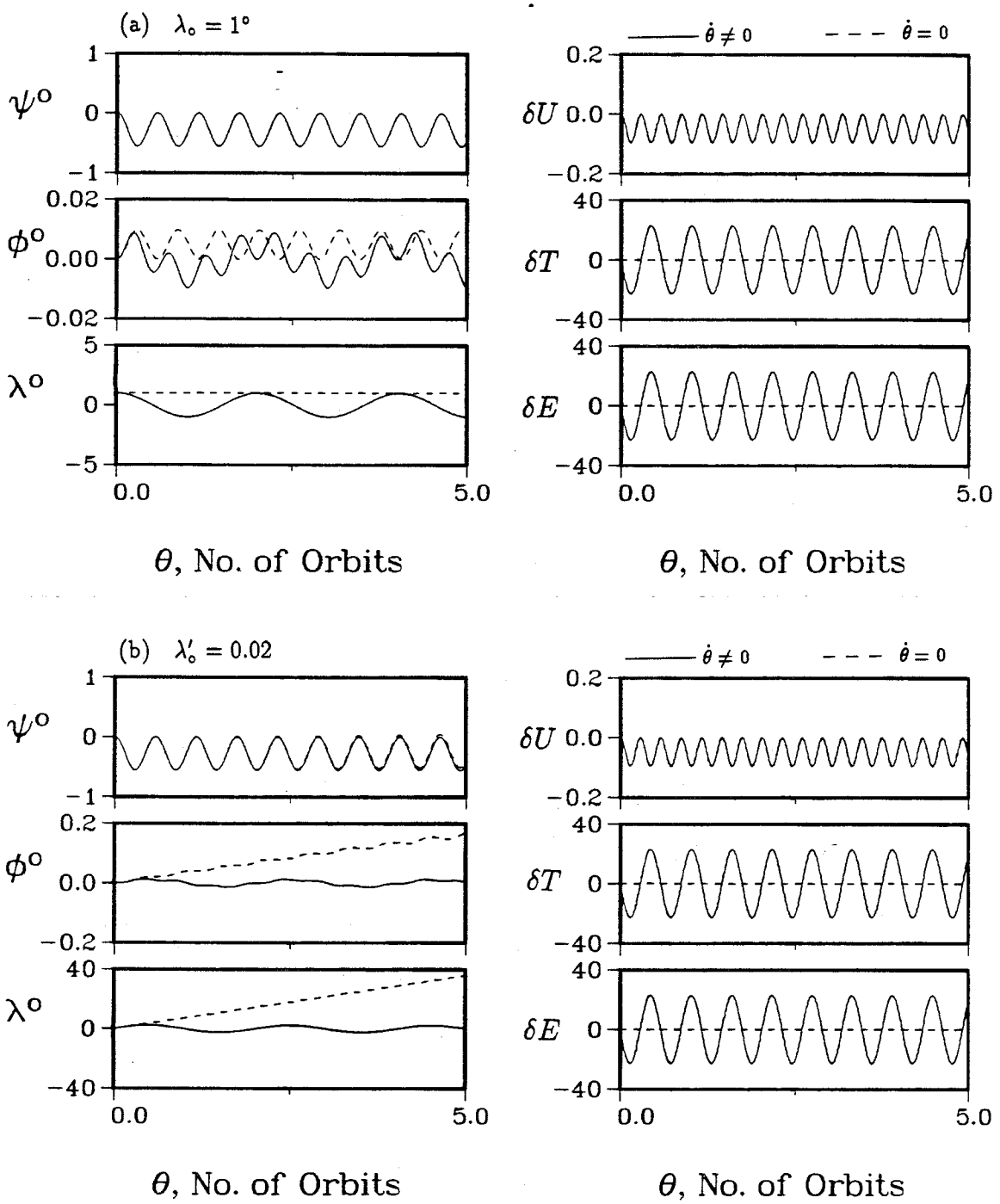

Figure 3-6 Dynamical response and energy variation of a rigid satellite with an initial condition in the yaw degree of freedom: (a) $\lambda_o = 1°$; (b) $\lambda'_o = 0.02$.

energies as given by Eq. (3.13) is not zero. Even though this implies that the system is not truly conservative, Eq. (2.41) is not a poor assumption. With the first three terms in Eq. (3.12) of several orders of magnitude higher than the remaining two, the percentage change in total energy $(\delta T + \delta U)/(T + U)$ is hardly significant. For the present satellite orbiting at 300 km altitude, the change is less than 10^{-8} %. The conclusion from this study is that energy variation can be used to verify the computer code by setting the orbital rate to zero.

Next, a comparative study with two cases reported in the literature was undertaken. Ng [90] studied the librational and vibrational dynamics of a gravity-gradient stabilized satellite with two thermally flexed appendages (Figure 3-7). The present formulation can handle this model by treating the rigid central body to be B_c and the two appendages as body $B_i (i = 1, 2)$. Using the data in Table 3-3 for a satellite in a 90-minute orbit, the present formulation gives results identical to those obtained by Ng [90].

A set of typical response plots are presented in Figure 3-8 . Here, the generalized coordinates $\underline{P}_1^1$ and $\underline{P}_2^1$ correspond to the inplane vibration of B_1 and B_2 in the first mode, respectively. The initial condition applied is $(\underline{P}_1^1)_o = 0.05$ and the satellite is taken to be orbiting in an eccentric orbit with $\epsilon = 0.2$.

The second model used for verification is based on the two arm flexible manipulator as reported by Chan [15]. Here, the space station is treated as a rigid body (B_c) whereas the robot arms (B_1 and $B_{1,1}$) are taken to be cantilever beams supported on a mobile base (Figure 3-9). As the present formulation does not account for translational motion of any member, the base was considered stationary. The numerical values used in the simulation are listed in Table 3-4 . A 100-minute circular orbit is assumed in the simulation. The two formulations gave almost identical results (Figure

Table 3-3 Spacecraft data used to assess accuracy of the present formulation

Central Body (B_c)

m_c	=	42,000 kg	$(I_{xx})_c$	=	100,000 kg m^2
l_c	=	10 m	$(I_{yy})_c$	=	400,000 kg m^2
			$(I_{zz})_c$	=	400,000 kg m^2

Upper and Lower Appendages (B_1 and B_2)

m_1	=	m_2	=	10 kg	$(I_{xx})_1$	=	$(I_{xx})_2$	$\approx$	0
l_1	=	l_2	=	100 m	$(I_{yy})_1$	=	$(I_{yy})_2$	=	33,333 kg m^2
f_1	=	f_2	=	0.003 Hz	$(I_{zz})_1$	=	$(I_{zz})_2$	=	33,333 kg m^2

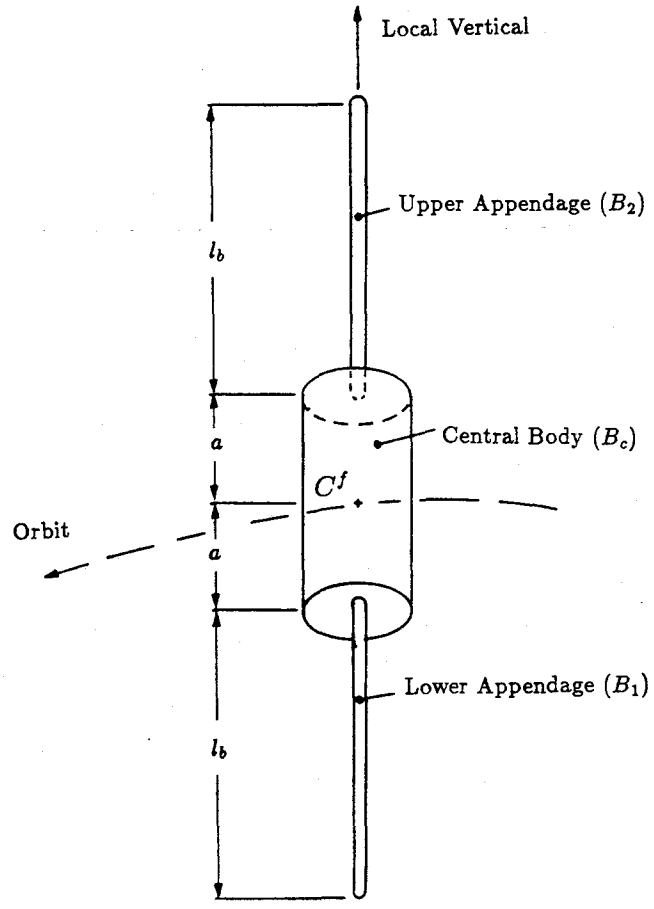

Figure 3-7 The spacecraft model used to assess accuracy of the present formulation.

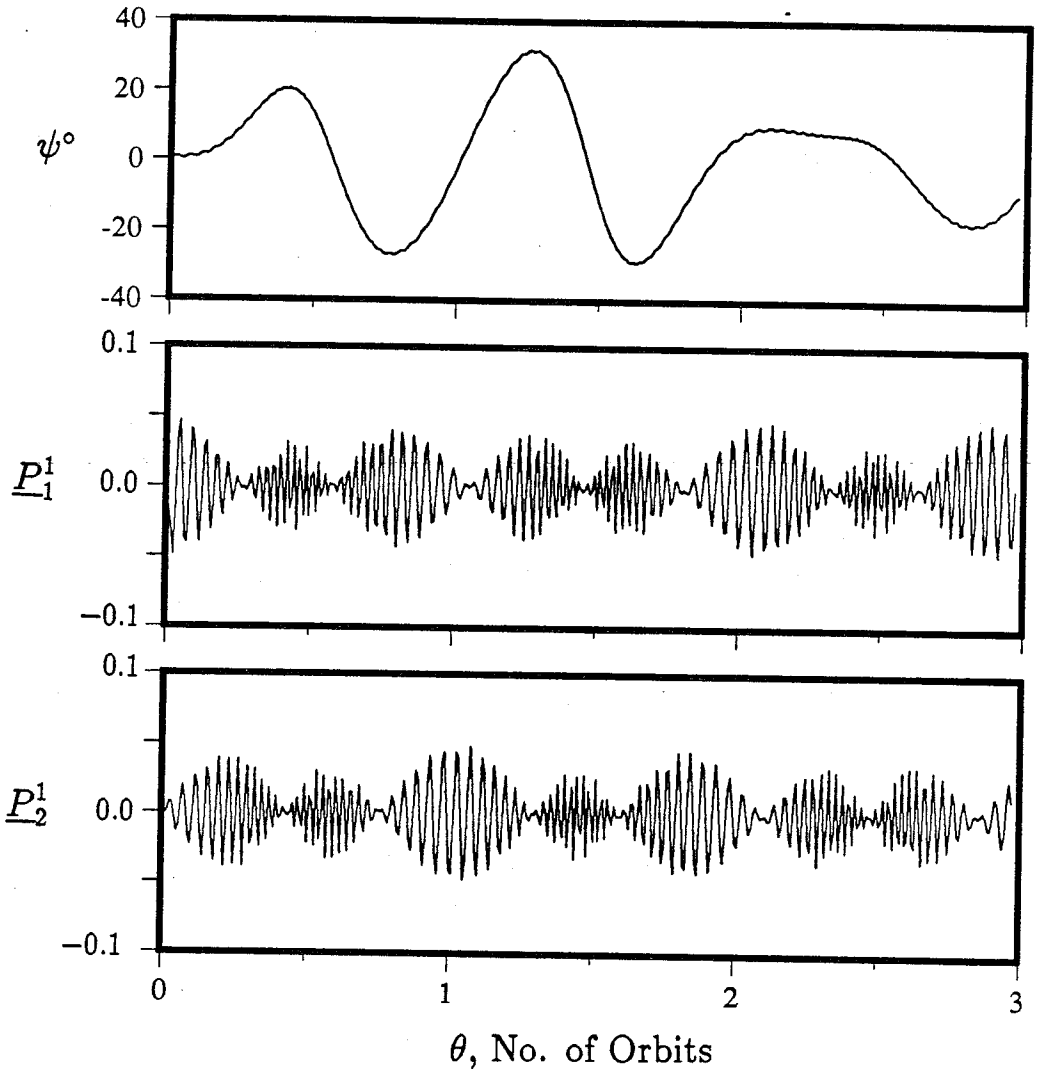

Figure 3-8 A typical response obtained by the present formulation simulating the spacecraft model studied by Ng [90]. The results showed perfect agreement.

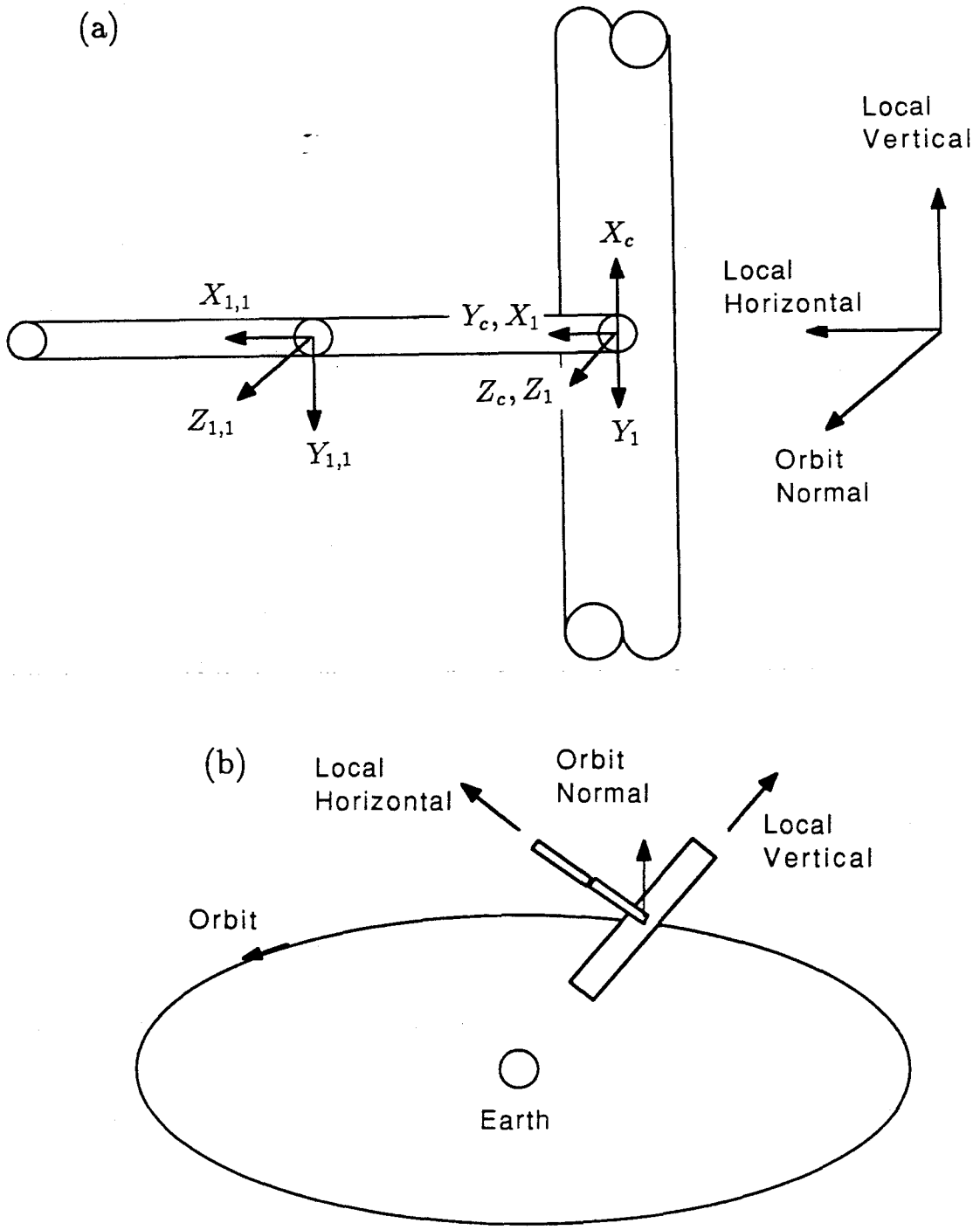

Figure 3-9 Schematic diagram of the space station based MSS studied by Chan [15]: (a) coordinate systems; (b) design configuration. It is used here to assess validity of the present general formulation.

Table 3-4 Data of the space station based MSS studied by Chan [15]

Space Station (B_c)

m_c	=	240,120 kg		$(I_{xx})_c$	=	8×10^5 kg m^2		
l_c	=	115.35 m		$(I_{yy})_c$	=	2.67×10^8 kg m^2		
				$(I_{zz})_c$	=	2.67×10^8 kg m^2		

Upper and Lower Appendages (B_1 and B_2)

m_1	=	$m_{1,1}$	=	10 kg	$(I_{xx})_1$	=	$(I_{xx})_2$	$\approx$	0
l_1	=	$l_{1,1}$	=	100 m	$(I_{yy})_1$	=	$(I_{yy})_2$	=	33,333 kg m^2
f_1	=	$f_{1,1}$	=	0.003 Hz	$(I_{zz})_1$	=	$(I_{zz})_2$	=	33,333 kg m^2

3-10). Minor discrepancies may be attributed to the modified cantilevered modes assumed by Chan [15].

The generalized coordinates for this model are:

$$q = \psi\ ,\ \phi\ ,\ \lambda\ ,\ \underline{P}_1^r\ ,\ \underline{Q}_1^r\ ,\ \underline{P}_{1,1}^r\ ,\ \underline{Q}_{1,1}^r\ ;$$

$$r = 1, \ldots, n_{r_i}\ ;$$

where n_{r_i} represents the number of modes selected. In Figure 3-10, using only one mode and with the initial condition being applied inplane ($(\underline{P}_1^1)_o = 0.05$), only ψ, $\underline{P}_1^1$ and $\underline{P}_{1,1}^1$ are excited.

A study of convergence in terms of the number of shape functions required is appropriate here. Four simulations are performed using one, two, three and four modes to represent beam vibrations of the MSS configuration. The results are shown in Figure 3-11 . For simplicity, the following discussion uses symbols I, II, III, and IV to indicate simulations and the associated number of modes. In general, irrespective of the number of modes chosen, the trend in response remains essentially the same. Discrepancies appear in the phase and amplitude.

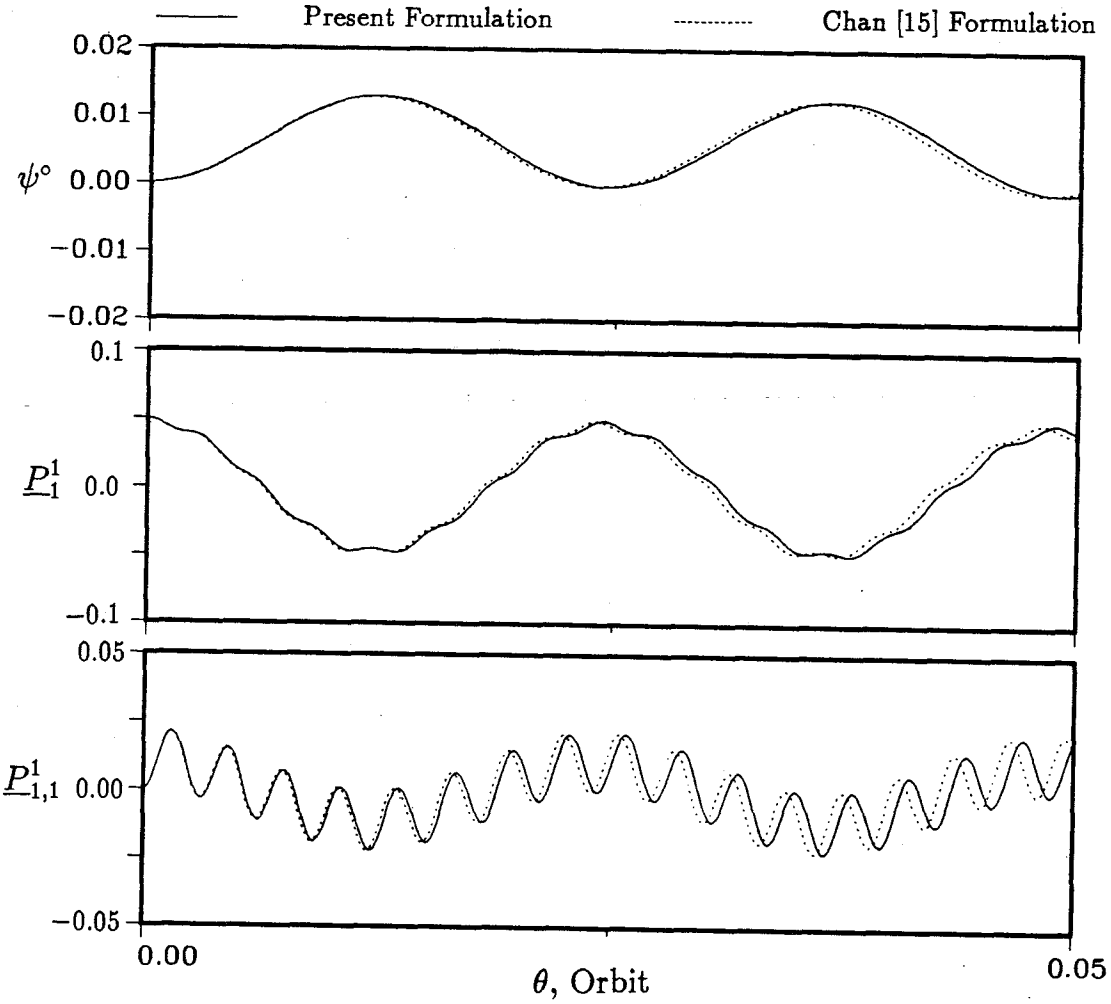

Figure 3-10 A comparison between the MSS response obtained by Chan [15] and the present formulation.

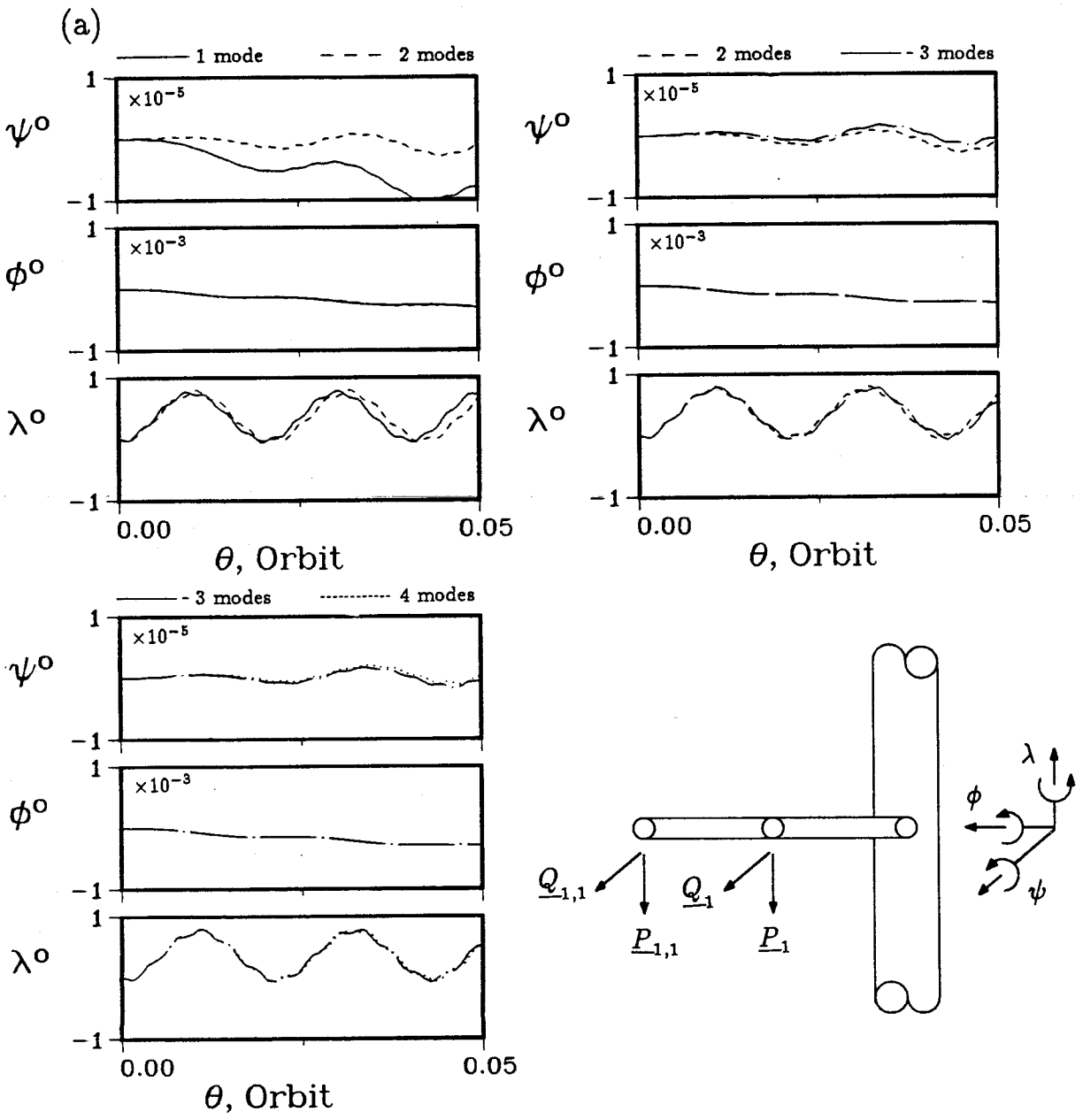

Figure 3-11 Dynamics of the MSS using one, two, three, and four assumed modes in the simulations: (a) librational response.

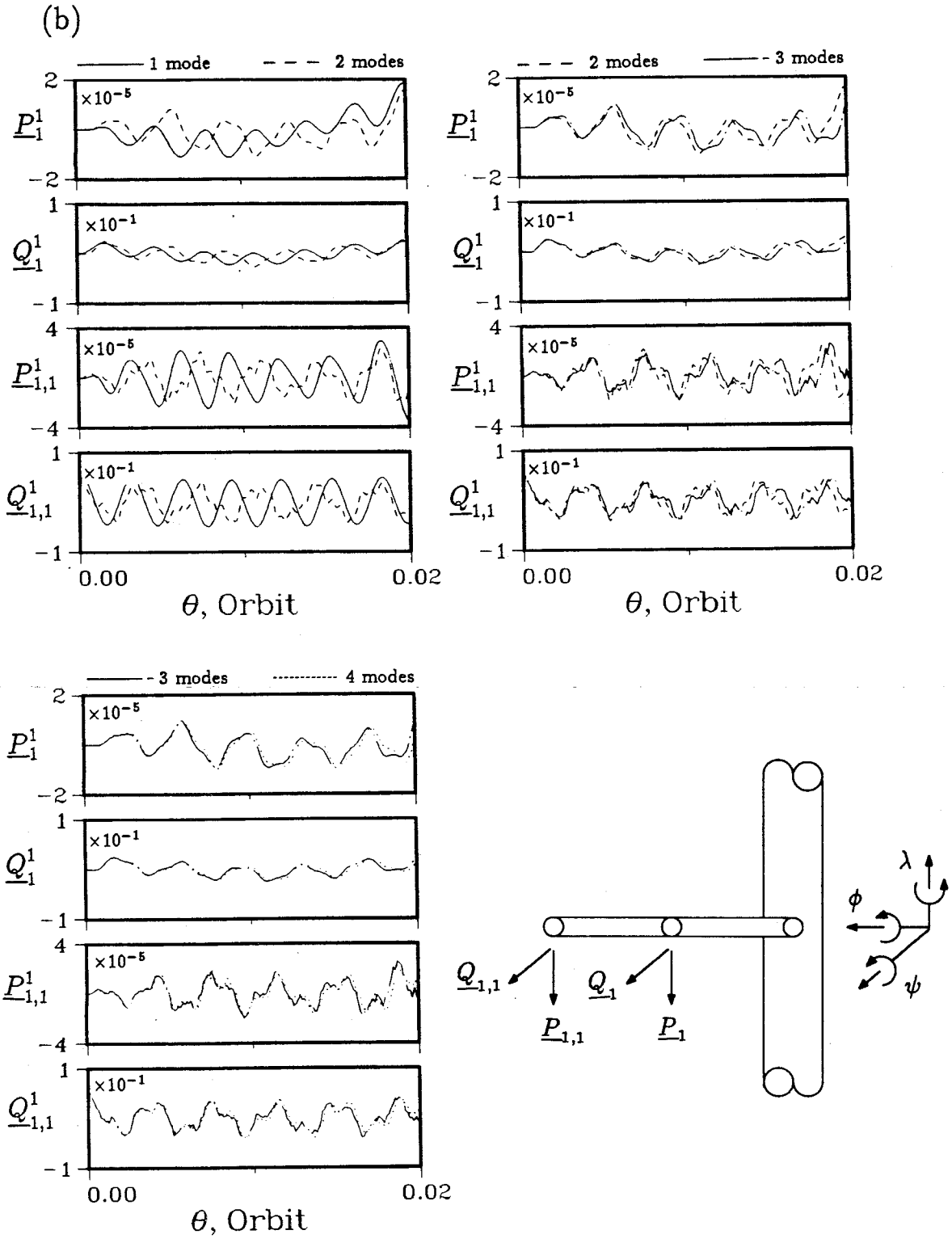

Figure 3-11 Dynamics of the MSS using one, two, three, and four assumed modes in the simulations: (b) the first mode vibrational response.

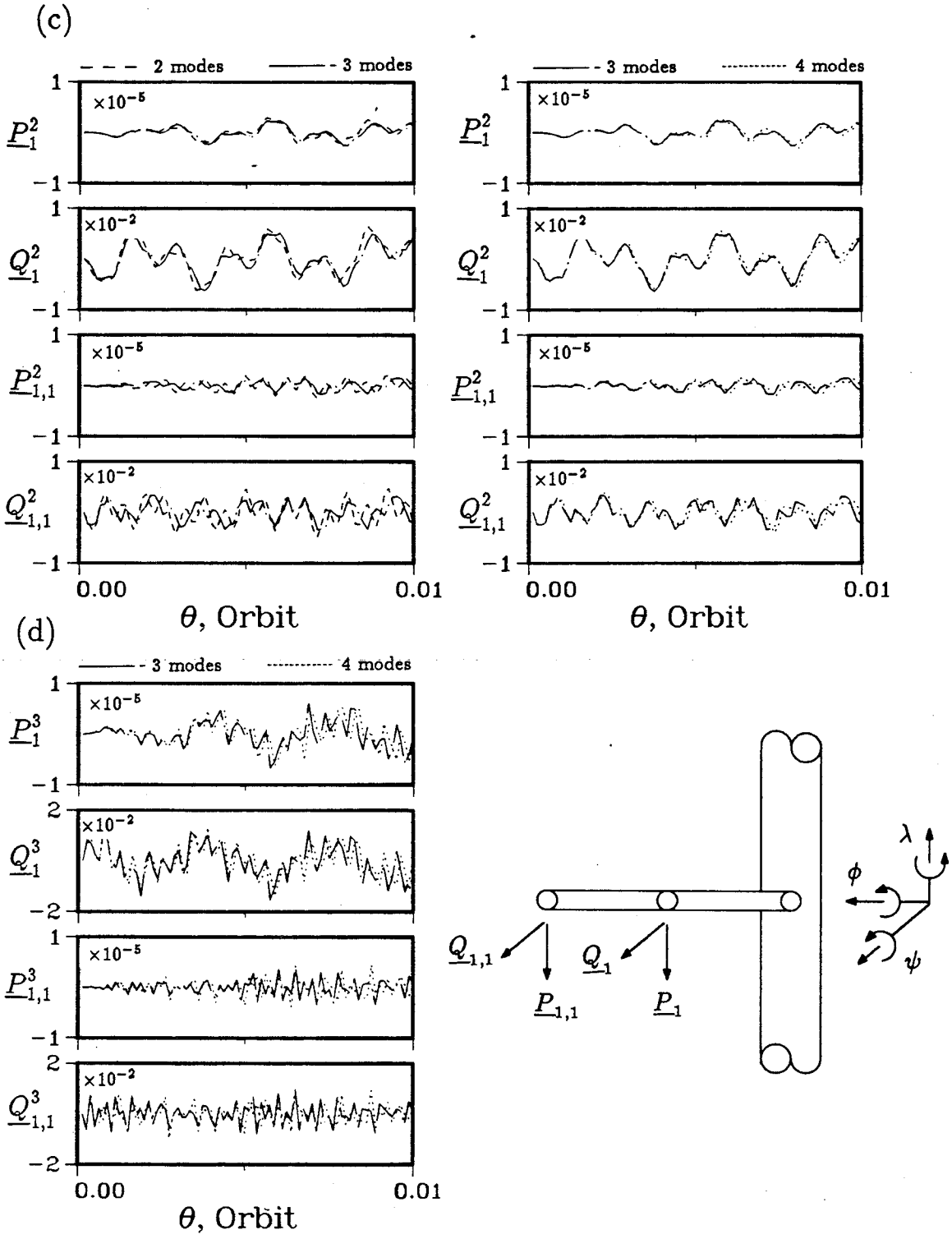

Figure 3-11 Dynamics of the MSS using one, two, three, and four assumed modes in the simulations: (c) the second mode vibrational response; (d) the third mode vibrational response.

The convergence of the libration angles is shown in Figure 3-11a. Comparing I and II, the following observations can be made:

(i) convergence of the pitch response, both in phase and amplitude, is significantly improved with an increase in the number of modes.

(ii) roll angle is essentially identical for both simulations;

(iii) although the yaw response has the largest amplitude, the difference in yaw response is confined to the phase only.

Simulation III shows a dramatic improvement in the pitch response prediction, both in phase and amplitude. As expected, the roll response continues to display insignificant discrepancy, while the phase error in the yaw is markedly reduced. With four modes (simulation IV), the librational response appears to have converged to the true value.

The convergence of the first mode response ($\underline{P}^1_1$, $\underline{Q}^1_1$, $\underline{P}^1_{1,1}$ and $\underline{Q}^1_{1,1}$) is shown in Figure 3-11b. Similar to the pitch response, a comparison between I and II shows discrepancies both in phase and amplitude. However, the deviations become smaller with the inclusion of the third mode; and finally become negligible in simulation IV. Figure 3-11c shows the convergence of the generalized coordinates ($\underline{P}^2_1$, $\underline{Q}^2_1$, $\underline{P}^2_{1,1}$ and $\underline{Q}^2_{1,1}$) associated with the second mode. A comparison between II and III shows errors in phase and amplitude. The situation improves with the addition of the fourth mode; however, the error still persists suggesting that higher modes are necessary to achieve better convergence. Finally, Figure 3-11d compares response of the generalized coordinates associated with the third mode ($\underline{P}^3_1$, $\underline{Q}^3_1$, $\underline{P}^3_{1,1}$ and $\underline{Q}^3_{1,1}$) using 3 and 4 modes in the simulation. The discrepancy between the two cases indicates the necessity to include higher modes for improving convergence to the true dynamics.

From the simulation results it can be concluded that, in general, both rigid and flexible dynamics converge as the number of modes in the simulation increases. Hence

the cantilever modes, used here as admissible functions, can predict the system dynamics with accuracy. In the present case, convergence of the librational degrees of freedom and the first generalized coordinates (generalized coordinates associated with the first mode) need at least three modes in the simulation. Convergence of the second generalized coordinates is only marginally improved with addition of the fourth mode and the convergence of the third generalized coordinates would certainly require higher modes.

Table 3-5 compares the CPU time required in the four cases. The number of equations increases from 14 (for one mode, $N_q = 7$) to 38 (with four modes, $N_q = 19$), with the CPU time required showing an increase of 34 fold. The enormous rise in the computational effort is attributed to the stiff equations associated with higher modes; hence, there is a tradeoff between accuracy and CPU time. In the present study, without sacrificing the physics of the problem, one mode is always assumed in the simulation. Higher accuracy, if necessary, can always be obtained using more modes and hence requiring more computational effort.

Table 3-5 Comparison of CPU time required using one, two, three and four assumed modes in the simulation of the MSS

No. of Modes	N_q	CPU time (sec)*	CPU/CPU_{ref}**
1	7	5,540.11	1.000
2	11	28,347.89	5.122
3	15	88,155.92	15.912
4	19	189,525.45	34.210

* based on VaxStation 320

**CPU_{ref} represents the time required using 1 mode

4. PARAMETRIC STUDIES

4.1 Preliminary Remarks

The objective of this chapter is to illustrate versatility of the relatively general formulation. To this end, dynamic simulations of five spacecraft models, of contemporary interest, were carried out. The three models are related to the proposed Space Station. It should be pointed out that the station is an extremely complex, highly flexible platform with diverse interconnected structural elements (beam, plate, shell, etc.) It will have a size of the soccer field. Of course, such a gigantic structure cannot be carried to the operational altitude in its entirety. It will be constructed in stages through integration of modular subassemblies extending over 30 flights of the Space Shuttle. Thus the proposed Space Station represents an evolving structure with time dependent geometry, inertia, flexibility, damping, and other properties during its constructional phase. Of course, the Space Station will operate in presence of a variety of disturbances induced by the environment, on board operations and interactions with the Shuttle flights. Thus each stage of its development would represent a challenging dynamical problem in design, dynamics, stability and control. Here, the dynamics of the FEL (First Element Launch) configuration, the PMC (Permanently Manned Configuration), and the on board MSS (Mobile Servicing System) which will assist in construction and operation of the station, are investigated at some length. Next generation of communications satellites represent a large class of configurations of significant importance. After all the revolution in communication is the gift of the space age that has affected the entire world. A rather novel design of the INdian SATellite II (INSAT II), the multipurpose Indian communications satellite to be launched this year, is considered for study here. Finally, dynamics of the SFU

(Space Flyer Unit), a Japanese experiment to be launched in 1993, is studied during deployment and retrieval of the solar arrays.

The amount of information obtained is enormous and only a sample of it is presented here in a condensed form. However, it does suggest trends, and lays foundation for the design and development of control strategies.

4.2 First Element Launch

The United States led Space Station *Freedom* program is currently in the design and development phase. The backbone of the station is the power boom. It is essentially a truss structure to which modules, equipment and subsystems are attached. There are five major modules (two Habitat, two Laboratory and one Logistics) clustered around the geometric centre of the power boom. The subsystems include the photovoltaic (PV) arrays and the associated power generation equipment, antennas, Attitude Control Assembly (ACA), Reaction Control System (RCS), and Mobile Remote Manipulator System (MRMS). Solar and stellar sensors, satellite servicing provisions, Orbital Maneuvring Vehicle (OMV), and shuttle berthing ports are some examples of the user equipment. In order to maximize solar energy input, the PV arrays can undergo predefined rotation via alpha and beta joints. Total power generated by each pair of PV array is 18.75 kW. Heat rejection of the station is achieved by two station radiators and four PV array radiators whereas waste disposal is accomplished by the resistojet located at the end of the stinger.

As pointed out before, the Space Station will be constructed utilizing around thirty Space Transportation System (STS) flights [102,103]. The first flight would result in construction of the First Element Launch (FEL) configuration. It will have an overall length of 60 m and a mass of 17,680 kg. Major equipment installed in the FEL configuration includes two PV arrays, an alpha joint, fuel storage tanks, stinger

and resistojet, avionics, and RCS.

The design configuration of the FEL would be such that the axial directions of the power boom and PV arrays are parallel to the orbit normal and local vertical, respectively. It should be pointed out that, in general, the design configuration is not identical to the equilibrium configuration. The FEL is simulated here by the power boom, a free-free beam, with lumped masses representing the alpha joint, fuel storage tanks, avionics, and RCS. The stinger and the resistojet are treated as a cantilever beam and point mass, respectively. The PV arrays and PV array radiator are represented as cantilevered plates. Figure 4-1 shows the coordinate system used in the numerical simulation. Considering only the first mode of vibration for the flexible elements, the generalized coordinates and the degrees of freedom are:

$$q = \psi\,,\ \phi\,,\ \lambda\,,\ \underline{P}_c^1\,,\underline{Q}_c^1\,,\ \underline{P}_1^1\,,\ \underline{Q}_1^1\,,\ \underline{H}_2^{1,1}\,,\ \underline{H}_3^{1,1}\,,\ \text{and}\ \underline{H}_4^{1,1}\,;$$

$$N_q = 10\,.$$

The numerical data used in the simulations are obtained or estimated from the NASA reports [102,103] and are summarized in Table 4-1 . The nondimensional inertia diadic of the system is found to be,

$$\mathbf{I}_{sys} = \begin{bmatrix} 1.1715 & 0 & -0.1088 \\ 0 & 9.2108 & 0 \\ -0.1088 & 0 & 9.5538 \end{bmatrix}.$$

Consider first the rigid body dynamics of the FEL. Here, the power boom as well as the attached appendages are assumed to be rigid. The equilibrium configuration of the FEL corresponds to: $\psi_e = 0°$, $\phi_e = 0.74°$, and $\lambda_e = 0°$, which is different from the design configuration (power boom along the orbit normal, solar panels parallel to the local vertical). Hence the system, even in absence of any external or internal disturbance, would exhibit some motion as shown in Figure 4-2. Introduction of an

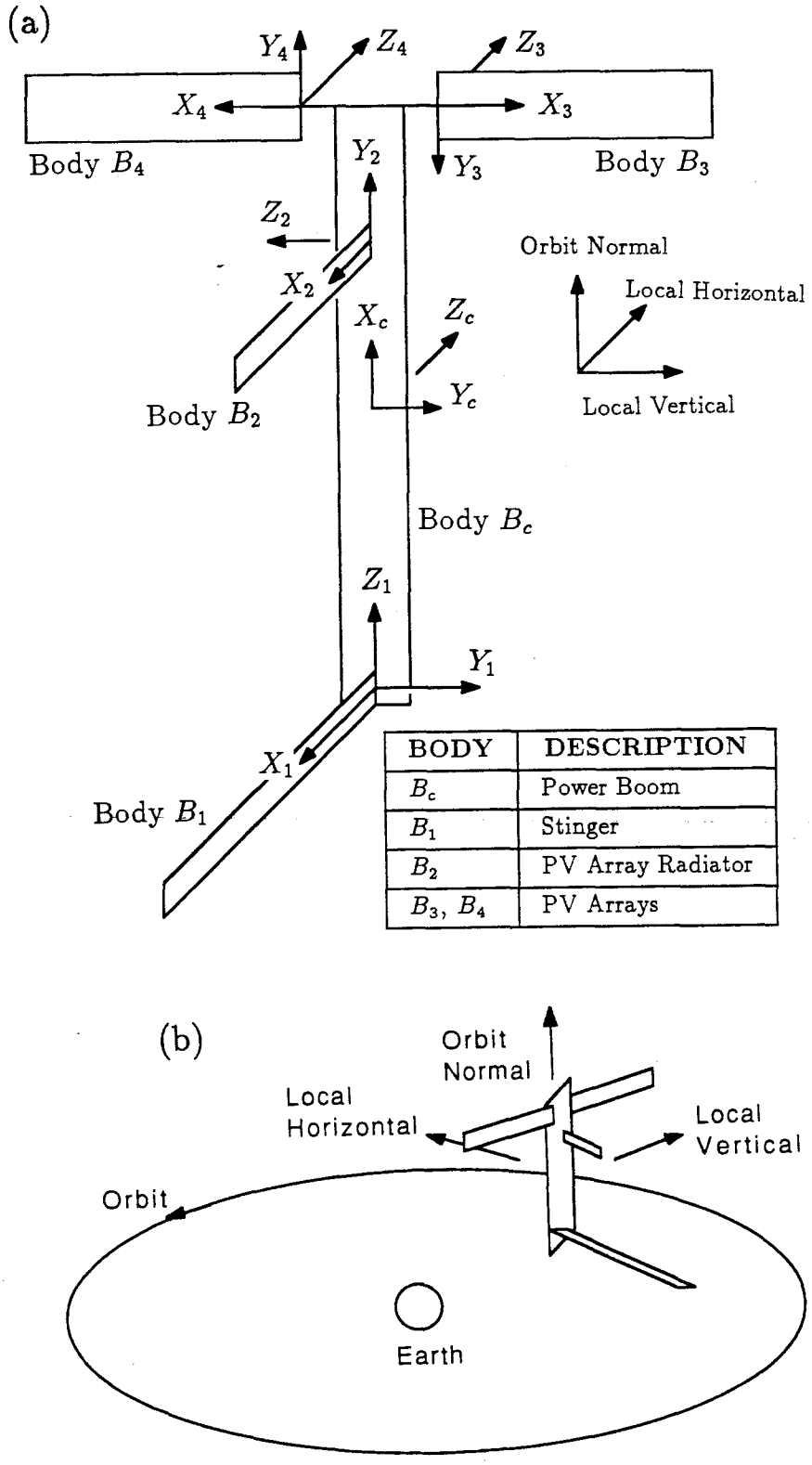

BODY	DESCRIPTION
B_c	Power Boom
B_1	Stinger
B_2	PV Array Radiator
B_3, B_4	PV Arrays

Figure 4-1 Configuration of the FEL used in the numerical simulation: (a) coordinate systems; (b) design configuration.

Table 4-1 Physical parameters of the major components of the FEL

Power Boom (Body B_c)			Stinger (Body B_1)		
l_c	=	60 m	l_1	=	26.7 m
m_c	=	15,840 kg	m_1	=	270 kg
f_c^1	=	1.936 Hz	f_1^1	=	0.5 Hz
$(I_{xx})_c$	=	0.15 $\times 10^6$ kg-m^2	$(I_{xx})_1$	$\approx$	0
$(I_{yy})_c$	=	4.37 $\times 10^6$ kg-m^2	$(I_{yy})_1$	=	64,160 kg-m^2
$(I_{zz})_c$	=	4.28 $\times 10^6$ kg-m^2	$(I_{zz})_1$	=	64,160 kg-m^2
PV Radiator (Body B_2)			**PV Array (Body B_i, $i = 3, 4$)**		
l_2	=	11.5 m	l_i	=	33 m
m_2	=	450 kg	m_i	=	444 kg
$f_2^{1,1}$	=	0.1 Hz	$f_i^{1,1}$	=	0.1 Hz
$(I_{xx})_2$	=	50 kg-m^2	$(I_{xx})_i$	=	1,332 kg-m^2
$(I_{yy})_2$	=	19,837 kg-m^2	$(I_{yy})_i$	=	161,172 kg-m^2
$(I_{zz})_2$	=	19,887 kg-m^2	$(I_{zz})_i$	=	162,504 kg-m^2

initial disturbance of 0.1° in pitch, roll or yaw only accentuates the unstable response and the system starts to tumble in less than one orbit (Figure 4-3).

Defining

$$K_1 = \frac{I_{zz} - I_{xx}}{I_{yy}} = 0.91\,;$$

$$K_2 = \frac{I_{xx} - I_{yy}}{I_{zz}} = -0.84\,;$$

Kane et al. [104] have shown that stable motion is possible if and only if $K_1 < 0$ and $K_2 > -K_1$. This confirms unstable orientation of the FEL and points to the need of a suitable control.

The effect of flexibility on the system response is shown in Figures 4-4 to 4-8.

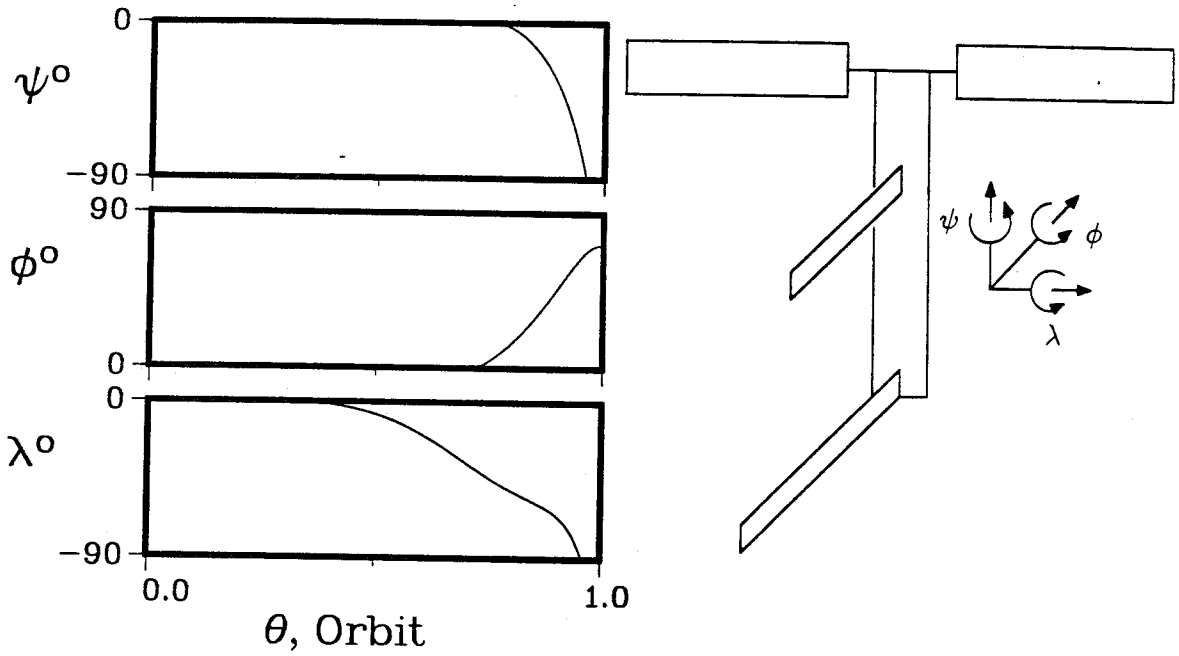

Figure 4-2 Librational response of the rigid FEL showing the inherent unstable character of its orientation.

For better appreciation of the response, the vibration degrees of freedom are plotted in terms of the tip deflection of the centerline. Using Eq. (2.23), the tip deflections δ_k^y and δ_k^z of a beam element (e.g. B_k) in Y_k and Z_k directions, respectively, are given by:

$$\delta_k^y = \sum_{r=1}^{n} P_k^r(t)\psi_k^r(l_k)\,;$$
$$\delta_k^z = \sum_{r=1}^{n} Q_k^r(t)\psi_k^r(l_k)\,. \tag{4.1}$$

For a plate element B_k, the displacement is a function of both the X_k and Y_k coordinates. Defining ϵ_k^x and ϵ_k^y to be the tip displacements of the line $Y_k = 0$ and $X_k = 0$, respectively, and using Eq. (2.25), ϵ_k^x and ϵ_k^y are then given by

$$\epsilon_k^x = \sum_{s=1}^{m}\sum_{t=1}^{n} H_k^{s,t}(t)\phi_k^s(l_k)\psi_k^t(0)\,; \tag{4.2a}$$

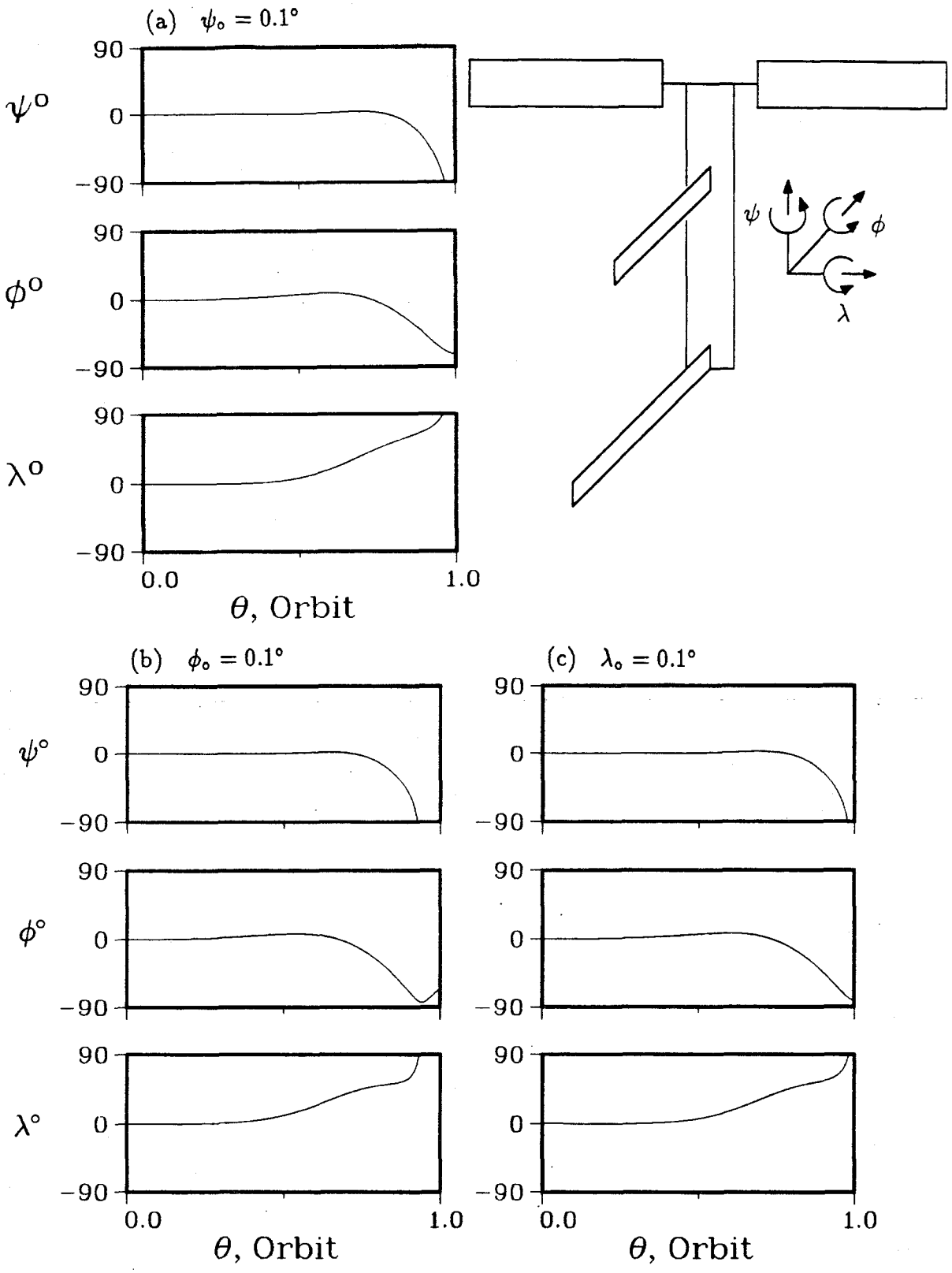

Figure 4-3 Librational behavior of the rigid FEL showing the unstable response in the presence of an external disturbance in pitch, roll or yaw of 0.1°.

$$\epsilon_k^y = \sum_{s=1}^{m} \sum_{t=1}^{n} H_k^{s,t}(t) \phi_k^s(0) \psi_k^t(w_k) \, . \tag{4.2b}$$

Note that, for a cantilever plate, since $\phi_k^s(0) = 0$, ϵ_k^y is identically zero. For instance, ϵ_2^x of Figure 4-4 represents the tip deformation of B_2 (station radiator) of the line $Y_k = 0$. The range of the deformation plotted is -0.5×10^{-5} cm and $+0.5 \times 10^{-5}$ cm.

Figure 4-4 shows response of the system initially in the design configuration. This result can be used as a reference for other cases with initial disturbances. Here, deviation from the equilibrium configuration serves as a disturbance to the system. Even with such a small disturbance, the system gradually undergoes unstable librational motion. The periodic oscillations of the flexible degrees of freedom in the direction of the local horizontal (δ_c^z, ϵ_3^x, and ϵ_4^x) or the orbit normal (δ_1^z) indicate their non-zero equilibrium position. On the other hand, the other degrees of freedom (δ_c^y, δ_1^y, and ϵ_2^x), which are parallel to the local vertical, have zero equilibrium position. Due to the coupling effect with librational and vibrational degrees of freedom, their response amplitudes gradually increase with time.

The effect of the power boom disturbance is shown in Figure 4-5. In Figure 4-5a, the power boom is initially deformed in the first mode with a tip deflection of 1 cm in the local vertical direction ($(\underline{P}_c^1)_\circ = 0.826 \times 10^{-4}$). Even with this small disturbance, the pitch response is excited significantly with high frequency harmonics of 0.02° in amplitude. Similar trend is observed in the roll response. Although the amplitude is lower than that in the pitch response, the roll motion is excited at a higher frequency. Under this initial condition, the power boom is expected to be vibrating symmetrically about the local vertical; hence, it is not surprising to see that δ_c^y and roll have similar response trend with the distinct beat phenomenon present. Modi and Ng [105] have investigated the beat phenomenon of a gravity-gradient

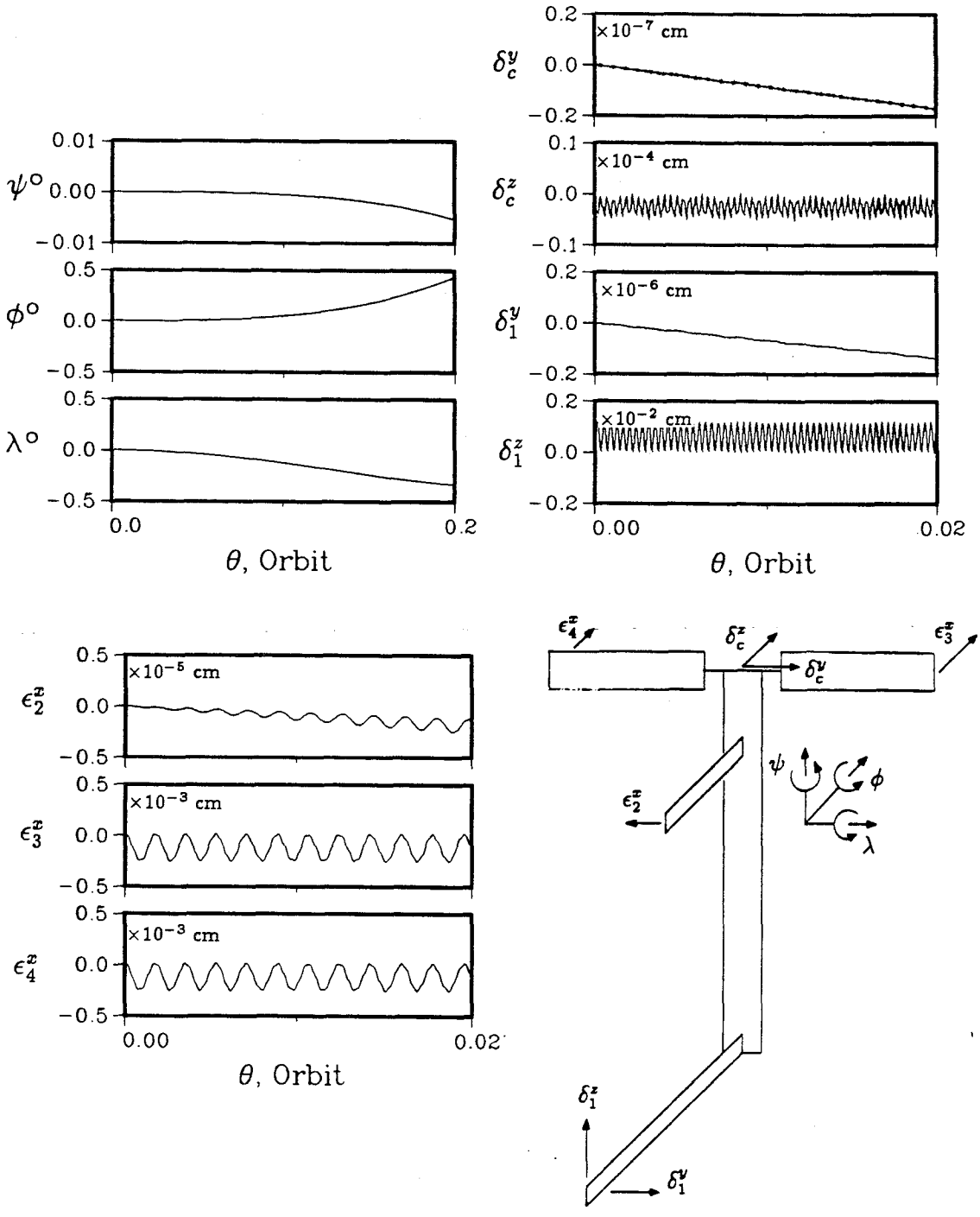

Figure 4-4 Dynamical response of the FEL in absence of an external initial disturbance.

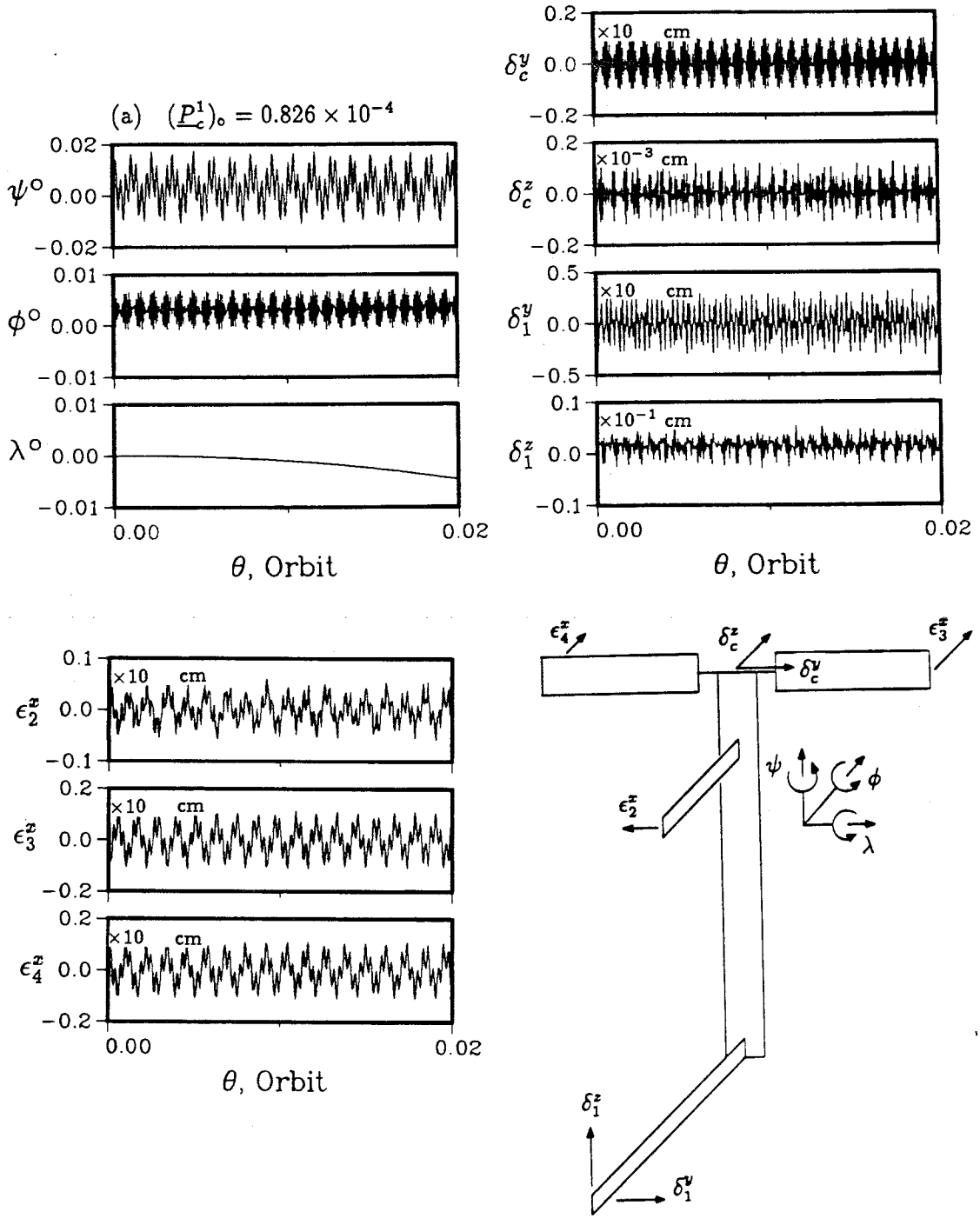

Figure 4-5 Effect of an initial 1 cm tip deflection of the power boom on the FEL dynamics: (a) initial deflection in the local vertical direction, $(\underline{P}_c^1)_o = 0.826 \times 10^{-4}$.

oriented satellite with two appendages. It is found that the beat is caused by the differential gravitational torques acting on the two appendages. In the present case, the beat response is attributed to asymmetrical loading on the power boom coupled with the gravitational disparity. As the arrays and the stinger become smaller, the beat gradually disappers (not shown). Compared to Figure 4-4, the yaw response remains unchanged. The flexible element experiencing the largest deflection is the stinger. Its maximum amplitude is about 3 cm in the local vertical direction.

In Figure 4-5b, the power boom is initially disturbed in the local horizontal direction ($(\underline{Q}_c^1)_o = 0.826 \times 10^{-4}$). Since this initial condition gives rise to predominantly symmetrical motion about the local horizontal, the yaw motion is excited with high frequency harmonics. However, as can be expected, both pitch and roll remain essentially unexcited. Compare to Figure 4-5a, the beat phenomenon is no longer present in the power boom or rigid body response. Also, note that in Figure 4-5a, the maximum value of δ_c^z is about 0.1×10^{-3} cm when excited by the initial disturbance in Y_c direction; whereas in the present case, δ_c^y is an order of magnitude higher when the same disturbance is applied in the Z_c direction. These show the directional characteristics of the FEL power boom: given the response in direction B when disturbed in direction A, one cannot predict the response in direction A when disturbed in direction B. Once again, the stinger experiences the largest deflection with an amplitude of 5 cm in the orbit normal direction. Note that the PV array response has the same amplitude as the previous case; however, now the low frequency component is more pronounced.

Response of the system with the stinger subjected to an initial disturbance is shown in Figure 4-6 . The stinger is deformed initially in the first mode of a cantilever beam with a tip deflection of 1 cm in either the local vertical direction ($(\underline{P}_1^1)_o =$

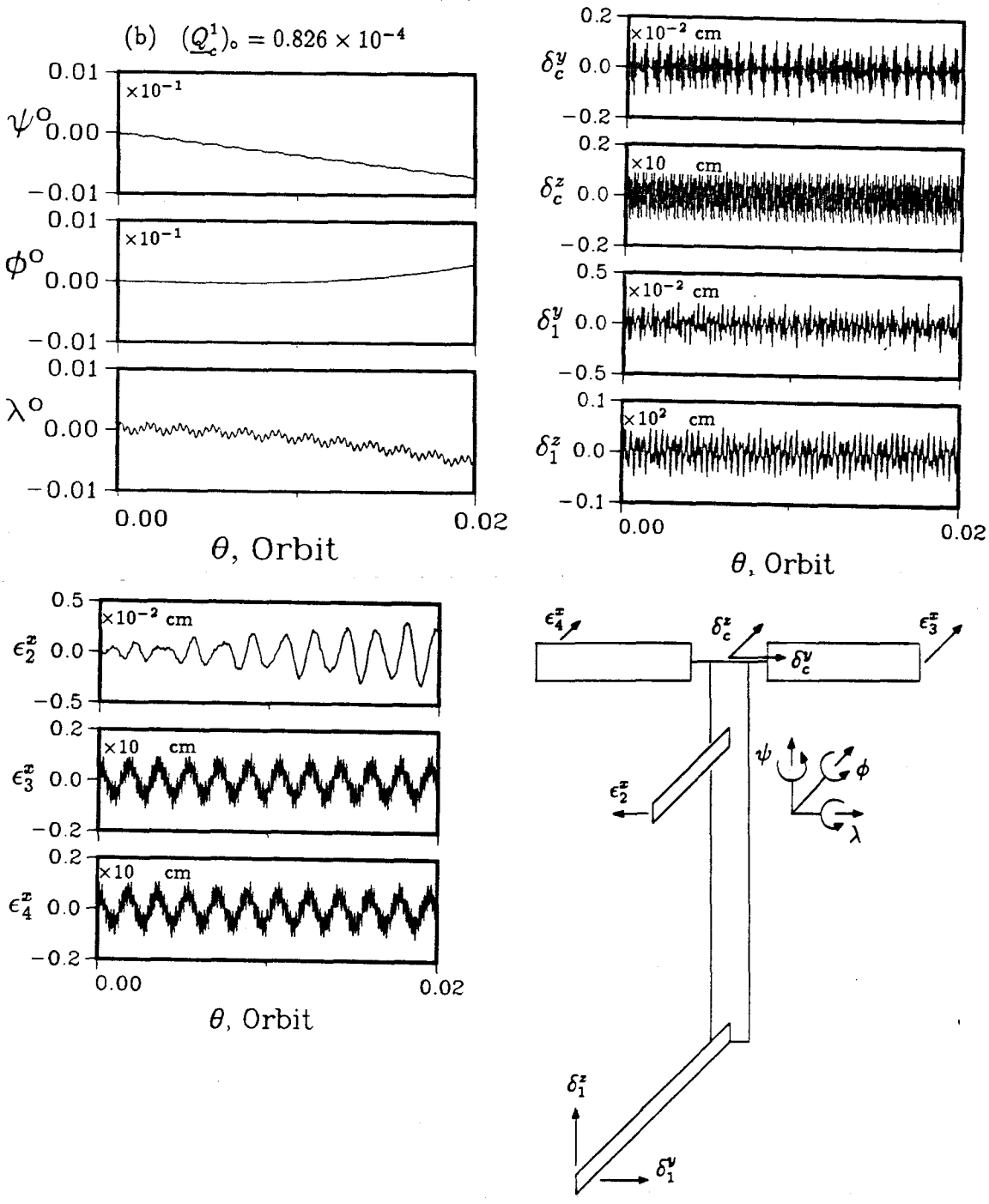

Figure 4-5 The effect of an initial 1 cm tip deflection of the power boom on the FEL dynamics: (b) initial deflection in the local horizontal direction, $(\underline{Q}_c^1)_\circ = 0.826 \times 10^{-4}$.

0.1872×10^{-3}, Figure 4-6a) or along the orbit normal ($(\underline{Q}_1^1)_o = 0.1872 \times 10^{-3}$, Figure 4-6b). Similar to the power boom disturbance case, Figure 4-6a shows that both pitch and roll responses have high frequency harmonics although the roll motion is hardly noticeable. Also, the initial condition has no effect on the yaw response at all. As for the power boom, it is slightly excited with a peak amplitude of about 0.005 cm in the local vertical direction. The excitation of other flexible members are also small: 0.25 cm for ϵ_2^x and 0.5 cm for ϵ_3^x and ϵ_4^x. Figure 4-6b shows that disturbance along the orbit normal has very little impact on librational and vibrational motions of the system. Compared to Figure 4-4, the librational response remains essentially the same. The effect on the power boom is again minor while amplitudes of the PV array and radiator vibrations are one and three orders of magnitude smaller, respectively. Also, analogous to the power boom response of Figure 4-5, δ_1^y has a peak amplitude of only 0.1×10^{-4} cm when excited by the initial condition on $\underline{Q}_1^1$ whereas δ_1^z is two orders of magnitude higher when excited by the initial disturbance of $\underline{P}_1^1$.

Figure 4-7 shows the influence of PV array and radiator disturbance on the system response. In Figure 4-7a, the PV array radiator is initially deflected in the first mode of a cantilever plate with a tip deflection of 0.5 cm ($(\underline{H}_2^{1,1})_o = 0.2485 \times 10^{-3}$). Note, both roll and yaw responses are hardly affected. Pitch response shows low frequency harmonics of a small amplitude. The excitation of the power boom and the stinger is also small: the peak amplitudes of δ_c^y and δ_1^y being only 0.25×10^{-4} cm and 0.02 cm, respectively. The only flexible member that shows noticeable deformation is the PV array with a peak amplitude of about 0.25 cm. With the same initial disturbance applied to the PV array ($(\underline{H}_3^{1,1})_o = 0.866 \times 10^{-4}$), Figure 4-7b shows response results similar to those observed in Figure 4-6a: the rigid body dynamics as well as power boom and stinger motions are virtually absent. However, it is of interest to note a degree of similarity in the response trends of δ_c^z and ϵ_3^x (or ϵ_4^x) in Figure 4-4b, where

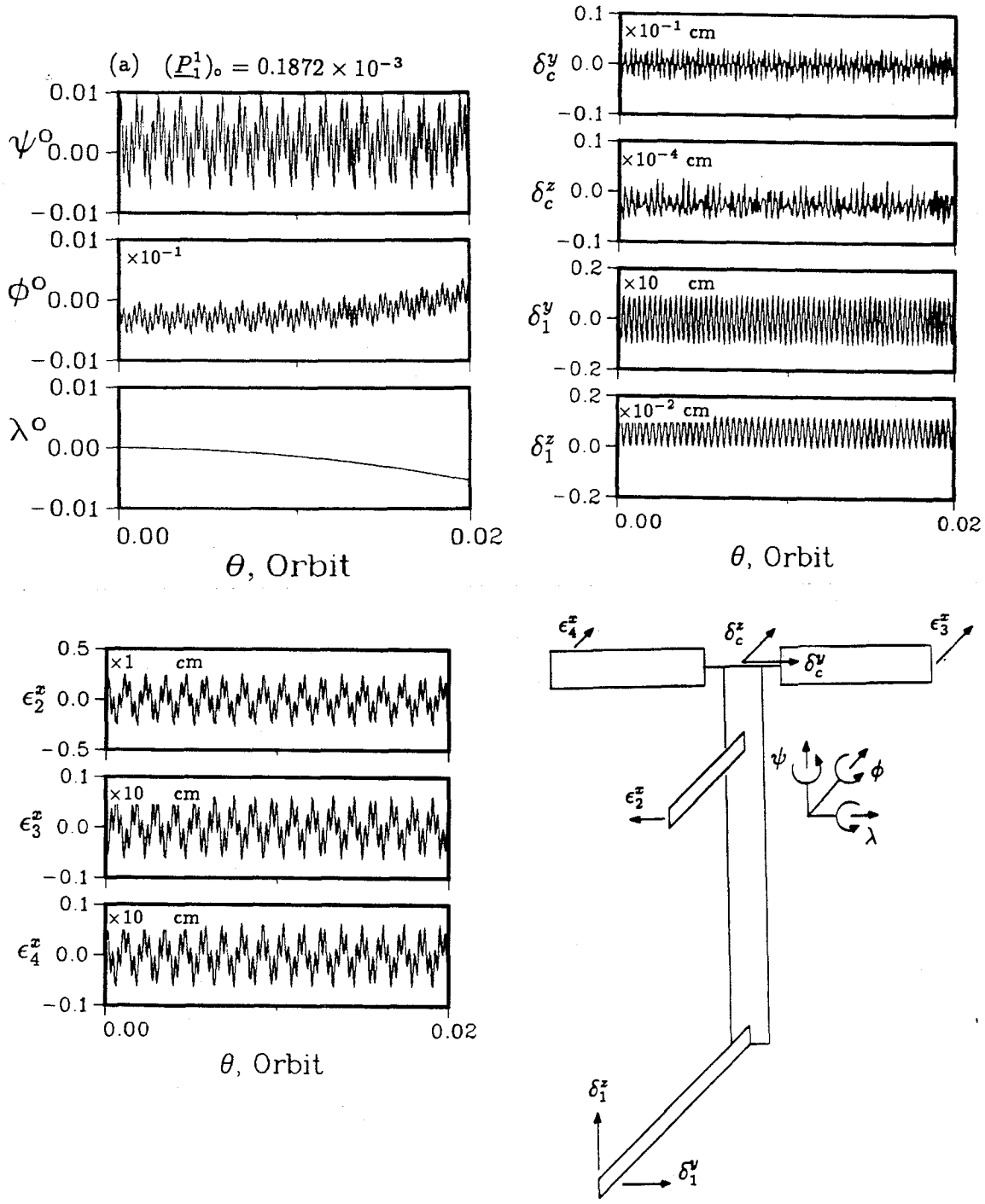

Figure 4-6 Librational and vibrational dynamics of the FEL subjected to an initial 1 cm tip deflection of the stinger: (a) initial deflection in the local vertical direction, $(\underline{P}_1^1)_o = 0.1872 \times 10^{-3}$.

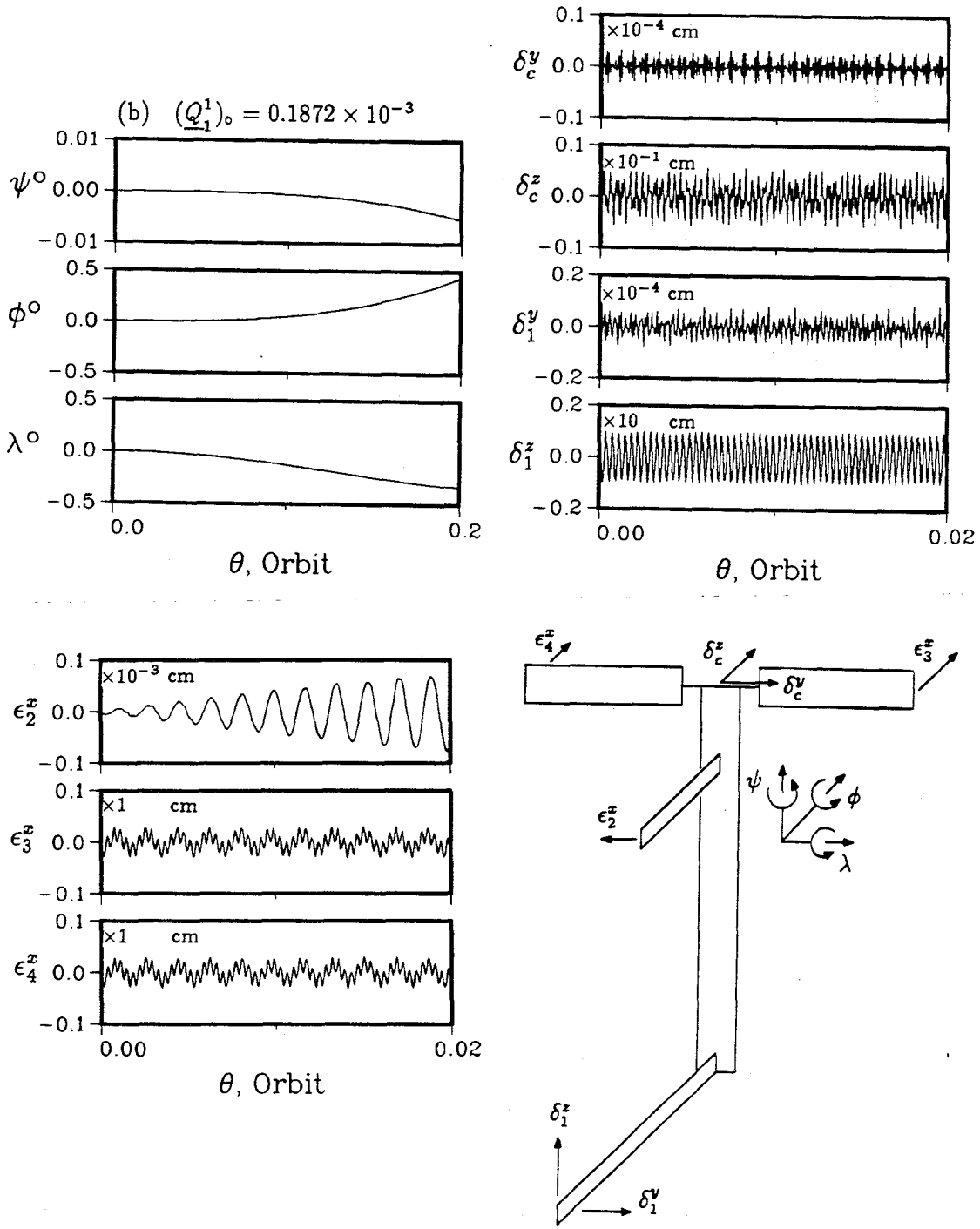

Figure 4-6 Librational and vibrational dynamics of the FEL subjected to an initial 1 cm tip deflection of the stinger: (b) initial deflection in the local vertical direction, $(\underline{Q}_1^1)_o = 0.1872 \times 10^{-3}$.

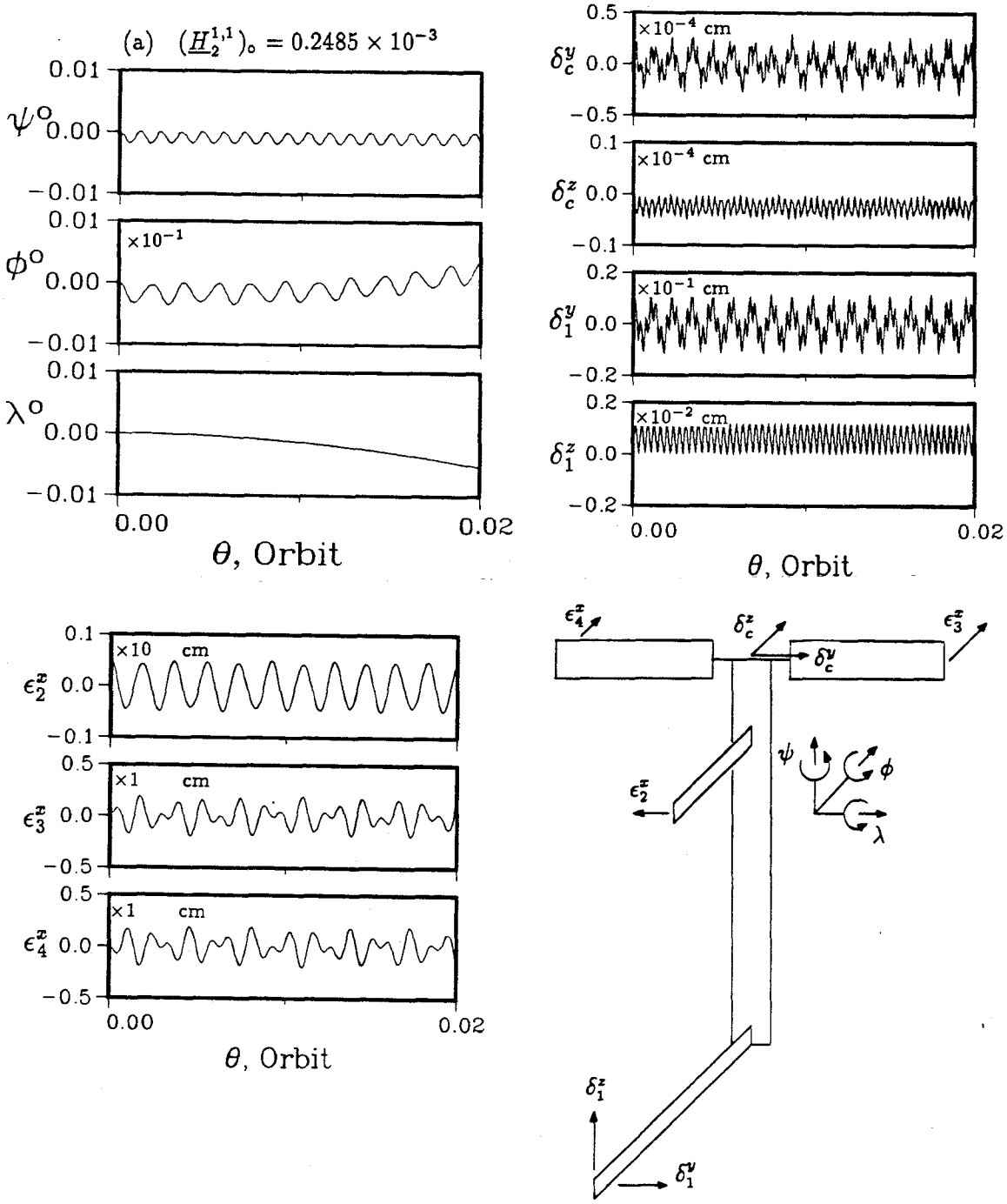

Figure 4-7 The response of the FEL with an initial condition on the PV array or the radiator: (a) PV array radiator with a tip deflection of 0.5 cm, $(\underline{H}_2^{1,1})_o = 0.2485 \times 10^{-3}$.

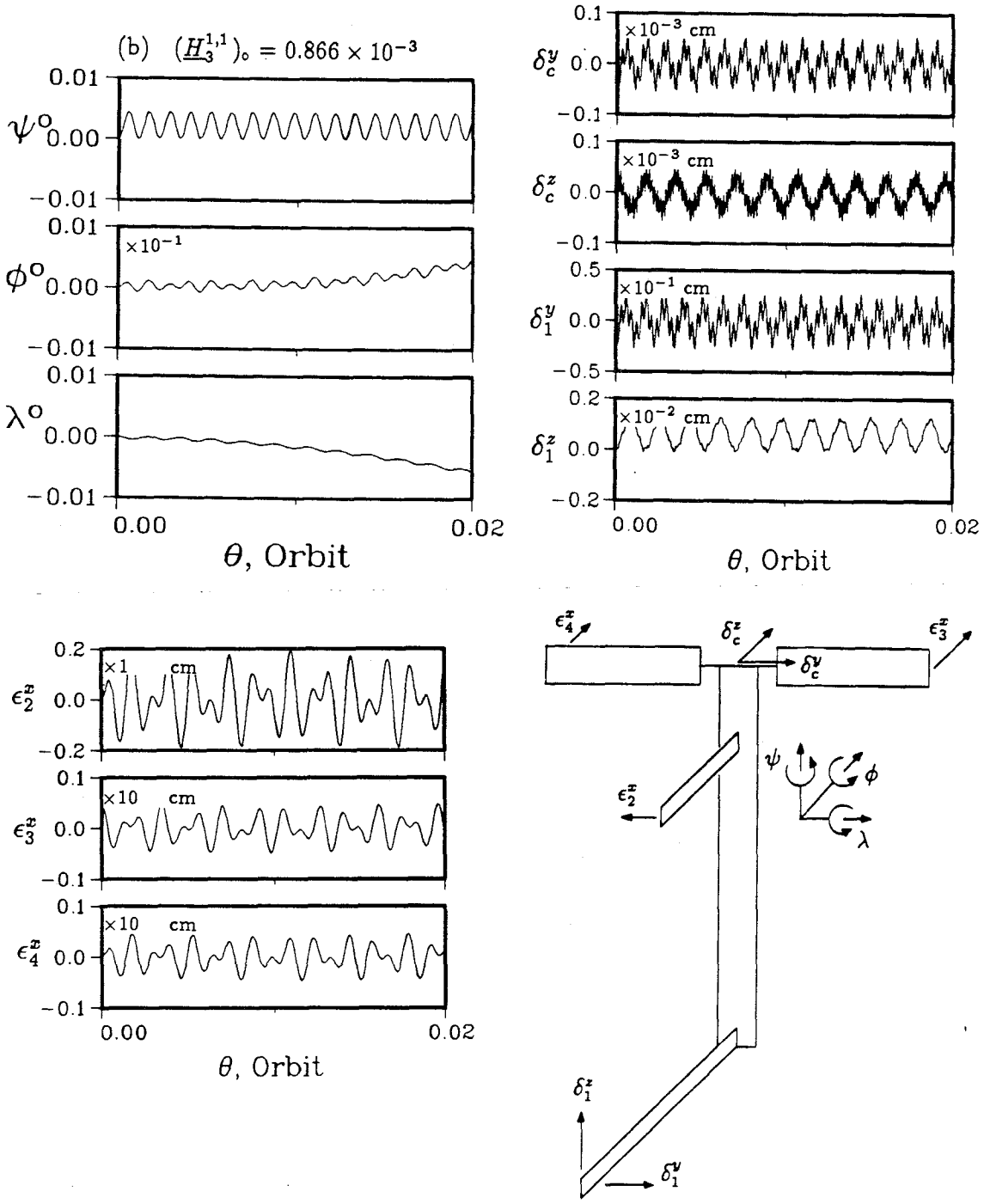

Figure 4-7 The response of the FEL with an initial condition on the PV array or the radiator: (b) PV array with a tip deflection of 0.5 cm, $(\underline{H}_3^{1,1})_o = 0.866 \times 10^{-3}$.

the initial condition corresponds to $\delta_c^z = 1$ cm. This points to the coupling of power boom vibration in the local horizontal direction with the PV array deformation.

In summary, Figures 4-1 to 4-7 demonstrate that flexibility effects on the FEL response cannot be overlooked. A small disturbance applied to any flexible member can affect the rigid body motion significantly. The power boom disturbance in the local vertical direction is the most critical one as the resulting high frequency modulated pitch and roll responses would require high bandwidth controllers. Furthermore, with the power boom or the stinger subjected to a given magnitude of disturbance, its direction is critical in predicting the rigid body as well as vibratory responses of other components.

4.3 Permanently Manned Configuration

4.3.1 Dynamic response

The PMC will be established after fifteen STS flights. It will be 115 m in length and 160,972 kg in mass. The major difference from the FEL configuration is an additional pair of PV arrays and their radiator, two station radiators, and the modules. The two pairs of PV arrays are expected to provide a total power of 37.5 kW for the station. The orientation of the PMC will be similar to that of the FEL: the power boom is aligned with its axis parallel to the orbit normal; the axial directions of radiators (station and PV arrays) and the stinger are parallel to the local horizontal; and the PV arrays in stationary mode have their axes parallel to the local vertical. The coordinate systems for the numerical simulation are shown in Figure 4-8 . Here the PMC is idealized as a free-free beam (power boom) supporting the stinger modelled as a cantilever beam and eight cantilever plates representing arrays and radiators (4 PV arrays, 2 PV array radiators and 2 station radiators). Considering only the first

mode of vibration, the generalized coordinates and the number of degrees of freedom are:

$$q = \psi\ ,\ \phi\ ,\ \lambda\ ,\ \underline{P}_c^1\ ,\underline{Q}_c^1\ ,\ \underline{P}_1^1\ ,\ \underline{Q}_1^1\ ,\ \underline{H}_2^{1,1}\ ,\ \underline{H}_3^{1,1}\ ,\ \underline{H}_4^{1,1}\ ,$$
$$\underline{H}_5^{1,1}\ ,\ \underline{H}_6^{1,1}\ ,\ \underline{H}_7^{1,1}\ ,\ \underline{H}_8^{1,1}\ ,\text{and}\ \underline{H}_9^{1,1}\ ;$$
$$N_q = 15\ .$$

The numerical data for the components are the same as before except for the power boom and station radiators and are summarized in Table 4-2 .

To begin with, the rigid body dynamics of the PMC is considered. The equilibrium configuration of the PMC is found to be at $\psi_e = 0°$, $\phi_e = -0.002°$, and $\lambda_e = 0°$. Even in the absence of any disturbance, the PMC exhibits some librational motion as shown in Figure 4-9. An initial displacement of 0.1° in pitch, roll or yaw is applied. Like the FEL, Figure 4-10 shows that the PMC is inherently in an unstable orientation. However, unlike the FEL, librational disturbances result in different response trends. Figure 4-10a shows that an initial pitch disturbance results in a relatively gradual librational instability with the pitch, roll, and yaw amplitudes reaching 10°, 7°, and 5°, respectively, at the end of one orbit ($\approx$ 90 min). With an initial roll displacement, Figure 4-10b shows that the divergence sets in much faster. Actually, the PMC starts to tumble after one orbit when the yaw angle reaches $-110°$ although the pitch and roll angles (34° and 29°, respectively) are still less than 90°. Finally, with an initial yaw disturbance, Figure 4-10c shows that the response is similar to that in the pitch disturbance case; however, the magnitudes in roll (39°) and yaw (22°) are significantly higher. The nondimensional inertia diadic of the PMC is found to be

$$\mathbf{I}_{sys} = \begin{bmatrix} 0.6706 & 0 & 0.0046 \\ 0 & 13.4346 & 0 \\ 0.0046 & 0 & 13.2783 \end{bmatrix}$$

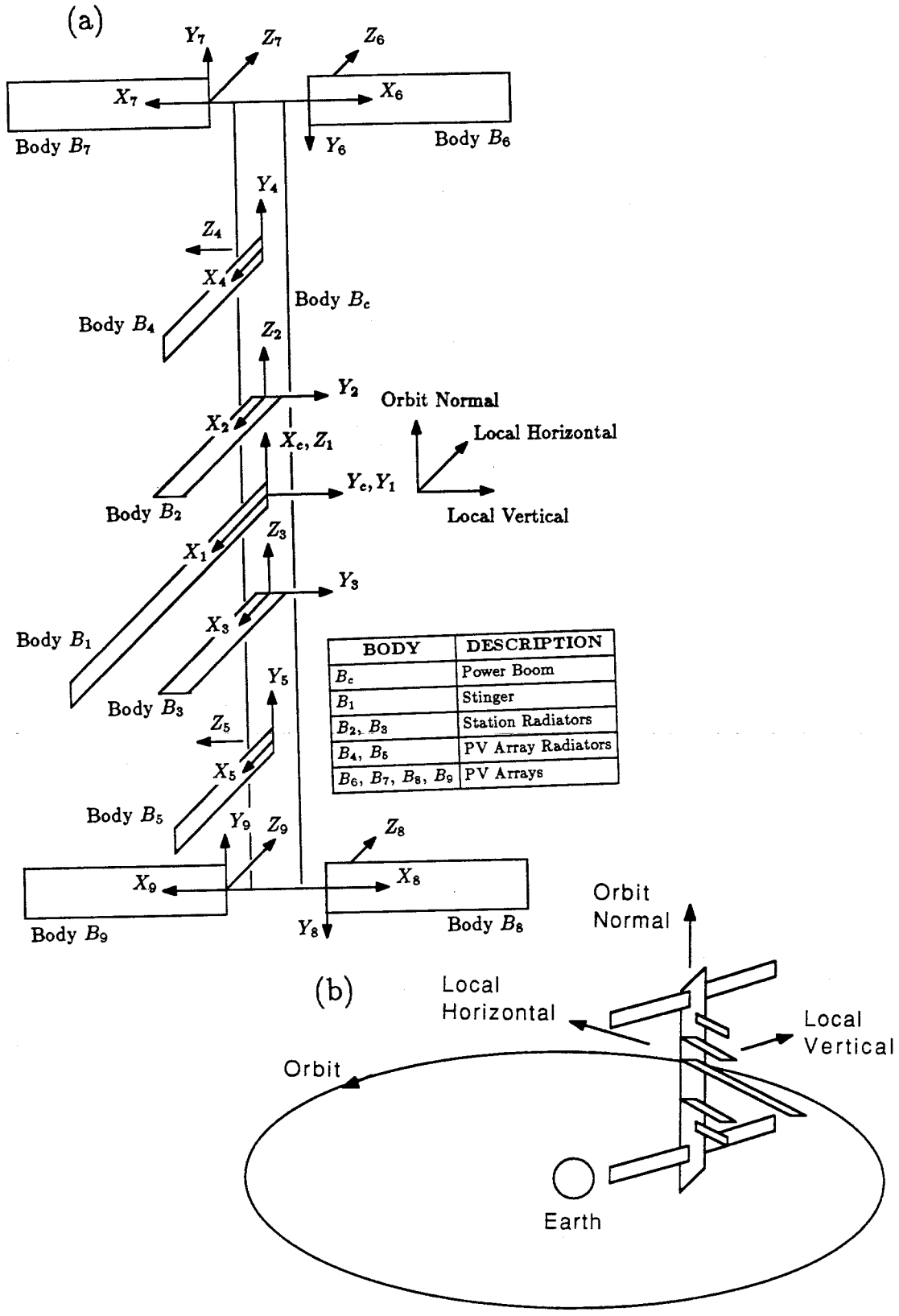

BODY	DESCRIPTION
B_c	Power Boom
B_1	Stinger
B_2, B_3	Station Radiators
B_4, B_5	PV Array Radiators
B_6, B_7, B_8, B_9	PV Arrays

Figure 4-8 Schematic diagram of the PMC used in the numerical simulations: (a) coordinate systems; (b) design configuration.

Table 4-2 Physical parameters of the major components of the PMC

Power Boom (Body B_c)

l_c	=	115 m
m_c	=	154,583 kg
f_c^1	=	0.193 Hz
$(I_{xx})_c$	=	1.44×10^6 kg-m^2
$(I_{yy})_c$	=	43.26×10^6 kg-m^2
$(I_{zz})_c$	=	43.26×10^6 kg-m^2
$(I_{xz})_c$	=	0.18×10^5 kg-m^2

Stinger (Body B_1)

l_1	=	26.7 m
m_1	=	270 kg
f_1^1	=	0.5 Hz
$(I_{xx})_1$	=	3,844 kg-m^2
$(I_{yy})_1$	=	64,160 kg-m^2
$(I_{zz})_1$	=	64,160 kg-m^2

Station Radiator (Body B_i, $i = 2, 3$)

l_i	=	11.5 m
m_i	=	1,395 kg
$f_i^{1,1}$	=	0.1 Hz
$(I_{xx})_i$	$\approx$	0
$(I_{yy})_i$	=	61,496 kg-m^2
$(I_{zz})_i$	=	65,340 kg-m^2

PV Radiator (Body B_i, $i = 4, 5$)

l_i	=	11.5 m
m_i	=	450 kg
$f_i^{1,1}$	=	0.1 Hz
$(I_{xx})_i$	=	50 kg-m^2
$(I_{yy})_i$	=	19,837 kg-m^2
$(I_{zz})_i$	=	19,887 kg-m^2

PV Array (Body B_i, $i = 6, \ldots 9$)

l_i	=	33 m
m_i	=	444 kg
$f_i^{1,1}$	=	0.1 Hz
$(I_{xx})_i$	=	1,332 kg-m^2
$(I_{yy})_i$	=	161,172 kg-m^2
$(I_{zz})_i$	=	162,504 kg-m^2

giving $K_1 = 0.94$ and $K_2 = -0.961$. Although these values are similar to those of the FEL ($K_1 = 0.91$ and $K_2 = -0.84$), the trend of the libration responses for the two cases are different. This points to the difficulty in predicting response trends based on K_1 and K_2 values only.

The system response of the PMC with the inclusion of component flexibility is shown in Figures 4-11 to 4-14. For conciseness, only the response of one station

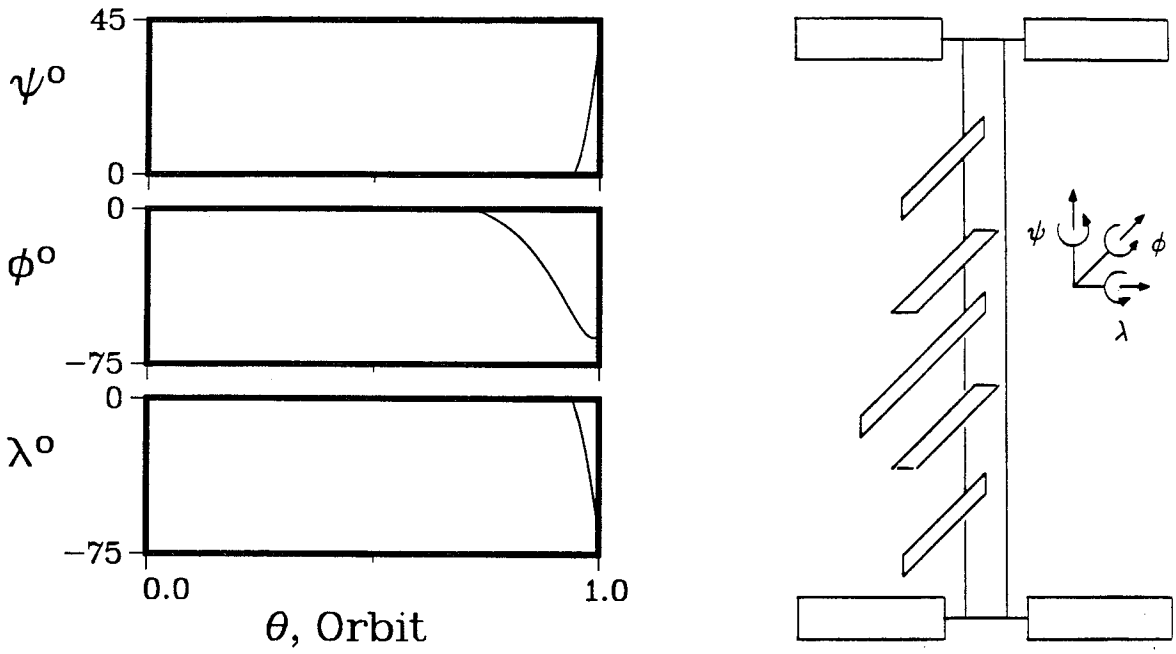

Figure 4-9 Libration response of the PMC due to deviation from the equlibrium configuration.

radiator (B_2), PV array radiator (B_4) and PV array (B_6) are plotted. The system behaviour indicates some similarities as well as dissimilarities with the corresponding FEL responses.

Figure 4-11 shows response of the system initially in the design configuration. The motion ensues due to deviation of the system orientation from its equilibrium configuration. Note, the pitch motion is essentially unexcited. Although the roll and yaw degrees of freedom are excited, their amplitudes increase very slowly. Unlike the FEL, only the power boom vibration in the local horizontal direction (δ_c^z) and the station radiator (ϵ_2^x) have non-zero equilibrium positions. In the power boom response, the component in the local vertical direction (δ_c^y) is hardly excited. The stinger experiences a peak vibrational amplitude of about 0.1×10^{-5} cm. Note that, unlike the FEL, the stinger is stiffer than the power boom and hence has the highest

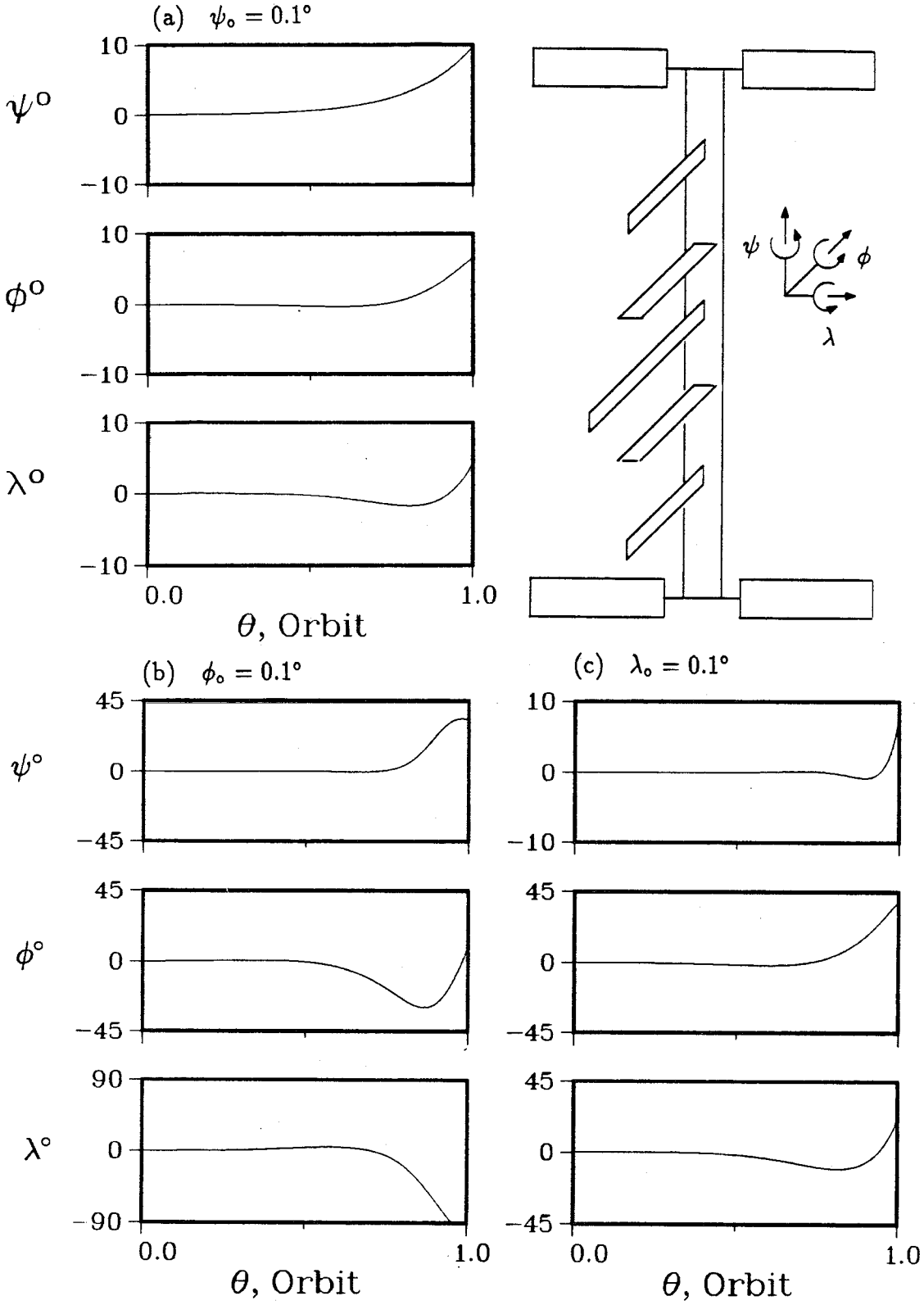

Figure 4-10 Rigid body response of the PMC to rotational disturbances.

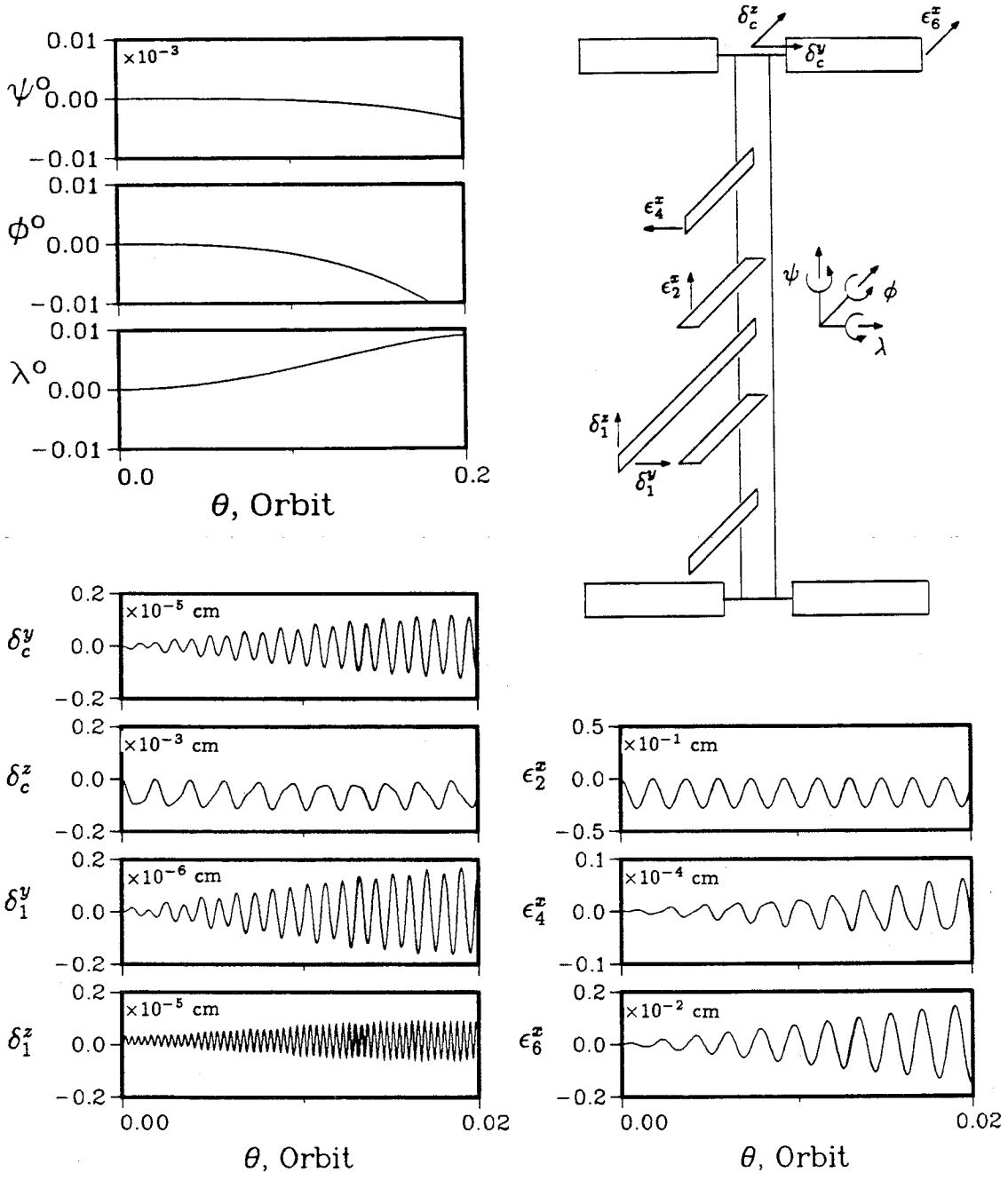

Figure 4-11 Response of the PMC due to deviation from the equilibrium orientation.

number of oscillations per unit time.

Next, the system is subjected to an initial disturbance corresponding to the power boom deformed in the first mode with a tip deflection of 1 cm. With the initial deflection in the local vertical direction, $(\underline{P}_c^1)_\circ = 0.4348 \times 10^{-4}$, Figure 4-12 shows the system response over 0.02 orbit. Note that similar to the FEL, the power boom disturbance in the local vertical direction excites the libration motion with high frequency modulations superposed on it. Yet, unlike the FEL, only the pitch motion is excited in the present case, with a considerably lower frequency due to a more flexible power boom. Also, the beat phenomenom no longer exists since the powerboom is now loaded symmetrically. The stinger, though excited, vibrates predominantly in the local vertical direction with a magnitude of 0.6 cm peak-to-peak. Other flexible components oscillate with frequencies of the power boom vibration. Even with this small initial disturbance, the PV array radiators experience a large deflection with a peak amplitude of 2.5 cm. In Figure 4-12b, response of the PMC is to an initial disturbance in the local horizontal direction ($(\underline{Q}_c^1)_\circ = 0.4348 \times 10^{-4}$). In the FEL case, yaw is the only librational motion excited. Here, only the pitch response is present with a negligible amplitude. The stinger and the PV array radiator responses are also small with peak amplitudes of 0.01 cm and 0.1 cm, respectively. It is interesting to note that both the station radiators and PV arrays have similar response trends but with different amplitudes: 1 cm for the station radiators and 2.5 cm for the PV arrays, although the latter are more massive.

The focus is now turned to the stinger disturbance. The initial condition of the stinger is identical to that of Figure 4-6. The system behaviour may be expected to be similar to that observed for the FEL case. Yet, since the PMC is about ten times as heavy as the FEL, the forced response to the stinger disturbance is expected to be

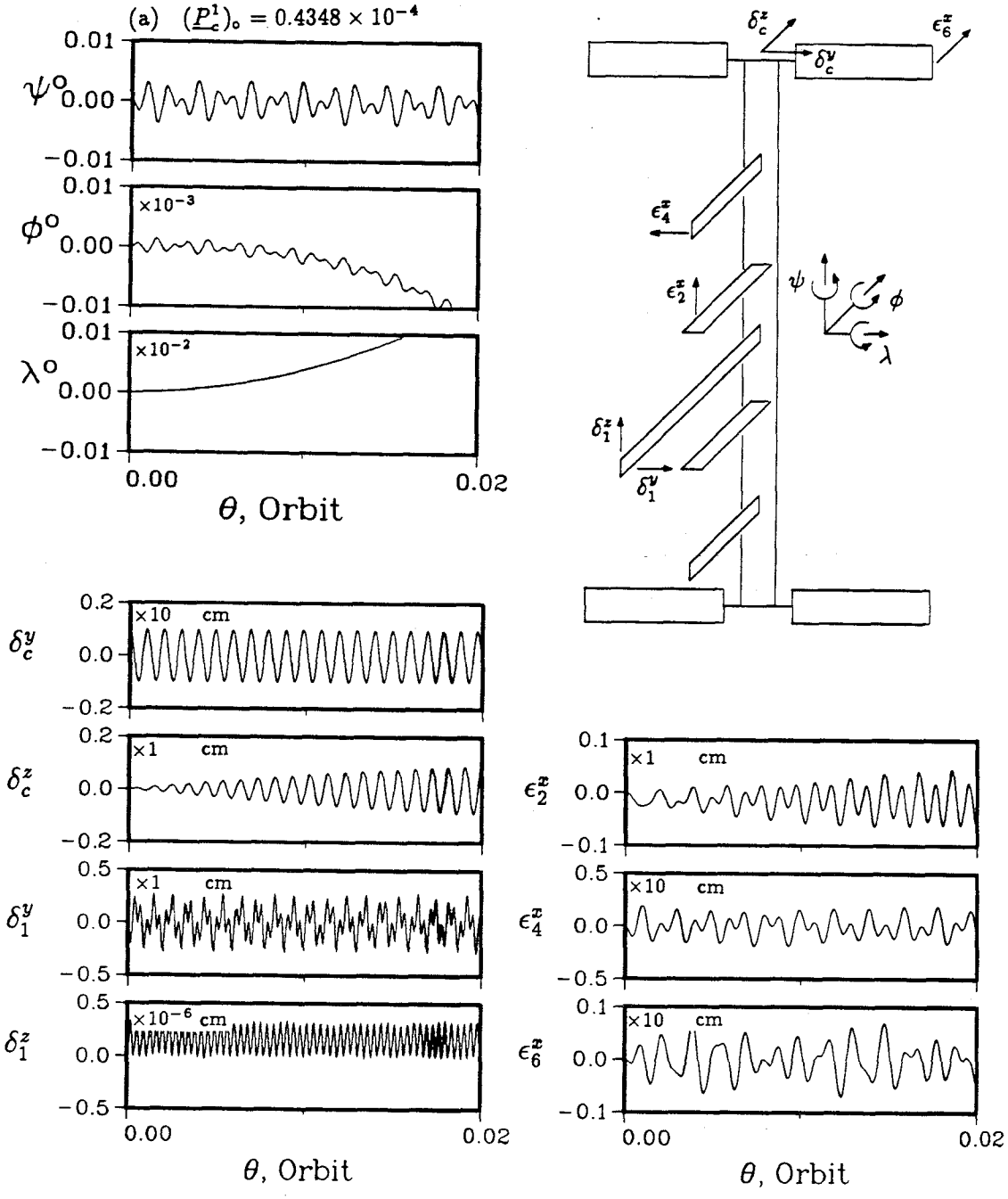

Figure 4-12 The influence of the power boom initial tip displacement of 1 cm on the PMC response: (a) displacement in the local vertical direction, $(\underline{P}_c^1)_o = 0.4348 \times 10^{-4}$.

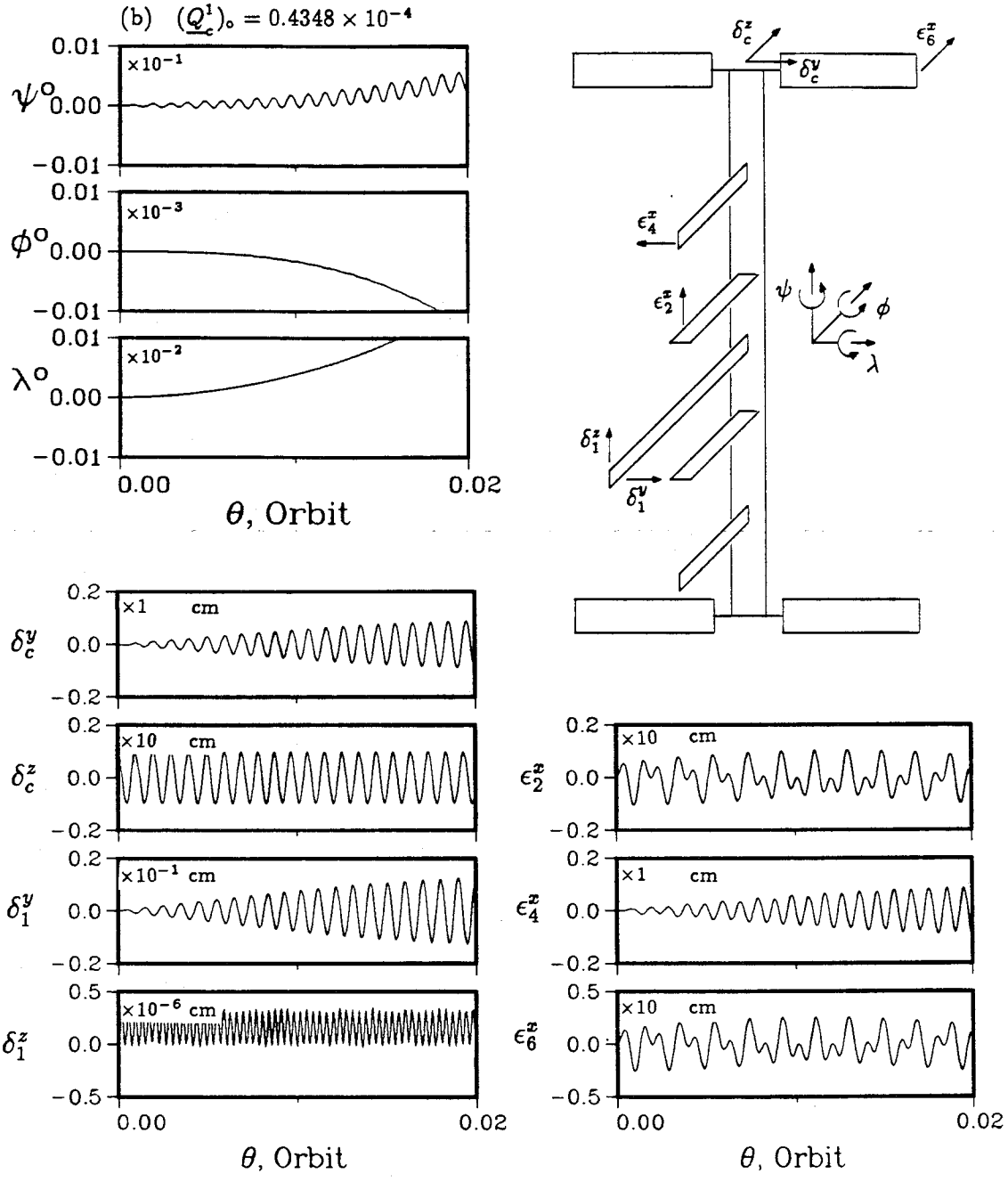

Figure 4-12 The influence of the power boom initial tip displacement of 1 cm on the PMC response: (b) displacement in the local horizontal direction, $(\underline{Q}_c^1)_o = 0.4348 \times 10^{-4}$.

smaller in magnitude. Figure 4-13 a verifies these predictions. With the initial stinger disturbance in the local vertical direction, the figure shows that the PMC is pitching about the orbit normal at a higher frequency. However, the amplitude is considerably smaller than that for the FEL case. The power boom, PV array and radiator oscillate with maximum amplitudes of 0.003 cm, 0.1 cm and 0.05 cm, respectively. These values are about an order of magnitude smaller than the corresponding ones in the FEL case. Note that the stinger response in the orbit normal direction attained a maximum amplitude of 0.001 cm in the FEL case, whereas now the same degree of freedom is hardly excited. The response of the PMC with initial stinger disturbance in the orbit normal direction is shown in Figure 4-13b. Similar to the FEL, the librational motion is unaffected by the stinger disturbance. The PMC librates as if no initial condition was applied to the system (other than deviation from the equilibrium orientation, Figure 4-11). Likewise, the power boom and the stinger deformations in the local vertical direction are excited slightly. The response trends of the PV array and radiator are also similar to those in the FEL case; however, the amplitudes of the response in the PMC case are considerably smaller. In the FEL configuration, the maximum array displacement was 0.05 cm whereas it is only 0.01 cm in the PMC case.

The flexibility effects of the station radiator, as well as PV array and radiator are shown in Figure 4-14. In Figure 4-14a, an initial tip displacement of 0.5 cm is applied to one of the station radiators ($(\underline{H}_2^{1,1})_o = 0.2485 \times 10^{-3}$). As can be seen, this disturbance has no influence on the librational response of the PMC. For the power boom, the response δ_c^z is identical to ϵ_2^x in Figure 4-12b where the initial condition was applied to δ_c^z. This illustrates the coupling of $\underline{Q}_c^1$ and $\underline{H}_2^{1,1}$ degrees of freedom. The peak amplitude of the power boom motion is found to be 0.002 cm. As expected, the forced oscillation of the stinger is predominantly in the direction parallel to the

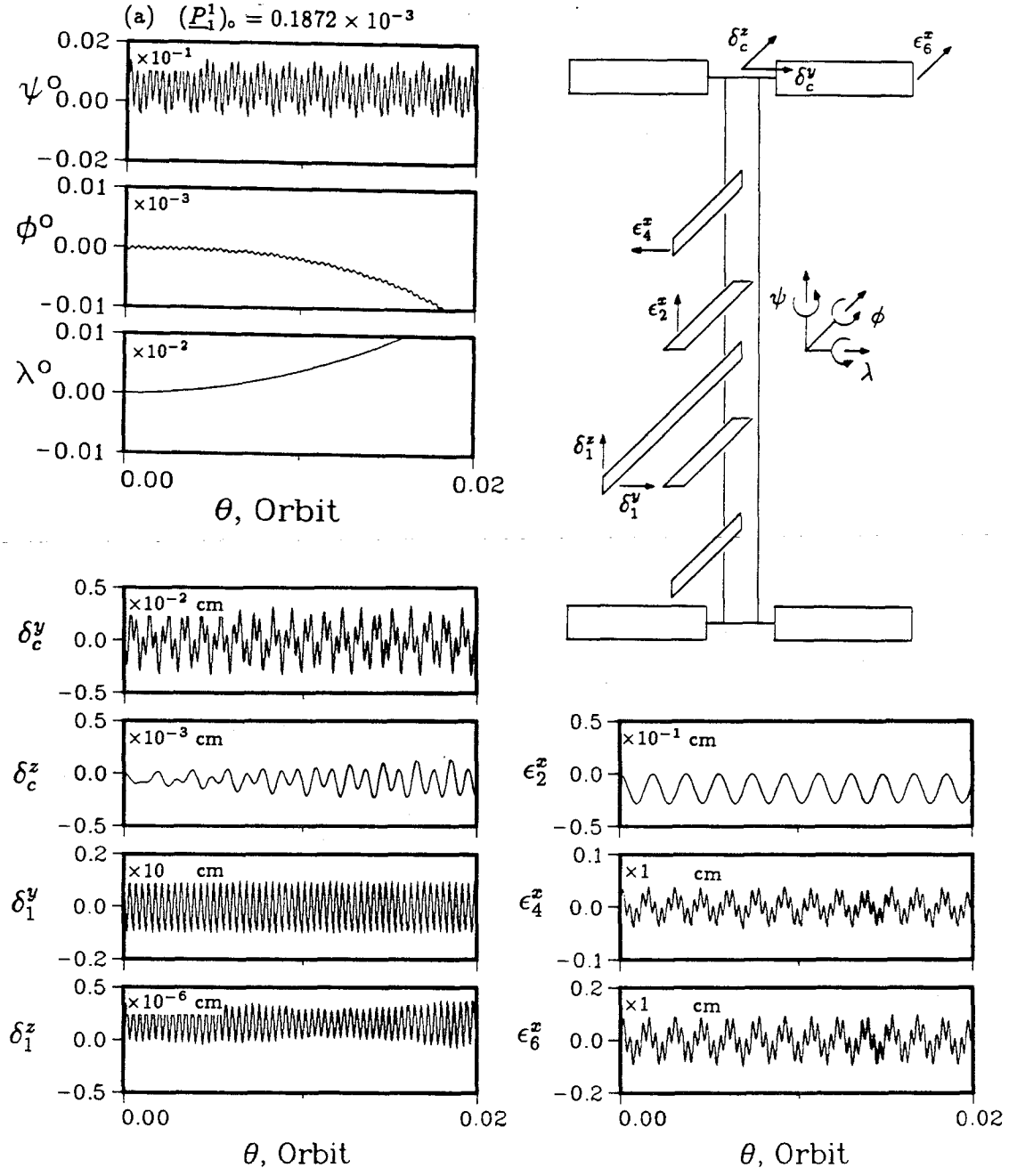

Figure 4-13 Response of the PMC subjected to an initial 1 cm tip deflection of the stinger: (a) deflection in the local vertical direction, $(\underline{P}_1^1)_o = 0.1872 \times 10^{-3}$.

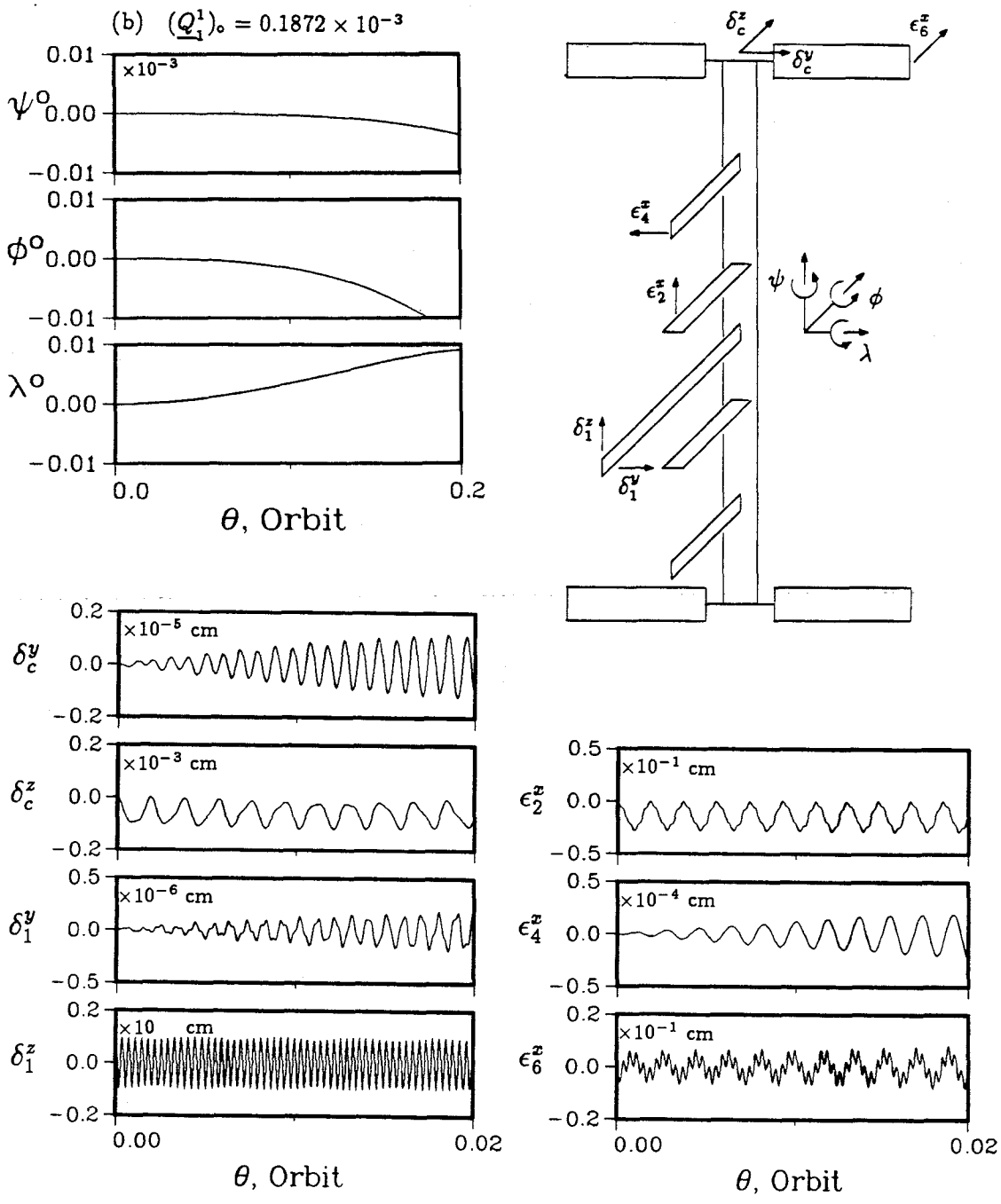

Figure 4-13 The response of the PMC subjected to an initial 1 cm tip deflection of the stinger: (b) deflection in the orbit normal direction, $(\underline{Q}_1^1)_o = 0.1872 \times 10^{-3}$.

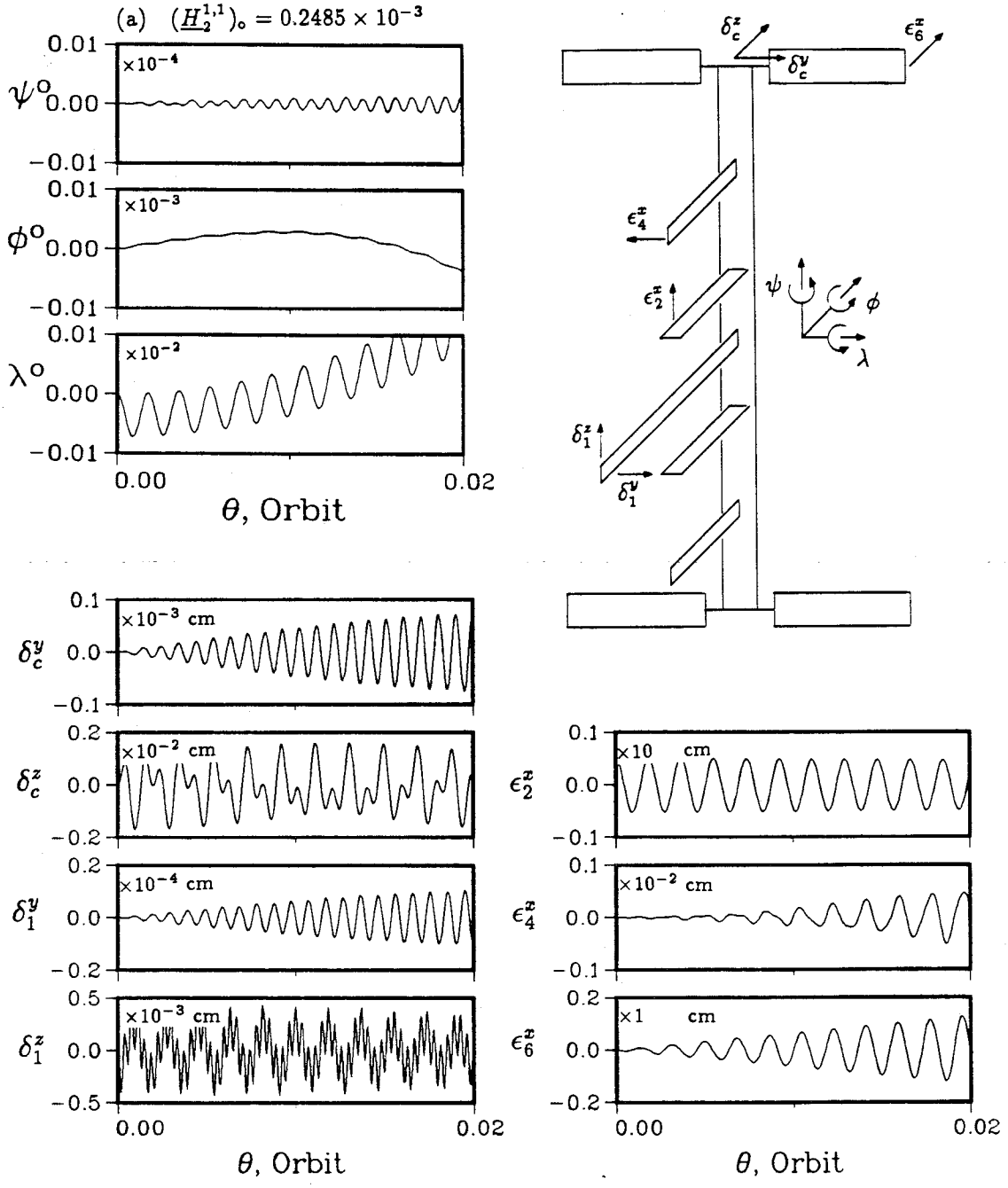

Figure 4-14 Effect of the station radiator, PV array, and radiator disturbance on the PMC dynamics: (a) station radiator subjected to a tip deflection of 0.5 cm, $(\underline{H}_2^{1,1})_o = 0.2485 \times 10^{-3}$.

radiator disturbance, i.e. along the orbit normal. Since the stinger is stiffer than the power boom, the amplitude of the stinger motion is only 0.0005 cm. It should be pointed out that since ϵ_2^x is perpendicular to ϵ_4^x or ϵ_6^x, the PV array and radiator should not be excited. However, since δ_c^y is excited gradually, the coupling effect induces the response ϵ_4^x and ϵ_6^x. At the end of 0.02 orbit, the magnitudes of vibration are 0.001 cm and 0.2 cm for the PV array and radiator, respectively.

The disturbance is now applied to the PV array radiator with a tip deflection of 0.5 cm ($(\underline{H}_4^{1,1})_\circ = 0.2485 \times 10^{-3}$, Figure 4-14b). Similar to the FEL, the PV array radiator disturbance has minor effect on the librational motion. It is interesting to note that δ_c^y exhibits the same response trend as that of ϵ_4^x in Figure 4-12a. Once again, this shows the coupling between PV array radiator and the power boom deformation in the local vertical direction. The forced oscillation of the stinger is now predominantly in the local vertical direction, which is the same as the direction of ϵ_4^x. The station radiator response is insensitive to the PV array radiator disturbance; and ϵ_2^x is identical to the corresponding response in Figure 4-11 in absence of an external disturbance. The PV array is now vibrating with a peak amplitude of 0.1 cm. The response trend is similar to that of the PV array radiator in Figure 4-14c where an initial disturbance is now applied corresponding to the array tip deflection of 0.5 cm ($(\underline{H}_6^{1,1})_\circ = 0.866 \times 10^{-4}$). Other observations are similar to those made during the discussion of Figures 4-14a and 4-14b. Namely, the initial condition on PV array lead to only minor libration of the PMC. The distinct response trend of the power boom again appears in the δ_c^z. The stinger response, with its characteristic high frequency harmonics, vibrates with a peak amplitude of about 0.005 cm in the local vertical direction. Once again, the station radiator is insensitive to this particular initial condition.

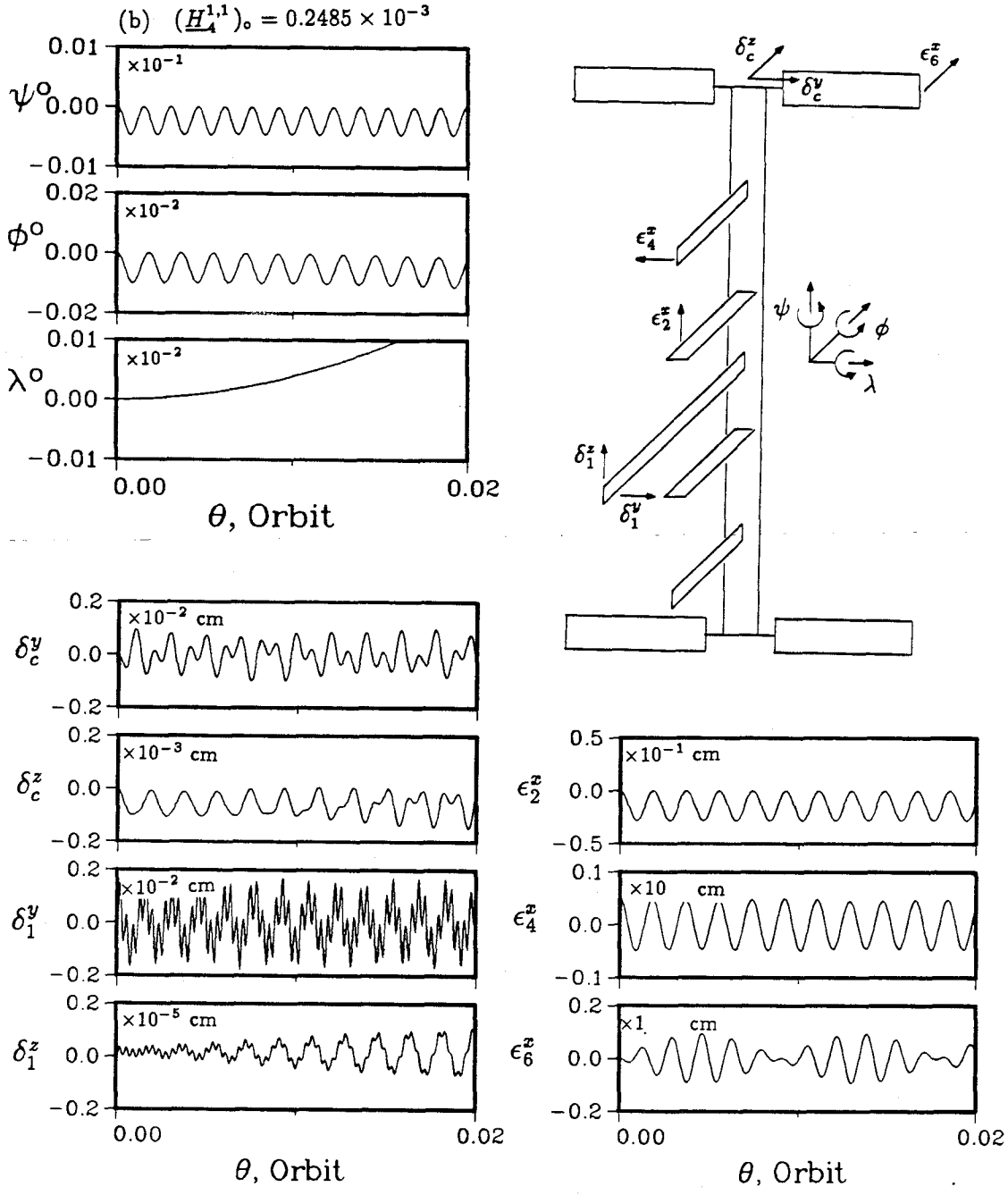

Figure 4-14 Effect of station radiator, PV array, and radiator disturbance on the PMC dynamics: (b) PV array radiator subjected to a tip deflection of 0.5 cm, $(\underline{H}_4^{1,1})_o = 0.2485 \times 10^{-3}$.

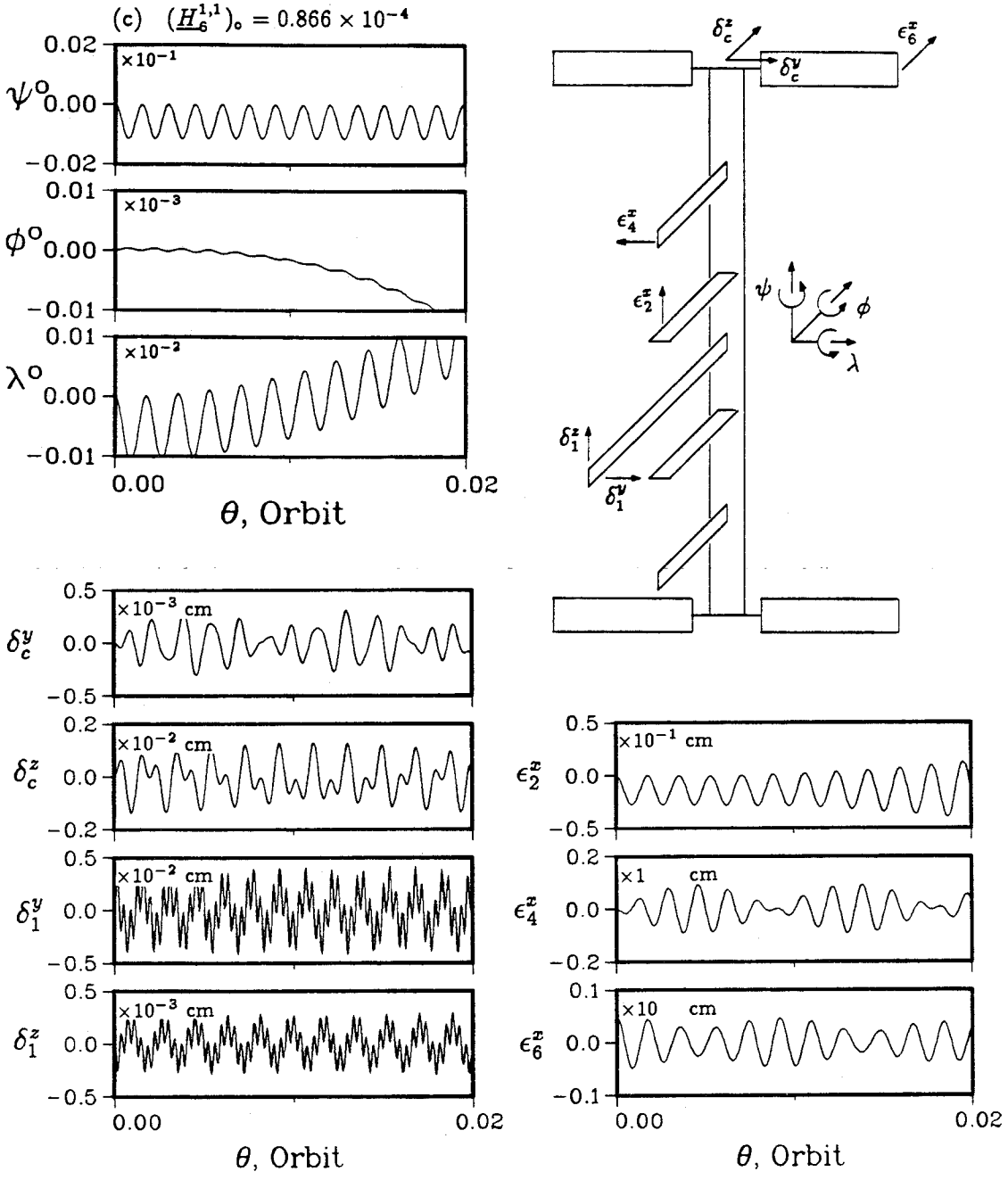

Figure 4-14 Effect of station radiator, PV array, and radiator disturbance on the PMC dynamics: (c) PV array subjected to a tip deflection of 0.5 cm, $(\underline{H}_6^{1,1})_o = 0.866 \times 10^{-4}$.

Figures 4-12 to 4-14 show that, as in the case of the FEL, the rigid body motion is sensitive to the deformations of the flexible members. Even for the same flexible member, different directions of excitation results in different librational response. Due to the relatively large mass and inertia of the power boom, even its small excitation induces large deflections of the arrays and radiators. The stinger, which has the largest stiffness among all the flexible components, excites librational and vibrational responses with high frequency modulations. Disturbances applied to the radiator or array, in general, have little influence on the rigid body motion of the system as well as flexible deformations of the power boom and stinger.

4.3.2 Thermal deformation and eccentricity

With a large surface area of over 1,500 m^2, it is important to investigate the effect of thermal deformation of the flexible members. The simulation here considers only the differential heating of the PV arrays, which have a total area of over 790 m^2 and are facing the sun at all times. Since no reliable data on the physical properties of arrays are available, the value of L_i^* is assumed to be 0.01 $(i = 6, \ldots, 9)$ where

$$L_i^* = l_i / l_i^* \,,$$

and l_i^*, the thermal reference length, is as given by Eq. (2.19). Thermal reference length can be visualized as the radius of curvature of the thermally deformed element. A large l_i^*, and hence small L_i^*, implies little thermal deformation effect. An assumed value of $L_i^* = 0.01$ corresponds to $l_i^* = 3,300$ m, which represents little differential heating of the arrays. Even with this small L_i^* value, the effect on the PMC response is not negligible as shown in Figure 4-15. Here, there is no initial disturbance applied to the system, i.e. the excitation is purely due to deviation from the equilibrium configuration. A comparison with Figure 4-11 would be appropriate.

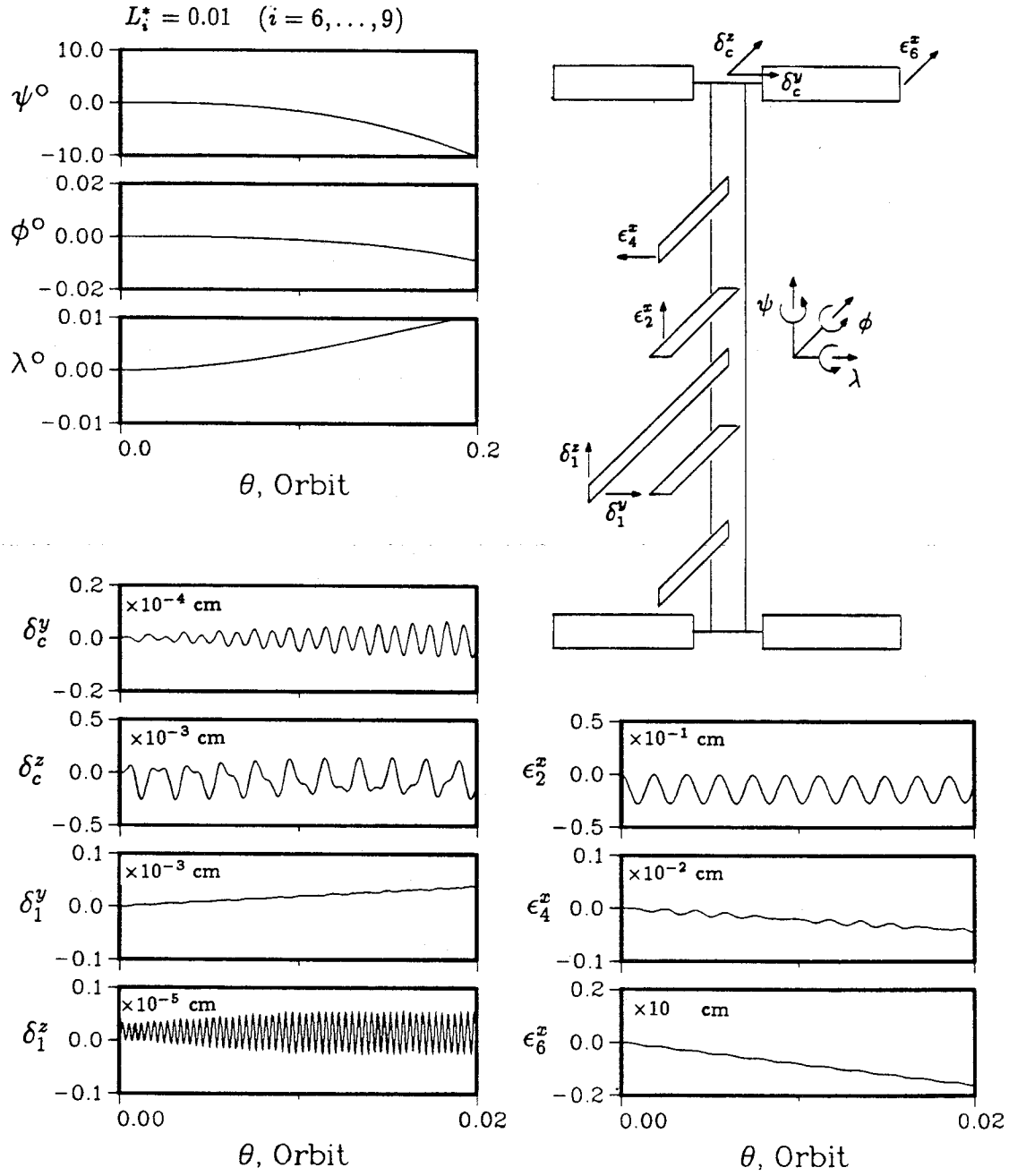

Figure 4-15 Librational and vibrational responses of the PMC in absence of external excitation showing the effect of thermally deformed PV arrays.

Since the PV arrays deform in planes parallel to the orbital plane, the pitch motion is strongly affected. At 0.2 orbit, the pitch angle attains a magnitude of $-10°$ and is still increasing. Most of the flexible generalized coordinates, except those corresponding to deformations in the orbit normal direction, are also affected. In general, thermal deformations of the PV arrays induce larger response. The stinger and the PV array radiators experience the highest increase in deflections.

As the space station will be orbiting in a near circular orbit ($\epsilon = 0.02$), Figure 4-16 studies the effect of eccentricity. With the system initially in the design configuration, a comparison with Figure 4-11 shows that both pitch and roll responses are affected. As for the flexible degrees of freedom, a small eccentricity does not produce any noticeable change in their response.

Figures 4-15 and 4-16 illustrate that both thermal deformation and eccentricity affect the pitch response. However, thermal deformations, even of a small magnitude, also influence response of the flexible members.

4.3.3 Velocities and accelerations

One of the stated missions of the space station is to provide microgravity environment for the purpose of scientific research. As stated in the NASA report [106], the objective of the station is to provide a $1 - 10$ μg environment in some portion of the Laboratory Module. Furthermore, a drift rate, apart from the orbital rate ($\dot{\theta}$), below 0.005 °/s (0.872×10^{-4} rad/s) is desired. Using the data obtained for Figures 4-11 to 4-16, variations of angular velocities (ω_x, ω_y, ω_z) and angular accelartions (α_x, α_y, α_z) about the X_c,Y_c,Z_c-axes and power boom accelerations (a_c^y, a_c^z) at the system c.m. are plotted. Note, Eq. (3.11), where the orbital rate is assumed to be zero, is purposely used to calculate angular velocities isolated from any effect of the orbital rate. The angular accelerations expressed as μg/m can be interpreted as the μg level

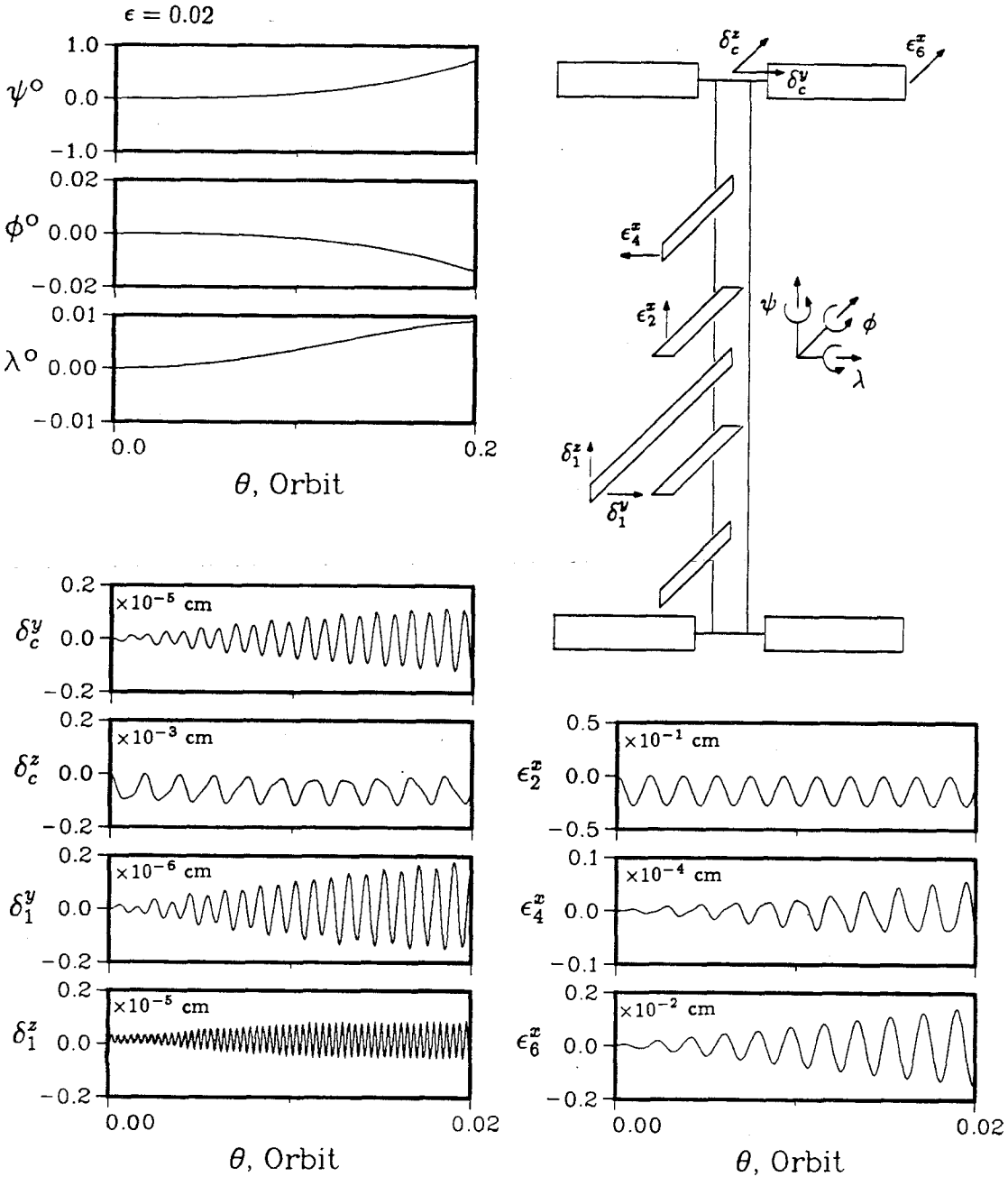

Figure 4-16 Response of the PMC in eccentric orbit ($\epsilon = 0.02$). Initial disturbance is due to deviation from the equilibrium orientation.

at 1 m from O_c, the origin of the X_c,Y_c,Z_c-axes. For instance, $\alpha_x = 1$ μg/m implies that a point at 1 m along the Y_c or Z_c-axis experiences an acceleration of 1 μg due to the angular acceleration about the X_c-axis. Assuming the microgravity experiment workspace to be about 10 m from O_c, a $1 - 10$ μg/m environment would therefore require the angular acceleration about any axis to be less than 1 μg/m. Finally, the power boom accelerations, expressed in terms of microgravity, are evaluated at the centre of the boom using the following expressions:

$$a_c^y(\theta) = \ddot{P}_c^1(\theta)\phi_c^1(0)\,;$$
$$a_c^z(\theta) = \ddot{Q}_c^1(\theta)\phi_c^1(0)\,; \tag{4.3}$$

since only one mode is considered in the boom vibration to illustrate the methodology. Of course, the formulation and the program are quite general and can readily accommodate desired number of modes.

The dynamic response of the PMC in the design configuration was shown in Figure 4-11. The corresponding velocity and acceleration variations are presented in Figure 4-17. Note, the only disturbance being that corresponding to a small deviation from the equilibrium configuration ($\psi_o = 0$, $\phi_o = 0.002°$, and $\lambda_o = 0$), the resulting response is extremely small. Obviously, a word of caution is in order in the analysis of such virtually insignificant numbers. Stability of the numerical procedure and truncation error may lead to noise. What is important is to recognize that all the responses, even in the presence of 'noise', are within the permissible limits. Thus, this can serve as a reference while assessing influence of the initial disturbances.

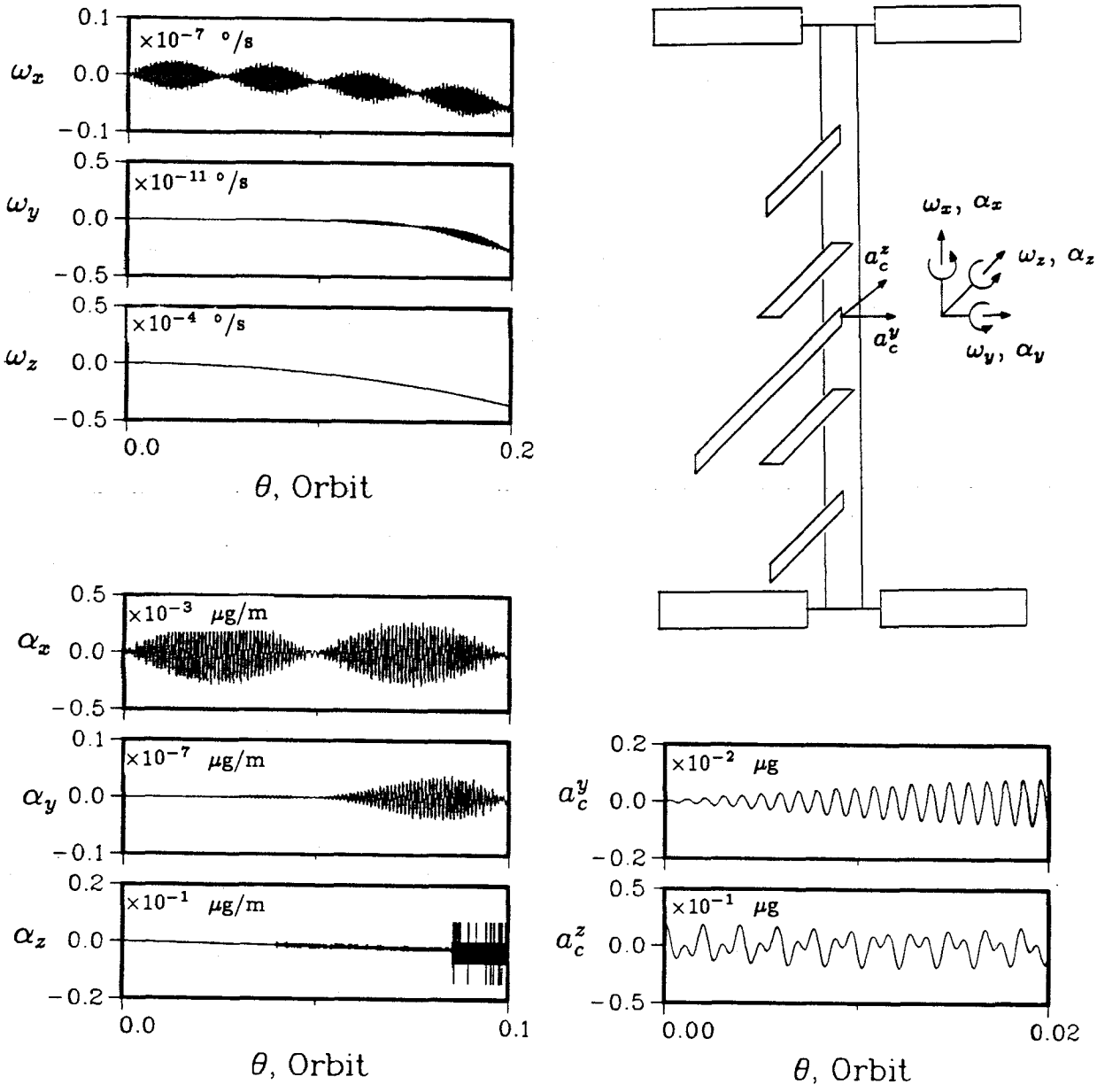

Figure 4-17 Variation of angular velocities as well as and linear and angular acceleration fields for the PMC in absence of active disturbances.

Figure 4-18 illustrates velocity and acceleration variations for the PMC subjected to an initial power boom or stinger disturbance. Figure 4-18a corresponds to the case shown in Figure 4-12a, where the power boom is initially given 1 cm tip deflection in the local vertical direction. Even with such a small disturbance, the resulting angular velocities and accelerations approach or exceed the specified limit. For instance, maximum ω_x and α_x attain values of 0.004 °/s and 500 μg/m, respectively. The microgravity level near the power boom centre is over 1,000 μg. When the initial disturbance is applied in the local horizontal direction, the magnitudes of both velocities and accelerations are about one order smaller (Figure 4-18b); however, the accelerations still exceed the design limit. Once again, angular velocity and acceleration about the X_c-axis are largest with magnitudes of 2×10^{-4} °/s and 10 μg/m, respectively. The boom acceleration results in a microgravity level exceeding 1,000 μg in the local horizontal direction.

Figure 4-13 showed that the influence of the stinger disturbance on the PMC response is small; hence, it is reasonable to expect the corresponding angular velocities and accelerations to be small. The prediction turned out to be correct; however, they are not negligible when the disturbance is applied in the local vertical direction. Under this condition, Figure 4-18c illustrates that the maximum drift rate is 0.0025 °/s about the X_c-axis but the maximum angular acceleration has an amplitude of 300 μg/m about Y_c-axis. The microgravity level due to the boom accelerations reaches a value of 6 μg in the local vertical direction. When the same stinger disturbance is applied in the out-of-plane direction, both the velocities and accelerations stay within the allowable limit (Figure 4-18d). Now the maximum angular velocity (0.3×10^{-6} °/s) and acceleration (0.01 μg/m) are about Z_c-axis, while the boom vibration results in 0.02 μg acceleration.

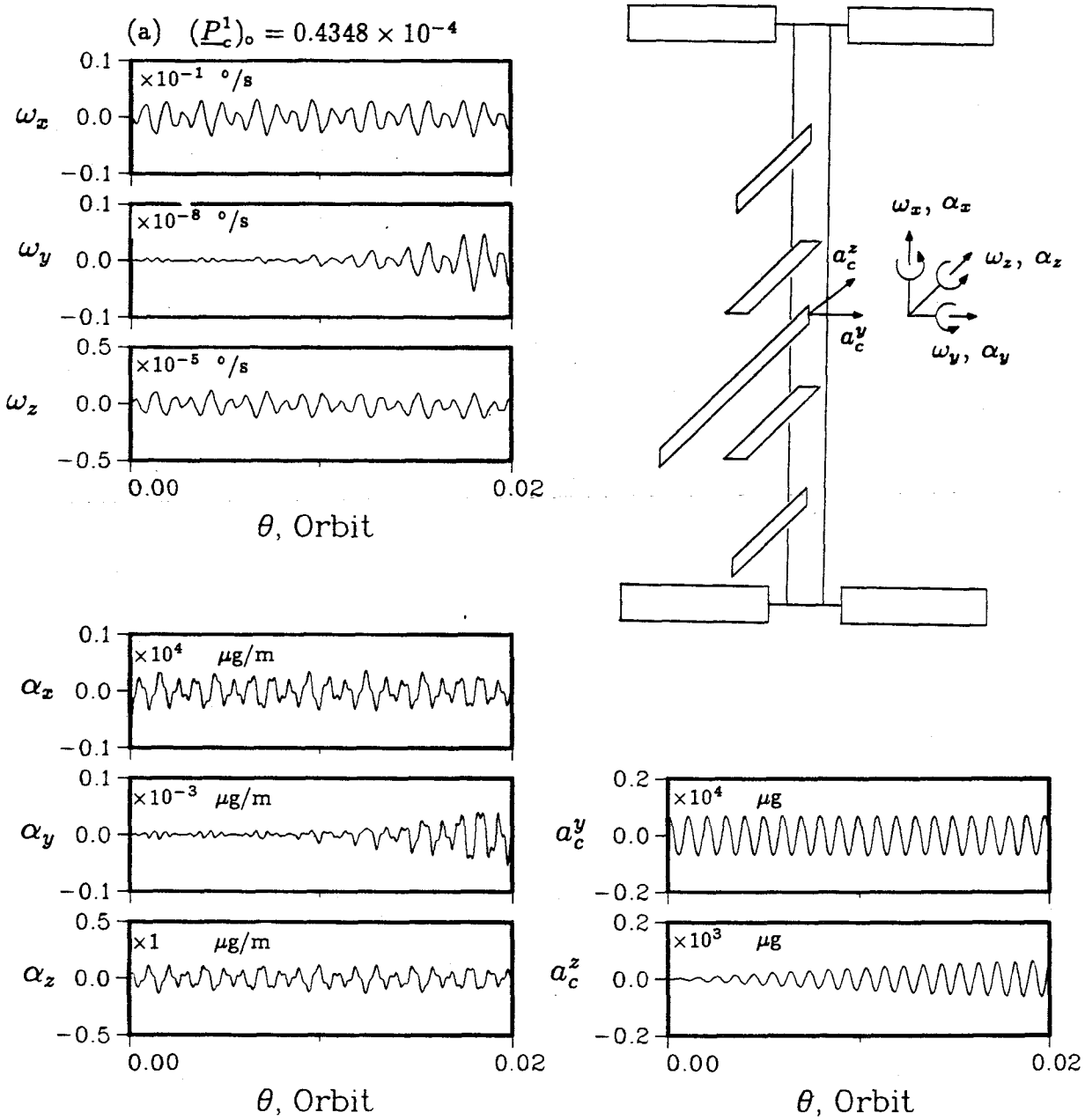

Figure 4-18 The effect of power boom and stinger disturbances on the PMC velocities and accelerations: (a) initial power boom tip displacement of 1 cm in the local vertical direction.

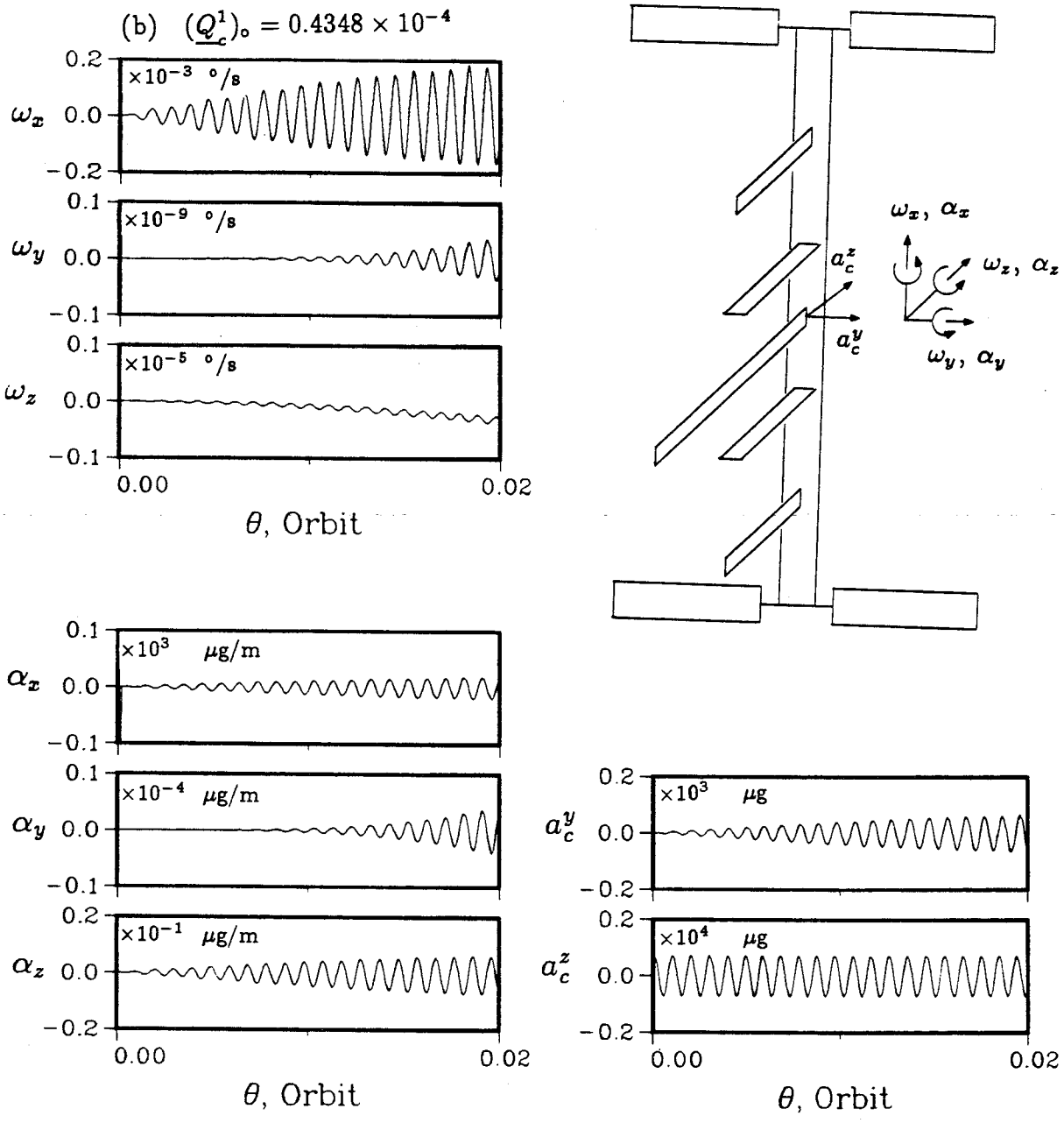

Figure 4-18 The effect of power boom and stinger disturbance on the PMC velocities and accelerations: (b) initial power boom tip displacement of 1 cm in the local horizontal direction.

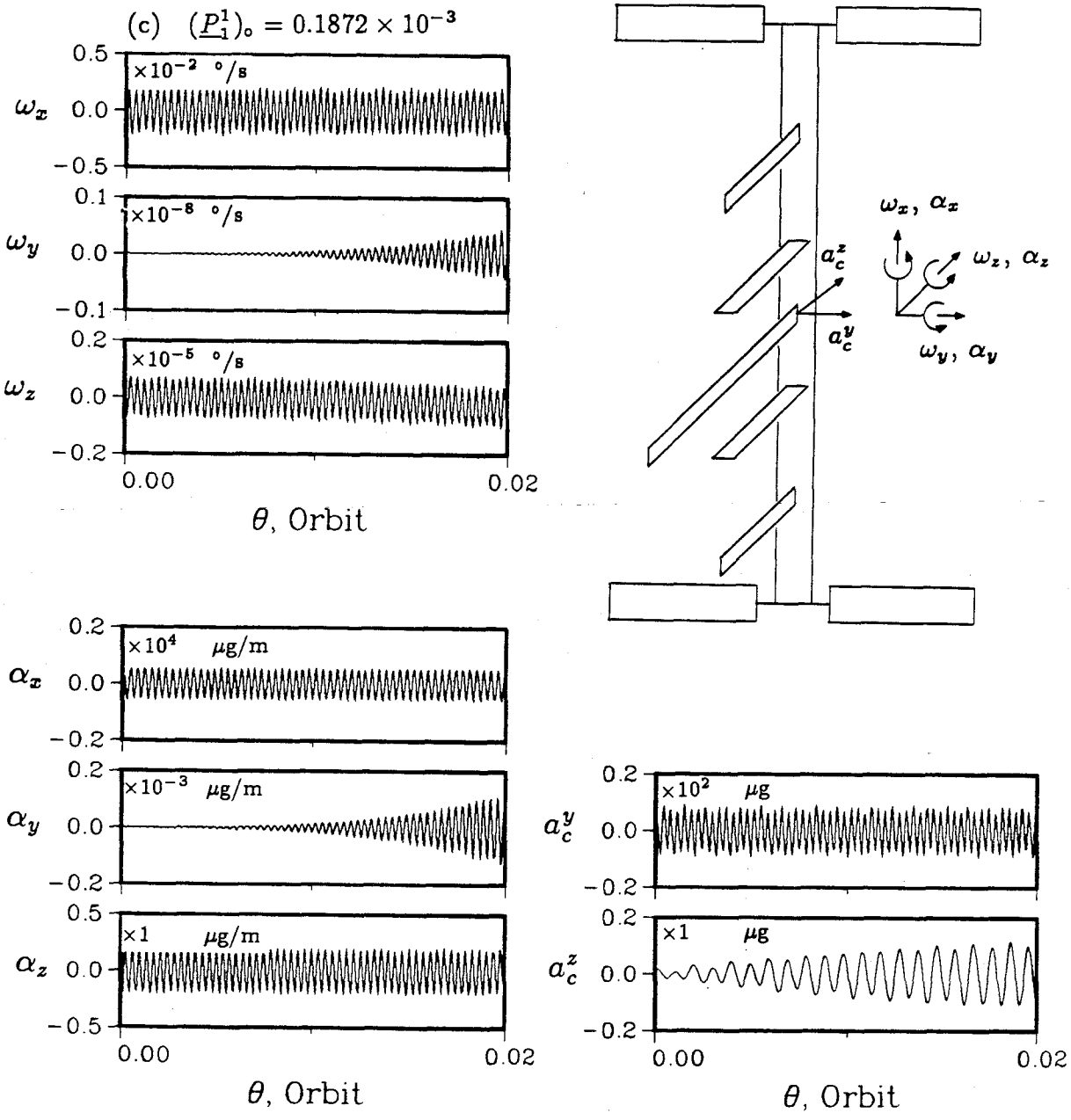

Figure 4-18 The effect of power boom and stinger disturbance on the PMC velocities and accelerations: (c) initial stinger tip displacement of 1 cm in the local vertical direction.

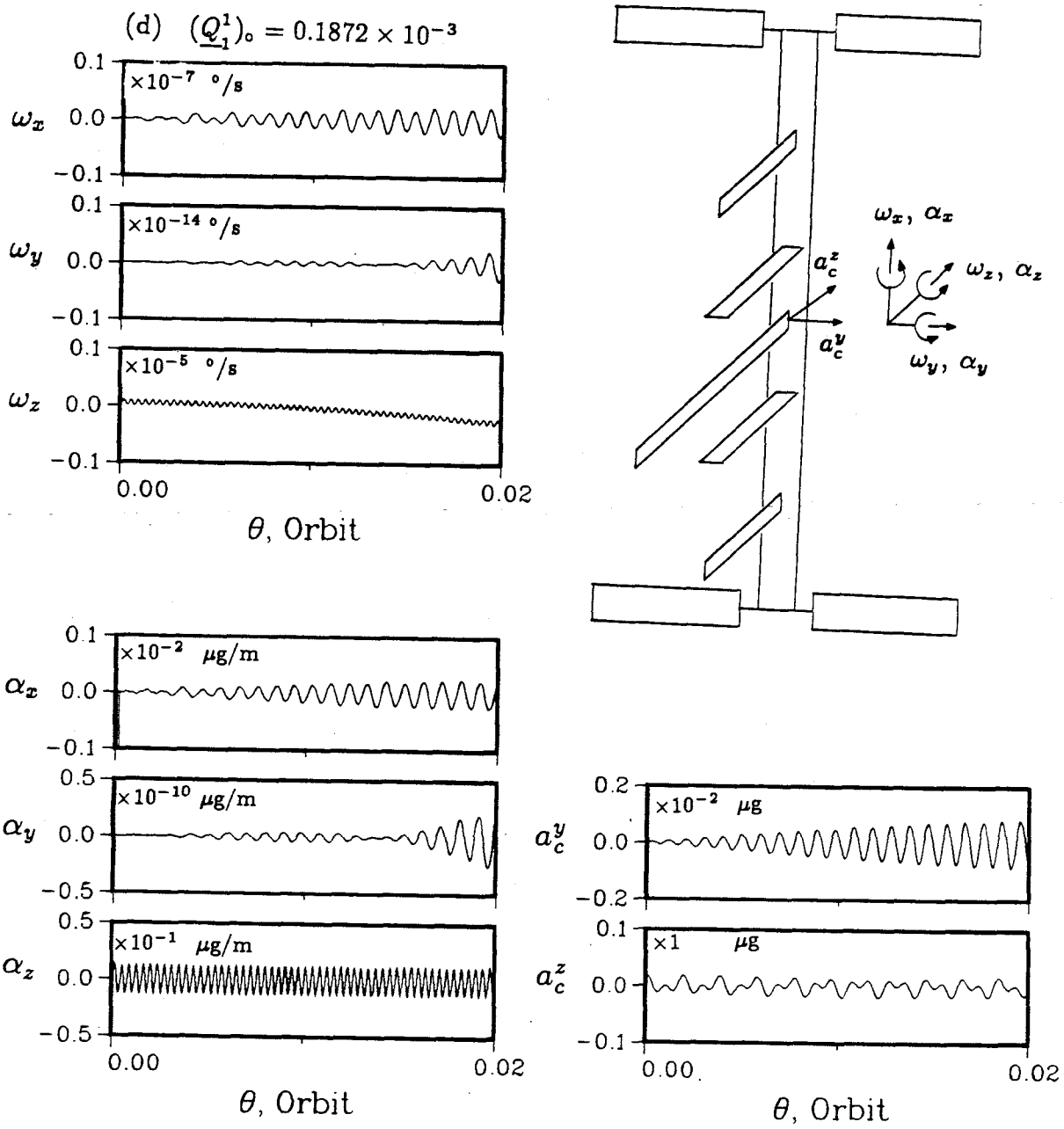

Figure 4-18 The effect of power boom and stinger disturbance on the PMC velocities and accelerations: (d) initial stinger tip displacement of 1 cm in the orbit normal direction.

Effects of station radiator, PV array and radiator disturbances on the PMC dynamics were presented earlier in Figure 4-14. The corresponding velocity and acceleration variations are shown in Figure 4-19 . Since the station radiator disturbance has virtually no effect on the PMC response (Figure 4-14a), the resulting velocities and accelerations are indeed small as shown in Figure 4-19a. Here, the maximum angular velocity, which is about the Z_c-axis, is only 3×10^{-7} °/s. The maximum angular acceleration, which is about the X_c-axis, is only 0.02 μg/m. Note also the beat type variations of velocity and acceleration about the Y_c-axis. The maximum acceleration at the power boom centre is about 1 μg and acts in the local horizontal direction. From Figure 4-14b, an initially deformed PV array radiator results in very small amplitudes of libration and vibration. Yet, the corresponding angular velocities and accelerations arising from such a disturbance barely meet the desired limit (Figure 4-19b). Although the magnitude of power boom acceleration is only 0.5 μg, the maximum angular velocity and acceleration, which are about X_c-axis, have magnitudes of 1×10^{-4} °/s and 10 μg/m, respectively. For the disturbance arising from the PV array, Figure 4-19c shows results to be relatively favorable compared to those in Figure 4-19b. Angular velocities and accelerations about the Y_c and Z_c-axes are about an order of magnitude smaller and the microgravity level at the boom centre is only 1 μg. On the other hand, α_x is about an order of magnitude higher than that in Figure 4-19b, and exceeds the specification.

As shown in Figure 4-15, the PV arrays subjected to even a small amount of thermal deformation can have a significant impact on the PMC response. The influence of thermal deformation on velocities and accelerations is shown in Figure 4-20a. A comparison with Figure 4-17 shows that the thermally deformed PV arrays have a significant influence on the angular velocities and accelerations about the X_c and Y_c-axes. Without the thermal deformation, the maximum ω_x and α_x are 1×10^{-8} °/s

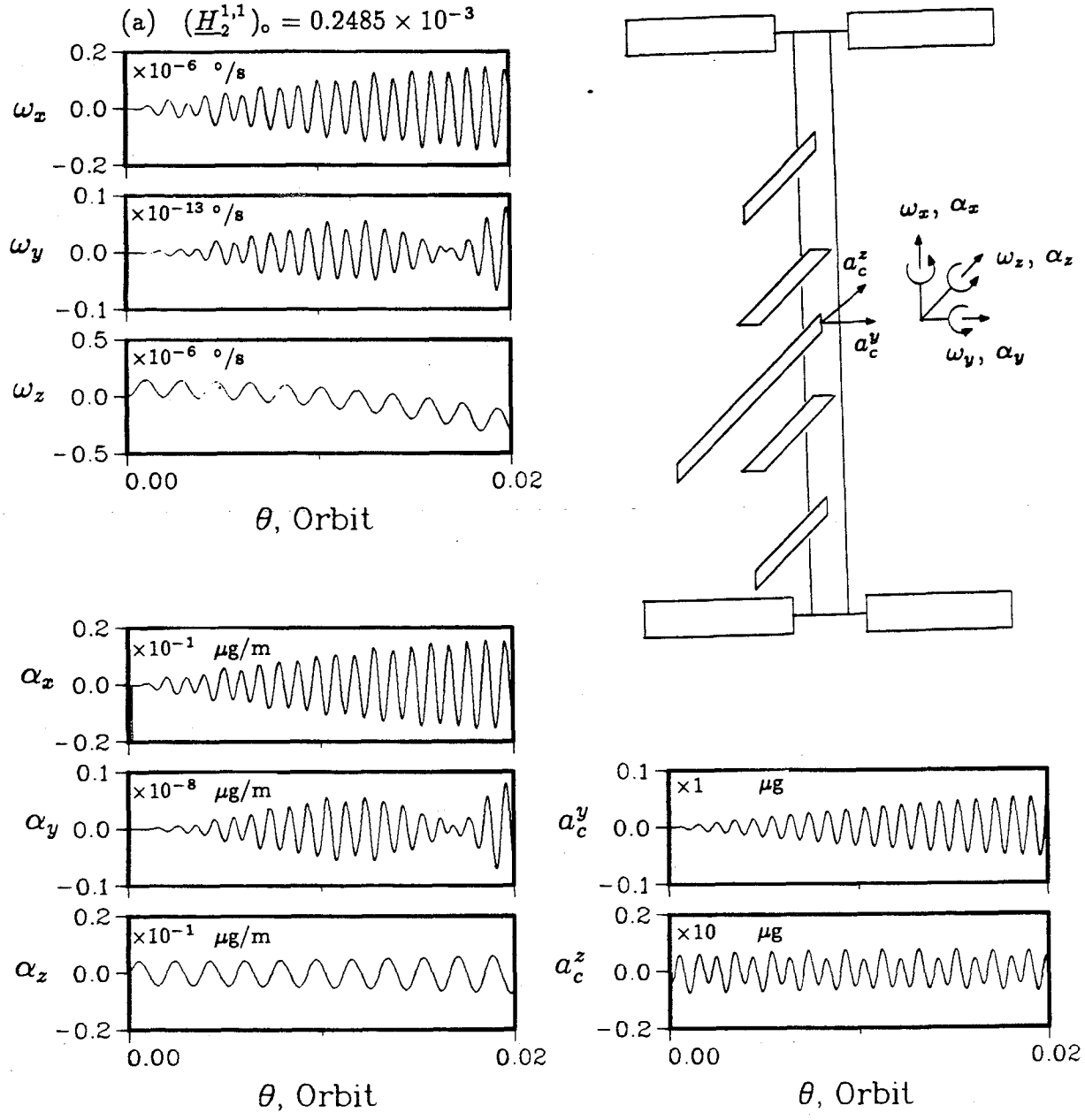

Figure 4-19 Variations of PMC velocities and accelerations showing the effect of station radiator, PV array and radiator disturbances: (a) station radiator with a tip deflection of 0.5 cm.

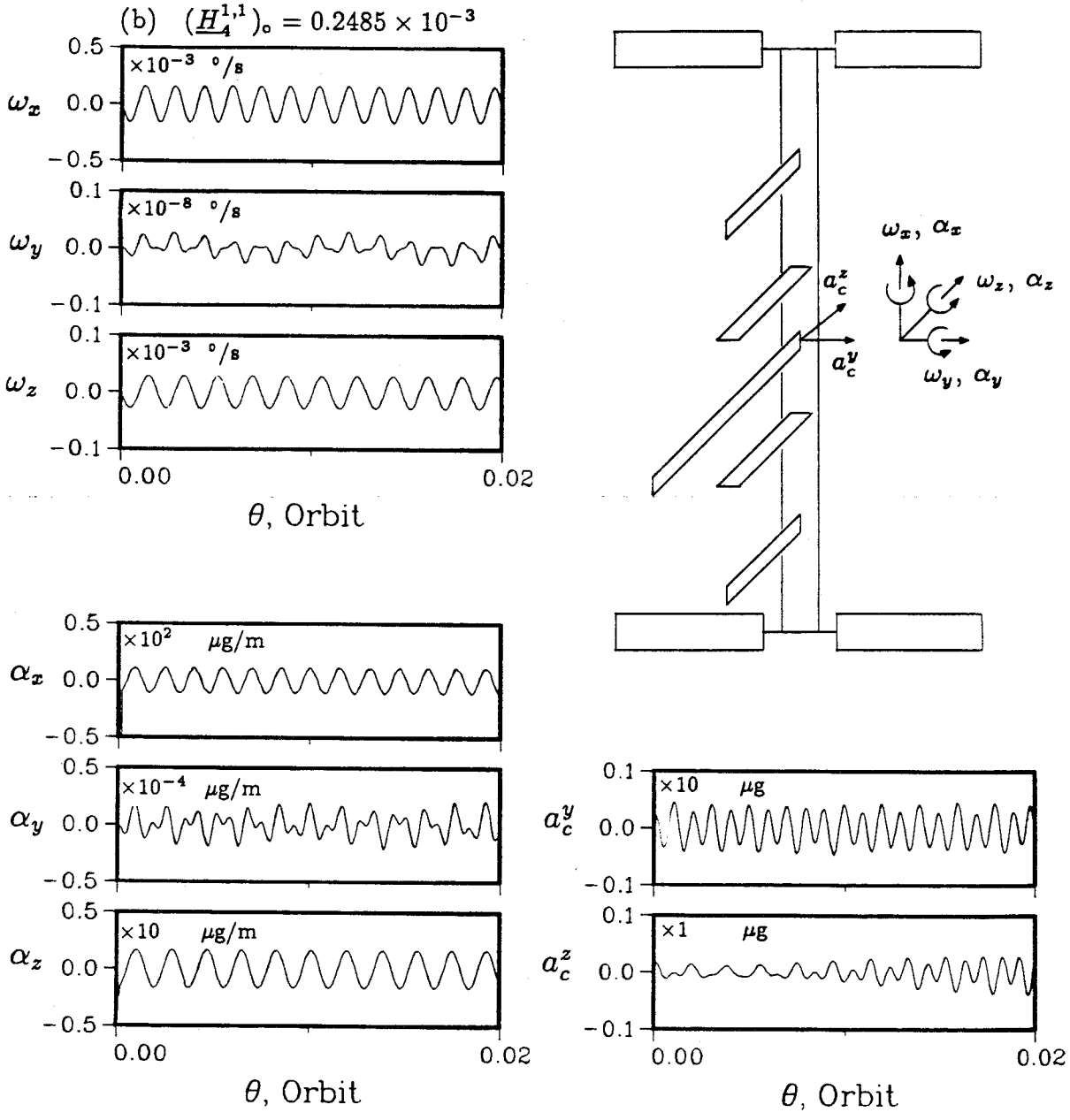

Figure 4-19 Variations of PMC velocities and accelerations showing the effect of station radiator, PV array and radiator disturbances: (b) PV array radiator with a tip deflection of 0.5 cm.

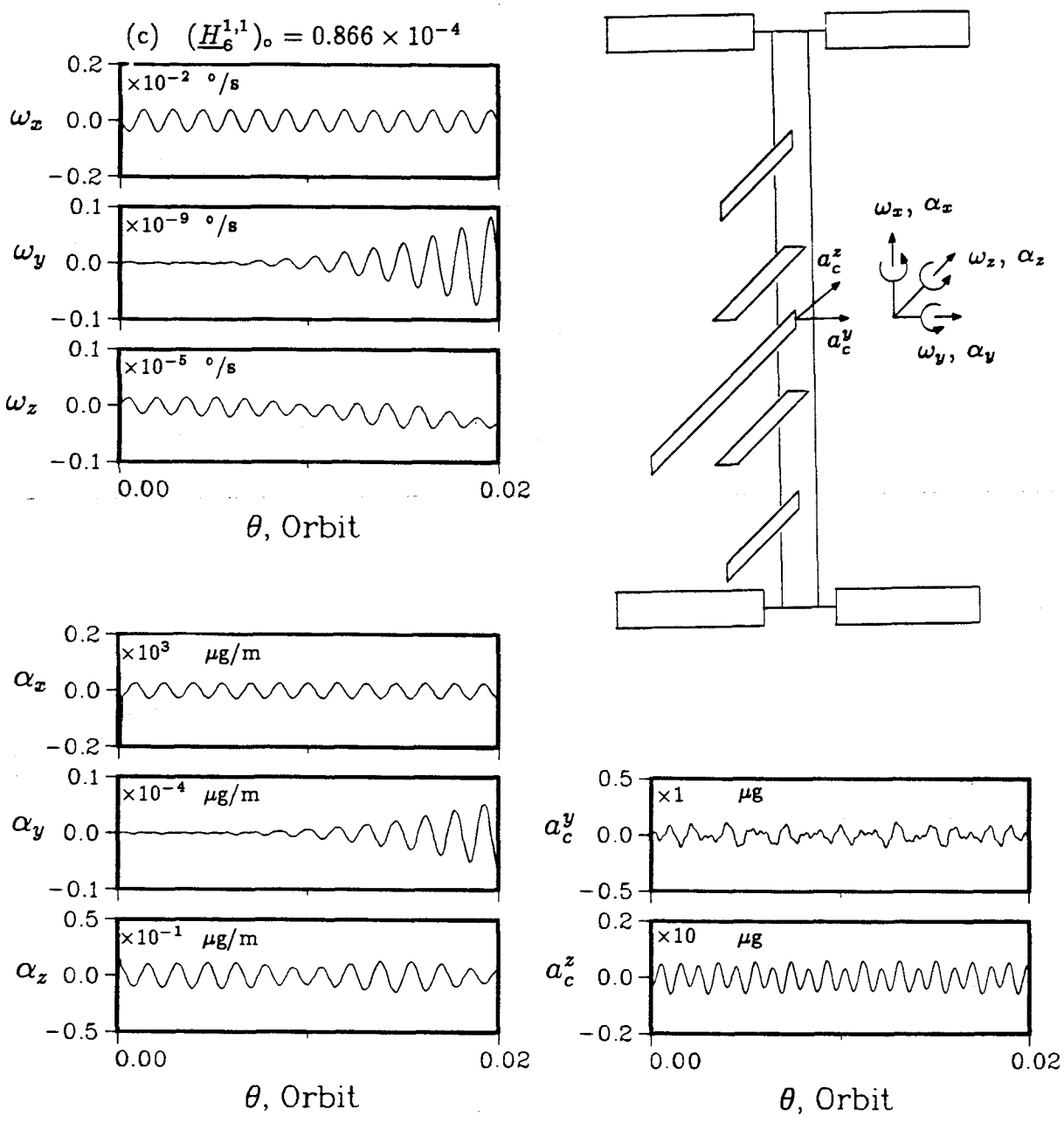

Figure 4-19 Variations of PMC velocities and accelerations showing the effect of station radiator, PV array and radiator disturbances: (c) PV array radiator with a tip deflection of 0.5 cm.

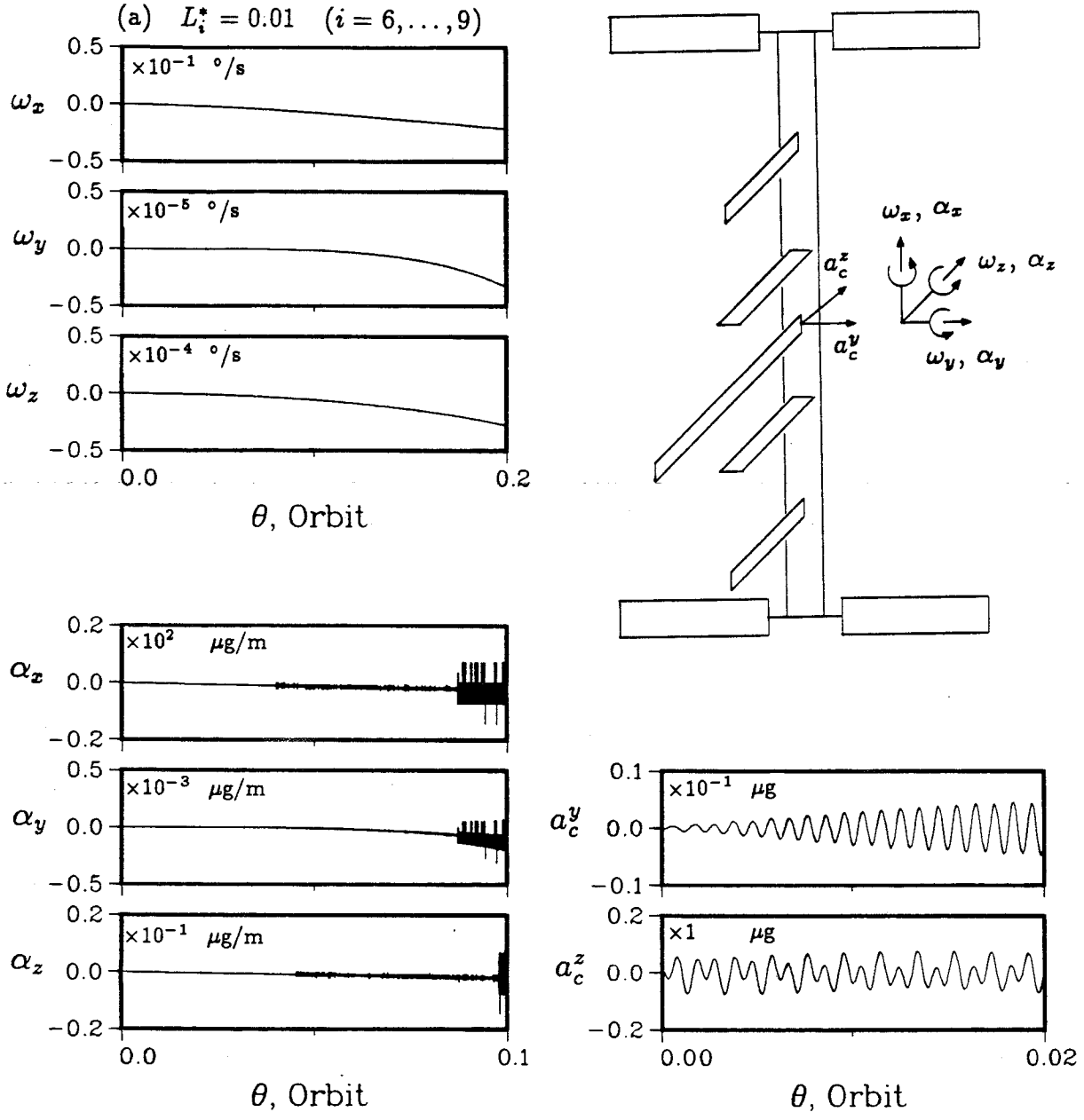

Figure 4-20 Influence of the thermal deformations and orbital eccentricity on the PMC velocities and accelerations: (a) thermally deformed PV arrays.

and 3×10^{-4} μg/m, respectively. With inclusion of the thermal deformation, the corresponding maximum magnitudes are 0.02 °/s and 10 μg/m, an increase of over 5 orders. The ω_z and α_z remain essentially unchanged while the microgravity level at the boom centre increases slightly.

The velocity and acceleration variations in an eccentric orbit ($\epsilon = 0.02$) are shown in Figure 4-20b. Recall from Figure 4-16 that eccentricity effects are limited to pitch and roll responses only. Indeed, Figure 4-20b shows that the power boom acceleration remains unchanged with a maximum value of 0.03 μg. As for angular velocities and accelerations, those about X_c and Y_c-axes show a large increase as compared to those in Figure 4-17 while ω_z registers only a small increase. Comparing with the thermal deformation case (Figure 4-20a), the eccentricity influence is about an order smaller; the maximum ω_x and α_x in eccentric orbit are 0.002 °/s and 0.3 μg/m, which are still within the permissible limit.

The results of Figures 4-17 to 4-20 provide valuable information pertaining to the velocity and microgravity environment of the PMC. The results indicate that the requirements on velocity and acceleration are stringent. With the system initially in the design configuration, the velocity and microgravity level stay within the design limit. However, even with a small disturbance applied to any flexible member in the local vertical or local horizontal direction, the system velocities and accelerations easily reach or exceed the acceptable value. A little thermal deformation of the PV arrays gives rise to angular velocities and accelerations above the specifications. On the other hand, a small orbit eccentricity does not adversely affect the system performance.

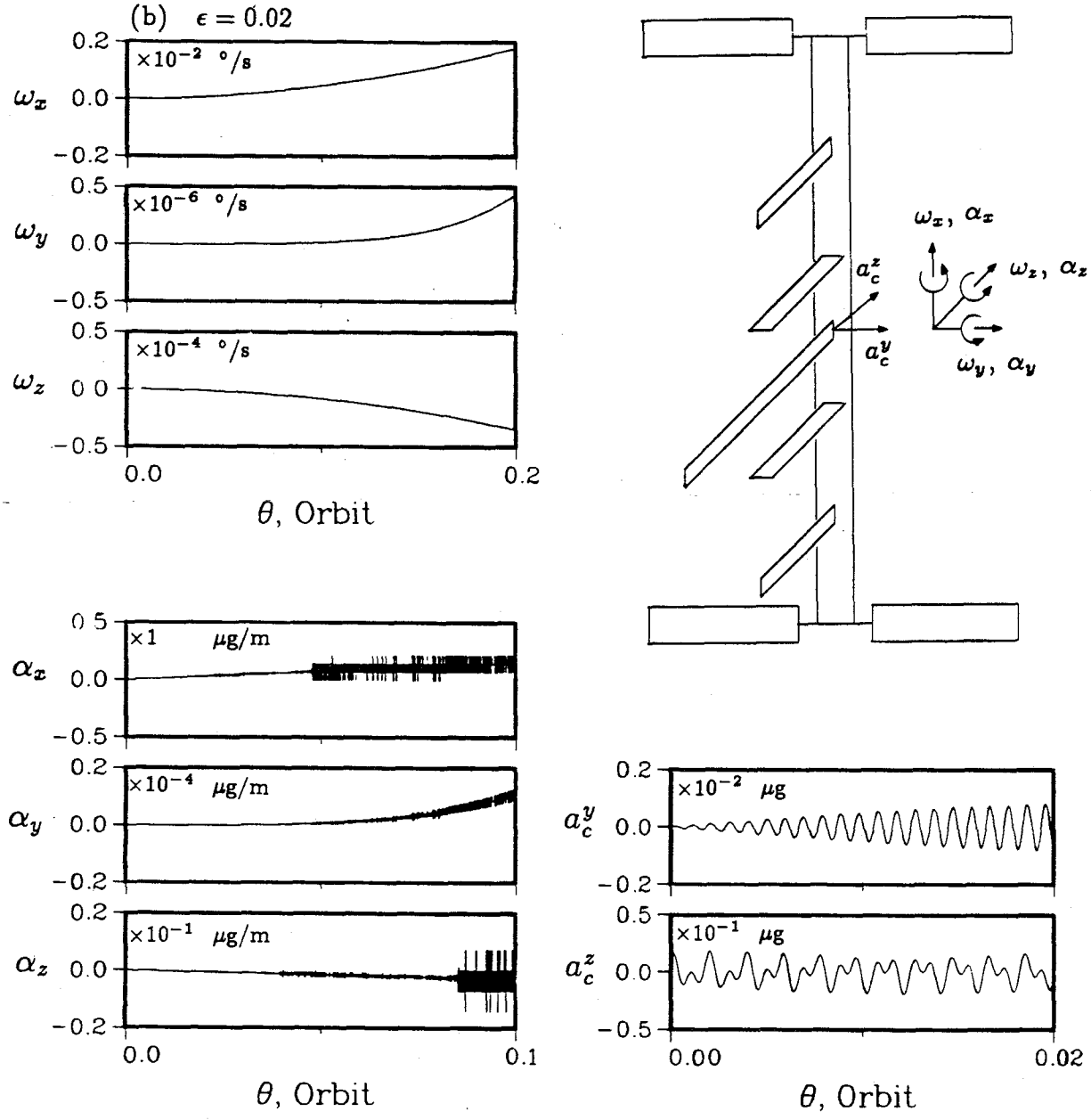

Figure 4-20 Influence of the thermal deformations and orbital eccentricity on the PMC velocities and accelerations: (b) orbital eccentricity ($\epsilon = 0.02$).

4.4 Mobile Servicing System

On board the space shuttle is a remote manipulator system designed mainly for satellite retrieval and release. A similar system, known as Mobile Servicing System (MSS), is planned for the Space Station. The MSS is essentially a two link manipulator attached to a mobile base which traverses along the station power boom. The functions of the MSS would not be limited to satellite retrieval and release. In fact, it is expected to be the workhorse for the station's construction, maintenance, operation, and future evolution.

The MSS, being flexible in the links as well as the joints, is an extremely complicated system to study. Chan [15] has investigated in details the dynamics and control of the MSS; however, the study is limited to the inplane maneuver case. The objective here is twofold: (i) to demonstrate versatility of the computer program through simulation of systems with slewing B_{ij} bodies; (ii) to explore system dynamics during general inplane (IP) and out-of-plane (OP) maneuvers of the manipulator. The following assumptions are used in the present study to have some appreciation of the complex system dynamics:

(i) joint flexibility is assumed to be negligible as compared to the link flexibility;

(ii) since the formulation does not consider translational motion, the MSS base is assumed to be stationary; however, the MSS can still be placed at an arbitrary position on the power boom;

(iii) in order to isolate effects of slewing maneuvers on the librational dynamics, the station is assumed to be a rigid body and in the stable gravity gradient orientation.

The numerical values used in the simulation correspond to those employed by Chan [15] and are listed in Table 4-3 .

Table 4-3 Data of the space station based MSS used in the simulation

Space Station (B_c)

m_c	=	240,120 kg	$(I_{xx})_c$	=	8×10^5 kg m^2
l_c	=	115.35 m	$(I_{yy})_c$	=	2.67×10^8 kg m^2
			$(I_{zz})_c$	=	2.67×10^8 kg m^2

Upper and Lower Links (B_1 and $B_{1,1}$)

m_1	=	$m_{1,1}$	=	1,800 kg	$(I_{xx})_1$	=	$(I_{xx})_2$	=	101 kg m^2
l_1	=	$l_{1,1}$	=	7.5 m	$(I_{yy})_1$	=	$(I_{yy})_2$	=	33,750 kg m^2
f_1^1	=	$f_{1,1}^1$	=	0.03 Hz	$(I_{zz})_1$	=	$(I_{zz})_2$	=	33,750 kg m^2

The simulation is based on a 100 minute orbit using the coordinate systems shown in Figure 4-21 . Considering only the first mode of vibration, the generalized coordinates are:

$$q = \psi\,,\ \phi\,,\ \lambda\,,\ \underline{P}_1^1\,,\ \underline{Q}_1^1\,,\ \underline{P}_{1,1}^1\,,\quad \text{and}\quad \underline{Q}_{1,1}^1\,,\qquad \text{hence,}\qquad N_q = 7\,.$$

It is desirable to undertake a slewing maneuver with zero velocity and acceleration at the beginning and the end of the maneuver. The present simulation uses a sine-ramp function which has the required characteristic:

$$\alpha_{sl} = \begin{cases} \alpha_m\theta/\tau_{sl} - (\alpha_m/2\pi)\,sin\big(2\pi\theta/\tau_{sl}\big) & \text{for } \theta \le \tau_{sl}\,; \\ \alpha_m & \text{for } \theta > \tau_{sl}\,. \end{cases} \tag{4.4}$$

where α_{sl} and α_m are the slew angle and its maximum value, respectively; τ_{sl} is the slewing period; and θ is the true anomaly. Effect of the slewing period on the system response is shown in Figures 4-22 to 4-24. Here, the lower link is assumed to undergo a 180° maneuver in 5, 7.5, and 10 minutes. For each of the slewing periods, performance of the system is compared when subjected to two distinct maneuvers: the OP (out-of-plane) and IP (inplane) maneuvers. In the former case, the maneuver

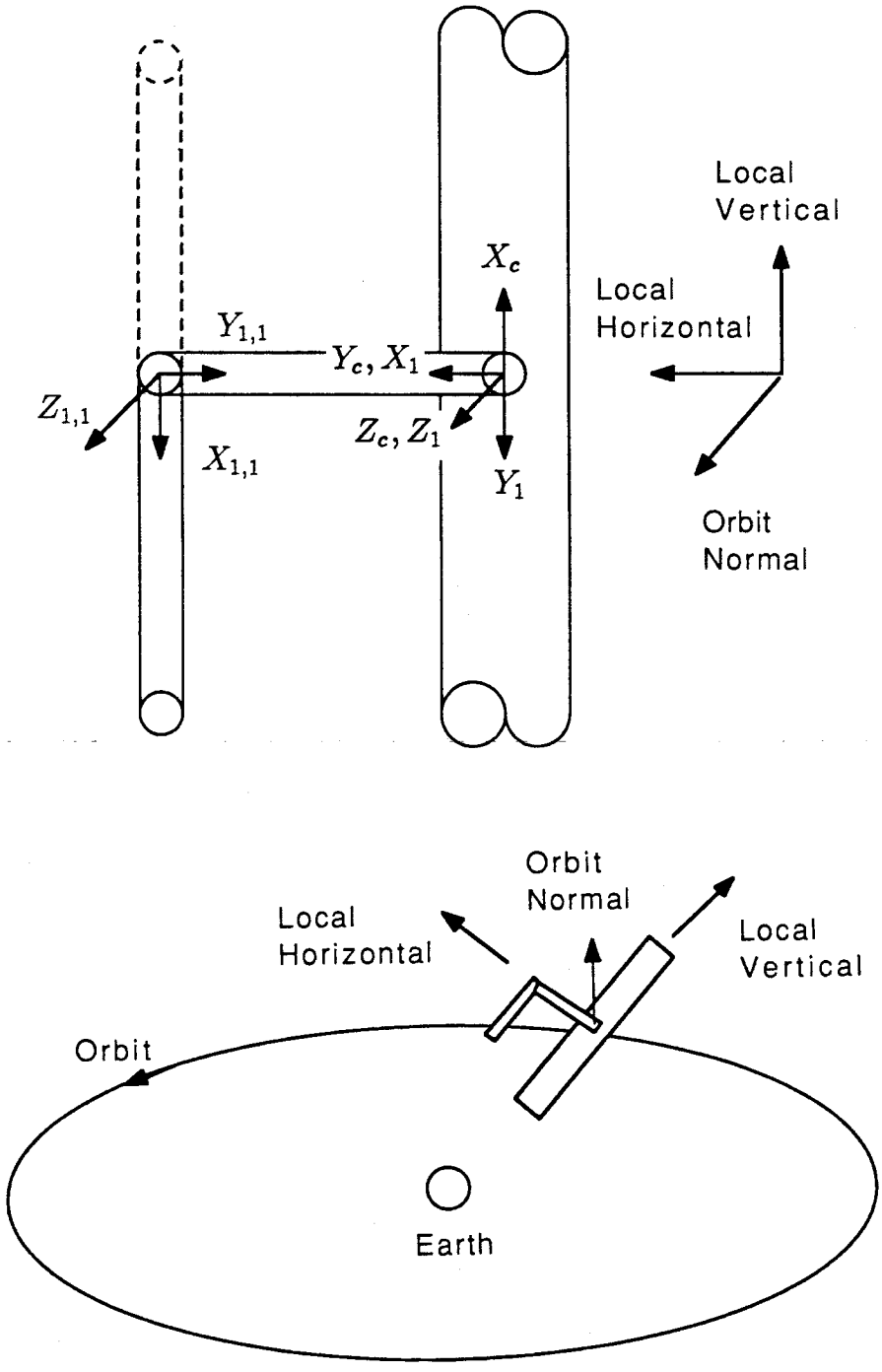

Figure 4-21 Coordinate systems and design configuration used in the simulations of MSS slewing maneuvers.

is about the $Y_{1,1}$-axis resulting in the link traversing in a plane normal to the orbital plane. In contrast, the link rotates about the $Z_{1,1}$-axis and travels in the orbital plane in the latter case.

The system response when subjected to a 5-minute maneuver of the lower link is shown in Figure 4-22. For the OP maneuver, all the libration degrees are excited with the yaw amplitude increasing most rapidly. With such a fast maneuver, the flexible links experience large deflections during the maneuver. The maximum deflections for the upper and lower links are 33.3 cm and 9.5 cm, respectively. With the IP maneuver, Figure 4-22b shows that only the pitch librational motion is excited with a slightly higher amplitude than that of the OP case. In addition, the pitch response shows high frequency modulations corresponding to the flexible member's frequency. The flexible members experience unacceptably high tip deflections of 62.4 cm and 17.0 cm for the upper and lower links, respectively.

As the maneuver time increases from 5 to 7.5 minutes, Figure 4-23 shows improvements in the system response. With the OP maneuver (Figure 4-23a), the yaw motion is still significant; however, maximum tip deflections of the upper and lower links have decreased to 11.4 cm and 3.4 cm, respectively. Similarly, the IP maneuver case shows reductions in tip deflections to 19.2 cm and 4.6 cm, for the upper and lower links, respectively. Notice also the disappearance of the high frequency modulations in the pitch motion (Figure 4-23b).

As the maneuver period is increased to 10 minutes (Figure 4-24), further reductions in tip deflections is apparent. After 0.25 orbit, Figure 4-24a shows that the yaw amplitude reaches 6.6°. This is lower than that observed before (8.2° for 5-minute maneuver and 7.2° for 7.5-minute maneuver); however, it is still significantly higher than the pitch or roll motion. The maximum tip deflections for the upper link is

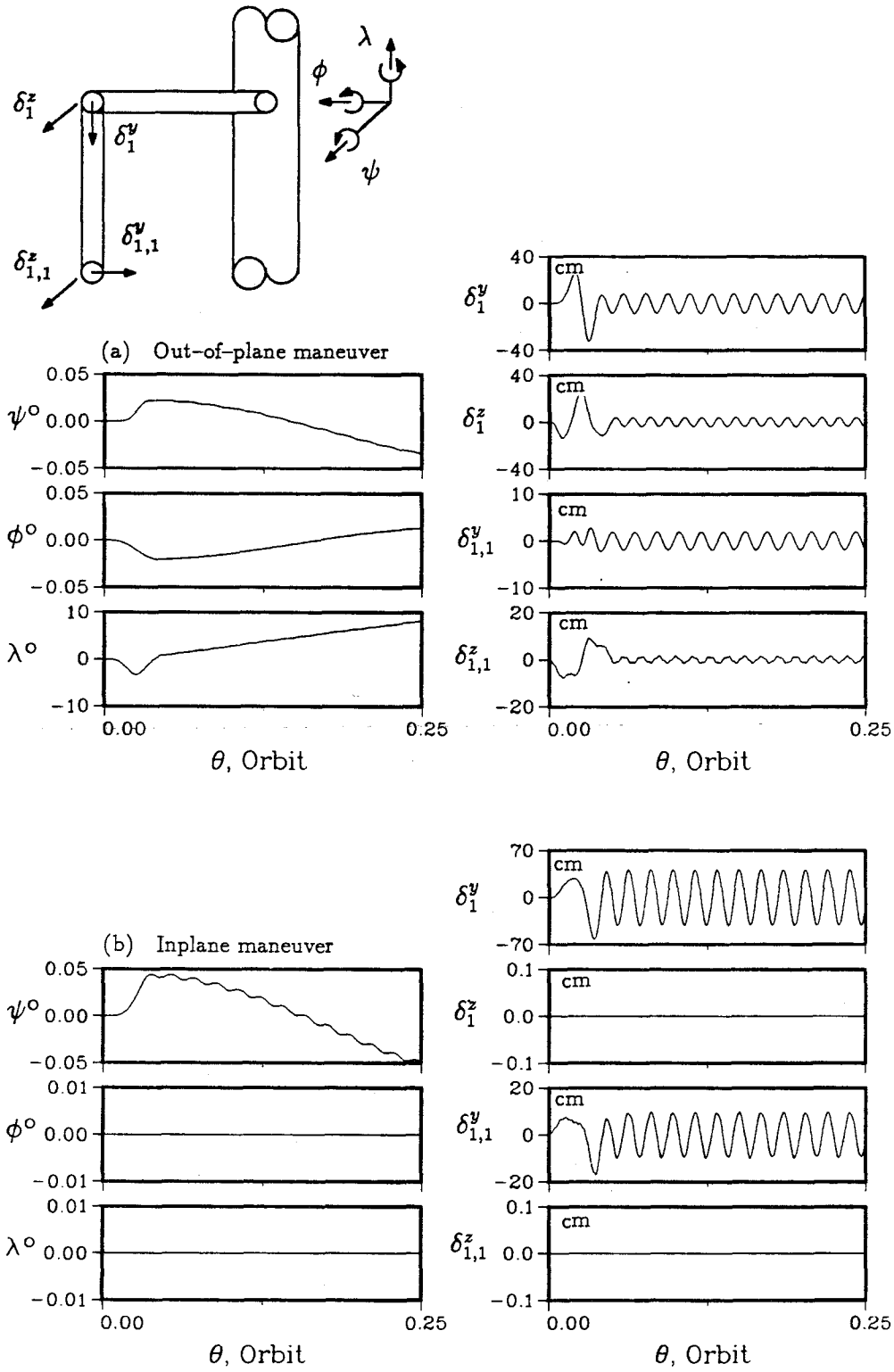

Figure 4-22 System response with the lower link of the MSS undergoing a 180° maneuver in 5 minutes: (a) out-of-plane maneuver; (b) inplane maneuver.

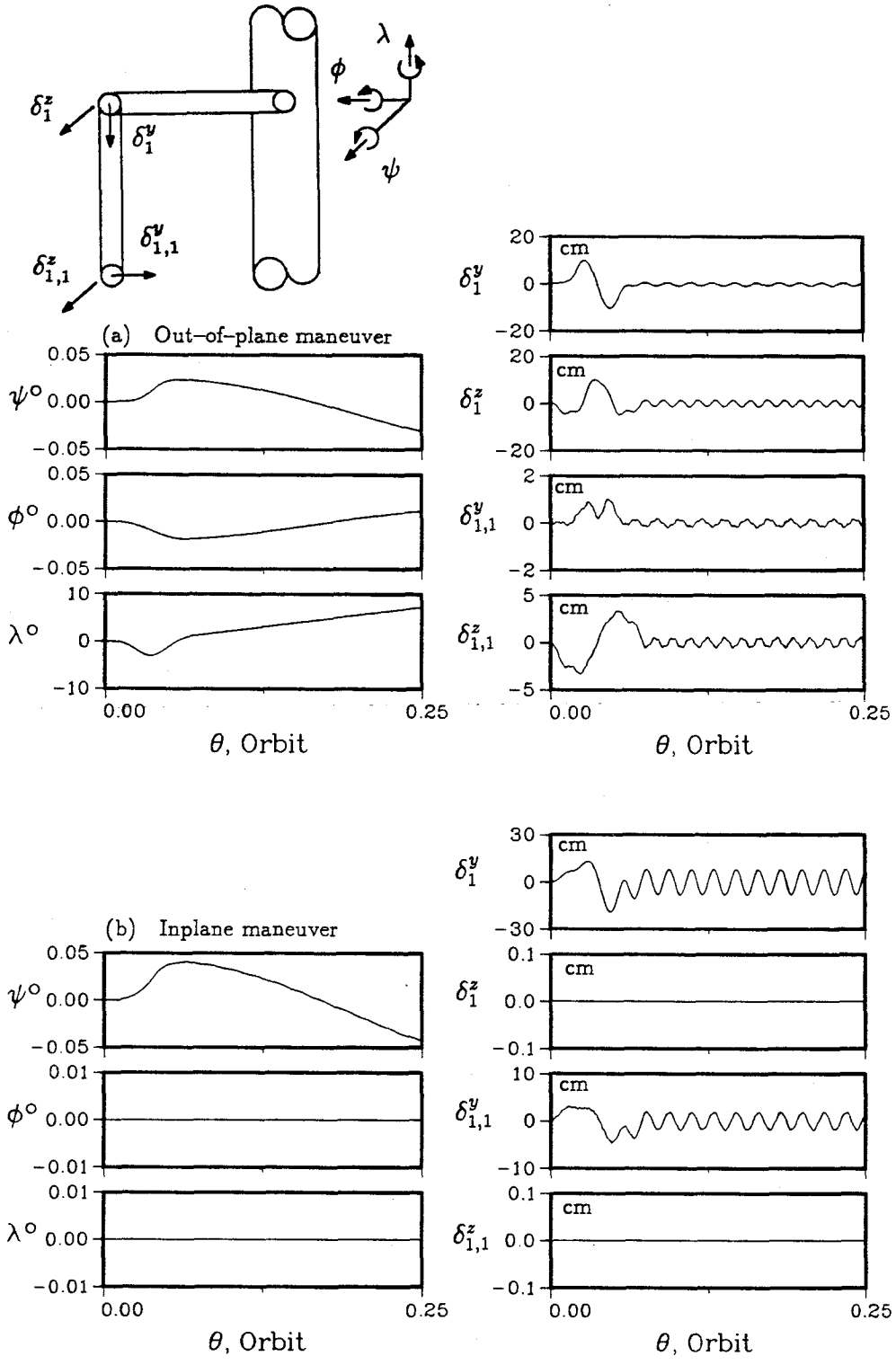

Figure 4-23 Forced oscillations of the space station showing the effect of a 180° maneuver in 7.5 minutes of the lower link of the MSS: (a) out-of-plane maneuver; (b) inplane maneuver.

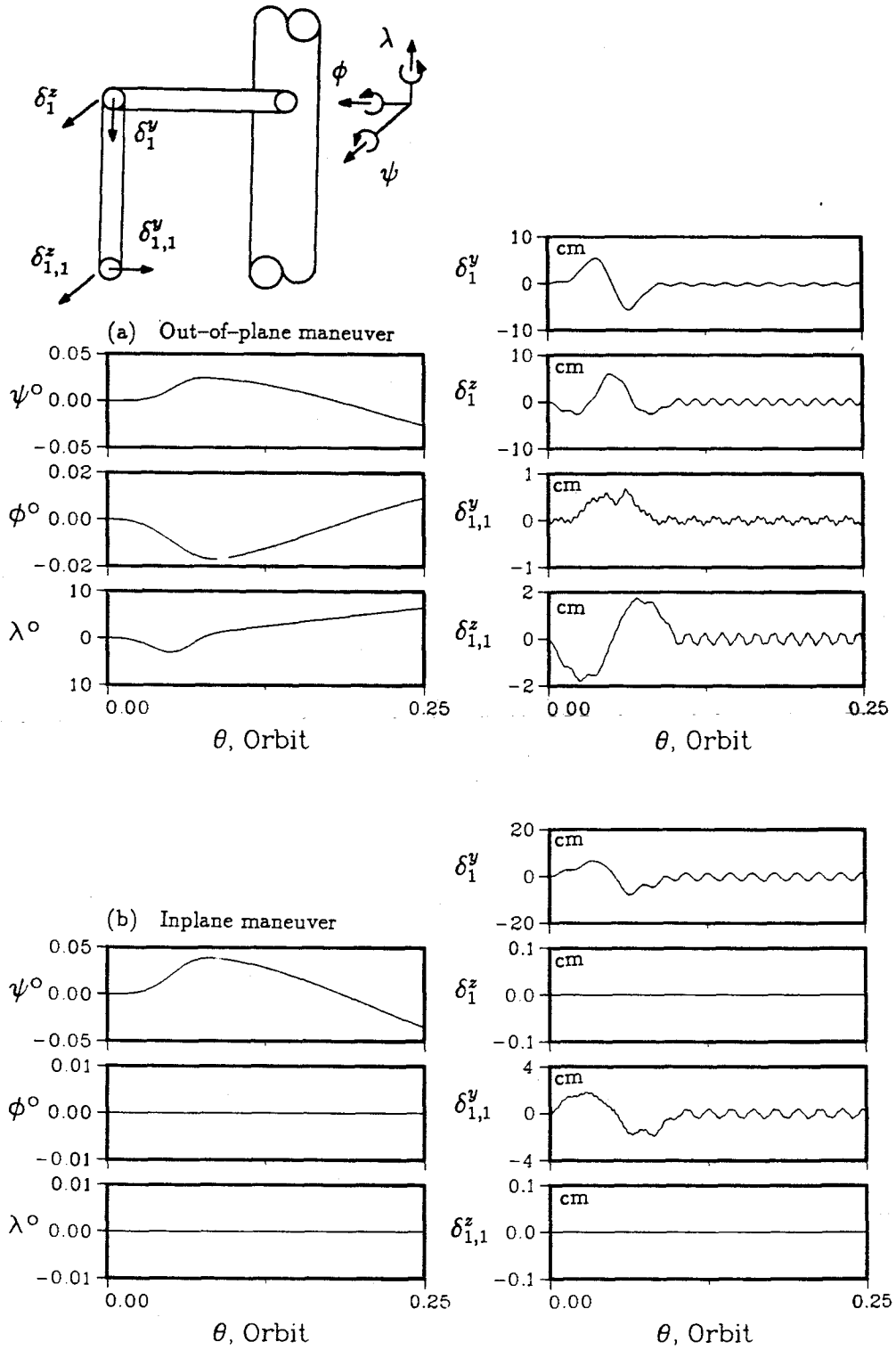

Figure 4-24 Response of the space station with the MSS subjected to a 180° maneuver of the lower link in 10 minutes: (a) out-of-plane maneuver; (b) inplane maneuver.

6.3 cm and only 1.8 cm for the lower link. For the IP maneuver, there is no significant reduction in the pitch motion (Figure 4-24b). In contrast, the maximum link deflections reduce to 7.9 cm (upper link) and 1.9 cm (lower link).

Simulation results in Figures 4-22 to 4-24 indicate that the OP maneuver results in relatively smaller tip deflections of the links. However, it excites a large amplitude yaw motion. Since the primary function of a manipulator is to position a payload at a desired location, it would be useful to investigate the resulting pointing errors due to the maneuver. A suitable reference for measuring the error would be the orbital frame, X_s,Y_s,Z_s. With this as reference, errors due to flexible deflections as well as rigid body libration must be accounted for. The 180° maneuver as before is considered. With respect to X_s,Y_s,Z_s axes, the tip of the manipulator ideally (i.e., in absence of librational and flexibility errors) travels from a point with coordinates (0, −7.5 m, 7.5 m) to the destination with coordinates (0, 7.5 m, 7.5 m). Let the coordinates of the manipulator tip be (s_x, s_y s_z) and define the errors in distance to be S_x, S_y, and S_z in X_s, Y_s, and Z_s directions, respectively, then

$$
\begin{aligned}
S_x &= s_x \,; \\
S_y &= 7.5 - s_y \,; \\
S_z &= 7.5 - s_z \,; \\
\text{and} \qquad S_{tot} &= \sqrt{S_x^2 + S_y^2 + S_z^2} \,.
\end{aligned}
\tag{4.5}
$$

Using the results in Figures 4-22 to 4-24, Figure 4-25 shows the variation of errors with maneuver time and path. The results of Figure 4-25a corresponds to the maneuver of Figure 4-22. Notice that S_x, S_y, and S_z are, in general, oscillatory due to vibratory character of the link response. For the rigid body motion, the mean values of S_x, S_y, and S_z are not necessarily constant. For the OP maneuver, effect of the

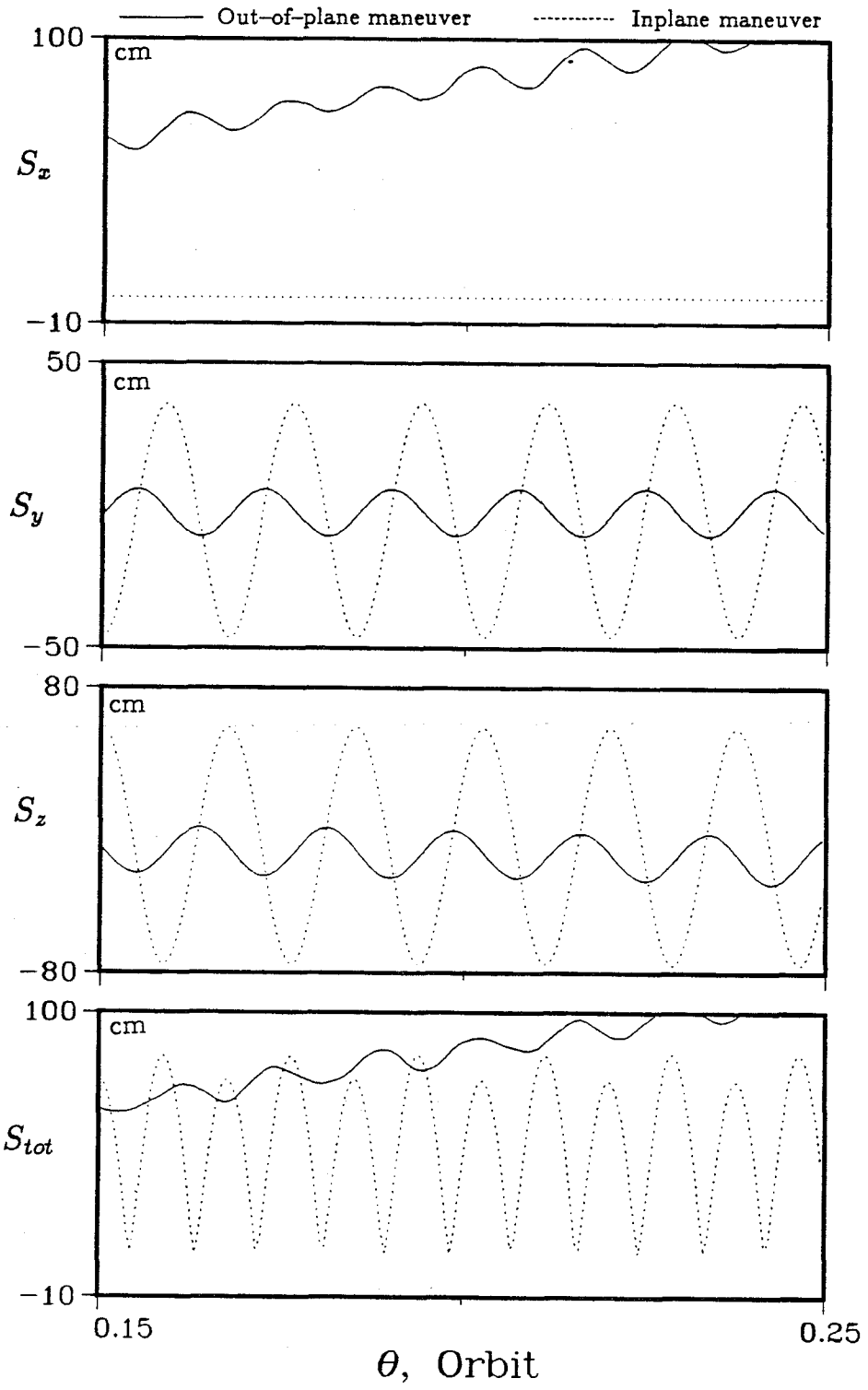

Figure 4-25 Effect of the maneuver time on the pointing error with the lower link slewing through 180°: (a) 5-minute maneuver.

large yaw motion can be seen in the rapidly increasing amplitude of S_x. At the end of 0.25 orbit, S_x has a mean value of over 1 m with an oscillatory contribution of 14.5 cm peak-to-peak (p-p) superposed on it. Due to small amplitudes of pitch and yaw, S_y and S_z variations remain fairly constant with p-p amplitudes of 16.4 cm and 25.6 cm, respectively. For the IP maneuver, since the yaw motion is not excited, S_x remains zero. However, the large link deflections result in prohibitively large magnitudes of S_y and S_z with p-p amplitudes of 82.3 cm and 132.6 cm, respectively. Although the OP maneuver results in smaller errors in the Y_s and Z_s directions, it leads to a large error in the X_s direction. At the end of 0.25 orbit, the manipulator is 103.4 cm off the target and the error is still increasing. On the other hand, the IP maneuver results in a mean error of 40.9 cm.

As the maneuver time increases to 7.5 minutes (Figure 4-25b), there is a significant improvement in S_y and S_z for both the maneuvers. The p-p amplitudes of S_y and S_z have reduced to 1.3 cm and 2 cm, respectively whereas the corresponding values are 16 cm and 25.8 cm for the IP maneuver. However, the yaw motion for the OP maneuver remains large resulting in a large error in the orbit normal direction; hence, S_{tot} attains a magnitude of 94.4 cm after 0.25 orbit. In the IP maneuver case, the mean value of the total error has dropped from 40.9 cm to 14.7 cm. As the maneuver time further increases to 10 minutes (Figure 4-25c), the IP maneuver error shows further improvement. The difference in the p-p amplitudes of S_y and S_z between the two maneuvers is now relatively small. For instance the p-p amplitude of S_y is 0.5 cm for the OP maneuver and 3.3 cm for the IP slew case. The major difference between the two cases is the large amplitude of S_x resulting from the yaw motion in the OP maneuver. Consequently, the mean pointing error in the IP case is only 9.5 cm at the end of 0.25 orbit compared to 86 cm for the OP slew.

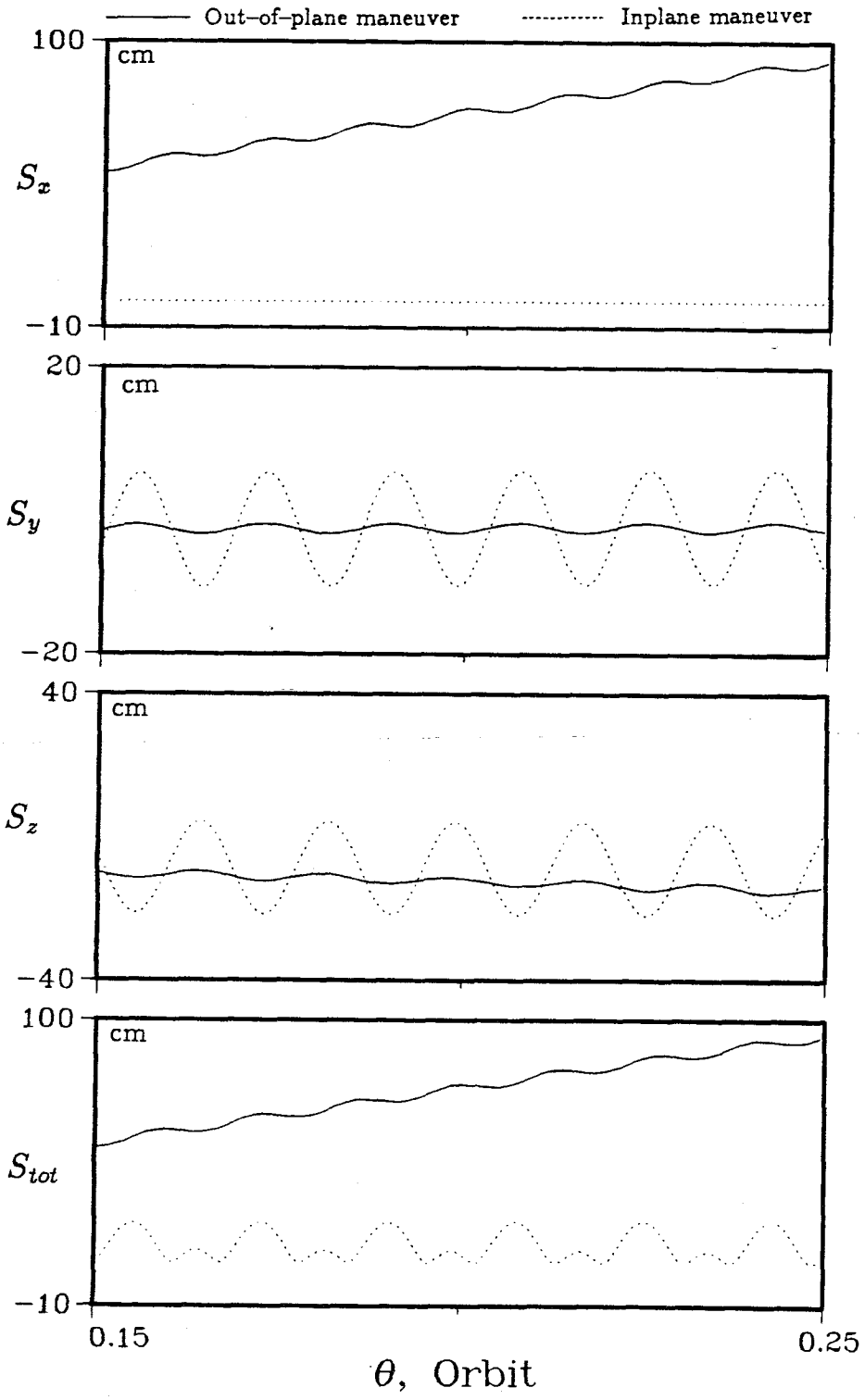

Figure 4-25 Effect of the maneuver time on the pointing error with the lower link slewing through 180°: (b) 7.5-minute maneuver.

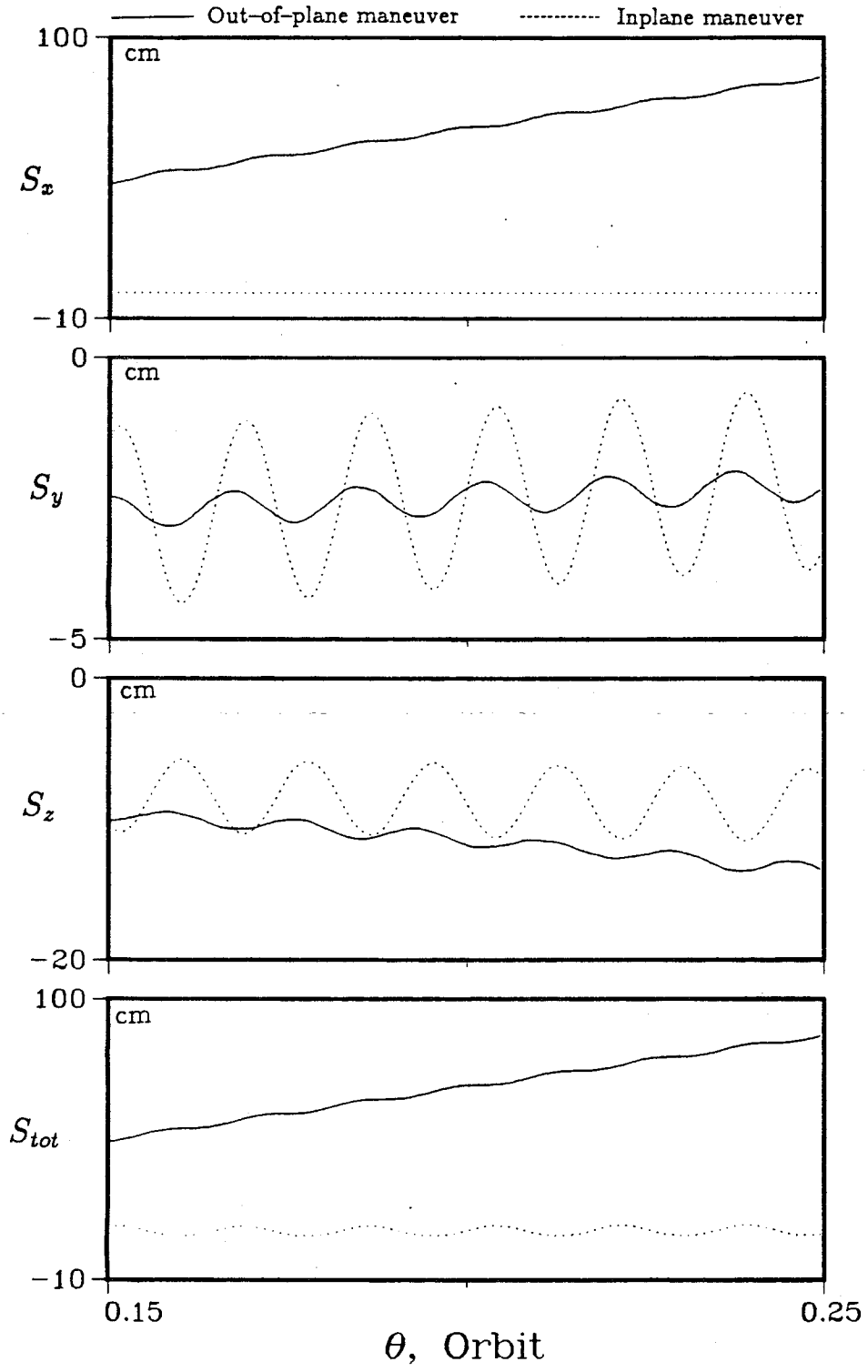

Figure 4-25 Effect of the maneuver time on the pointing error with the lower link slewing through 180°: (c) 10-minute maneuver.

The manipulator is now moved 50 m in the X_c direction from the central body's c.m. The effect of this offset on the system performance is shown in Figures 4-26 and 4-27 . Using a 10-minute maneuver, Figure 4-26 shows that the OP case results in increase in pitch and roll amplitudes; whereas the yaw response remains the same as before. The maximum tip deflections also increase for both the links; from 6.3 cm to 10.4 cm for the upper link and from 1.8 cm to 3.1 cm for the lower link. These observations remain valid, in general, for the IP maneuver; the pitch motion increases in amplitude and so does the flexible links.

Due to the increased librational motion, the pointing accuracy deteriorates for both the IP and OP maneuver cases (Figure 4-27). For the OP maneuver, since the yaw motion is unaffected by the manipulator offset, the pointing error in X_s direction remains the same as before. With the increase in the pitch motion, the variation of S_y and S_z is similar to S_x, i.e. the absolute mean values of S_y and S_z increase with time. Also, the increase in the link deflections results in larger p-p amplitudes of S_y and S_z. In the present case, they amount to 5 cm and 5.5 cm, respectively. Similar trends of S_y and S_z variations can be observed for the IP maneuver. It is interesting to note that the p-p amplitudes for S_y and S_z, 3 cm and 2.7 cm, respectively, are smaller than those for the OP maneuver. However, this is not enough to offset the effect of rigid body motion. At the end of 0.25 orbit, both maneuvers have poor pointing accuracy; the IP maneuver is 95.9 cm off the target whereas the OP maneuver has an error of 126.7 cm.

Effect of increased link stiffness on the system performance is studied in Figures 4-28 and 4-29 . The links are assumed to have the stiffness doubled and the lower link is undergoing a 180° maneuver in 5 minutes. With this fast maneuver, a comparison between Figures 4-22 and 4-28 shows that there is no apparent improvement in the

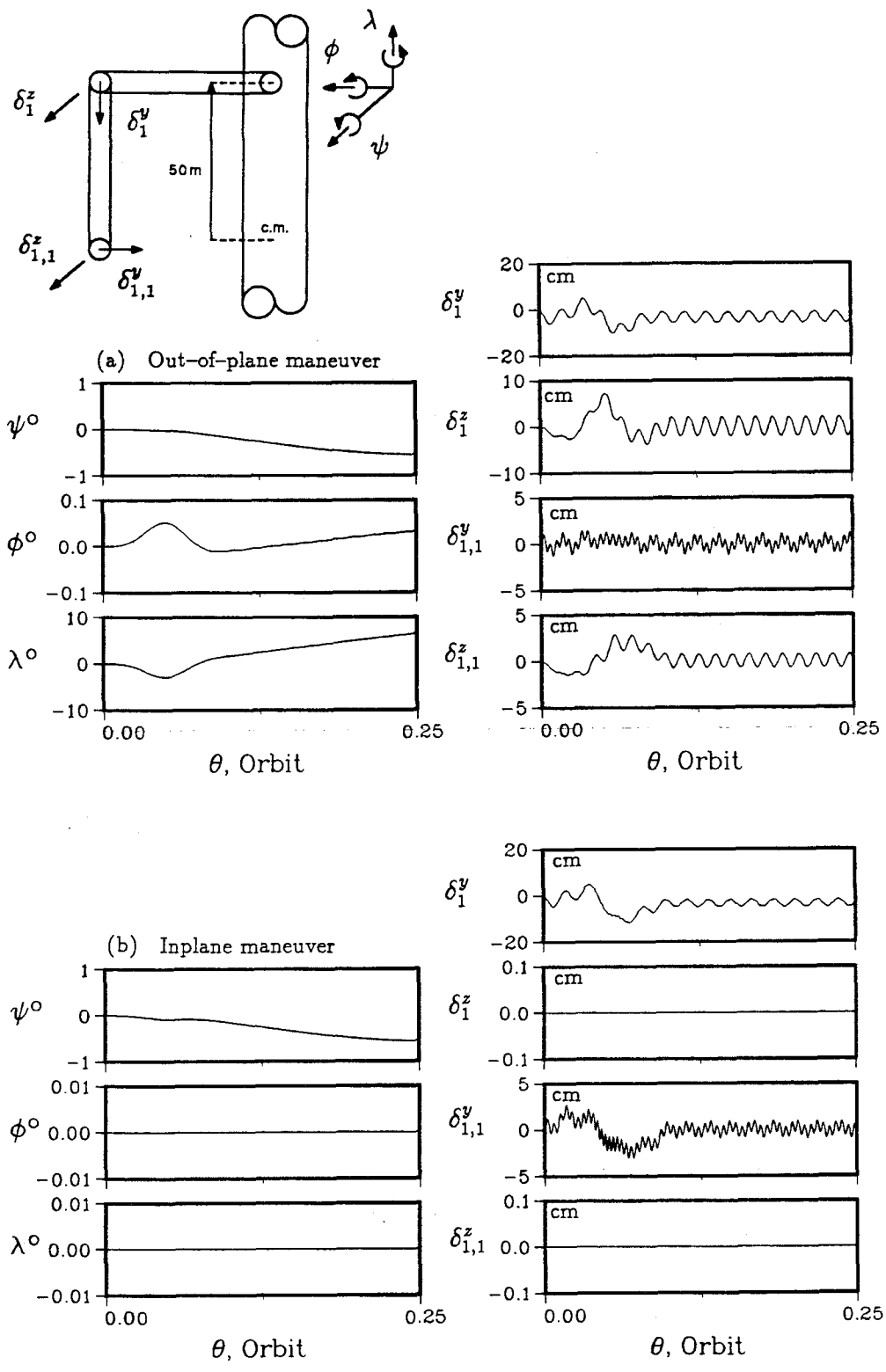

Figure 4-26 Dynamical response of the space station with the MSS located 50 m from the central body c.m.: (a) out-of-plane maneuver; (b) inplane maneuver.

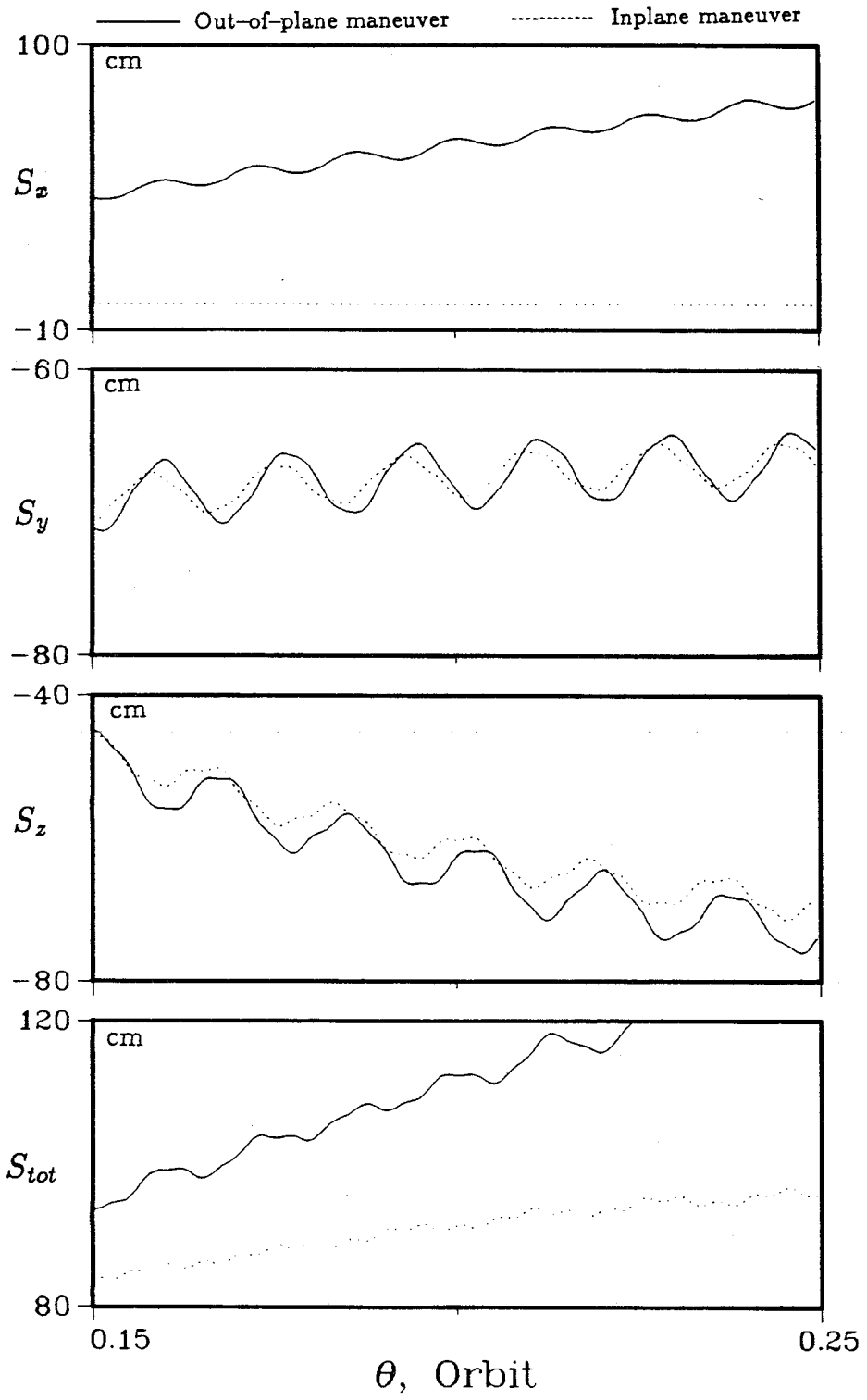

Figure 4-27 Pointing error of the MSS, located 50 m from the central body c.m., with the lower link undergoing a 180° maneuver.

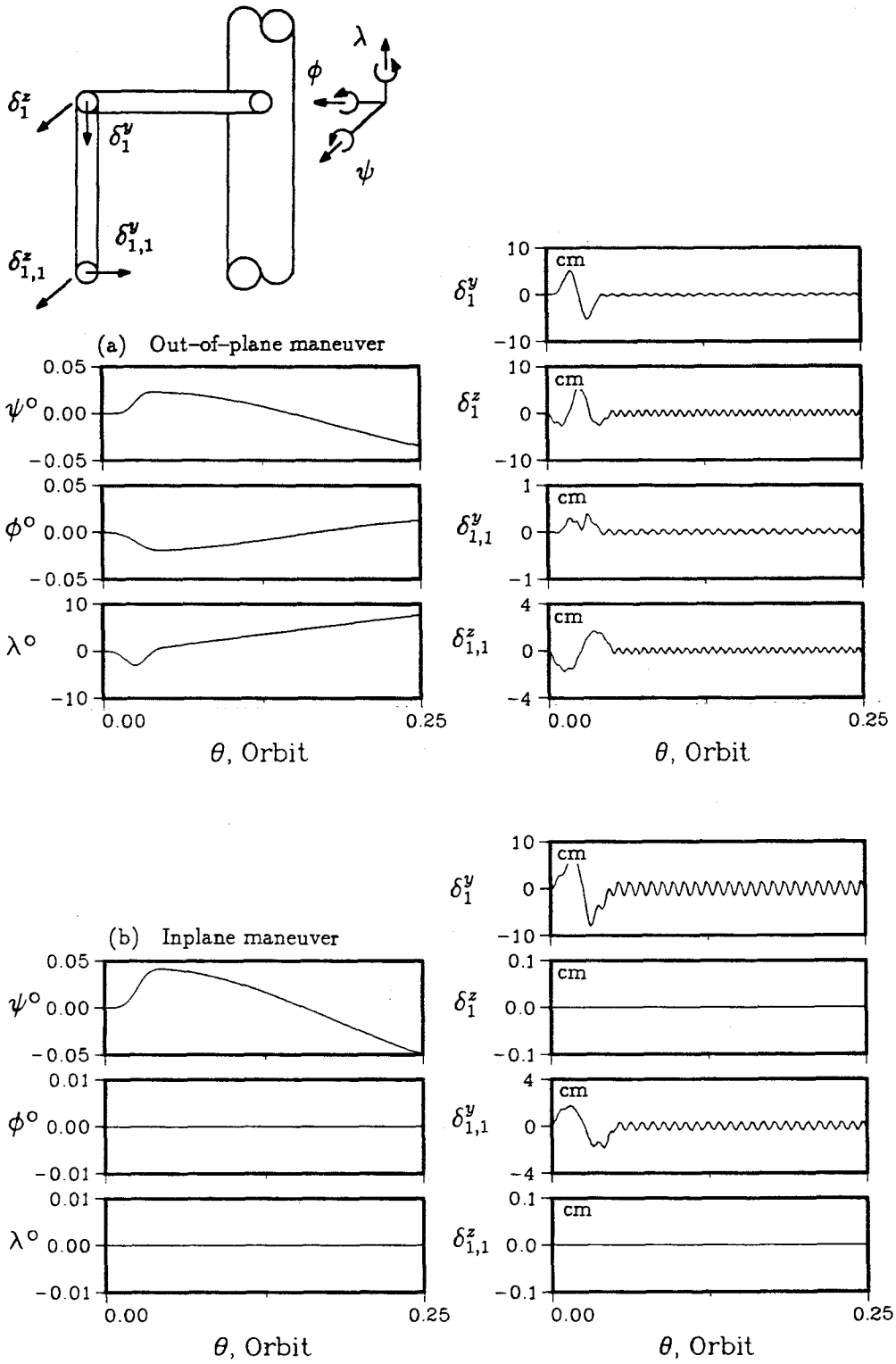

Figure 4-28 Effect of the increased MSS stiffness on the response of the space station with the lower link undergoing a 180° maneuver in 5 minutes: (a) out-of-plane maneuver; (b) inplane maneuver.

librational response. The main advantage is the significant reduction in amplitude of the flexible link vibrations. For the OP maneuver, the maximum deflection of the upper link is only 5.9 cm whereas it was 33.3 cm before. Even for the IP maneuver, the original deflection was 62.4 cm for the upper link but, with the stiffness increased, it is now reduced to only 8 cm. Thus the benefit of the increased stiffness is larger for the IP maneuver. This point is further illustrated in the pointing accuracy plot (Figure 4-29). The errors in the local vertical and local horizontal directions have reduced significantly for both the maneuvers. Originally, for the OP case, the p-p amplitudes for S_y and S_z were 16.4 cm and 25.6 cm, respectively. With the stiffness increased, both these values have dropped to 0.5 cm. Similarly, there is a sharp reduction in the p-p amplitude of S_y and S_z for the IP maneuver. For instance, S_z was 132.6 cm before and is only 4.7 cm with the stiffness of the link doubled. Since the librational response is hardly changed, the OP maneuver still suffers from the large error in the orbit normal direction. At the end of 0.25 orbit, the OP maneuver has a total error of 101.4 cm. The IP maneuver has now a reduced error of 9.5 cm, which was obtained before only with a 10-minute slew.

A summary of the maximum tip deflections and pointing error at the end of 0.25 orbit is presented in Table 4-4 .

4.5 Space Flyer Unit

The Space Flyer Unit (SFU) is an unmanned, reusable and free-flying platform for multipurpose use. The SFU is developed by a consortium of Japanese government agencies including the Institute of Space and Astronautical Science, the National Space Development Agency, and the Ministry of International Trade and Industry [107]. The unit is scheduled to be launched in early 1993. The SFU consists of an octagonal shaped central body which includes eight modules of scientific experiments.

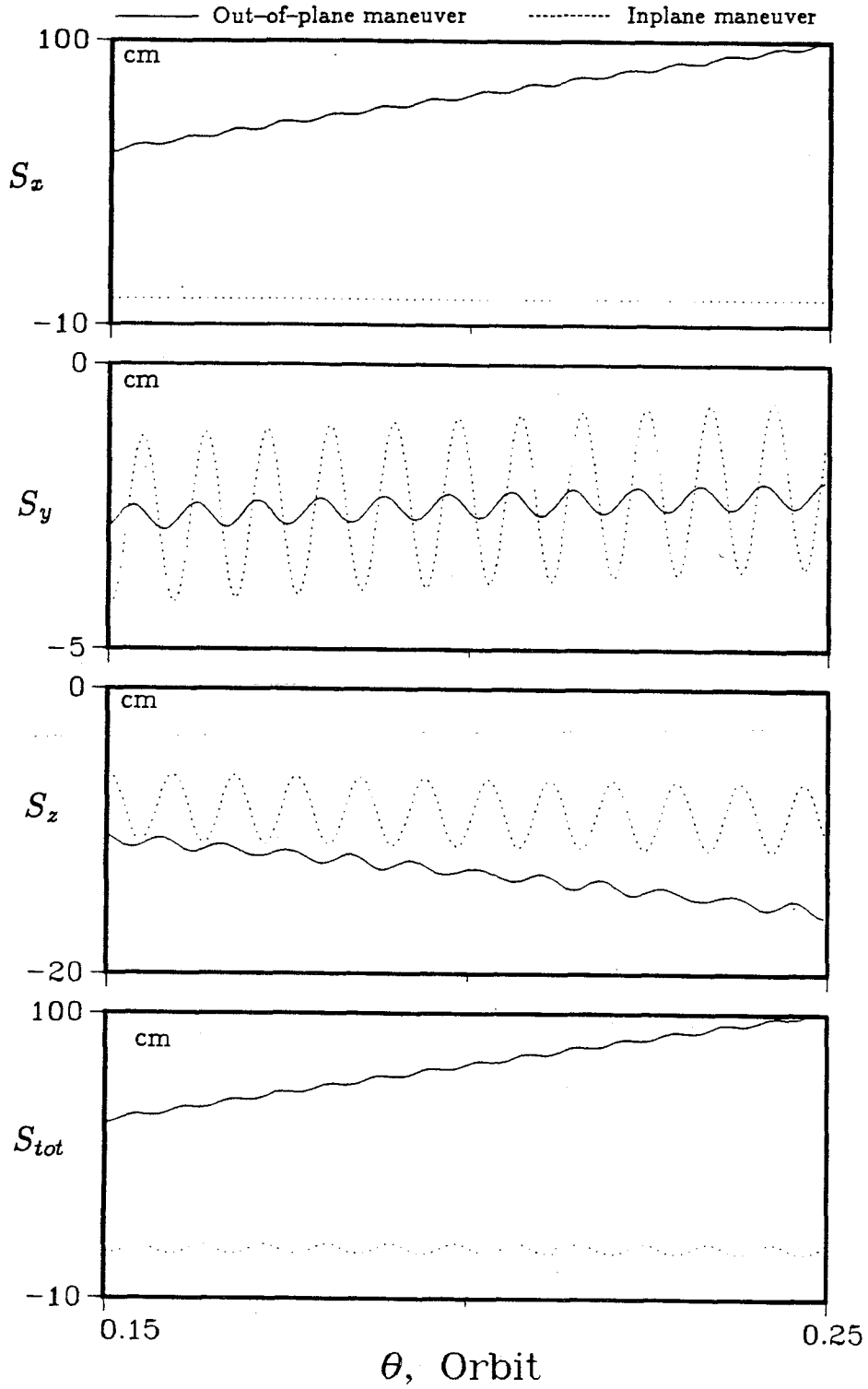

Figure 4-29 Pointing error of the MSS, of increased stiffness, with the lower link undergoing a 180° maneuver.

Table 4-4 System performance vs. type of the maneuver and its period

Maneuver Period	Maneuver Type	Maximum Deflections (cm) Upper Link	Lower Link	Pointing Error at 0.25 Orbit (cm)*
5 minutes	Out-of-plane	33.3	9.5	103.4
	In-plane	62.4	17.0	40.9
7.5 minutes	Out-of-plane	11.4	3.4	94.4
	In-plane	19.2	4.6	14.7
10 minutes	Out-of-plane	6.3	1.8	86.0
	In-plane	7.9	1.9	9.5
10 minutes**	Out-of-plane	10.4	3.1	126.7
	In-plane	11.8	3.1	95.9
5 minutes***	Out-of-plane	5.9	1.8	101.4
	In-plane	8.0	1.9	9.5

* Mean pointing error for the inplane case
** Manipulator located at 50 m from O_c
*** Stiffness of the links doubled

Two solar array pedals (SAPs), each 9.7 m × 2.4 m, are deployed at either end of the central body. The SAPs, besides generating power, are used for the High Voltage Solar Array (HVSA) experiment. The objectives of the experiment are to determine:

(i) dynamical characteristics of the unit during deployment and retrieval of the flexible SAPs;

(ii) the upper limit of the voltage generated which would be free from surface breakdown, power drain through space plasma, and enhancement of the aerodynamic drag.

Here, the present formulation is used to simulate the dynamics of the SFU during deployment and retrieval of the pedals. To this end, modifications to the present formulation are necessary to account for (i) time varying component mass and stiffness and (ii) rate of change of mode shape.

Recall that from the Lagrangian formulation, the governing equations of motion are given by

$$\frac{d}{d\theta}\left(\frac{\partial T}{\partial q'}\right) - \frac{\partial T}{\partial q} + \frac{\partial U}{\partial q} = 0\,,$$

in absence of any generalized forces. The terms, $\partial T/\partial q$ and $\partial U/\partial q$, remain the same as before except that the mass and stiffness are functions of deployment and retrieval strategies. The term $d/d\theta(\partial T/\partial q')$ can be written into the first and second order components, $O_1(d/d\theta(\partial T/\partial q')$ and $O_2(d/d\theta(\partial T/\partial q')$, as given by Eq. (3.10). To account for the rate of change of mass (m'), the first order component is now rewritten as:

$$\begin{aligned} O_1\Big(\frac{d}{d\theta}\frac{\partial T}{\partial q'}\Big) = O_1\Big(\frac{d}{d\theta}\frac{\partial T_{sys}}{\partial q'}\Big) &+ \frac{d}{d\theta}\frac{\partial \bar{\omega}^T}{\partial q'}\Big[\mathbf{I}_{sys}\bar{\omega} + \bar{H}_{sys}\Big] \\ &+ \frac{\partial \bar{\omega}^T}{\partial q'}\Big[\frac{d\mathbf{I}_{sys}}{d\theta}\bar{\omega} + \mathbf{I}_{sys}O_1\Big(\frac{d\bar{\omega}}{d\theta}\Big) + O_1\Big(\frac{d\bar{H}_{sys}}{d\theta}\Big)\Big] \\ &+ O_1\Big(\frac{d\bar{\omega}^T}{d\theta}\Big)\frac{\partial \bar{H}_{sys}}{\partial q'} + \bar{\omega}^T\frac{d}{d\theta}\frac{\partial \bar{H}_{sys}}{\partial q'} + \frac{m'}{m}\left(\frac{\partial T}{\partial q'}\right)\,; \end{aligned} \qquad (4.6)$$

Note that, except for the last term, O_1 is essentially the same as before except that the mass is a function of time. Similarly O_2 term is given by Eq. (3.10b) with mass as a variable.

In the assumed mode method, flexural displacement (δ) and velocity (δ') are given by

$$\delta = \sum_{r=1}^{n_r} q_r(\theta)\phi_r(\zeta)\,;$$
$$\delta' = \sum_{r=1}^{n_r} q_r'(\theta)\phi_r(\zeta)\,;$$

where q_r and ϕ_r are the generalized coordinate and mode shape, respectively. With the inclusion of deployment/retrieval , Ibrahim [14] has shown that the velocity of

flexural displacement is modified to include the variation of mode shape, i.e.

$$\delta' = \sum_{r=1}^{n_r} (q_r'(\theta)\phi_r(\zeta) + q_r(\theta)\phi_r'(\zeta)) \; ; \tag{4.7}$$

where $\phi_r'(\zeta)$ is the rate of change of mode shape and is given by

$$\phi_r'(\zeta) = \frac{\partial \phi_r(\zeta)}{\partial \zeta} \cdot \zeta' \; .$$

Incorporation of Eqs. (4.6) and (4.7) into the present formulation makes it possible to study deployment/retrieval effects on the dynamics of the SFU. The unit is idealized as a rigid central body (B_c) with two deployable cantilevered plates (B_1 and B_2) attached. Assuming a 90-minute orbit, the simulation is based on the data given in Talbe 4-5 and using the coordinate system as shown in Figure 4-30. Considering only the first mode of the SAP vibrations, five generalized coordinates are required to describe the system dynamics:

$$q = \psi \, , \phi \, , \lambda \, , \underline{H}_1^{1,1} \, , \underline{H}_2^{1,1} \, .$$

The same data-set is used in the retrieval study except that the two columns of data are interchanged. For instance, the length of the SAP before and after retrieval would be 9.7 m and 3 m, respectively. Ideally, simulations should be based on SAP length from 0 m to 9.7 m. However, this would make the governing equations of motion extremely stiff initially and hence would require a lot of computational effort. It is, therefore, assumed that the pedal remains rigid until 3 m of its deployment. Even with this simplification, the natural frequency of the array would reach a high of 1.93 Hz.

The planned deployment/retrieval strategy of the SAPs can be separated into three stages as summarized below:

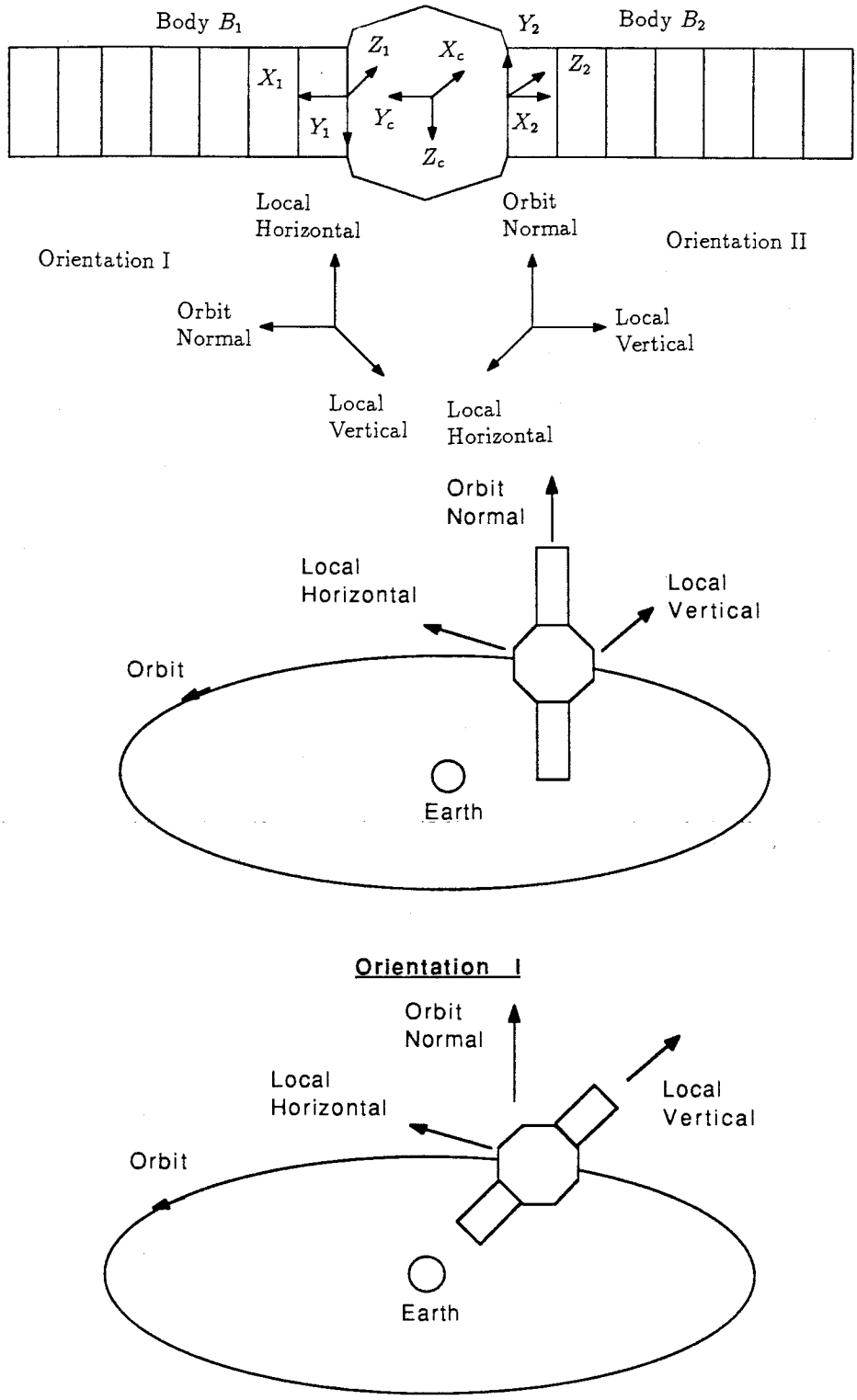

Figure 4-30 Coordinate systems and the two possible design configurations for the SFU central body and arrays.

Table 4-5 Data of the SFU used in the simulation

Main Body (Body B_c)

		Before Deployment	After Deployment	
l_c	=	4.9	4.9	m
m_c	=	3,964.8	3,886	kg
$(I_{xx})_c$	=	7,839.2	7,524	kg-m^2
$(I_{yy})_c$	=	4,410.0	4,410.0	kg-m^2
$(I_{zz})_c$	=	6,079.2	5,764	kg-m^2

Solar Array Pedal (Body B_i, $i = 1, 2$)

		Before Deployment	After Deployment	
l_i	=	3	9.7	m
m_i	=	17.6	57	kg
f_i^1	=	1.934	0.185	Hz
$(I_{xx})_i$	=	20	20	kg-m^2
$(I_{yy})_i$	=	68.7	2,321	kg-m^2
$(I_{zz})_i$	=	69	2,331	kg-m^2

(i) The SAPs are deployed in 15 minutes with the longitudinal axis parallel to the local vertical, i.e., one SAP points toward the earth while the other away from the earth.

(ii) The SFU then undergoes a 90° roll so that the longitudinal axes of the SAPs are aligned with the orbit normal.

(iii) At the end of the mission, the SAPs are retrieved with the SFU in the same orientation as in (ii). The retrieval time is also 15 minutes.

Contingency plans are also drafted in the event that either SAP fails to deploy or retrieve.

The parametric analysis presented here aims at studying the dynamical response

of the SFU during the deployment/retrieval of the SAPs. Since it is assumed that the pedal length varies from 3 to 9.7 m instead of 0 to 9.7 m, the deployment/retrieval time is adjusted to 10 minutes. The deployment velocity is taken to be constant.

Figure 4-31 shows the system response during the deployment of the SAP. With the SAPs deployed in the nominal orientation, the SFU response is shown in Figure 4-31a. Since the SAPs are deployed in the inplane direction, only pitch motion is excited. Although the SFU remains stable, it undergoes a large amplitude pitch motion reaching a minimum of $-63°$. As the SAP becomes more flexible during deployment, the tip deflection increases too; however, the SAPs hardly oscillate. As soon as the deployment terminates, the pedals start to vibrate with a peak-to-peak amplitude of about 0.0025 cm. Figure 4-31b studies the feasibility of an alternative deployment strategy. Here, the SFU undergoes a 90° roll before the deployment, i.e., the SAPs are deployed in the out-of-plane direction. Advantages of this strategy are obvious. The pitch libration has a considerably smaller amplitude with a minimum of $-5.8°$. At the end of the deployment, the SAPs vibrate at amplitudes about two orders smaller than the corresponding ones in Figure 4-31a. The only disadvantage with this strategy is that both roll and yaw are also excited; however, their amplitudes are of the order 10^{-5} even after 0.5 orbit.

Even if one SAP fails to deploy, the SFU remains stable under asymmetric deployment (Figure 4-32). Here, only B_2 is assumed to deploy successfully. In Figure 4-32a, B_2 is deployed in the direction towards the earth. The figure shows that both the librational and vibrational responses remain essentially the same as if both pedals were deployed. In contrast, when only B_2 is deployed in the out-of-plane direction, the SFU response is different from that in Figure 4-31b. Although the pitch motion has reduced its minimum amplitude to $-2.6°$ from $-5.8°$, the roll and yaw ampli-

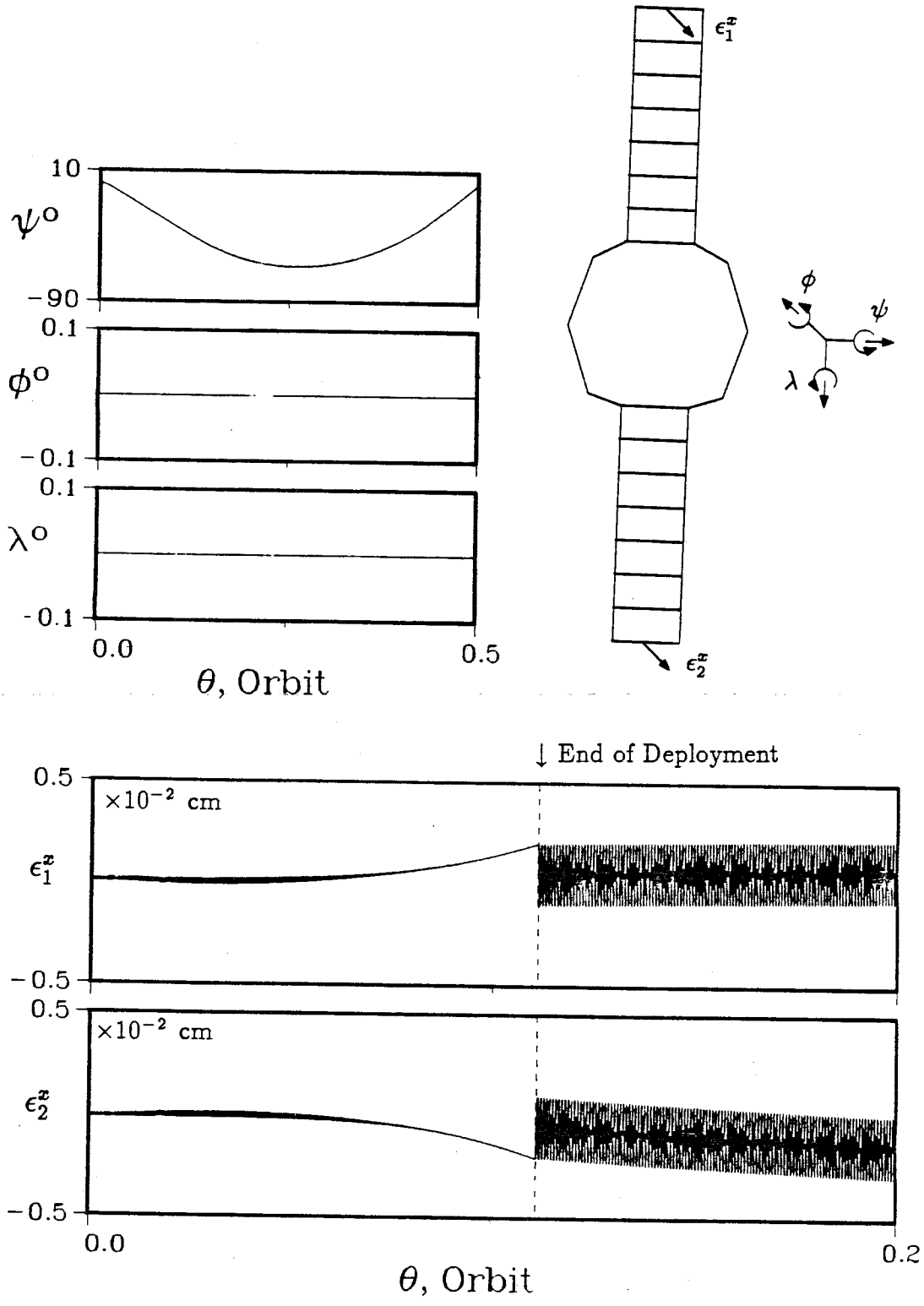

Figure 4-31 Dynamical response of the SFU during deployment of the solar array pedals: (a) inplane deployment.

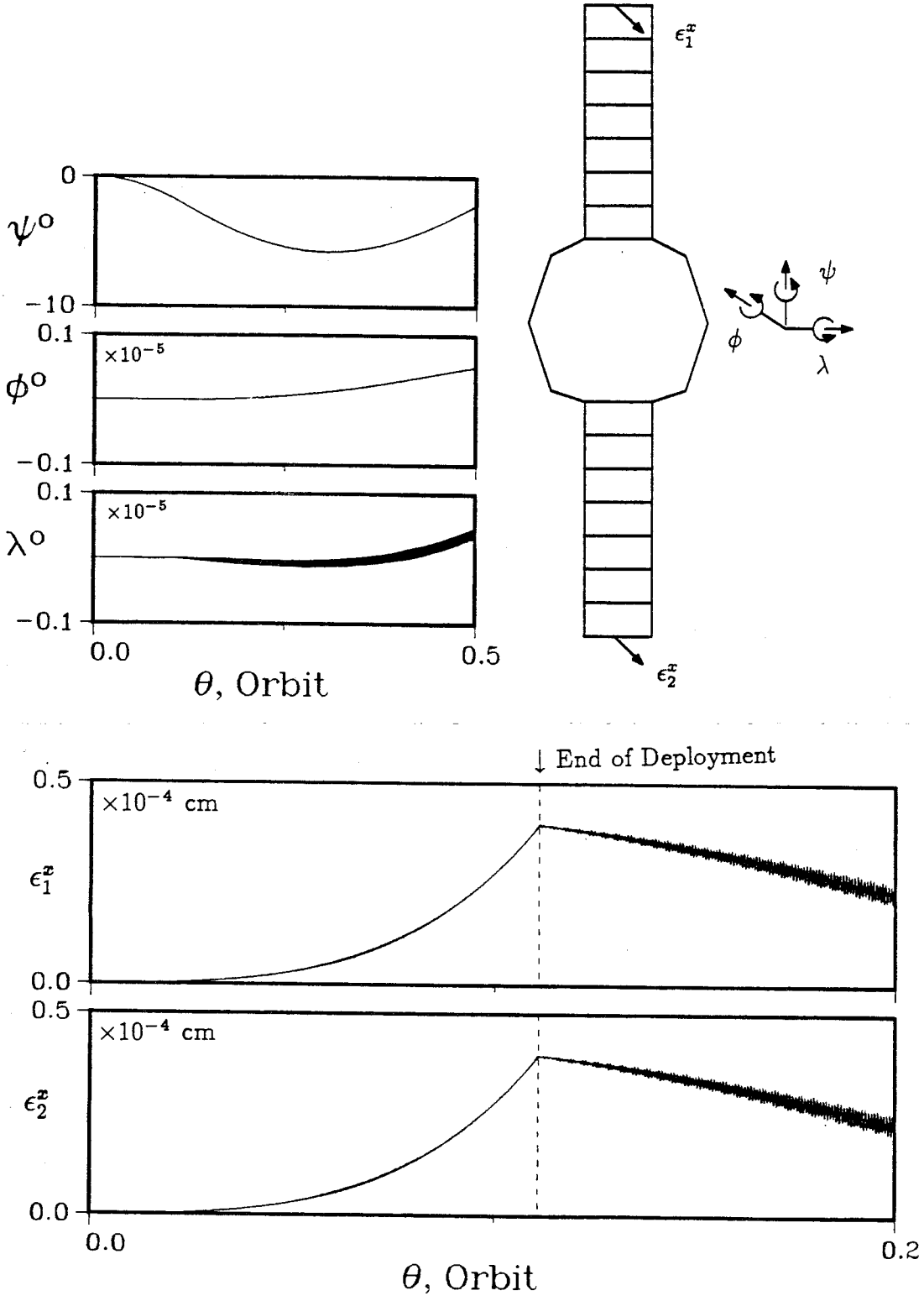

Figure 4-31 Dynamical response of the SFU during deployment of the solar array pedals: (b) out-of-plane deployment.

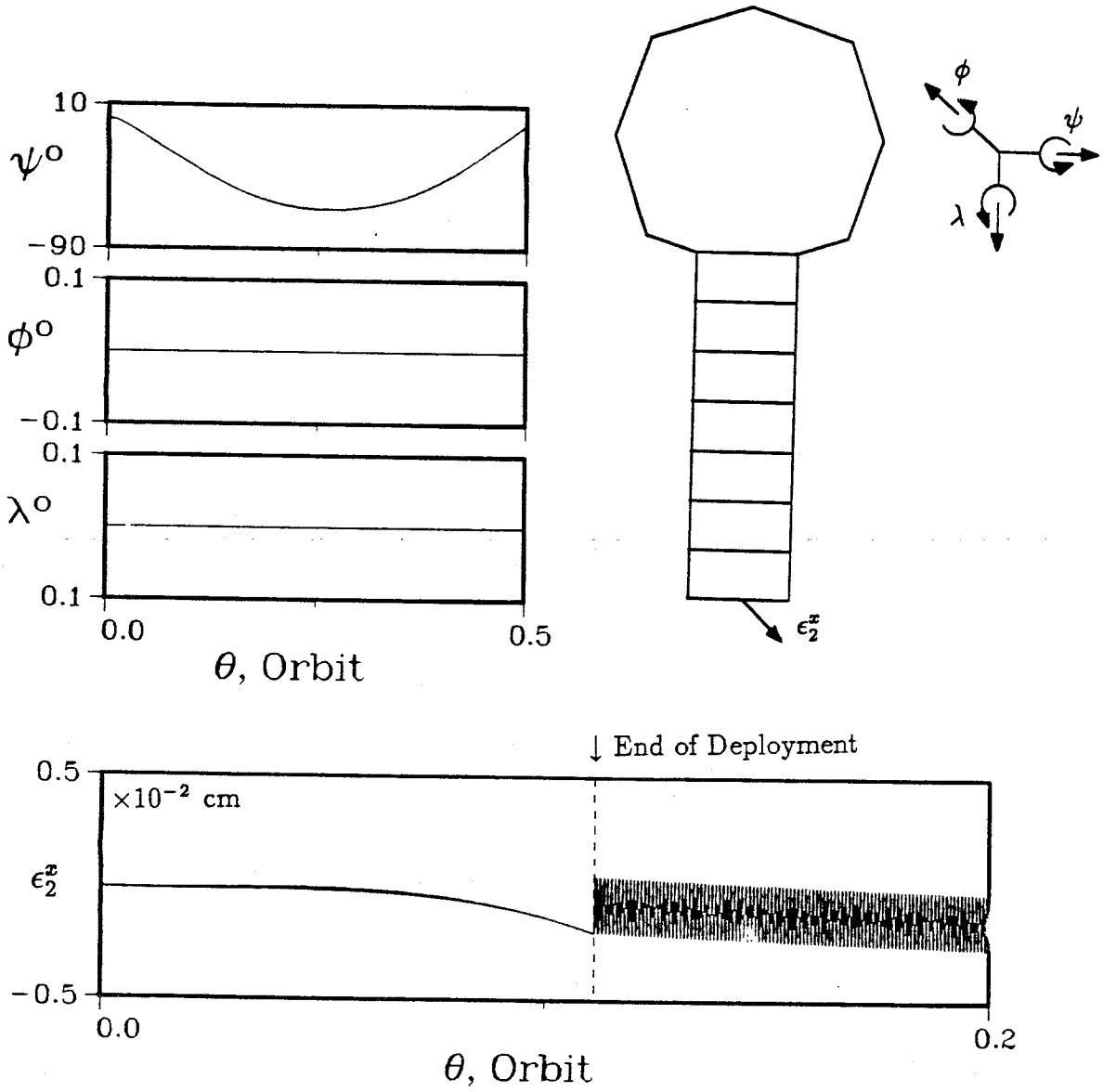

Figure 4-32 Response characteristics of the SFU during deployment of the solar array pedal B_2: (a) inplane deployment.

tudes increase significantly (Figure 4-32b). With both the pedals deployed, the order of magnitude of roll and yaw is about 10^{-5} at the end of 0.5 orbit. With only B_2 deployed, roll and yaw attain values of $-12.9°$ and $-2.7°$, respectively, over the same period. The response trend of the SAP vibration also changes. At the end of the deployment, the SAP oscillates with a peak-to-peak amplitude of 0.0002 cm. This value, though small, is about one order higher than that in the case with both the SAPs deployed.

Figure 4-33 shows the system response during the SAPs retrieval. The effect of retrieval time is studied here. In Figure 4-33a, a 5-minute retrieval period is assumed. Even with this fast retrieval, the SFU remains stable with a maximum pitch angle of 6°, which is about the same in magnitude as the deployment case. The roll and yaw angles remain small but are considerably larger than those during the deployment. At the end of 0.5 orbit, their amplitudes are $-0.0013°$ and $-0.0005°$, respectively. As the SAPs are becoming more and more rigid with the progress of retrieval, it is reasonable that they attain lower deflection (-0.5×10^{-5} cm) during retrieval and oscillate with a peak-to-peak amplitude of less than 10^{-7} cm afterwards. With the retrieval time increased to 10 minutes, Figure 4-33b shows that the libration response remains unchanged. Furthermore, the SAP vibration retains the same response trend and has about the same minimum deflection (-0.64×10^{-5} cm). Even with the retrieval time further increased to 20 minutes, the pitch and SAP responses remain the same; however, the roll and yaw degrees of freedom are no longer excited (Figure 4-33c).

As seen before, the SFU remained stable for inplane or out-of-plane deployment of the SAPs. This is no longer true for the SAP retrieval. Although out-of-plane retrieval of the SAPs has no adverse effect on the SFU dynamics, the inplane retrieval tends to destabilize the system. Figure 4-34a shows that with a 5-minute inplane retrieval,

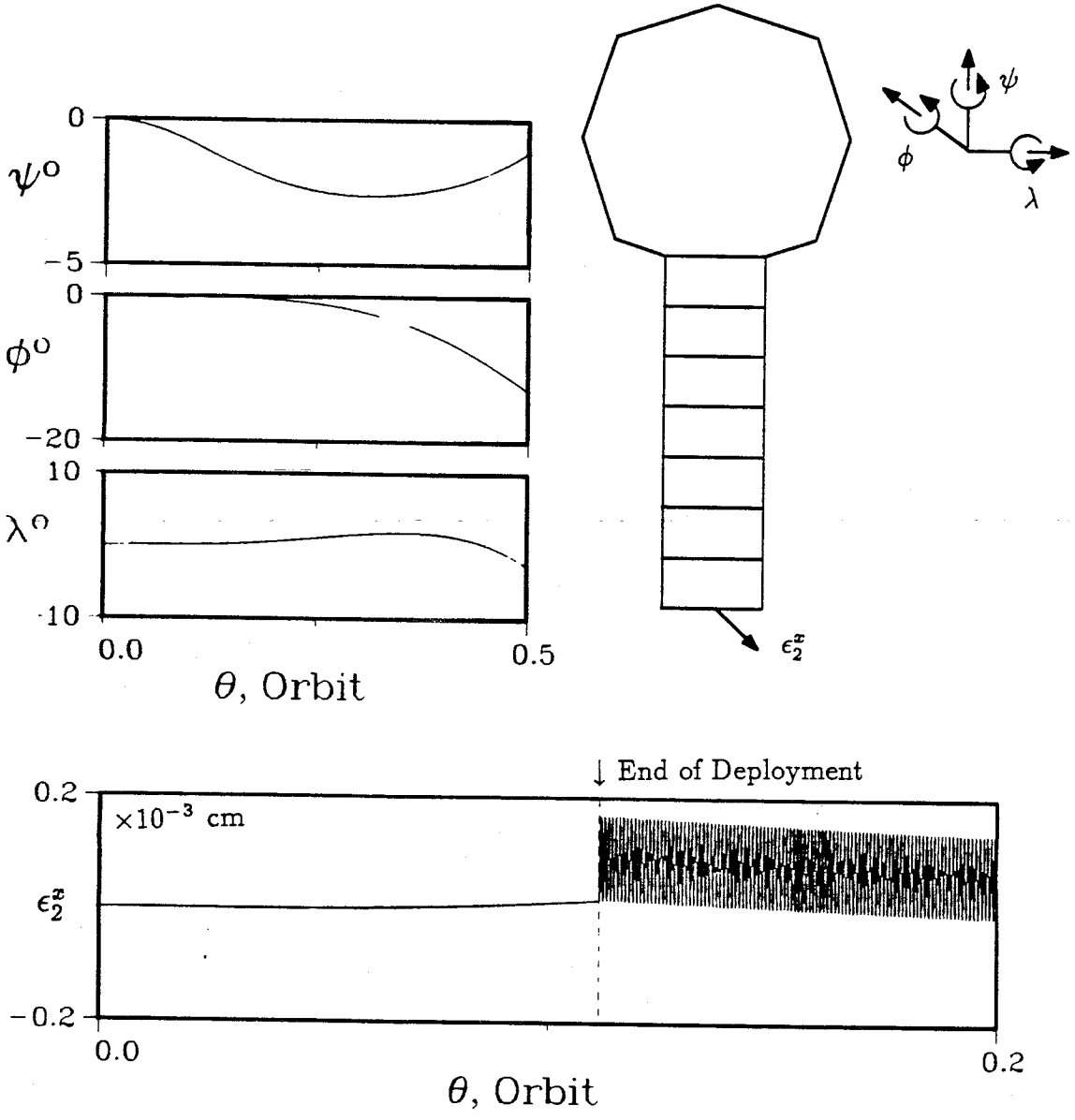

Figure 4-32 Response characteristics of the SFU during deployment of the solar array pedal B_2: (b) out-of-plane deployment.

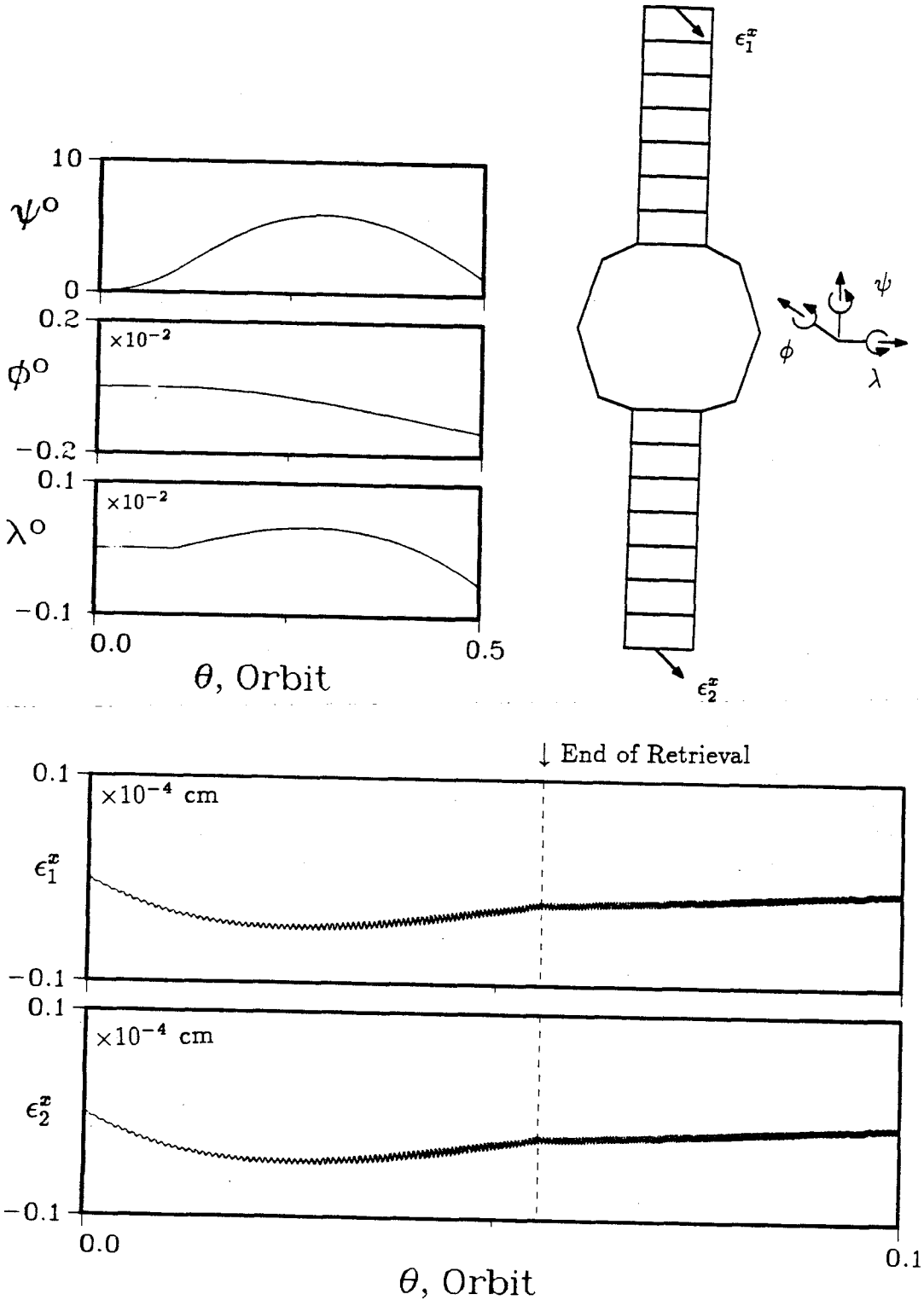

Figure 4-33 Librational and vibrational responses of the SFU during the out-of-plane retrieval maneuver of the solar array pedals: (a) 5-minute retrieval period.

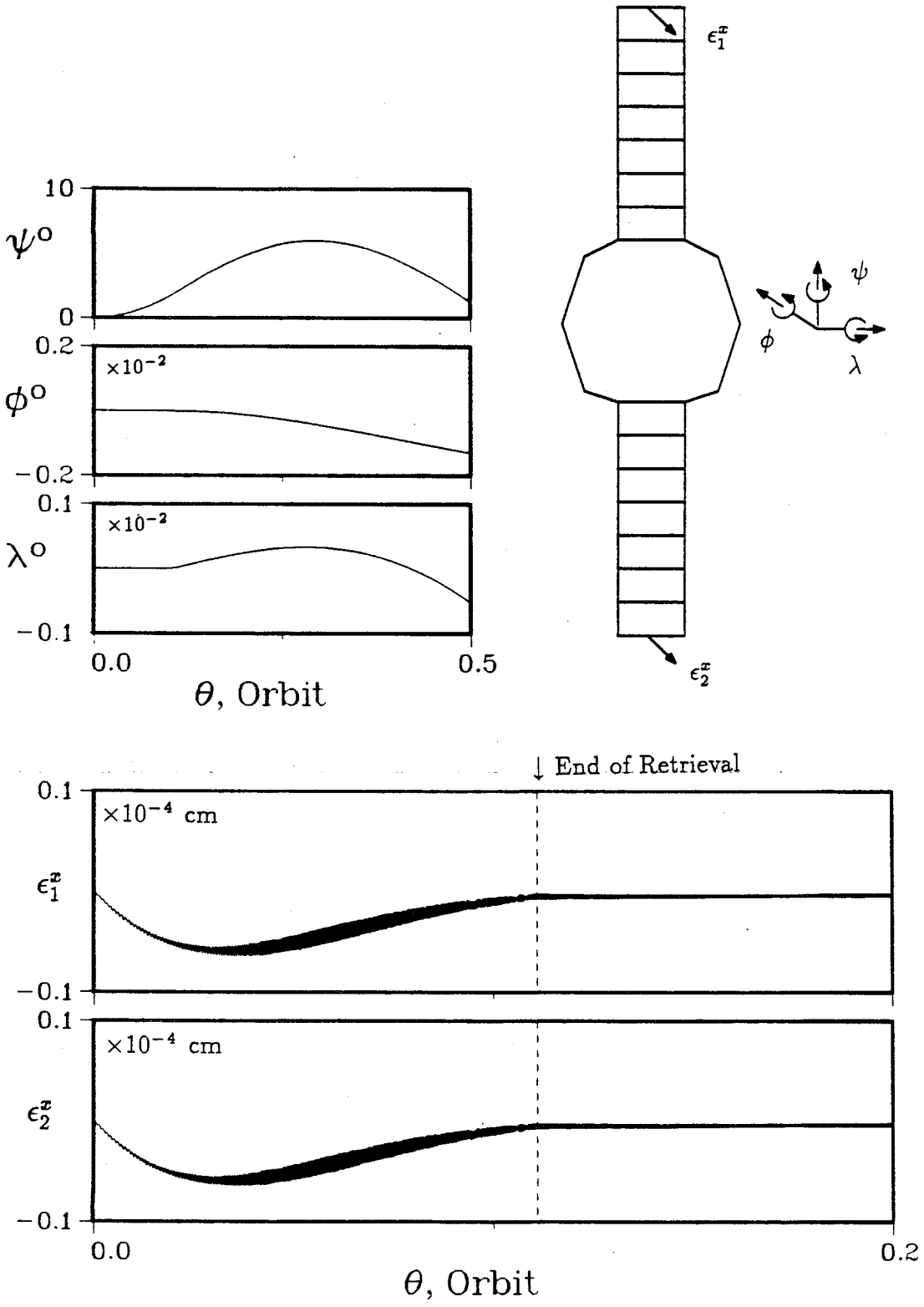

Figure 4-33 Librational and vibrational responses of the SFU during the out-of-plane retrieval maneuver of the solar array pedals: (b) 10-minute retrieval period.

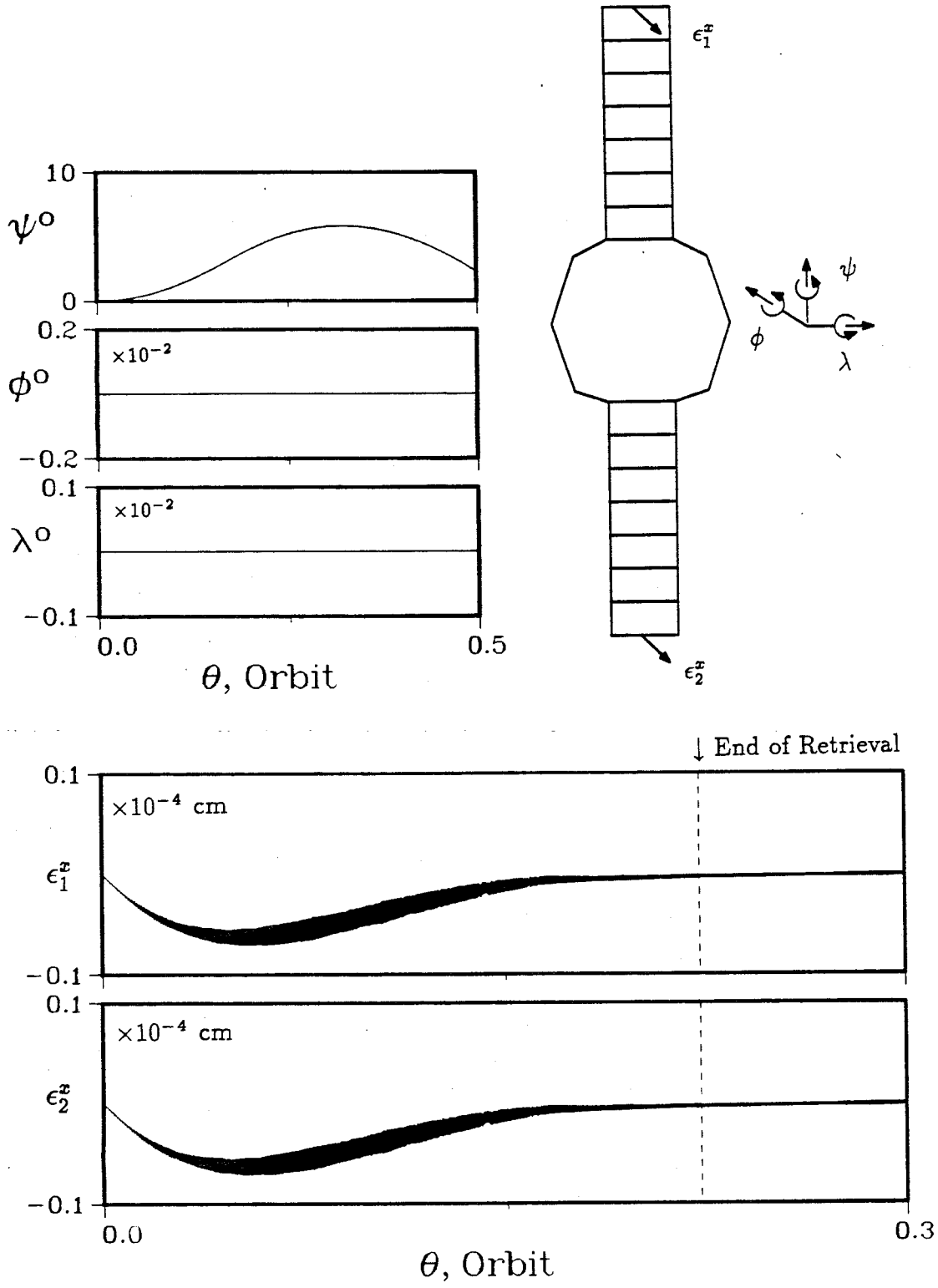

Figure 4-33 Librational and vibrational responses of the SFU during the out-of-plane retrieval maneuver of the solar array pedals: (c) 20-minute retrieval period.

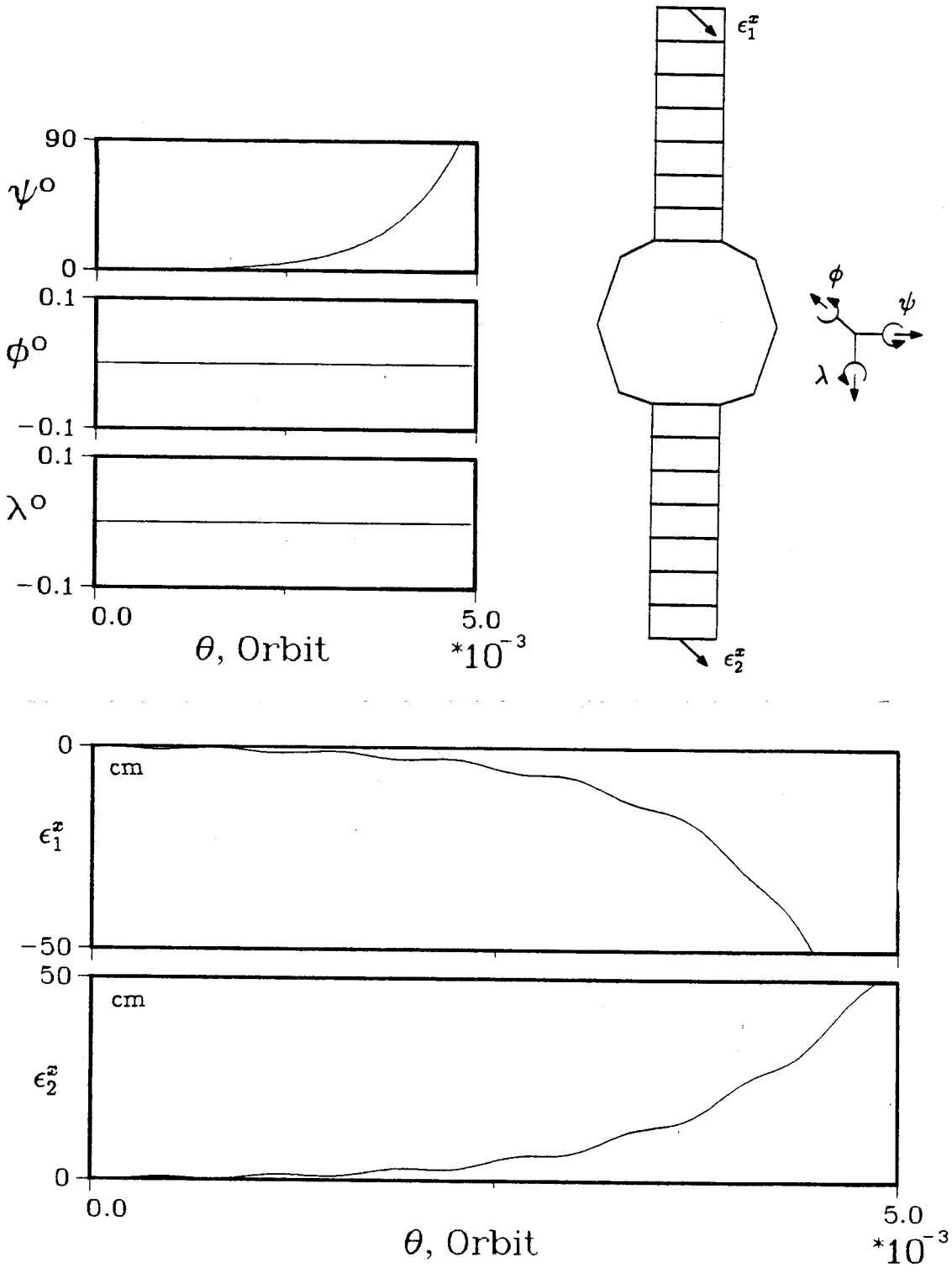

Figure 4-34 System response of the SFU showing unstable motion induced by the inplane retrieval of the solar array pedals: (a) 5-minute retrieval period.

the SFU starts to tumble almost immediately (after 0.0004 orbit). Over the same period, the tip deflections of the SAPs are over 50 cm. As the retrieval time increases to 10 minutes, Figure 4-34b illustrates that the system remains unstable although the onset of tumbling motion has been delayed to 0.008 orbit. Recall from Figure 4-31a that in the inplane deployment, both SAPs vibrate with the same magnitude but in opposite directions. Now both the SAPs deflect with different amplitudes. B_1, which points away from the earth, has a tip deflection of over 50 cm at the end of 0.01 orbit. B_2, which points towards the earth, deflects only 10 cm at 0.01 orbit. As can be seen from Figure 4-33, the appendages softens during retrieval. It is apparent that during the inplane retrieval case, the degree of SAP softening is higher and different for the two SAPs due to difference in the gravitational torque. This softening effect coupled with higher pitch rate result in large deflections of the SAPs; however, further studies are needed to confirm this observation. As the retrieval time is further increased to 20 minutes, the system remains stable until 0.13 orbit (Figure 4-34c). Once again, B_1 experiences a considerably larger deflection than B_2. At the end of 0.02 orbit, the tip deflections for B_1 and B_2 are 40 cm and 6 cm, respectively.

When only one of the SAPs is deployed, its retrieval is found to be a difficult task. Whether the maneuver is performed out-of-plane or inplane, the system remains unstable for either B_1 or B_2 retrieval. A typical response plot is shown in Figure 4-35. Here, B_2 is retrieved in the out-of-plane direction. Figure 4-35a corresponds to a 5-minute retrieval which clearly indicates that the system experiences large amplitudes of pitch, roll, and yaw motions. In less than 0.02 orbit, the SFU becomes unstable and starts tumbling. Note also the large deflection of B_2. As the retrieval time is increased to 10 minutes, the SFU manages to maintain its stability until about 0.03 orbit (Figure 4-35b). The duration of stable motion further increases to 0.05 orbit when the retrieval time is increased to 20 minutes (Figure 4-35c).

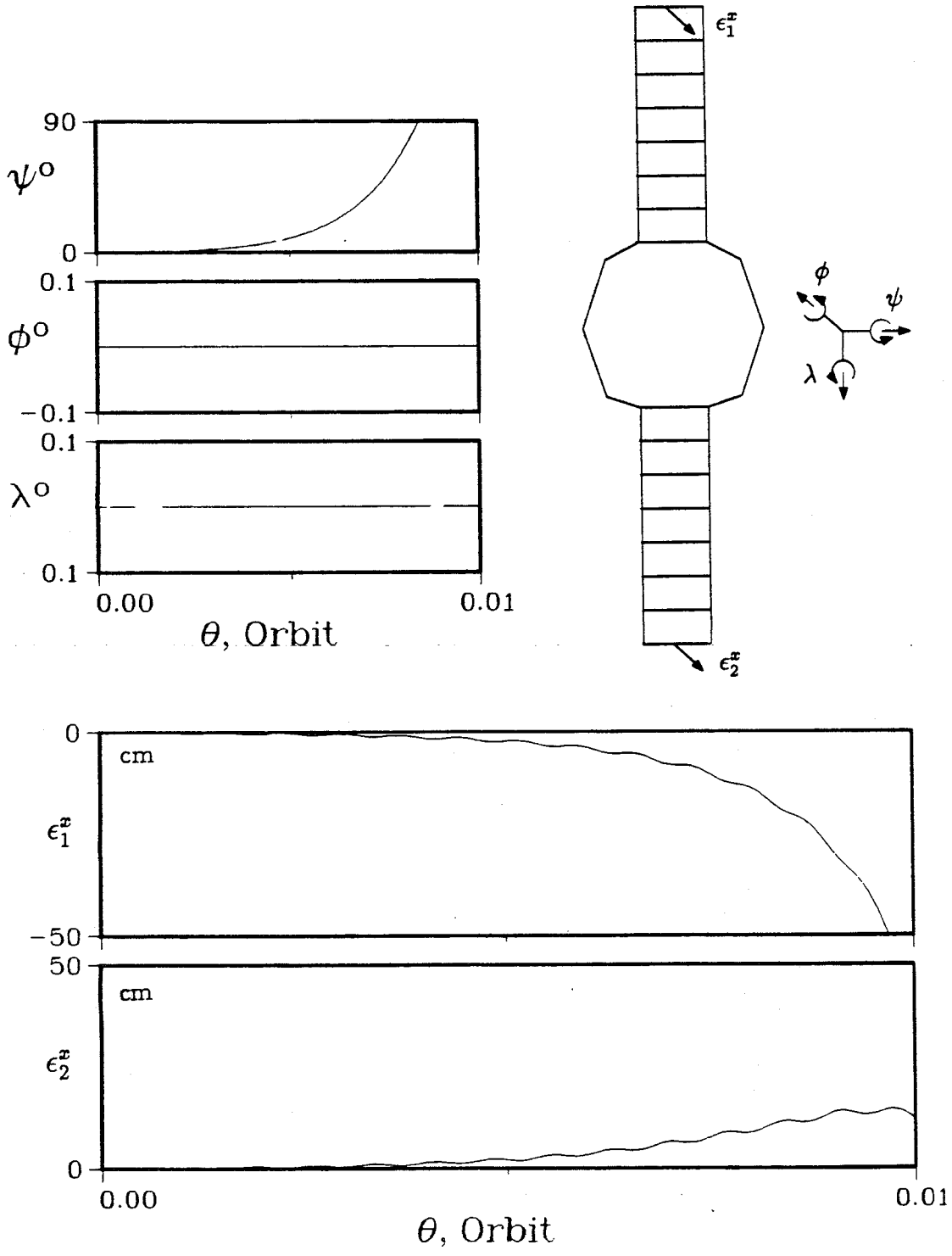

Figure 4-34 System response of the SFU showing unstable motion induced by the inplane retrieval of the solar array pedals: (b) 10-minute retrieval period.

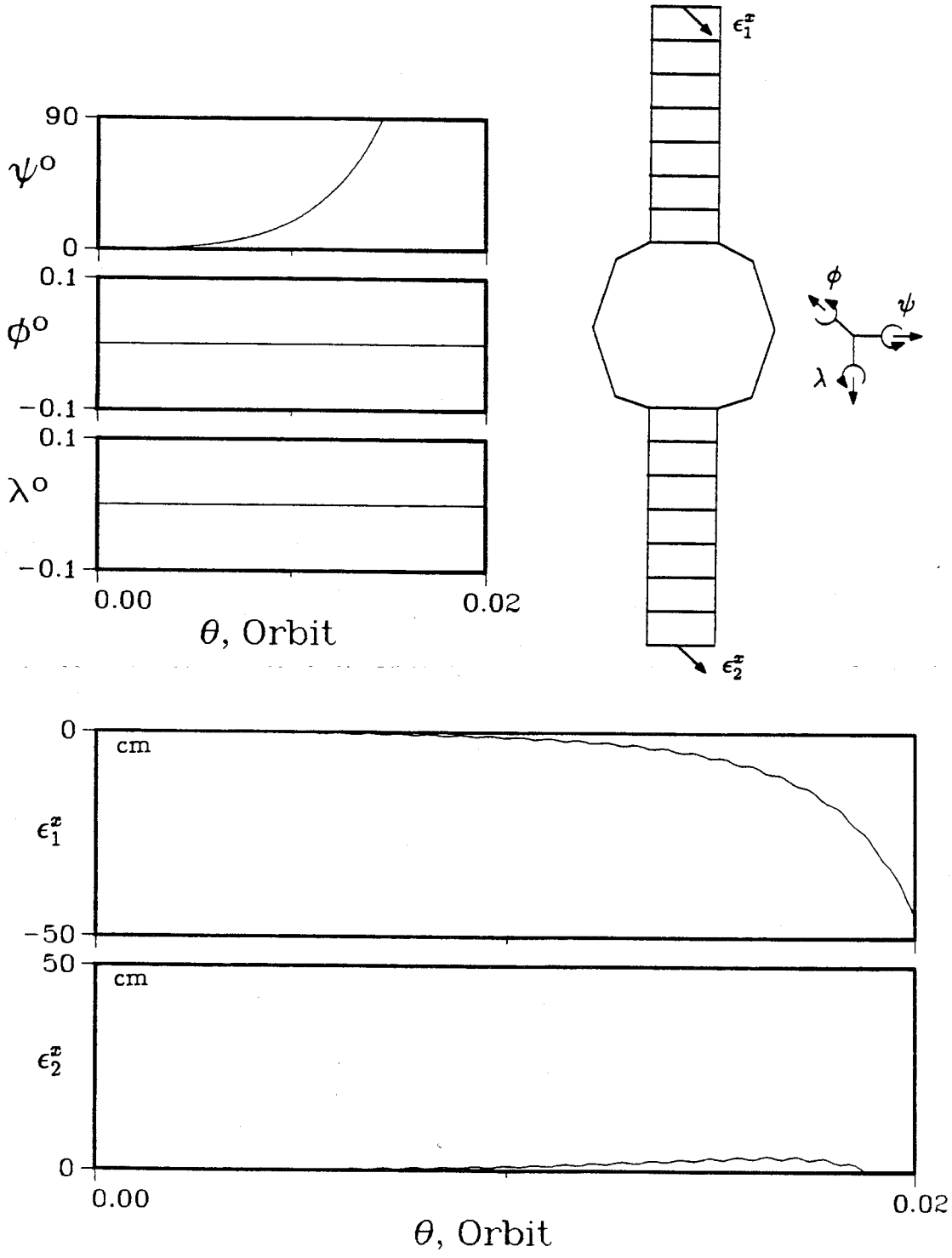

Figure 4-34 System response of the SFU showing unstable motion induced by the inplane retrieval of the solar array pedals: (c) 20-minute retrieval period.

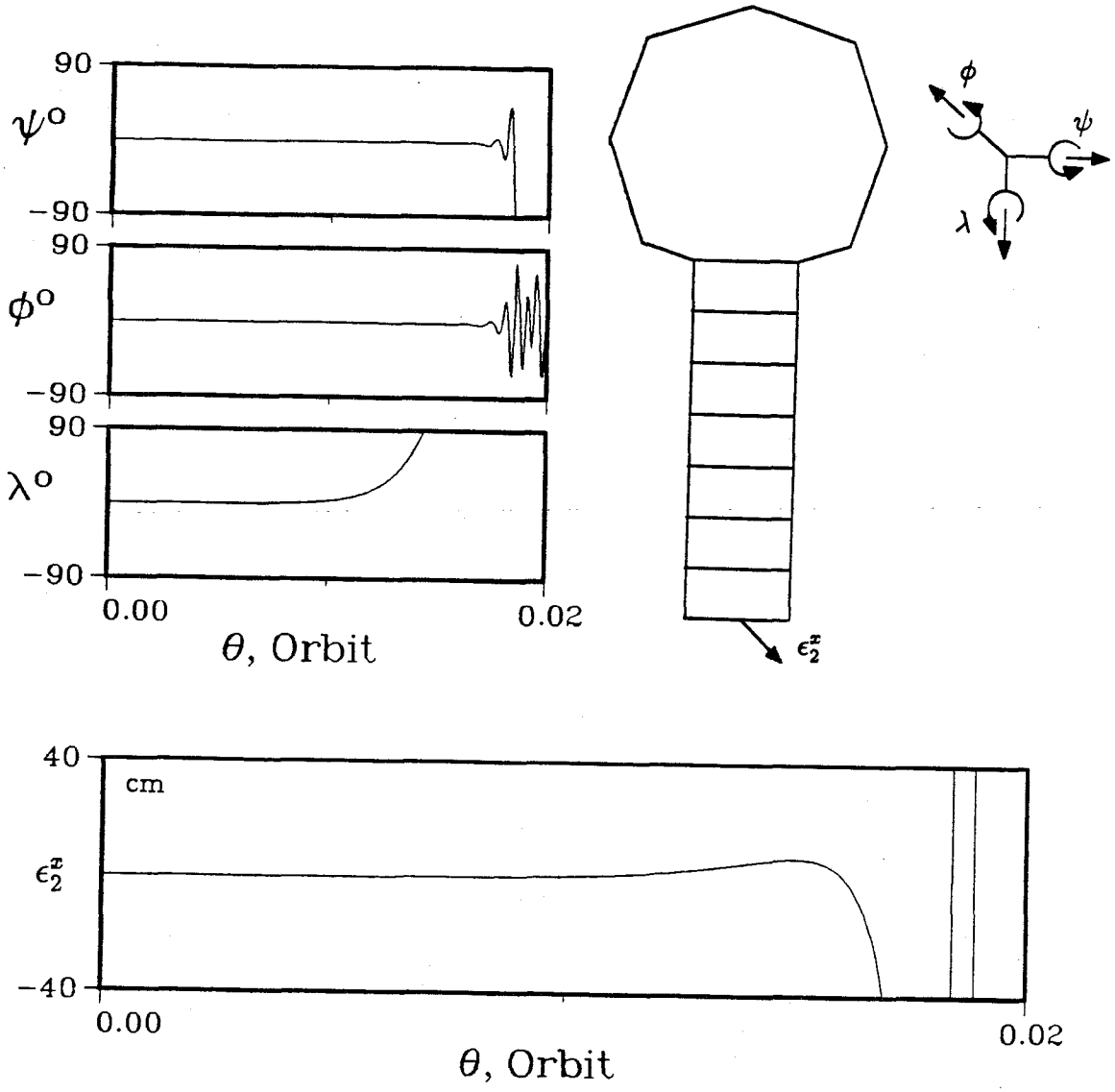

Figure 4-35 Out-of-plane retrieval of one of the solar array pedals (B_2) showing instability of the system: (a) 5-minute retrieval period.

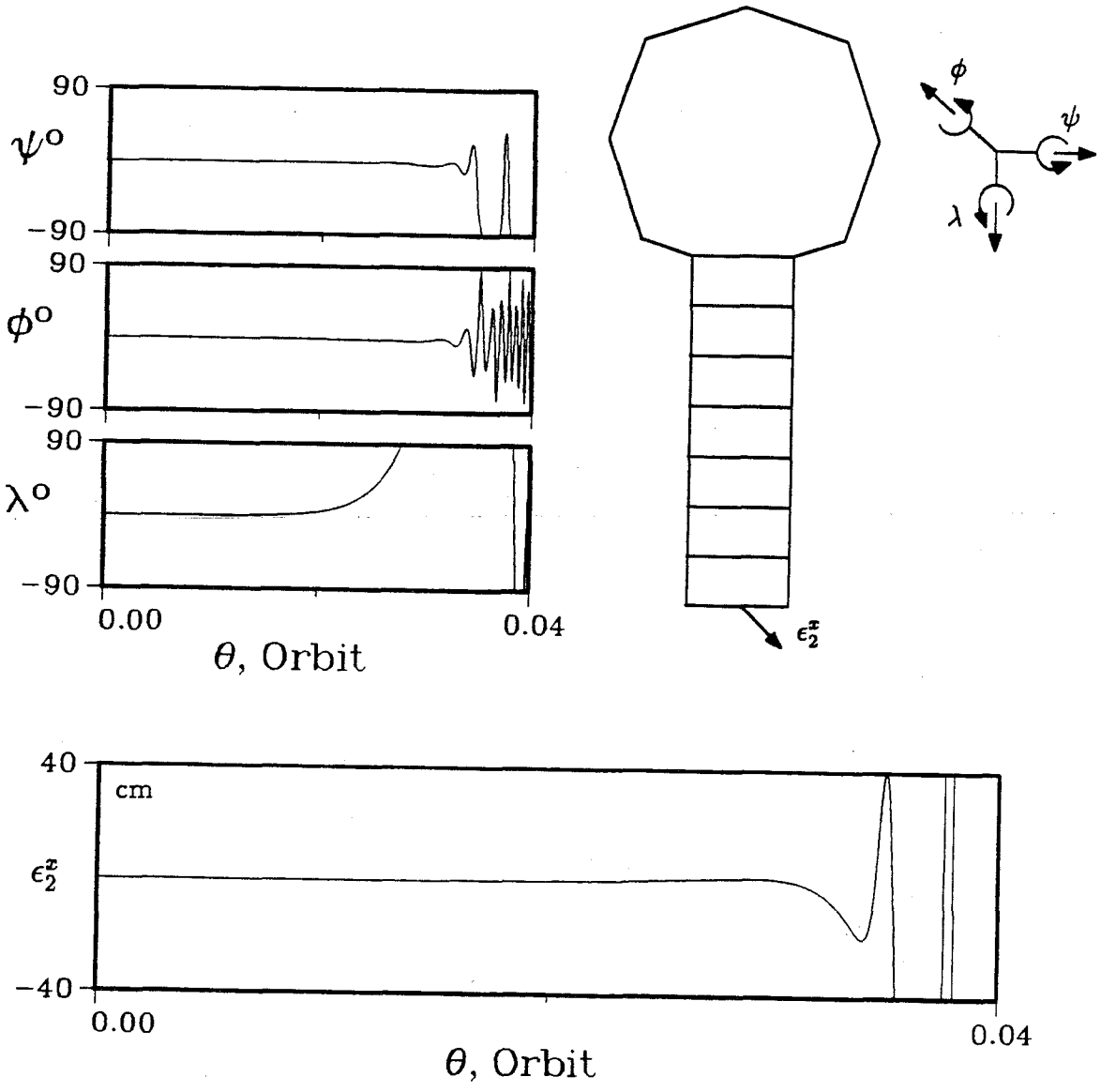

Figure 4-35 Out-of-plane retrieval of one of the solar array pedals (B_2) showing instability of the system: (b) 10-minute retrieval period.

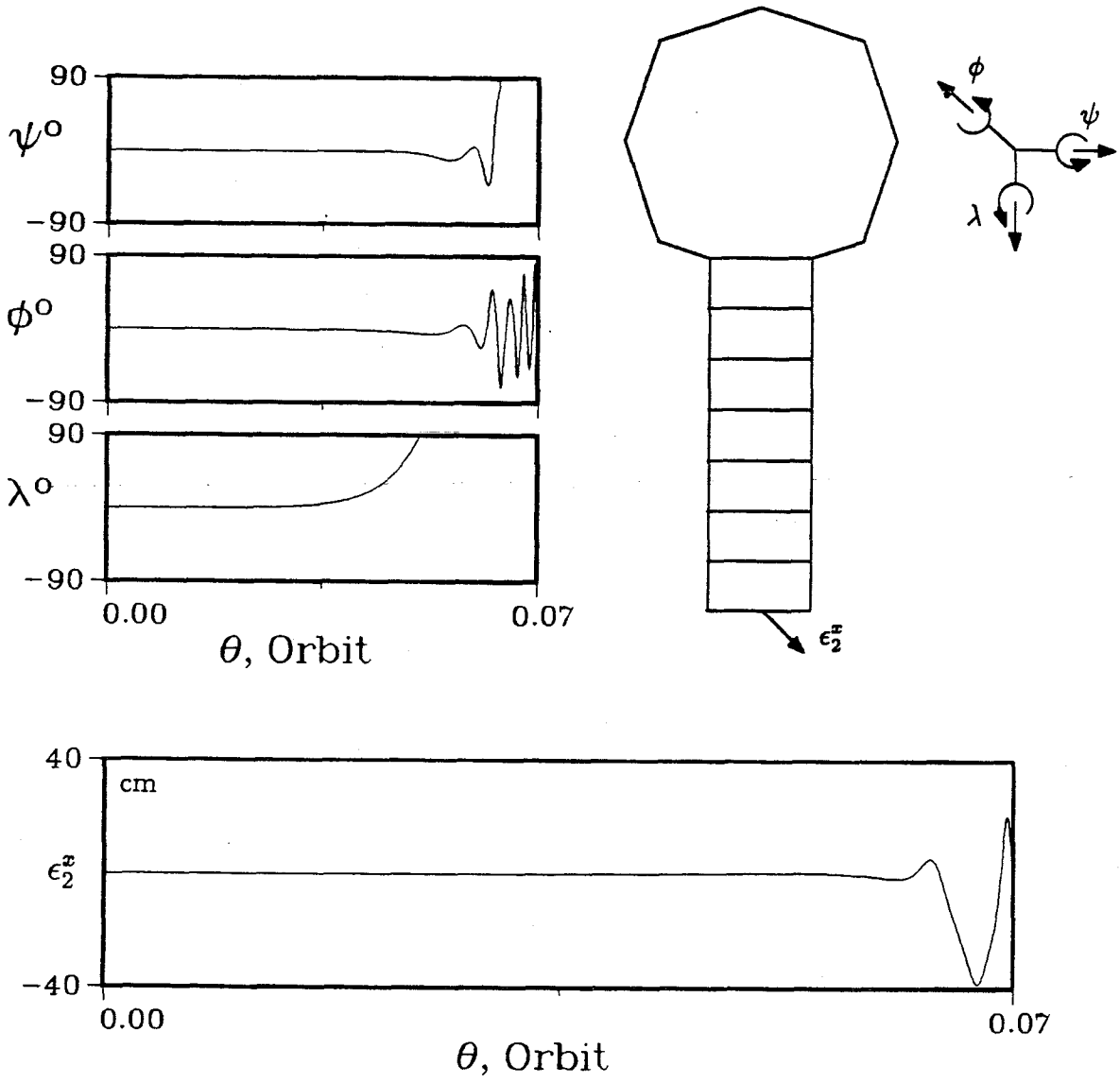

Figure 4-35 Out-of-plane retrieval of one of the solar array pedals (B_2) showing instability of the system: (c) 20-minute retrieval period.

A summary of the SFU stability subjected to various deployment/retrieval condition is presented in Table 4-6 . The results suggest that inplane or out-of-plane retrieval of the single SAP and inplane retrieval of both the SAPs require some control effort. Without that, it is apparent from Figures 4-34 and 4-35 that the retrieval can be successfully performed only if it is carried out at a very slow rate.

Table 4-6 Summary of SFU stability with respect to deployment/retrieval period and orientation

DEPLOYMENT			
Deployment Direction*	Array(s) Deployed	Deployment Period (min.)	Stability
IP	B_1 & B_2	10	Stable
OOP	B_1 & B_2	10	Stable
IP	B_1 or B_2	10	Stable
OOP	B_1 or B_2	10	Stable
RETRIEVAL			
Retrieval Direction*	Array(s) Retrieved	Retrieval Period (min.)	Stability
IP	B_1 & B_2	5	Unstable
OOP	B_1 & B_2	5	Stable
IP	B_1 & B_2	10	Unstable
OOP	B_1 & B_2	10	Stable
IP	B_1 & B_2	20	Unstable
OOP	B_1 & B_2	20	Stable
IP	B_1 or B_2	5	Unstable
OOP	B_1 or B_2	5	Unstable
IP	B_1 or B_2	10	Unstable
OOP	B_1 or B_2	10	Unstable
IP	B_1 or B_2	20	Unstable
OOP	B_1 or B_2	20	Unstable

* OOP – out-of-plane deployment/retrieval
IP – inplane deployment/retrieval

4.6 Closing Comments

Since there are numerous combinations of system parameters and initial conditions of interest, the dynamical study presented in this chapter is in no way complete. The objective here is to demonstrate the versatility of the general formulation through the parametric analysis of four different spacecraft models. They represent a wide variety of situations: (i) arbitrary orientations in circular or elliptic orbit; (ii) entirely flexible structure; (iii) spacecraft with a large number of interconnected bodies; (iv) thermally deformed members; (v) slewing members; (vi) deployable/retrievable elements; and their combinations. Although the present formulation has been modified to simulate the SFU deployment/retrieval only, its implementation for a general case is rather straightforward.

5. NONLINEAR CONTROL

5.1 Preliminary Remarks

Versatility of the general formulation in studying dynamics of a variety of spacecraft configurations was demonstrated in Chapter 4. The next logical step is to implement a control algorithm suitable for the general equations of motion which are nonlinear, coupled and nonautonomous.

Nonlinear control has received considerable attention in the robotics research, particularly during the past decade. Control strategies based on linearized system models have been found to be inadequate. The working conditions of robot arms often deviated from those predicted by linearized approaches. One possible solution was put forward by Freund [107]. The idea is to use the state feedback to decouple the nonlinear system in such a way that an arbitrary placement of poles is possible. The technique, however, was found to be difficult to apply to systems with more than three degrees of freedom. Freund [108] subsequently showed that by careful partitioning of the equations of motion, the procedure can be extended to systems with more than three degrees of freedom. However, the approach did involve simplification of the equations of motion.

Slotine and Sastry [109] applied the sliding mode theory to the control of robot manipulators. Consider a differential equation with the right-hand side discontinuous around a hypersurface. If the trajectory of the solution points toward the discontinuity, it is plausible that the trajectory eventually slides along the hypersurface. By a suitable choice of sliding surfaces, control laws can be formulated to force the manipulator to travel along a specified trajectory defined by the surfaces. However, unmodelled dynamics usually results in high frequency oscillations of the manipulator

as it slides along the surface. Slotine [110,111] improved the performance by using a filtering process with a high bandwidth for the sliding variable. Slotine and Li [112] also incorporated the sliding mode control in an adaptive PD feedback controller. The idea is to utilize the PD controller to give zero velocity error. The nonzero position errors are then eliminated through the sliding mode controller.

Inverse control, based on the Feedback Linearization Technique (FLT), was first investigated by Beijczy [113] and used by Singh and Schy [114] for rigid arm control. Spong and Vidyasagar [115,116] also used the FLT to formulate a robust control procedure for rigid manipulators. Using the FLT and given the dynamics model of the manipulator, the controller first utilizes the feedback to linearize the system followed by a linear compensator to achieve the desired system output. At times, the method is also referred to as the Computed Torque Technique which is, to be precise, is a particular case of the FLT. Spong [117] later extended the method to the control of robots with elastic joints. Advantages of this approach are twofold: (i) the control algorithm based on the FLT is simple; and (ii) the compensator design, based on a feedback linearized model, is straightforward. Recently, Modi et al. [118,119] extended the technique to include structural flexibility for a model of an orbiting manipulator system studied by Chan [15]. The technique is found to provide adequate control for both rigid as well as flexible manipulator.

The study in this chapter is based on the FLT as applied to the INdian SATellite II (INSAT II) and the MSS. The chapter begins with an introduction to the FLT. To begin with, the method is utilized to control the rigid INSAT II. Next, the more realistic situation of flexibility is tackled. Both, the quasi-open loop and quasi-closed loop control strategies are discussed. This is followed by the application of the quasi-closed loop control to the flexible INSAT II subjected to disturbances from librational motion, flexibility and thermal deformation of the appendages. Finally, the control strategy is implemented to improve pointing accuracy of the Out-of-Plane (OP) ma-

neuver of the MSS.

5.2 Feedback Linearization Technique

Consider a rigid system given by

$$\mathbf{M}(q_r,t)\ddot{\bar{q}}_r + \bar{F}(q_r,\dot{q}_r,t) = \bar{Q}(q_r,\dot{q}_r,t)\,, \tag{5.1}$$

where q_r denotes rigid generalized coordinates and $\bar{Q}(q_r,\dot{q}_r,t)$ is the nonlinear control. Let the control have the form

$$\bar{Q}(q_r,\dot{q}_r,t) = \mathbf{M}(q_r,t)\bar{v} + \bar{F}(q_r,\dot{q}_r,t)\,, \tag{5.2a}$$

$$\text{where}\quad \bar{v} = (\ddot{\bar{q}}_r)_d + \mathbf{K_v}((\dot{\bar{q}}_r)_d - \dot{\bar{q}}_r) + \mathbf{K_p}((\bar{q}_r)_d - \bar{q}_r)\,, \tag{5.2b}$$

with $(\bar{q}_r)_d$, $(\dot{\bar{q}}_r)_d$, and $(\ddot{\bar{q}}_r)_d$ representing the desired displacement, velocity and acceleration, respectively. The nonlinear control when substituted into (5.1) results in a linear closed-loop system,

$$\ddot{\bar{q}}_r = \bar{v}\,; \tag{5.3a}$$

$$\text{or}\quad (\ddot{\bar{q}}_r)_d - \ddot{\bar{q}}_r + \mathbf{K_v}((\dot{\bar{q}}_r)_d - \dot{\bar{q}}_r) + \mathbf{K_p}((\bar{q}_r)_d - \bar{q}_r) = 0\,. \tag{5.3b}$$

Since $\bar{e} = (\bar{q}_r)_d - \bar{q}_r$ denotes the displacement error, Eq. (5.3) can be rewritten as

$$\ddot{\bar{e}} + \mathbf{K_v}\dot{\bar{e}} + \mathbf{K_p}\bar{e} = 0\,. \tag{5.4}$$

The function of $\mathbf{K_v}$ and $\mathbf{K_p}$ is now obvious; they are position and velocity gains to insure asymptotic behaviour of the closed-loop system. A suitable candidate for $\mathbf{K_p}$ and $\mathbf{K_v}$ would be diagonal matrices of the form

$$\mathbf{K_p} = \begin{bmatrix} \tilde{\omega}_1^2 & & \\ & \ddots & \\ & & \tilde{\omega}_n^2 \end{bmatrix}, \qquad \mathbf{K_v} = \begin{bmatrix} 2\tilde{\omega}_1 & & \\ & \ddots & \\ & & 2\tilde{\omega}_n \end{bmatrix}, \tag{5.5}$$

leading to a globally decoupled system with each generalized coordinate behaving as a critically damped oscillator. For attitude control of a rigid spacecraft, $\mathbf{K_p}$ and $\mathbf{K_v}$ are 3×3 matrices for pitch, roll, and yaw degrees of freedom. In general, a larger value of $\tilde{\omega}_n$ gives rise to a faster response of the n-th generalized coordinate.

As an example, the FLT is applied to the INSAT II. The satellite, designed by the Indian Space Research Organization (ISRO), is scheduled to be launched this year. INSAT II is a telecommunications satellite orbiting at the geosynchronous orbit. The main body itself has the dimensions of 1.7 m $\times$ 1.8 m $\times$ 1.9 m. It has two flexible components attached to the main body. An array extending to 9 m collects solar energy to power the electronic components onboard. A 15 m solar boom attached on the opposite end is used to counterbalance the torque produced by the solar radiation pressure exerted on the array and the main body. The simulation carried out here is based on the data presented in Table 5-1 and employs the coordinate systems of Figure 5-1 .

In the simulation, the main body is taken to be rigid whereas the solar array and boom are considered to be either rigid or flexible cantilevered plates and beam, respectively. The equilibrium configuration coincides with the design configuration, i.e., $\psi_e = \phi_e = \lambda_e = 0$. To begin with, the array and boom are considered to be rigid. Figure 5-2 shows the libration response for initial displacement and velocity disturbances. In Figure 5-2a, the satellite is initially given a displacement of 1° in pitch, roll, and yaw. The simulation results show that the satellite is in an inherently unstable orientation. At the end of 1/2 orbit, the amplitudes are 5.4°, $-1.9°$, and 26.1° for pitch, roll, and yaw, respectively. In Figure 5-2b, the satellite is given an initial velocity of 1 rad/rad in the direction of pitch, roll, and yaw axes. Once again, the initial condition leads to unstable motion of the satellite with pitch, roll and yaw

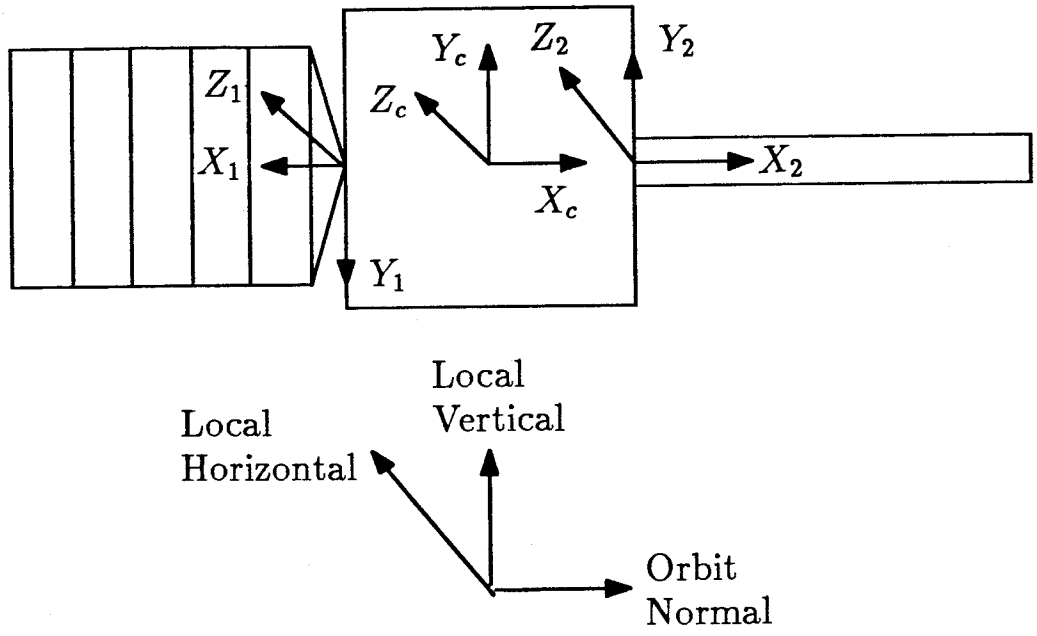

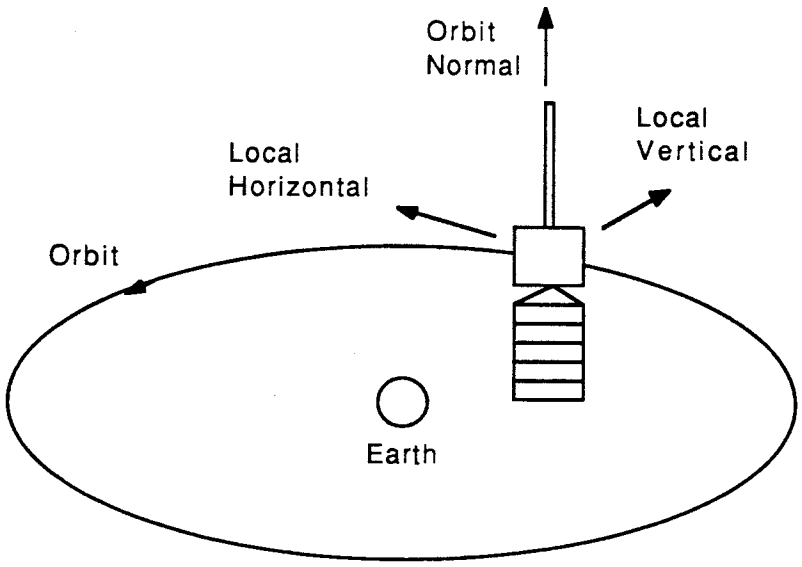

Figure 5-1 Coordinate systems and design configuration used in simulations of the INSAT II.

Table 5-1 The INSAT II data

Main Satellite (Body B_c)

l_c	=	1.7 m
m_c	=	1,035 kg
$(I_{xx})_c$	=	718 kg-m^2
$(I_{yy})_c$	=	1,960 kg-m^2
$(I_{zz})_c$	=	1,810 kg-m^2

Solar Array (Body B_1)

l_1	=	9 m
m_1	=	60 kg
$\omega_1^{1,1}$	=	0.29 Hz
$(I_{xx})_1$	=	50 kg-m^2
$(I_{yy})_1$	=	207 kg-m^2
$(I_{zz})_1$	=	257 kg-m^2

Solar Boom (Body B_2)

l_2	=	15 m
m_2	=	5 kg
ω_2^1	=	0.32 Hz
$(I_{xx})_2$	=	2
$(I_{yy})_2$	=	300 kg-m^2
$(I_{zz})_2$	=	300 kg-m^2

exceeding 90° in less than 1/2 orbit. The controlled response of the satellite subjected to the same initial disturbances is shown in Figure 5-3 . For simplicity, let

$$\mathbf{K_p} = K_p\mathbf{I}\,, \qquad \mathbf{K_v} = K_v\mathbf{I}\,,$$

where $\mathbf{I}$ is the identity matrix. It is required that

$$(\ddot{\bar{q}}_r)_d = (\dot{\bar{q}}_r)_d = (\bar{q}_r) = 0\,.$$

Since the satellite's main purpose is for telecommunications, the pointing error should not be greater than 0.1°. Three sets of control gains which would give critically damped response, are compared here: (i) $K_p = 36 \times 10^4, K_v = 1.2 \times 10^3$; (ii) $K_p = 64 \times 10^4, K_v = 1.6 \times 10^3$; and (iii) $K_p = 100 \times 10^4, K_v = 2.0 \times 10^3$. With an initial displacement of 1° in each direction, these gains are capable to reduce the error to about 0.1° in less than 2 minute (or 0.001 orbit). The critically damped

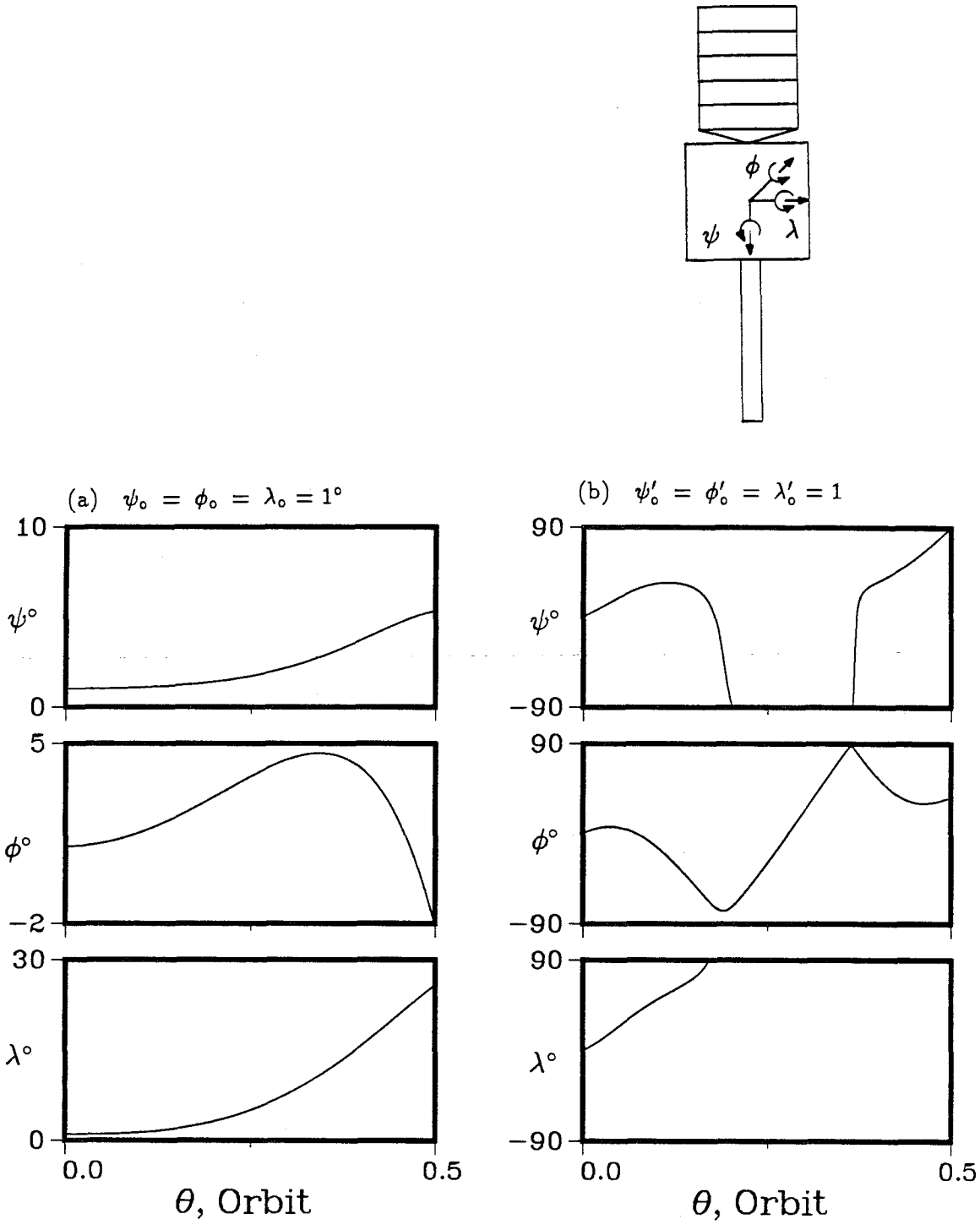

Figure 5-2 Uncontrolled response of the rigid INSAT II showing instability of the system: (a) $\psi_o = \phi_o = \lambda_o = 1°$; (b) $\psi'_o = \phi'_o = \lambda'_o = 1$.

response is shown in Figure 5-3a. Since the same set of gains are applied to the librational degrees of freedom, the response is identical in pitch, roll, and yaw. In general, the larger the K_p, and hence K_v, the faster the response. The errors at the end of 0.001 orbit are 0.11°, 0.04°, and 0.01°, for $K_p = 36 \times 10^4$, 64×10^4, and 100×10^4, respectively. Figure 5-3b shows the critically damped response with an initial condition of 1 rad/rad in the pitch, roll, and yaw. With $K_p = 36 \times 10^4$, the librational amplitude increases to a mere 0.04° and then decreases to 0.009° at the end of 0.001 orbit. The corresponding values for $K_p = 64 \times 10^4$ are 0.03° and 0.002° whereas for $K_p = 100 \times 10^4$, they are only 0.02° and 0.001°, respectively.

Even though the response for each degree of freedom is identical, the control effort for each generalized coordinate is different due to differences in inertia. For the controlled response of Figure 5-3a, variations in the effort about the three axes, denoted by Q_ψ, Q_ϕ, and Q_λ, are shown in Figure 5-4 a. Since the inertia about the pitch axis is considerably smaller than that for the roll or yaw, the control torque Q_ψ is the smallest among the three. For $K_p = 36 \times 10^4$, an initial torque of -0.06 Nm is required which reaches a peak of 0.01 Nm before the magnitude finally decreases with the pitch attitude. A similar trend can be observed in the Q_ϕ variation: an initial -0.24 Nm effort gradually reaches a peak value of 0.04 Nm before the magnitude finally decreases. At the end of 0.001 orbit, the pitch and roll efforts required are negligible. Since the inertias about roll and yaw axes differ by about 5%, the magnitude and time history of control torque Q_λ are similar to those of Q_ϕ.

The control effort variation corresponding to the response in Figure 5-3b is shown in Figure 5-4b. Although the controlled response in Figures 5-3a and 5-3b are different, the corresponding effort time histories for the two cases are similar. For $K_p = 36 \times 10^4$, initial torque values of -0.007, -0.027, and -0.028 Nm are required

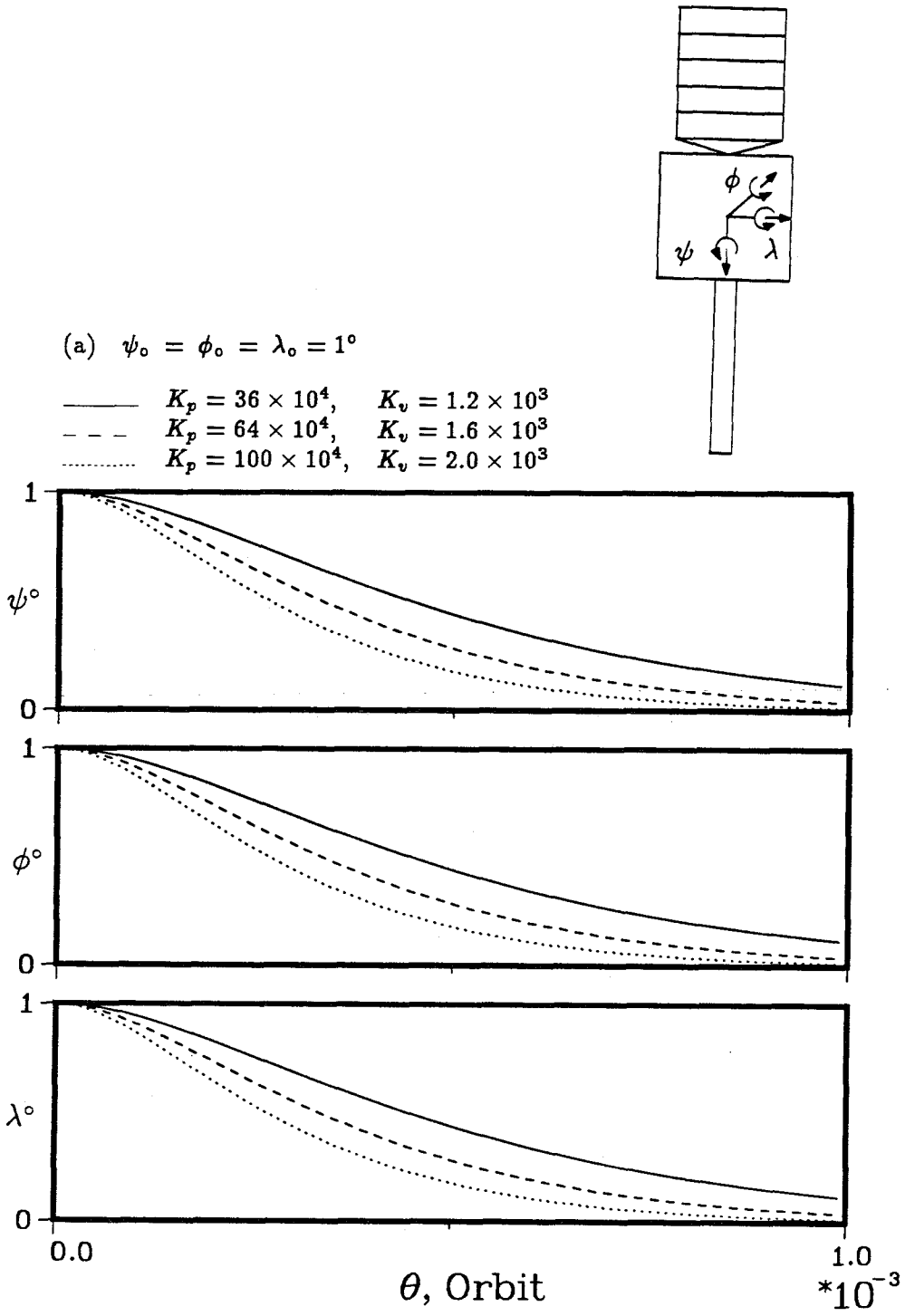

Figure 5-3 Controlled librational response of the INSAT II for three different sets of gains: (a) $\psi_o = \phi_o = \lambda_o = 1°$.

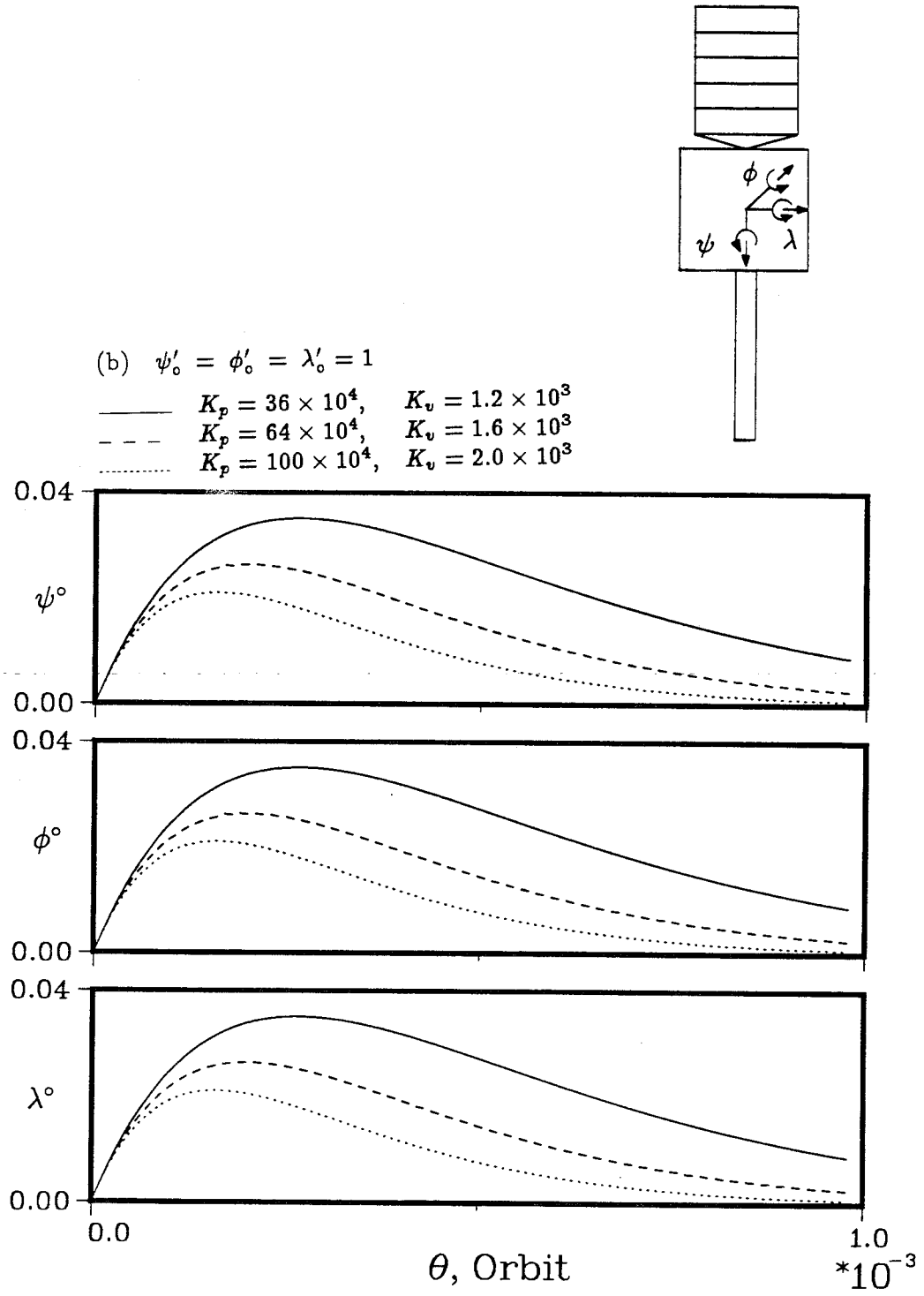

Figure 5-3 Controlled librational response of the INSAT II for three different sets of gains: (b) $\psi'_o = \phi'_o = \lambda'_o = 1$.

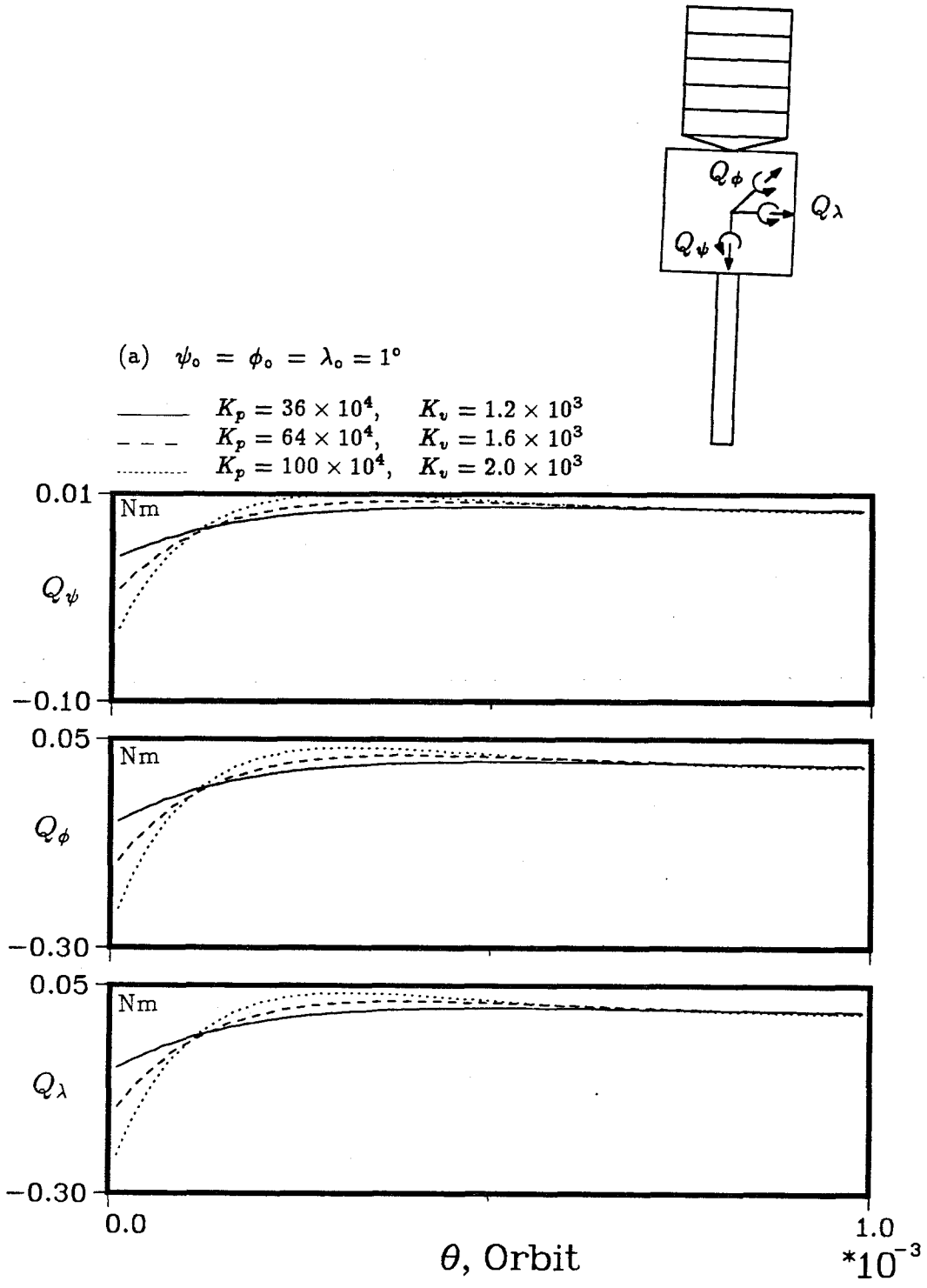

Figure 5-4 Comparison of control efforts for three different sets of gains used in the INSAT II attitude control: (a) $\psi_o = \phi_o = \lambda_o = 1°$.

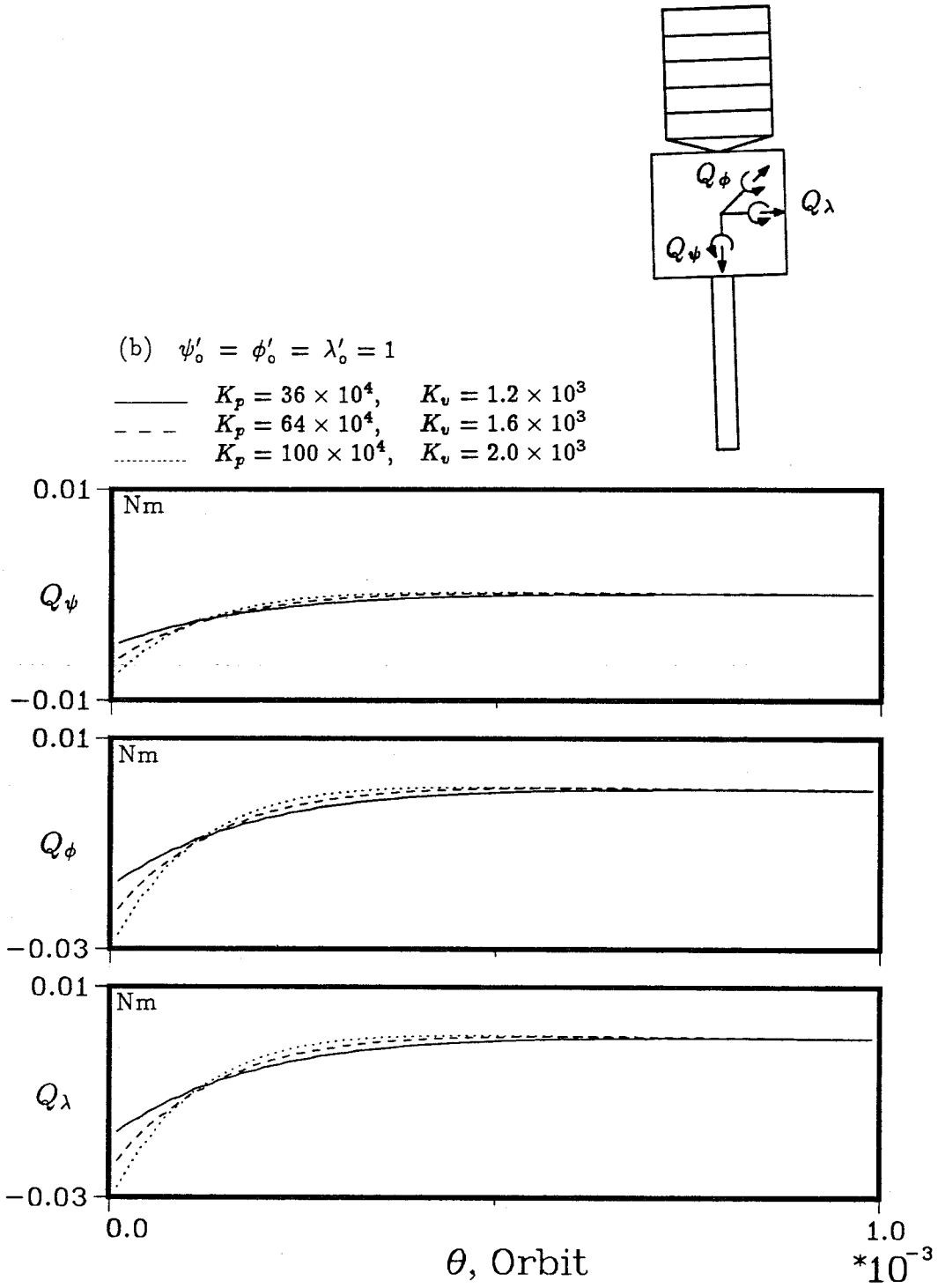

Figure 5-4 Comparison of control efforts for three different sets of gains used in the INSAT II attitude control: (b) $\psi'_o = \phi'_o = \lambda'_o = 1$.

for pitch, roll, and yaw control, respectively. Subsequently, the torque decreases steadily such that at the end of 0.001 orbit, the effort required is negligible.

One disadvantage of the FLT is the difficulty in predicting the torque requirement. From Eq. (5.2), it is apparent that the control torque has two components with one a linear function of the gain and states. The second component, which depends on the equations of motion, is a highly nonlinear function of the states. In general, the larger the gain, the faster the response; however, this does not necessarily imply higher control effort. For instance, for $K_p = 36 \times 10^4$, the direction of Q_λ is clockwise; however, the direction changes when K_p is reduced by four orders (not shown).

5.3 Control Implementation Procedures

In general, dynamics of a flexible spacecraft with $\bar{q}_r$ and $\bar{q}_f$ corresponding to librational and vibrational generalized coordinates, respectively, is governed by

$$\begin{bmatrix} \mathbf{M_{rr}} & \vdots & \mathbf{M_{rf}} \\ \cdots & \cdots & \cdots \\ \mathbf{M_{fr}} & \vdots & \mathbf{M_{ff}} \end{bmatrix} \begin{Bmatrix} \bar{q}_r \\ \cdots \\ \bar{q}_f \end{Bmatrix} + \begin{Bmatrix} \bar{F}_r \\ \cdots \\ \bar{F}_f \end{Bmatrix} = \begin{Bmatrix} \bar{Q}_r \\ \cdots \\ \bar{Q}_f \end{Bmatrix} . \tag{5.6}$$

Here $\mathbf{M_{rr}}(q_r)$ is a 3×3 submatrix for the librational degrees of freedom; $\mathbf{M_{rf}}(q_r, q_f)$, of dimension $3 \times N_q - 3$, represents the coupling between the rigid and flexible generalized coordinates; $\mathbf{M_{fr}} = \mathbf{M_{rf}}^T$; $\mathbf{M_{ff}}(q_f)$ is a $N_q - 3 \times N_q - 3$ submatrix for the flexible degrees of freedom only. $\bar{F}_r$ and $\bar{F}_f$ are 3×1 and $N_q - 3 \times 1$ vectors, respectively, representing first and second order coupling terms. Assuming only the librational degrees of freedom to be observable, the control force $\bar{Q}_f$ is not applicable and hence set to zero. The objective is to determine $\bar{Q}_r$ such that the closed-loop system is linearized. Rewriting Eq. (5.6) into two sets of equations and with $\bar{Q}_f = 0$ gives:

$$\mathbf{M_{rr}}\ddot{\bar{q}}_r + \mathbf{M_{rf}}\ddot{\bar{q}}_f + \bar{F}_r = \bar{Q}_r \; ; \tag{5.7a}$$

$$\mathbf{M_{fr}}\ddot{\bar{q}}_r + \mathbf{M_{ff}}\ddot{\bar{q}}_f + \bar{F}_f = 0\,; \tag{5.7b}$$

which can be solved for $\bar{q}_r$ and $\bar{q}_f$:

$$\tilde{\mathbf{M}}\ddot{\bar{q}}_r + \tilde{\mathbf{F}} = \bar{Q}_r\,; \tag{5.8a}$$

$$\ddot{\bar{q}}_f = -\mathbf{M_{ff}}^{-1}\mathbf{M_{fr}}\ddot{\bar{q}}_r - \mathbf{M_{ff}}^{-1}\bar{F}_f\,; \tag{5.8b}$$

where: $\tilde{\mathbf{M}} = \mathbf{M_{rr}} - \mathbf{M_{rf}}\mathbf{M_{ff}}^{-1}\mathbf{M_{fr}}\,;$

$$\tilde{\mathbf{F}} = \bar{F}_r - \mathbf{M_{rf}}\mathbf{M_{ff}}^{-1}\bar{F}_f\,.$$

As in the case of Eq. (5.2), a suitable choice of $\bar{Q}_r$ would be

$$\bar{Q}_r(q_r, q_f, \dot{q}_r, \dot{q}_f, t) = \tilde{\mathbf{M}}(q_r, q_f, t)\bar{v} + \tilde{\mathbf{F}}(q_r, q_f, \dot{q}_r, \dot{q}_f, t)\,,$$

$$\text{with} \quad \bar{v} = (\ddot{\bar{q}}_r)_d + \mathbf{K_v}((\dot{\bar{q}}_r)_d - \dot{\bar{q}}_r) + \mathbf{K_p}((\bar{q}_r)_d - \bar{q}_r)\,.$$

Now the controlled equations of motion become:

$$\ddot{\bar{q}}_r = \bar{v}\,; \tag{5.9a}$$

$$\ddot{\bar{q}}_f = -\mathbf{M_{ff}}^{-1}\mathbf{M_{fr}}\bar{v} - \mathbf{M_{ff}}^{-1}\bar{F}_f\,. \tag{5.9b}$$

Note that

$$\bar{Q}_r = \tilde{\mathbf{M}}(\ddot{\bar{q}}_r)_d + \tilde{\mathbf{F}} + \tilde{\mathbf{M}}(\mathbf{K_v}\dot{e} + \mathbf{K_p}e)\,,$$

which can be visualized as a combination of two controllers: primary ($\bar{Q}_{r,p}$) and secondary ($\bar{Q}_{r,s}$), where

$$\bar{Q}_{r,p} = \tilde{\mathbf{M}}(\ddot{\bar{q}}_r)_d + \tilde{\mathbf{F}}\,; \tag{5.10a}$$

$$\bar{Q}_{r,s} = \tilde{\mathbf{M}}(\mathbf{K_v}\dot{e} + \mathbf{K_p}e)\,. \tag{5.10b}$$

The function of the primary controller is to offset the nonlinear effects inherent in the rigid degrees of freedom; whereas the secondary controller ensures robust behaviour against the error.

To evaluate the control effort $\bar{Q}_r$ required, *a priori* information of $\tilde{\mathbf{M}}$ and $\tilde{\mathbf{F}}$ is needed. In turn, calculation of $\tilde{\mathbf{M}}$ and $\tilde{\mathbf{F}}$ requires the knowledge of $\bar{q}_f$ and $\dot{\bar{q}}_f$. To this end, two schemes, Quasi-Open Loop Control (QOLC) and Quasi-Closed Loop Control (QCLC), are suggested by Modi et al. [118].

5.3.1 Quasi-open loop control

In this scheme, the flexible coordinates are evaluated off-line, i.e. integration of Eq. (5.9b) is performed independently and with $\bar{q}_r$ substituted with $(\bar{q}_r)_d$. The main advantage of the scheme is a reduced computation effort. Under this scheme, discrepancies between the calculated and actual flexible coordinates would exist. Hence, the success of the scheme depends on the robustness of the controller.

5.3.2 Quasi-closed loop control

Under this scheme, both the rigid and flexible coordinates are evaluated simultaneously, i.e. Eqs. (5.9a) and (5.9b) are integrated concurrently. The disadvantage of the scheme is a relatively large computational effort as compared to the QOLC. On the other hand, the QCLC is less sensitive to system uncertainties.

Block diagrams for both the control schemes are shown in Figures 5-5a and 5-5b. Implementation of the QCLC into the present formulation is straightforward. The program can remain as it is with the inclusion of the subprogram CNTROL. The function of the subprogram is to partition the $\mathbf{M}$ matrix and then evaluate the $\tilde{\mathbf{M}}$ and $\tilde{\mathbf{F}}$. In contrast, the QOLC scheme requires considerable modification of the program codes. With this in mind, the present study is limited to the QCLC of the flexible INSAT II only.

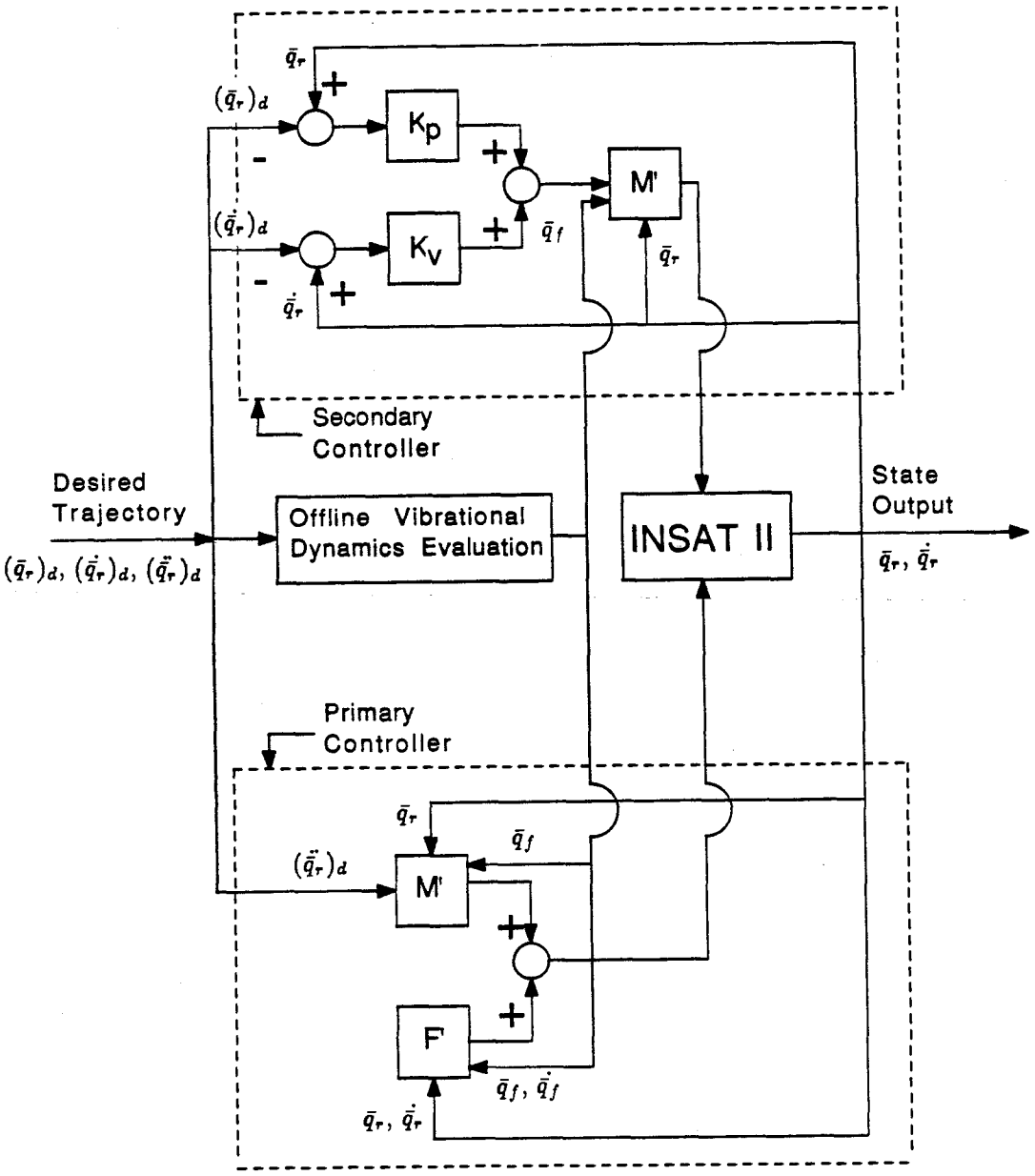

Figure 5-5 Block diagram for control of the flexible INSAT II: (a) quasi-open loop control.

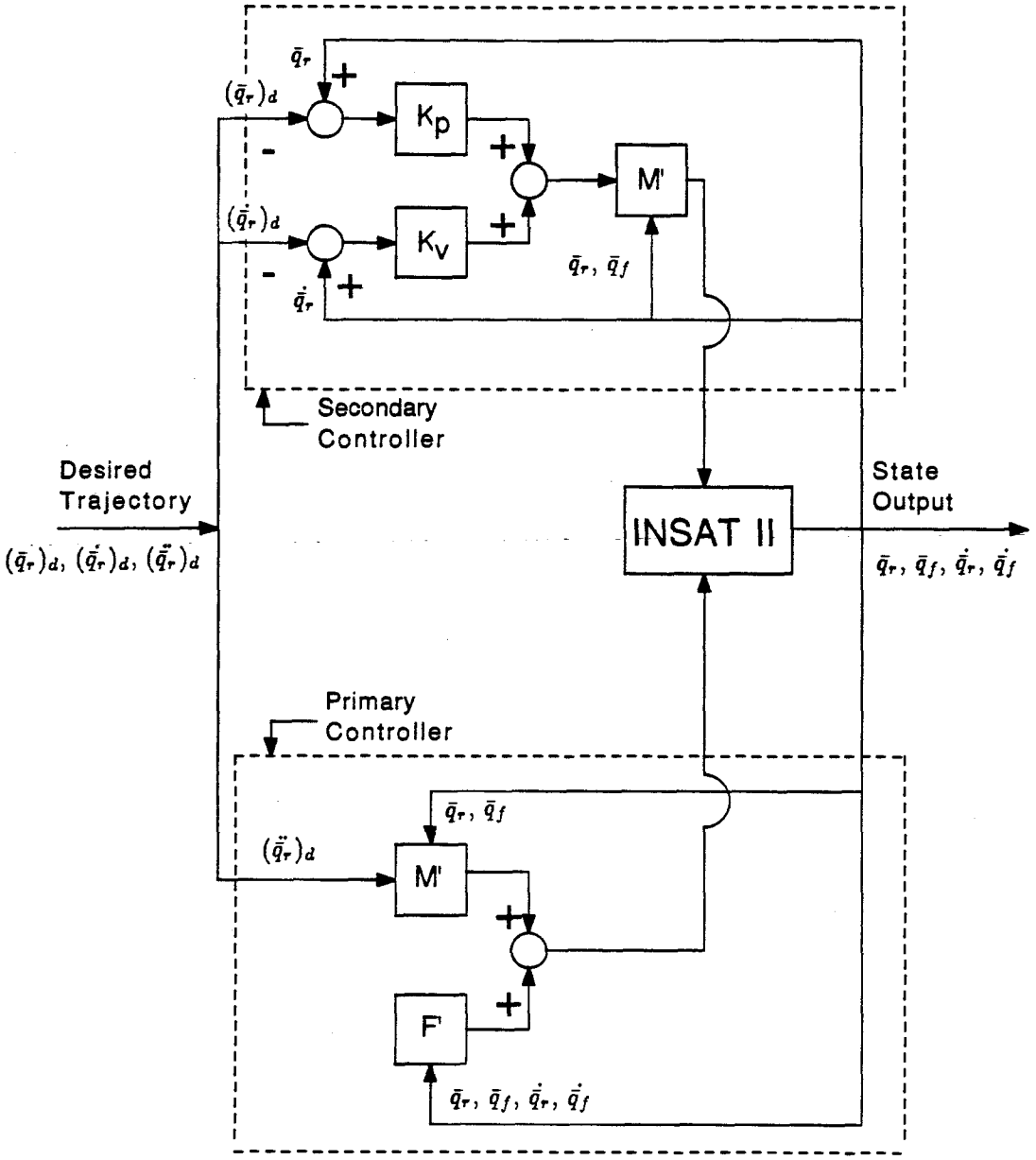

Figure 5-5 Block diagram for control of the flexible INSAT II: (b) quasi-closed loop control.

5.4 Application of the Quasi-closed Loop Control to INSAT II

With only the first mode of vibration in the system discretization process, the generalized coordinates for simulation are:

$$\bar{q}_r = \begin{Bmatrix} \psi \\ \phi \\ \lambda \end{Bmatrix} ; \qquad \bar{q}_f = \begin{Bmatrix} \underline{H}_1^{1,1} \\ \underline{P}_2^1 \\ \underline{Q}_2^1 \end{Bmatrix} ;$$

$$N_q = 6 .$$

Figure 5-6 shows system response of the INSAT II subjected to the same initial disturbance as in Figure 5-2a. With this initial condition, flexibility does not appear to have any influence on the librational motion as pitch, roll and yaw responses remain the same as in Figure 5-2a. Similarly, the librational disturbance hardly excites the flexible motion of the appendages. Maximum tip deflection of the solar array or boom is of the order of 10^{-6} cm.

Control is now applied to the system using the same three sets of gains as in Figure 5-3. For the librational response, integration of Eq. (5.9a) is essentially the same as that of Eq. (5.3a). For the same initial conditions, the controlled librational response would be identical to that in Figure 5-3a. The controlled response accounting for appendage flexibility is shown in Figure 5-7 . Note, each control gain setting affects the vibrational behaviour differently. In general, application of the control results in higher initial vibration amplitudes. For $K_p = 100 \times 10^4$, the peak amplitude of the array and boom are 0.054 cm and 0.073 cm, respectively, an increase of over four orders. As the control effort diminishes with attitude, the amplitude of vibration decreases; however, the rate of decay is minimal.

Figure 5-8 shows the control torque variation to give the desired rigid body response. Comparing with Figure 5-4a, the time history and the magnitude of the

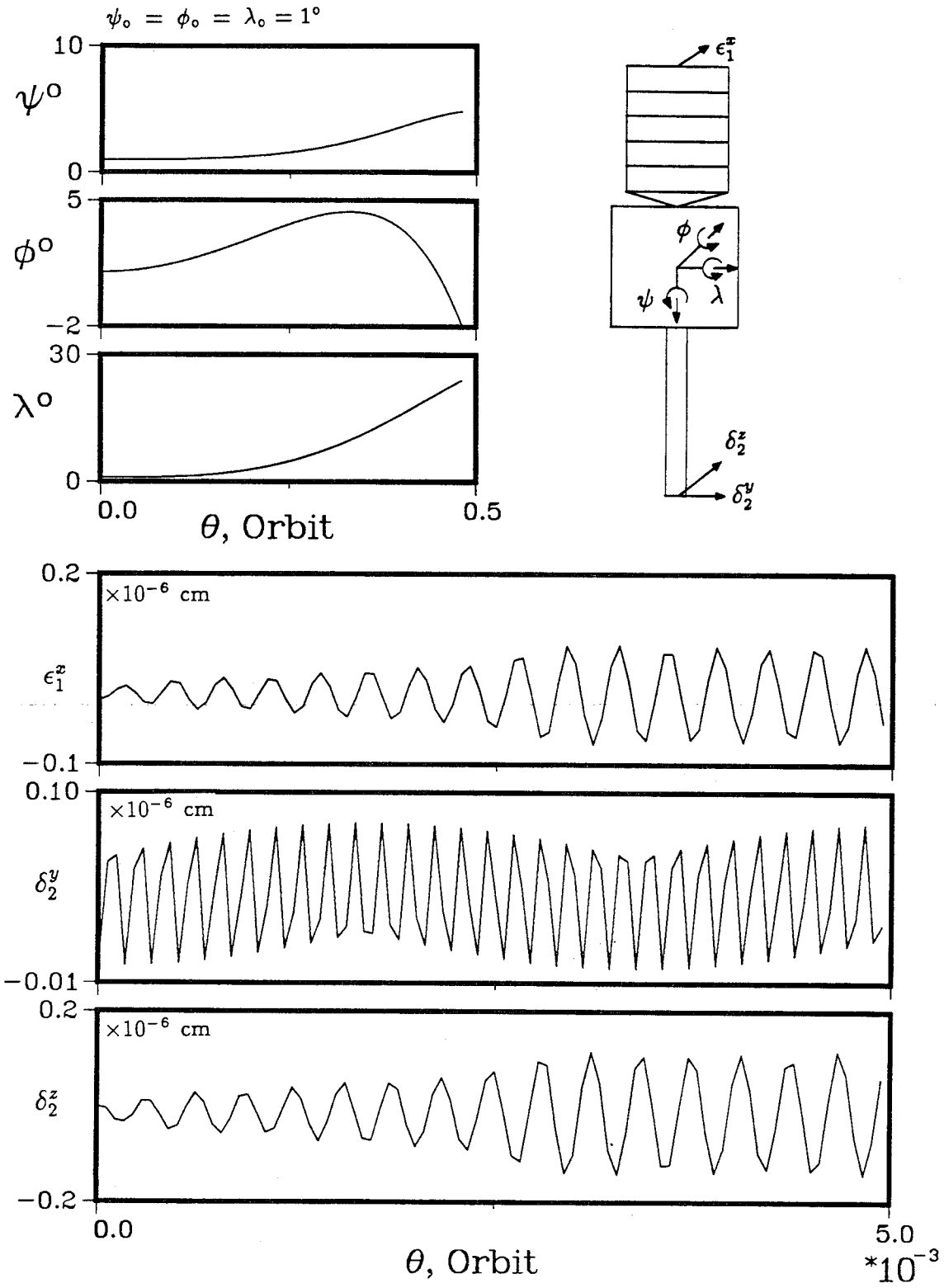

Figure 5-6 Librational and vibrational responses of the uncontrolled INSAT II with initial condition of $\psi_o = \phi_o = \lambda_o = 1°$.

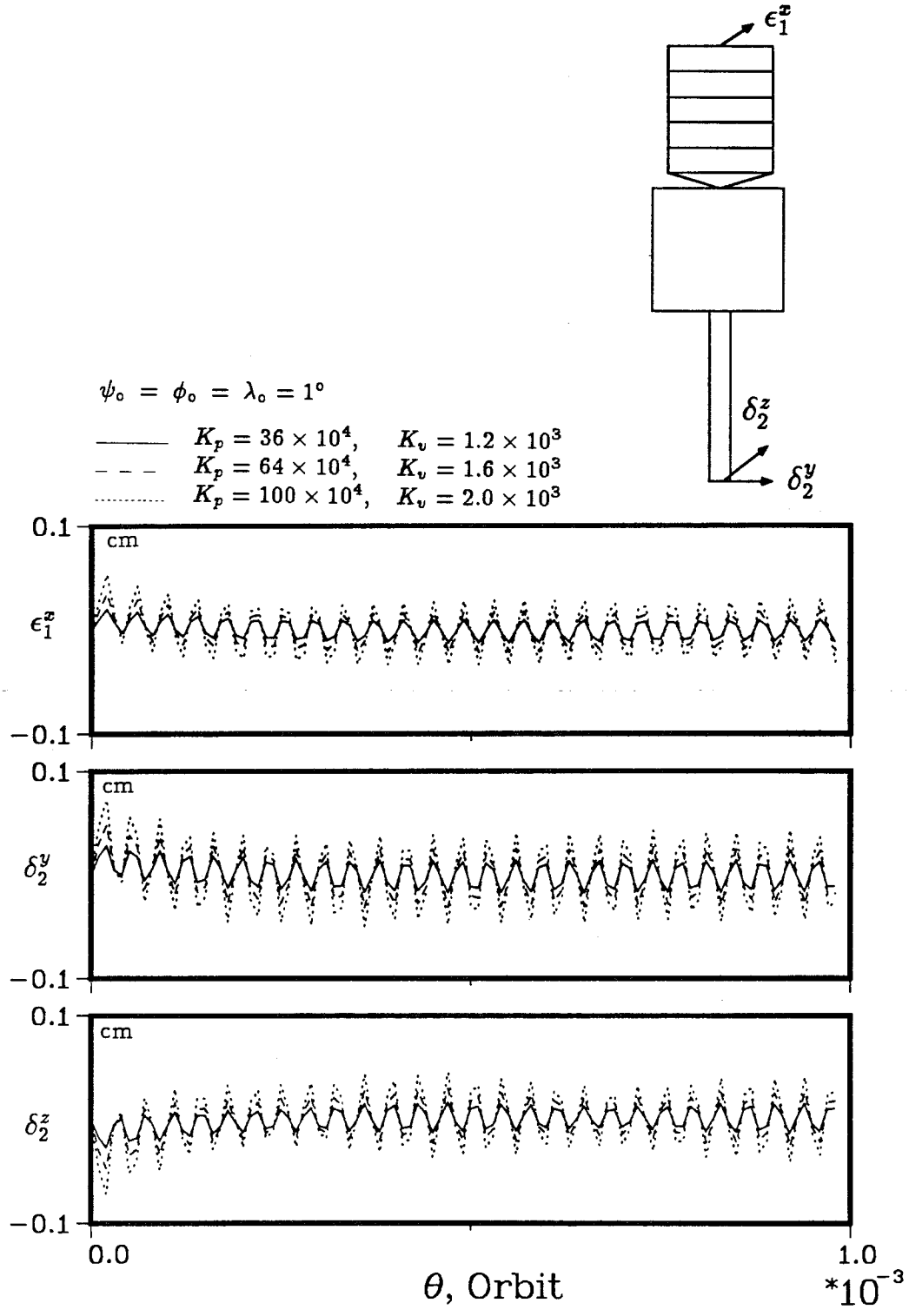

Figure 5-7 Variation of tip deflections of the INSAT II flexible appendages showing the effect of control gains.

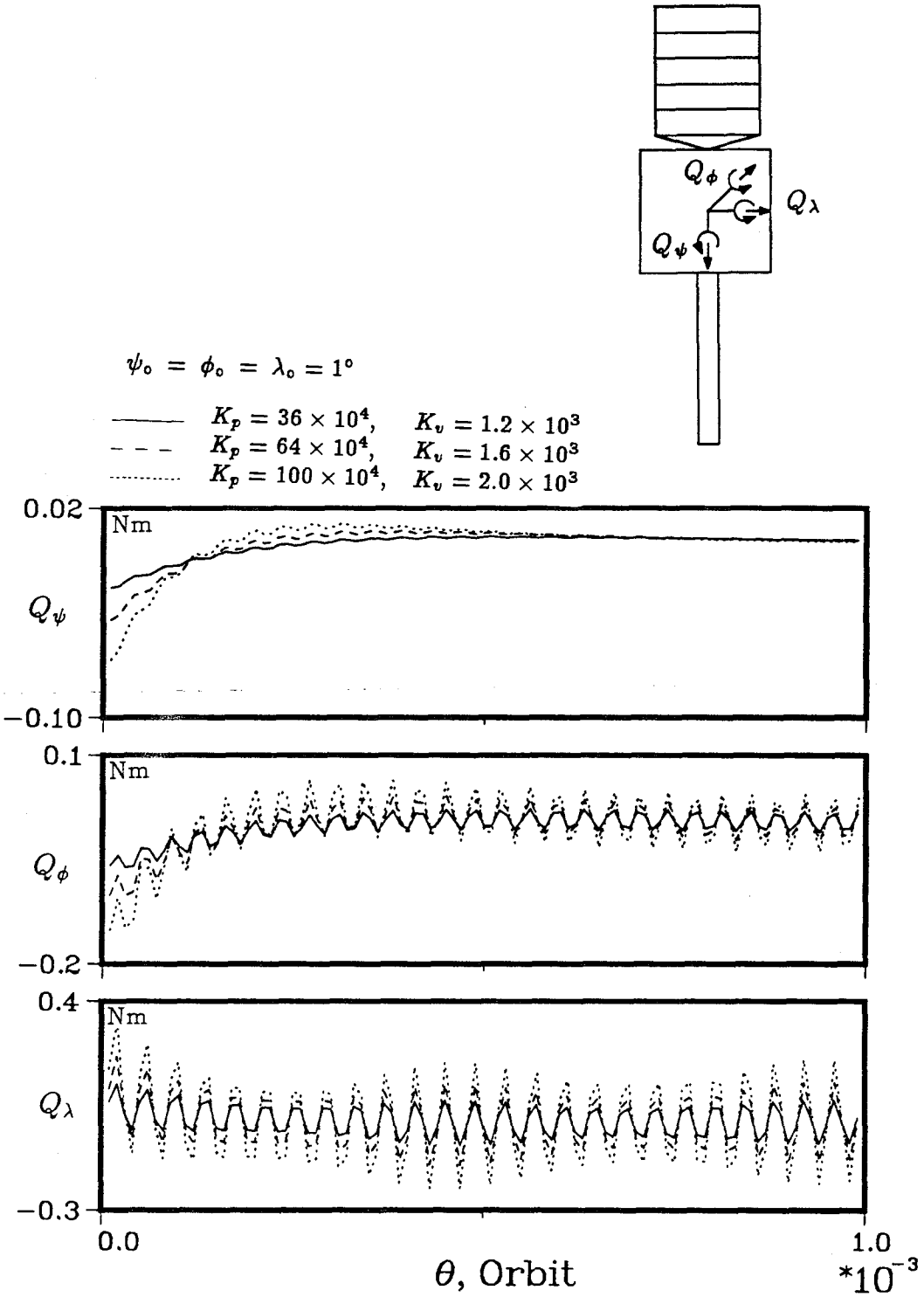

Figure 5-8 Control effort variations for the INSAT II subjected to three different combinations of control gains.

control torque Q_ψ is almost the same as before. For $K_p = 100 \times 10^4$, an initial torque of -0.067 Nm is required as compared to -0.061 Nm for the rigid spacecraft. However, flexibility has some influence on Q_ϕ and Q_λ. Since the beam vibration in the local vertical direction (δ_2^y) is about the roll axis, Q_ϕ can be expected to be affected. Similarly, both the array and beam vibrations in the local horizontal direction (ϵ_1^x and δ_2^z) are expected to influence Q_λ. It is, therefore, reasonable that the control torques Q_ϕ and Q_λ both oscillate at high frequencies to compensate for the vibration. The general trend for Q_ψ is the same for both rigid and flexible configurations of the satellite. In fact, in the present case, flexibility actually aids in reducing the maximum torque. For $K_p = 100 \times 10^4$, -0.235 Nm is needed for a rigid satellite but only -0.151 Nm is required when flexibility of the appendages is accounted for. On the other hand, the appendage flexibility results in higher Q_λ. For $K_p = 36 \times 10^4$, initial torque for yaw control is 0.329 Nm in the present case as compared to -0.236 Nm for the rigid spacecraft. Note that flexibility results in the reversal of the torque direction. As the vibration magnitude is gradually damped through control, the torque required also decreases. Again, as the vibration amplitude diminishes at a slow rate, so do the control torques Q_ϕ and Q_λ.

The effect of reduced stiffness of the flexible members is shown in Figure 5-9. Here, both the array and boom stiffnesses have been reduced to 10% of the design value. For the same initial librational disturbance, the rigid body response remains essentially unaffected by the flexibility. The array and boom vibration, however, have increased by about two orders. Note also that, with the beam natural frequency reduced ten times, it is now close to that of gravitational disturbance resulting in the beat response in δ_2^y. For the same three sets of control gains, the librational response was again observed to be the same as in Figure 5-3a. The corresponding vibrational behaviour is as shown in Figure 5-10. The controllers again have a significant influence on the

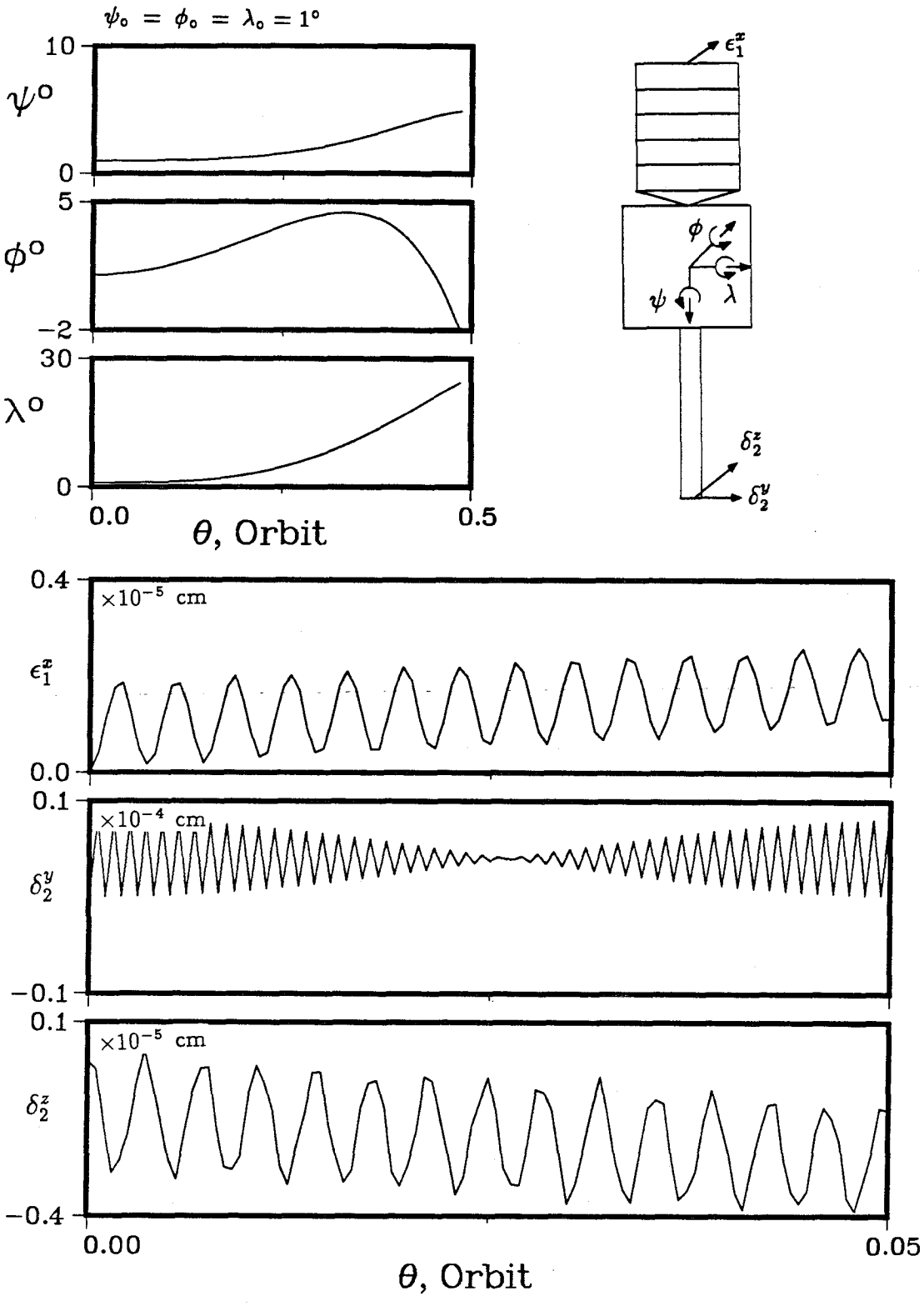

Figure 5-9 Response of the uncontrolled INSAT II, with reduced stiffness of the appendages, to the initial conditions of $\psi_o = \phi_o = \lambda_o = 1°$.

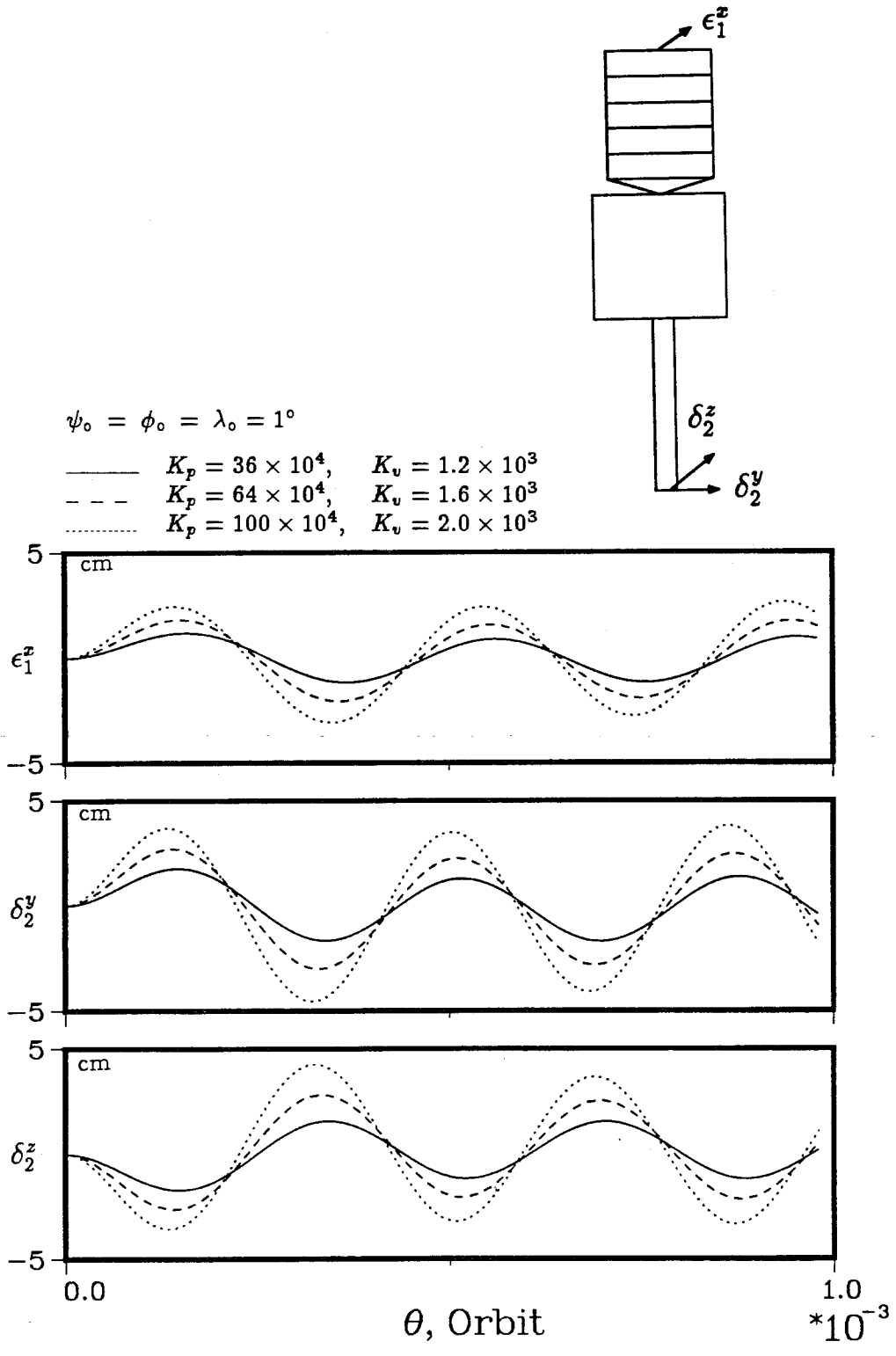

Figure 5-10 Vibrational response of the INSAT II with flexible appendages of reduced stiffness.

appendage motion leading to a significant increase (over four orders) in vibration amplitude. For $K_p = 100 \times 10^4$, the peak amplitude of ϵ_1^x, δ_2^y and δ_2^z are 3.1 cm, 4.5 cm and 4.3 cm, respectively. The values are about two orders of magnitude higher than the corresponding ones with the design stiffnesses (0.054 cm, 0.073 cm, and 0.071 cm). The time histories of Q_ψ and Q_ϕ are similar to those observed for the design case (i.e. without any reduction in stiffness), except for the amplitude modulation which now occur at lower frequencies (Figure 5-11). However, Q_λ now oscillates at constant amplitude because ϵ_1^x and δ_2^z do not exhibit any sign of decay. For $K_p = 100 \times 10^4$, Q_λ varies in the range of ± 0.207 Nm.

The performance of the controller under thermal disturbances on the array and boom is next investigated. Figure 5-12 shows the response of the satellite induced by the thermal deformations of the array and boom. The rigidity of the array and boom is again taken to be 10% of the design value. Thermal reference length parameters, L_1^* (for the array) and L_2^* (for the boom), are chosen to be 0.22% and 0.13%, respectively. With these values, maximum tip deflections of the array and boom due to thermal effect would be 1 cm. As can be seen, thermal deformations totally change the librational response of the satellite, with the pitch and roll most severely affected. In less than 0.5 orbit, the satellite starts to tumble (the pitch angle reaches $-90°$). The fast deterioration of the attitude is due to large amplitudes of array and boom vibrations. Without thermal deformation, the maximum displacements are 0.2×10^{-5} and 0.1×10^{-4} cm for the array and boom, respectively. These values increase to 1.7 and 3.6 cm in the presence of thermal deformations (from the deformed equilibrium state). With the inclusion of an initial libration disturbance of $1°$ in pitch, roll, and yaw, Figure 5-13 shows that the system response is almost identical to that of Figure 5-12.

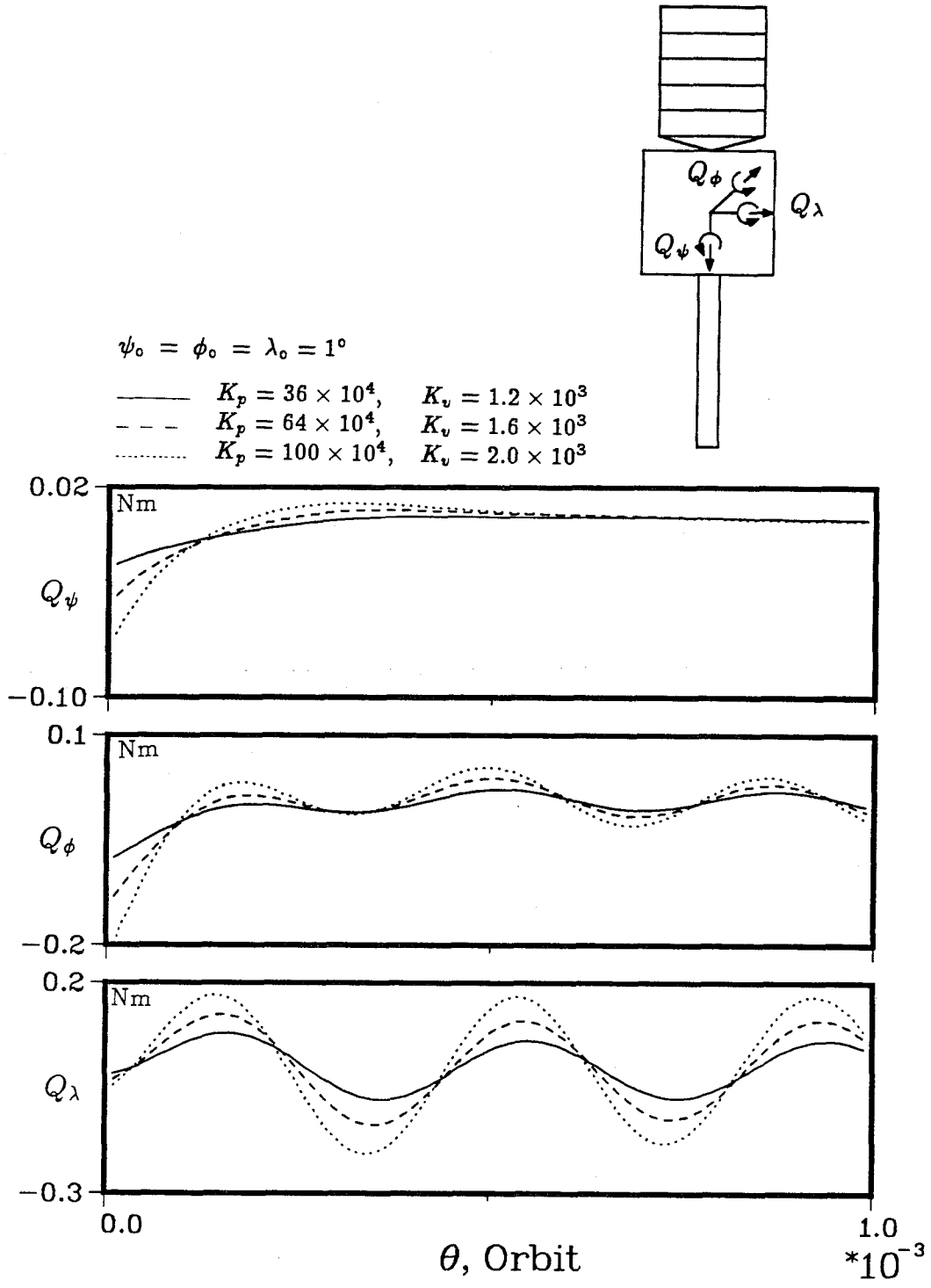

Figure 5-11 Comparison of the control effort variations for the INSAT II with appendages of reduced stiffness.

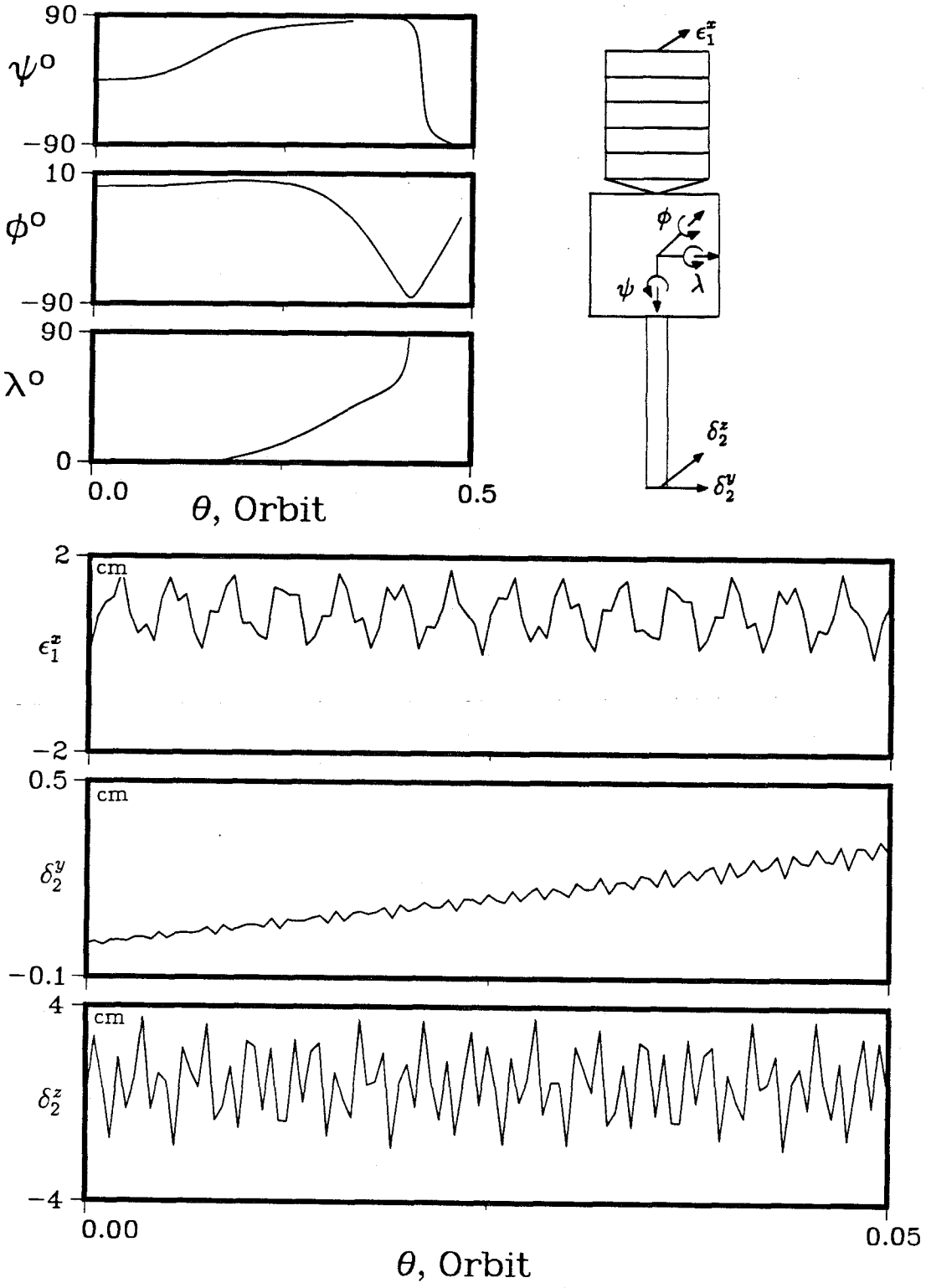

Figure 5-12 Librational and vibrational responses of the INSAT II showing the effect of thermally deformed appendages.

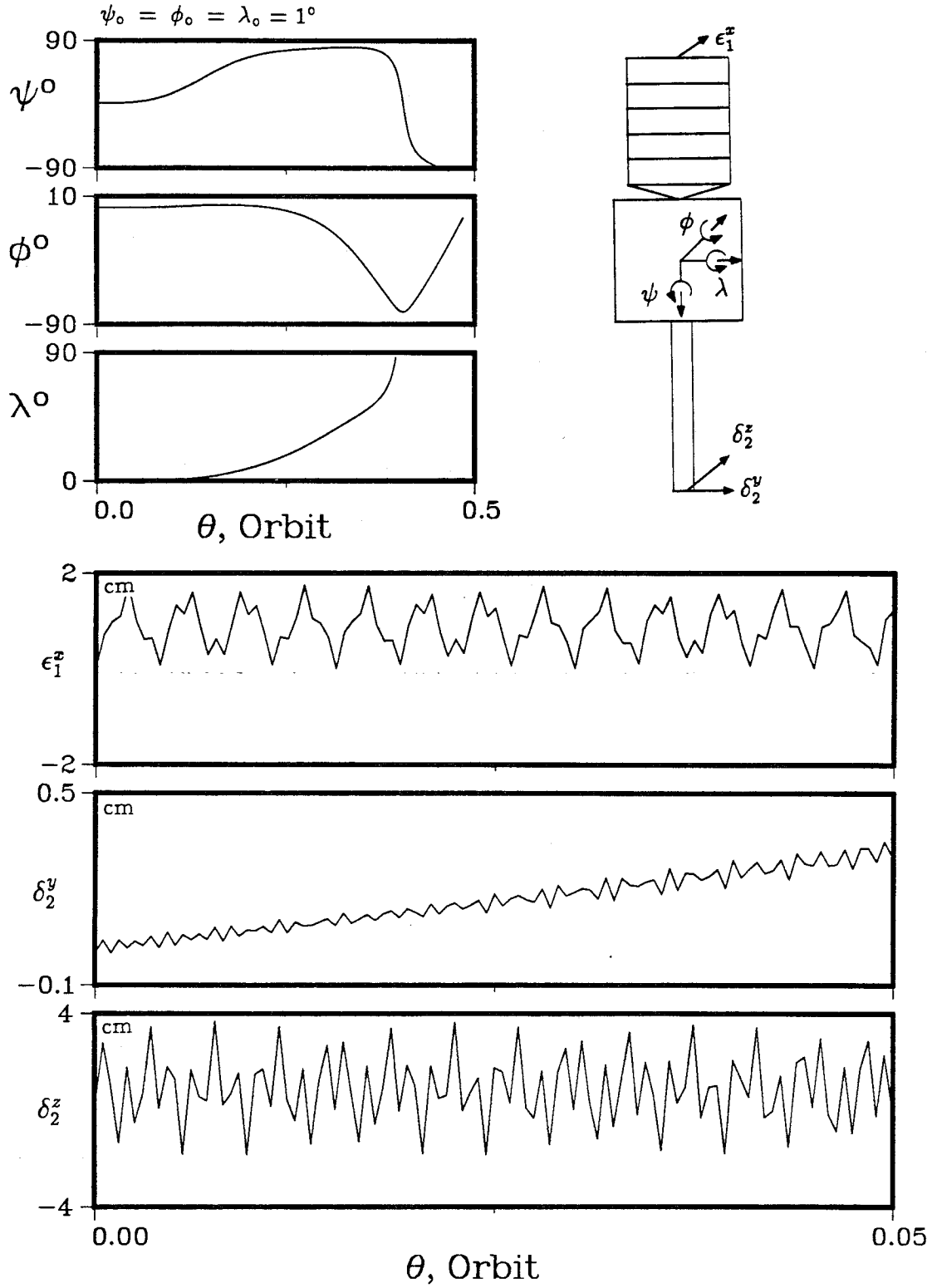

Figure 5-13 Dynamics of the INSAT II with thermally deformed appendages and initial conditions of $\psi_o = \phi_o = \lambda_o = 1°$.

Control is next applied to the case of Figure 5-13, i.e. thermal effect coupled with initial disturbance. Application of the control would once again result in the same librational response as in Figure 5-3a. The vibrational dynamics of the controlled satellite is shown in Figure 5-14 . Note, the response trends of the appendages are essentially the same as in Figure 5-10 indicating dominant influence of the controllers to offset the effect of thermal deformations. A typical control torque variation is shown in Figure 5-15 . As the attitude of the satellite increases rapidly without control, it is reasonable that larger control torques are needed to force the satellite into the desired trajectory. The increase is approximately 5% for Q_ψ and Q_ϕ, and about 15% for Q_λ. For instance, Q_λ increases from ± 0.207 Nm to ± 0.237 Nm for $K_p = 100 \times 10^4$.

The maximum control effort required for the cases studied is summarized in Table 5-2 .

5.5 Application of the Quasi-closed Loop Control to MSS

In Section 4.4, the performance of the Mobile Servicing System (MSS) during the robotic arm maneuver was discussed. The pitch, roll, and yaw motion excited by the Out-of-Plane (OP) maneuvers, resulted in poor pointing accuracy of the robot arm as compared to the InPlane (IP) maneuver. It is apparent that to improve the performance of the OP maneuver, the attitude of the MSS has to be first controlled. The objective here is to assess effectiveness of the QCLC as applied to the attitude control of the MSS.

The control gains selected in the present study are $K_p = 1.0$ and $K_v = 2.0$. As will be pointed out later, even such small gains are capable of improving the system performance significantly. To assess effectiveness of the controller, the error is purposely allowed to build up over an arbitrary duration before implementing the

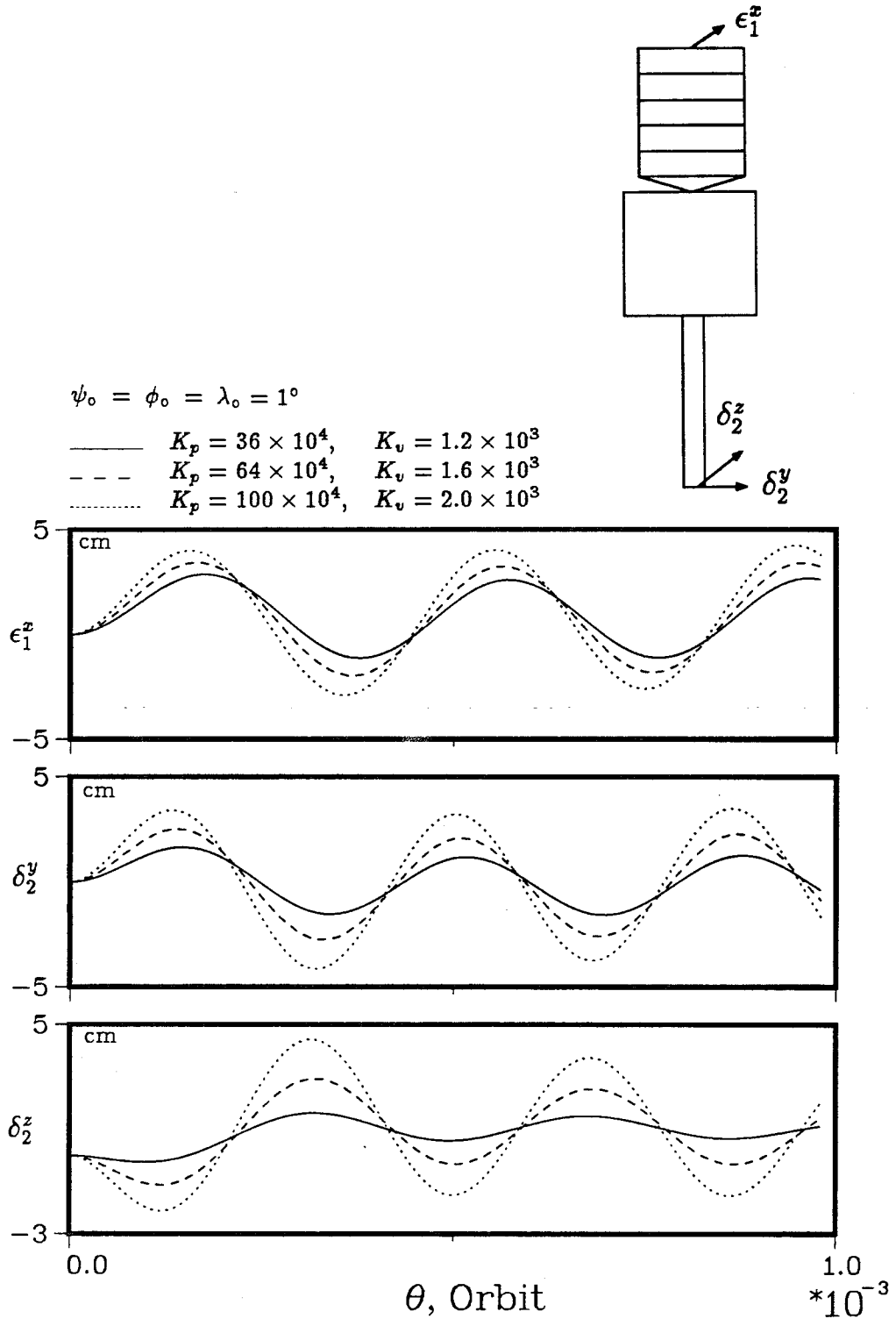

Figure 5-14 Tip deflections of the thermally deformed INSAT II appendages showing the effect of control gains.

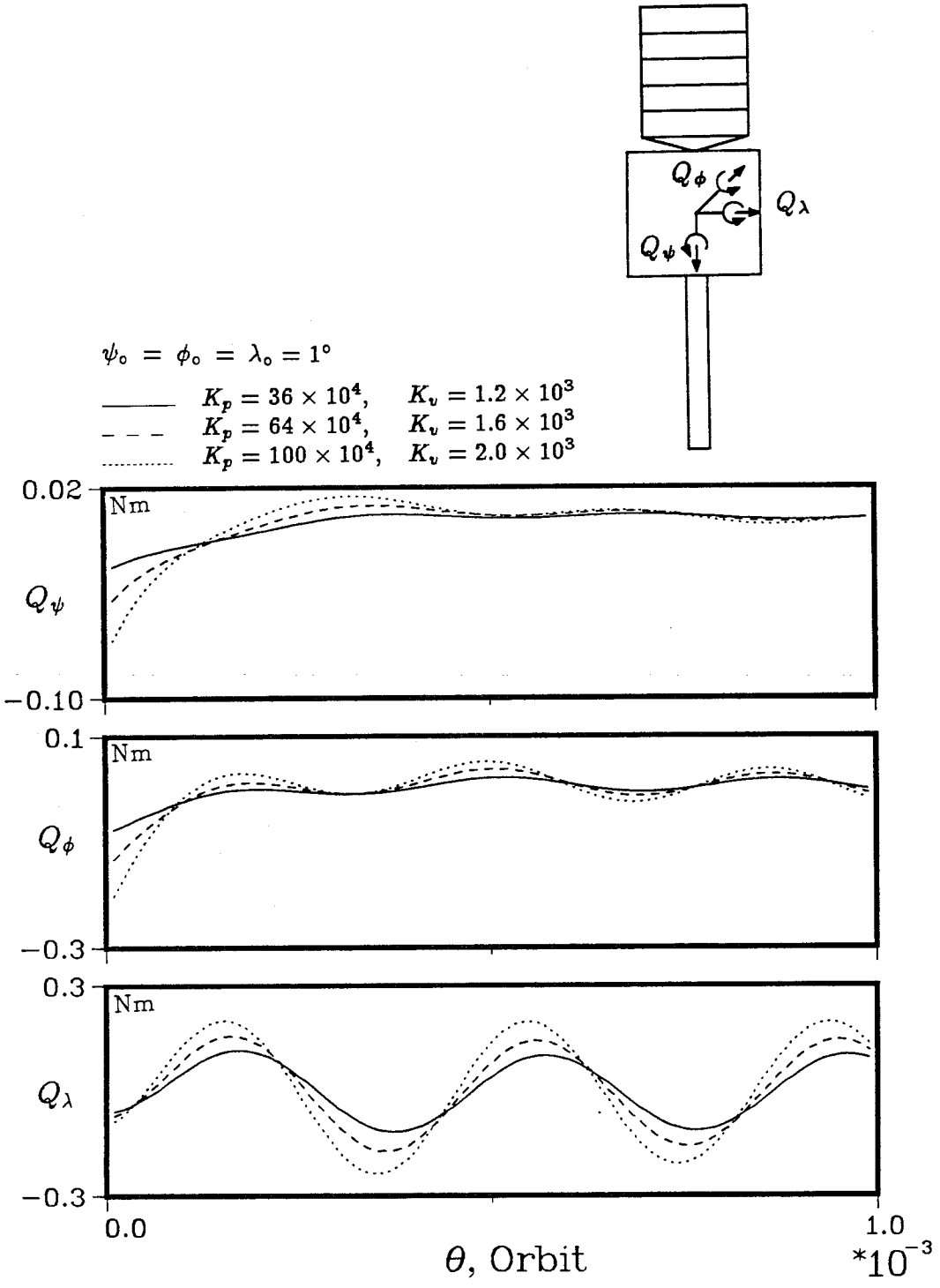

Figure 5-15 Plots of control efforts required for the INSAT II with thermally deformed appendages.

Table 5-2 Summary of maximum Q_ψ, Q_ϕ, and Q_λ required for the cases studied

Gain	Q_ψ Nm*	Q_ϕ Nm*	Q_λ Nm*
Rigid array & boom ($\psi_o = \phi_o = \lambda_o = 1°$)			
$K_p = 36 \times 10^4$, $K_v = 1.2 \times 10^3$	−0.023	−0.088	−0.089
$K_p = 64 \times 10^4$, $K_v = 1.6 \times 10^3$	−0.040	−0.154	−0.155
$K_p = 100 \times 10^4$, $K_v = 2.0 \times 10^3$	−0.061	−0.235	−0.236
Rigid array & boom ($\psi'_o = \phi'_o = \lambda'_o = 1$)			
$K_p = 36 \times 10^4$, $K_v = 1.2 \times 10^3$	−0.005	−0.017	−0.018
$K_p = 64 \times 10^4$, $K_v = 1.6 \times 10^3$	−0.006	−0.022	−0.023
$K_p = 100 \times 10^4$, $K_v = 2.0 \times 10^3$	−0.007	−0.027	−0.028
Flexible array & boom ($\psi_o = \phi_o = \lambda_o = 1°$)			
$K_p = 36 \times 10^4$, $K_v = 1.2 \times 10^3$	−0.025	−0.061	+0.124
$K_p = 64 \times 10^4$, $K_v = 1.6 \times 10^3$	−0.044	−0.102	+0.215
$K_p = 100 \times 10^4$, $K_v = 2.0 \times 10^3$	−0.067	−0.151	+0.329
Flexible array & boom (10% rigidity & $\psi_o = \phi_o = \lambda_o = 1°$)			
$K_p = 3.6 \times 10^4$, $K_v = 1.2 \times 10^3$	−0.024	−0.075	±0.080
$K_p = 64 \times 10^4$, $K_v = 1.6 \times 10^3$	−0.042	−0.130	±0.138
$K_p = 100 \times 10^4$, $K_v = 2.0 \times 10^3$	−0.064	−0.198	±0.207
Flexible array & boom (10% rigidity, thermal effect & $\psi_o = \phi_o = \lambda_o = 1°$)			
$K_p = 36 \times 10^4$, $K_v = 1.2 \times 10^3$	−0.025	−0.077	±0.117
$K_p = 64 \times 10^4$, $K_v = 1.6 \times 10^3$	−0.044	−0.133	±0.173
$K_p = 100 \times 10^4$, $K_v = 2.0 \times 10^3$	−0.067	−0.202	±0.237

* + and − signs represent counterclockwise and clockwise directions, respectively; ± denotes equal magnitudes for both directions.

control. In the present case, the operation of the controllers is assumed to begin at half-way of the maneuver. For instance, during a 10-minute maneuver, the controller is turned on 5 minutes after the commencement of the maneuver.

Figure 5-16 shows the controlled system performance for a 5-minute OP maneuvers. The controller is turned on 2.5 minutes after the robotic arm begins the

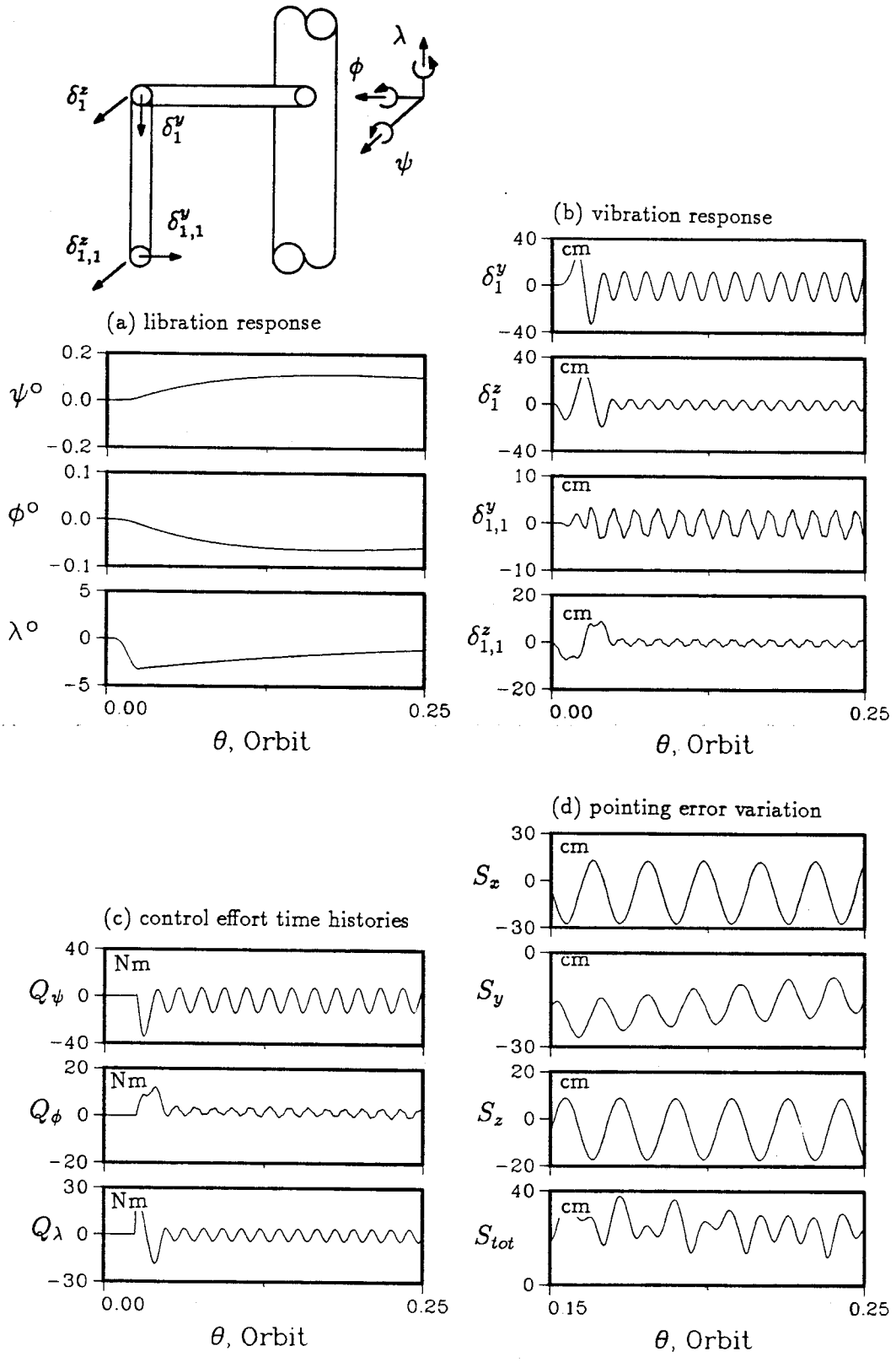

Figure 5-16 Controlled system performance of the MSS undergoing a 5-minute OP maneuver: (a) libration response; (b) vibration response; (c) control effort time histories; (d) pointing error variation.

maneuver. The controlled attitude response is shown in Figure 5-16a. A comparison with the uncontrolled case (Figure 4-22) is appropriate. With application of the control, there is no noticeable improvement in the pitch and roll response because their magnitudes are small already. On the other hand, the relatively large yaw angle is damped quite effectively. At the end of 0.25 orbit, the yaw angle is only $-1.1°$ as compared to $8.2°$ for the uncontrolled case. Note, influence of the controller on the appendage vibration is rather small (Figure 5-16b). The peak deflections of the upper and lower links are 35.9 and 9.4 cm, respectively. The corresponding values are 33.3 and 9.5 cm for the uncontrolled system. Since the inertias of the MSS about the pitch and roll axes are of the order 10^8 kg m^2, even a small error in pitch or roll requires a large control effort. Similarly, although the inertia about the yaw axis is about three orders of magnitude smaller, the relatively large error in the yaw angle demands a significant control torque. The peak torques Q_ψ, Q_ϕ, Q_λ are -34.5, 12.1, and 25.5 Nm, respectively (Figure 5-16c). The pointing accuracy has improved remarkably with the application of the control (Figure 5-16d). With the yaw attitude damped, the error in the orbit normal direction (S_x) no longer increases progressively as in Figure 4-25. Instead, S_x oscillates about a mean value of -15 cm with 30 cm p-p amplitude. At 0.25 orbit, the mean error is 25.7 cm with 9.8 cm p-p superposed. This is a significant improvement compared to the errors for the uncontrolled system which are 103.4 and 40.9 cm for OP and IP maneuvers, respectively.

With the maneuver time increased to 10 minutes, the performance of the MSS improves significantly (Figure 5-17). Here, the controller is turned on 5 minutes after the slewing maneuver begins. The attitude errors at 0.25 orbit are only $0.054°$, $-0.027°$, and $-0.862°$ for pitch, roll, and yaw, respectively (Figure 5-17a). These values are smaller than those in a 5-minute maneuver ($0.103°$, $-0.058°$, $-1.05°$ for pitch, roll and yaw). Comparing with Figure 4-24, the control effort results in a

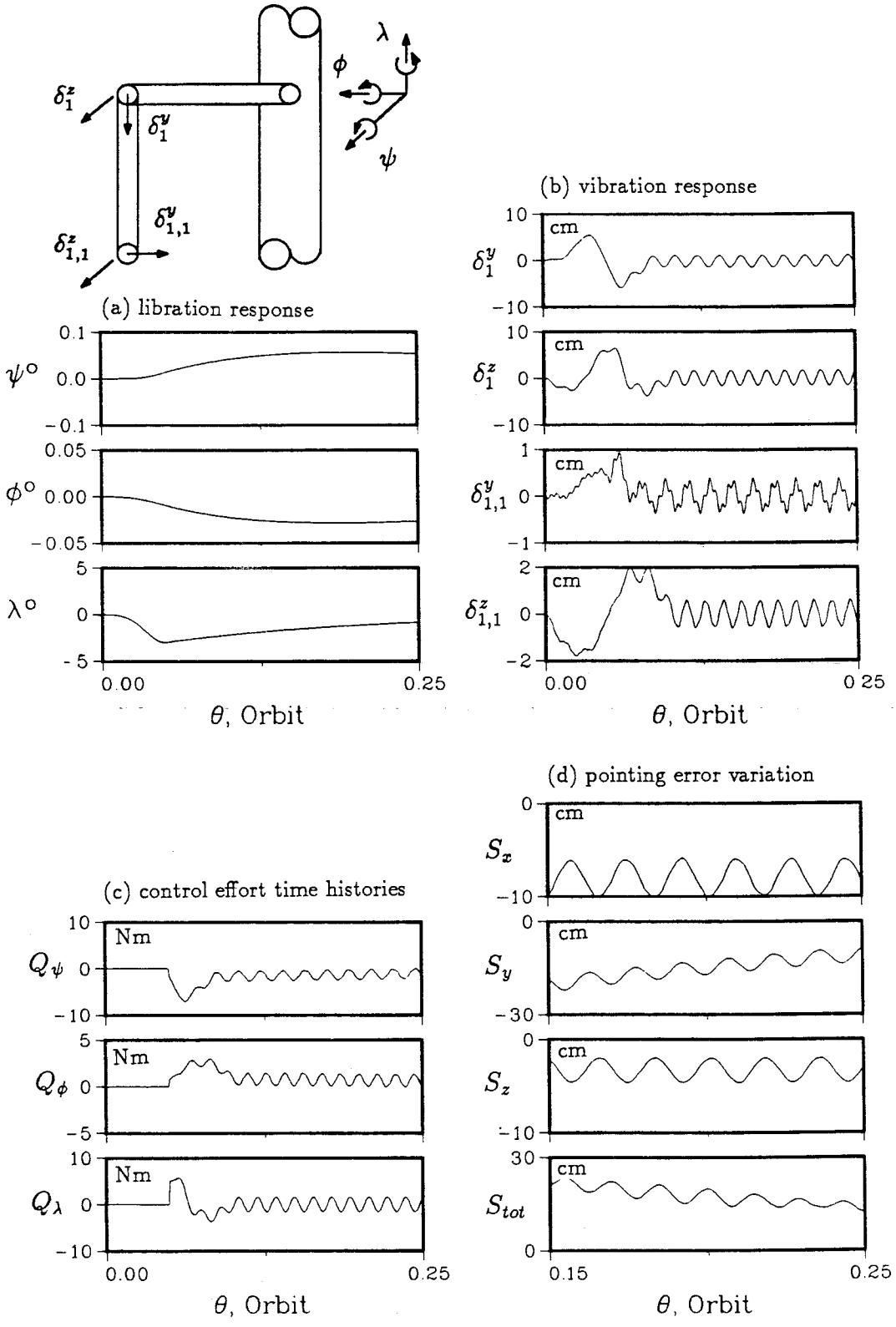

Figure 5-17 Controlled system performance of the MSS undergoing a 10-minute OP maneuver: (a) libration response; (b) vibration response; (c) control effort time histories; (d) pointing error variation.

slight increase in p-p amplitude of the robot arm vibration. For instance, without the attitude control, the maximum deflections for the upper and lower links were 6.3 and 1.8 cm, respectively. These values increase to 6.4 and 2.0 cm with the application of the control (Figure 5-17b). For a longer maneuver period, the peak control torque values are smaller (Figure 5-17c). With a 10-minute maneuver, the maximum values of the torques Q_ψ, Q_ϕ, and Q_λ (-7, 3, and 5.7 Nm) are about 20% of those for a 5-minute maneuver (-34.5, 12.1, and 25.5 Nm). Obviously, these savings are due to smaller excitation in attitude. Similarly, reduced attitude errors are sufficient to improve the pointing accuracy and offset the minor increase in link deflections. Once again, the control of the yaw angle helps stabilize the error in the orbit normal direction, S_x. At 0.25 orbit, the arm is only 14 cm from the target as compared to 86 cm for the uncontrolled case (Figure 5-17d).

Figure 4-26 shows that the MSS performs poorly when the robotic arm is located 50 m from the station centre of mass. Even with a 10-minute maneuver, the system attains a $-0.55°$ pitch, $0.03°$ roll and $6.5°$ yaw in 0.25 orbit. Consequently, the arm is already 126.7 cm from the target in 0.25 orbit (Figure 4-27). Figure 5-18 clearly demonstrates effectiveness of the controller, even for a 5-minute maneuver. Here, the attitude error is reduced to only $0.013°$ in pitch, $-0.016°$ in roll and $-0.8°$ in yaw at 0.25 orbit (Figure 5-18a). Again, the flexible motion of the arm is not adversely affected by the control torques. For instance, without attitude control, the maximum deflections for the upper and lower links are 33.4 and 9.6 cm, respectively. With attitude control, the corresponding values are 34.5 and 9.2 cm (Figure 5-18b). Since the controlled response for pitch and roll angles is different from that without any arm offset, the controlled torques Q_ψ and Q_ϕ are expected to be different for the two cases. In contrast, the controlled yaw response is the same, with or without offset implying that Q_λ should be similar in both the cases. This is substantiated

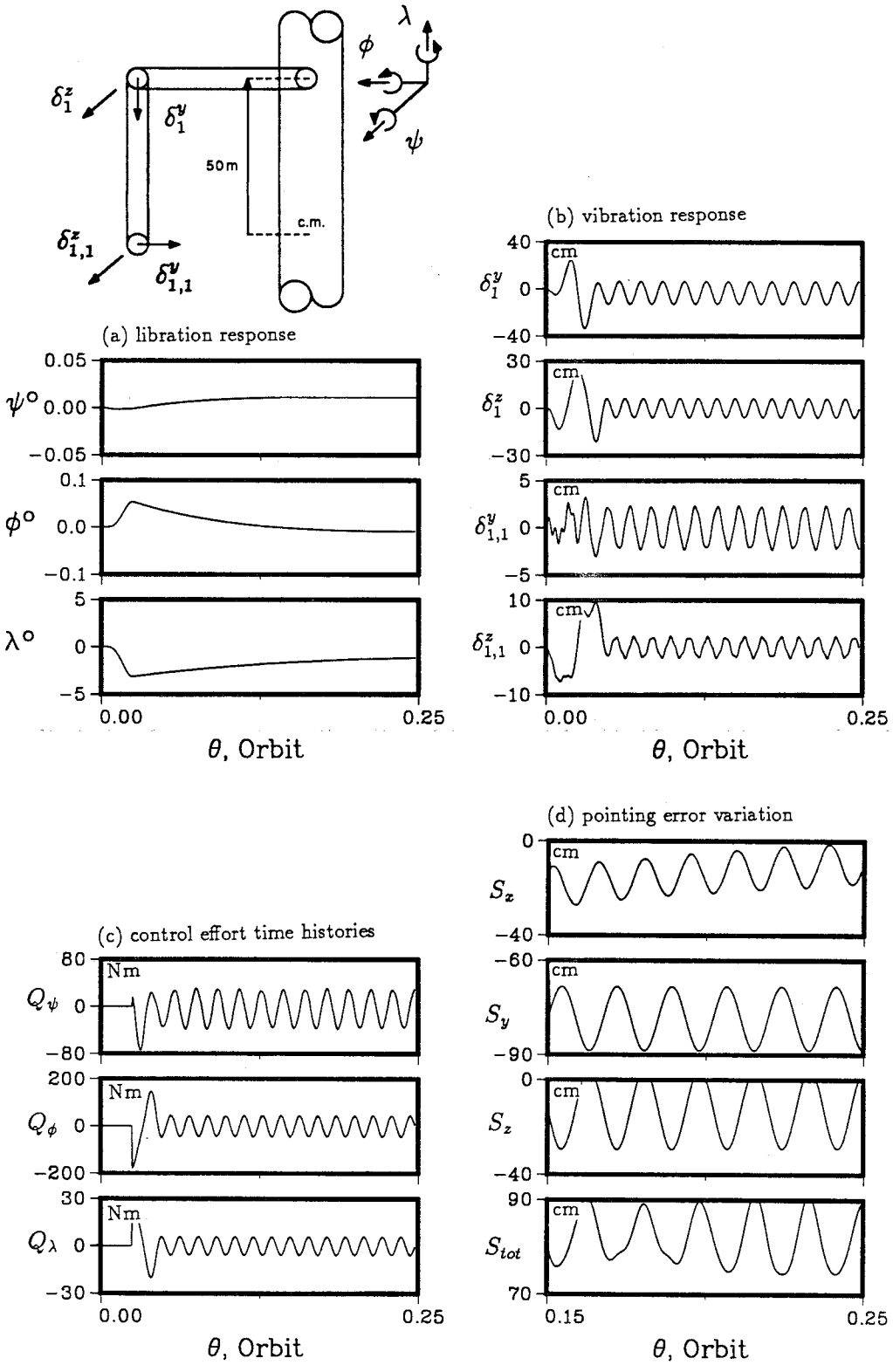

Figure 5-18 The performance of the MSS controller in the presence of offset and a 5-minute OP maneuver: (a) libration response; (b) vibration response; (c) control effort time histories; (d) pointing error variation.

by the control effort profiles in Figure 5-18c. Peak torques for Q_ψ, Q_ϕ, and Q_λ are -74.3, -175.8 and 24.5 Nm as compared to -34.5, 12.1 and 25.5 Nm when there is no offset. Without the attitude control, the errors S_x, S_y, and S_z increase with time (Figure 4-27). This is no longer true in the presence of control. The errors are periodic with mean values of -10.6, -78.5, and -14.6 cm for S_x, S_y, and S_z, respectively. At the end of 0.25 orbit, the mean pointing error of the arms is 82.6 cm with a p-p fluctuation of 8.3 cm. This error is larger than that for the case without the manipulator offset (25.7 ± 4.9 cm). This is due to the relatively large error in the local vertical direction, S_y in the present case. The robot arm points towards and away the earth before and after the maneuver, respectively. Consequently, there is a shift in centre of mass in the local vertical direction. Without the manipulator offset, this shift is negligible. However, this is no longer true when there is a manipulator offset. Thus, it is important to recognize that, even in presence of the attitude control, influence of the manipulator offset is still significant.

To determine advantages, if any, of longer maneuver period in the presence of arm offset, the maneuver is now increased to 10 minutes in Figure 5-19. Note that, the controlled pitch and roll responses in Figure 5-19a are no longer similar to those in the 5-minute maneuver (Figure 5-18a). At the end of 0.25 orbit, the pitch, roll, and yaw errors are $-0.085°$, $0.023°$, and $-1.43°$, respectively. These relatively large errors do not imply the ineffectiveness of the controller. Rather, it suggest lack of sufficient time to damp the attitude response in 0.25 orbit. Comparing the results with those in Figure 4-26, it is apparent that the controller once again does not have a significant influence on the arm vibrations (Figure 5-19b). In fact, the maximum deflection of the lower link reduced to 2.5 cm with attitude control (3.1 cm without attitude control). The biggest advantage of a longer maneuver period is the reduced demand on the control torques (Figure 5-19c). Maximum torques, though higher

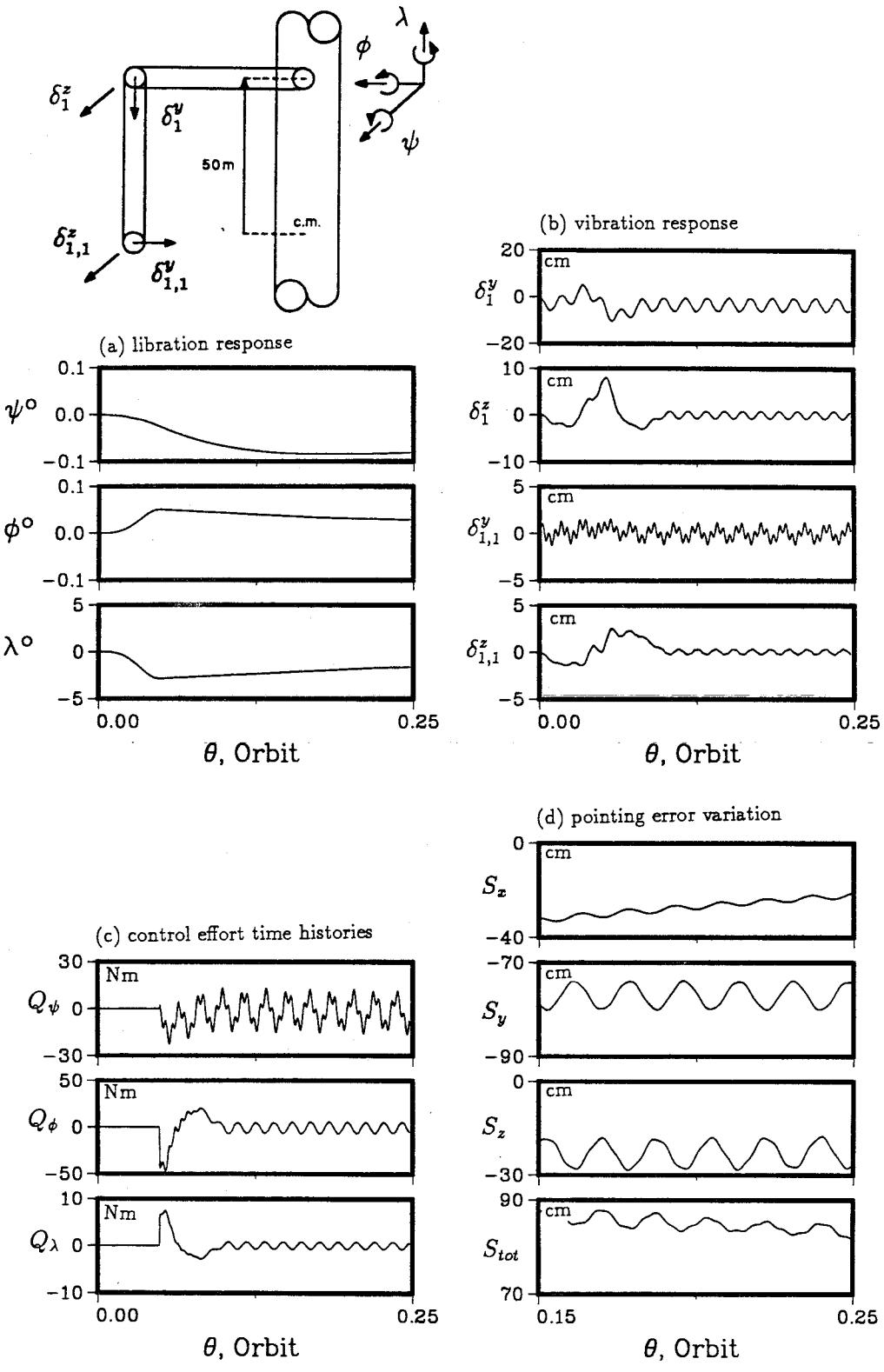

Figure 5-19 The performance of the MSS controller in the presence of offset and a 10-minute OP maneuver: (a) libration response; (b) vibration response; (c) control effort time histories; (d) pointing error variation.

than those without the offset case, are significantly lower than those for a 5-minute maneuver. Here, peak Q_ψ, Q_ϕ, and Q_λ are -22.6, -47.9 and 7.5 Nm, respectively. Since the attitude errors remain large at 0.25 orbit, the pointing accuracy (Figure 5-19d) is still poor compared to the case of a 10-minute maneuver without link offset. However, compared with Figure 5-18, the smaller p-p error together with a smaller control effort justify the use of a longer maneuver period.

Of course, implementing control at the beginning of the maneuver would restrict any librational motion as shown in Figure 5-20a. Here, a 5-minute maneuver of the robot arm is assumed. Comparing Figures 5-16b and 5-20b, the control strategy has little effect on the flexible motion of the links. When the libration error is not allowed to build up, the effect on the control torques is two-fold. On the one hand, less control effort is needed to drive a large error to zero. On the other hand, a larger control torque is necessary to maintain zero libration error. Consequently, depending on the dominance of these two effects, the peak control torques required might be larger or smaller. A comparison between Figures 5-16c and 5-20c show that with the control strategy implemented early, smaller Q_ψ and Q_ϕ are needed whereas Q_λ increased from 25.5 Nm to 32.1 Nm. With the elimination of the libration error, the positioning accuracy would definitely improve as shown in Figure 5-20d. At the end of 0.25 orbit, the mean error is only 18.9 cm as compared to 25.7 cm when the controller was implemented half-way through the maneuver.

With the inclusion of a 50 m offset of the manipulator, the controller implemented at the beginning of the maneuver once again helps eliminate the libration error (Figure5-21a) and improve the positioning error (Figure 5-21d). Once again, the control strategy has negligible influence on the flexible motion of the links (Figure 5-21b). Compared with the case when the control was implemented half-way through

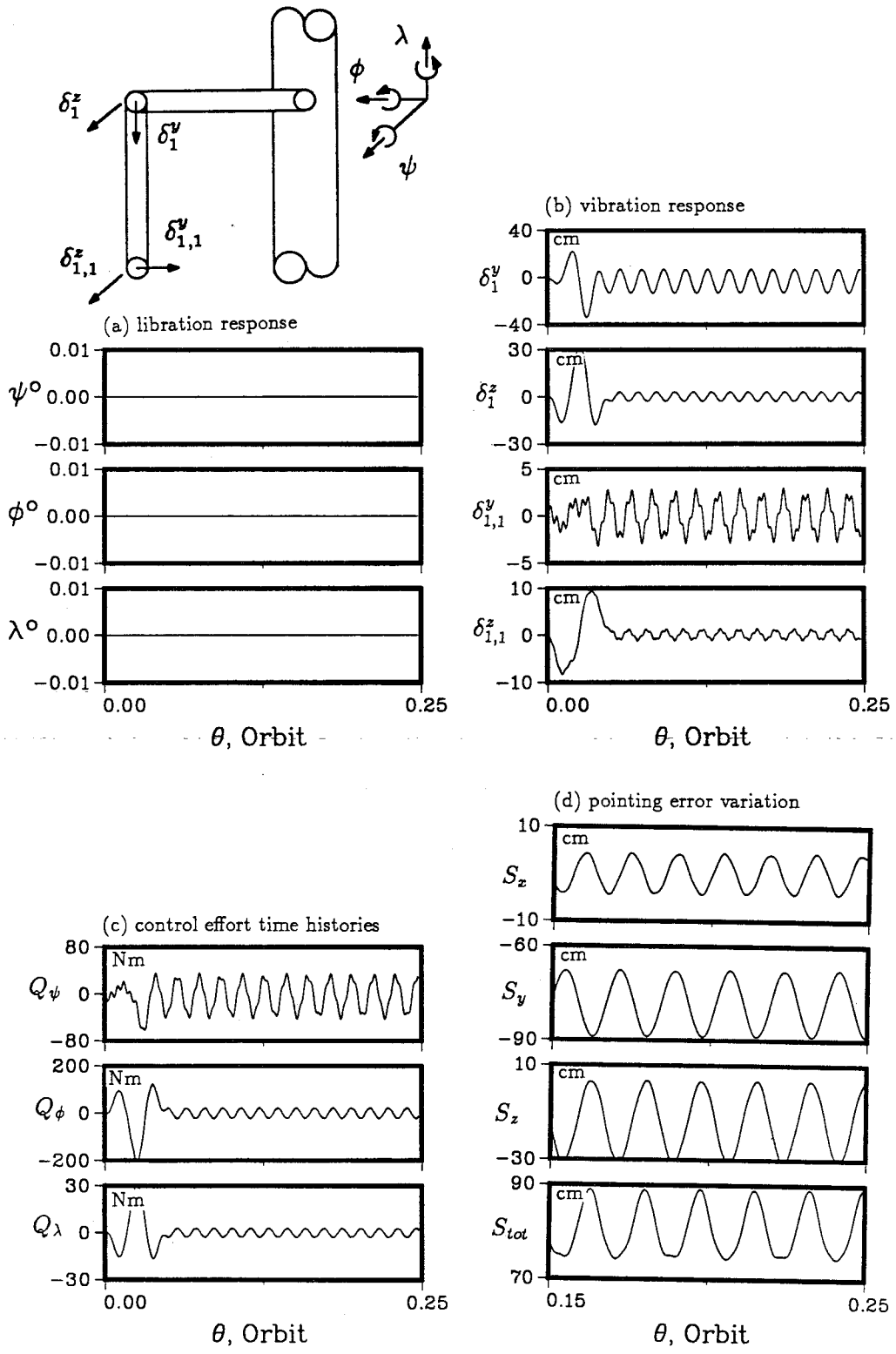

Figure 5-20 The performance of the MSS undergoing a 5-minute OP maneuver with the controller implemented at the beginning of the slew: (a) libration response; (b) vibration response; (c) control effort time histories; (d) pointing error variation.

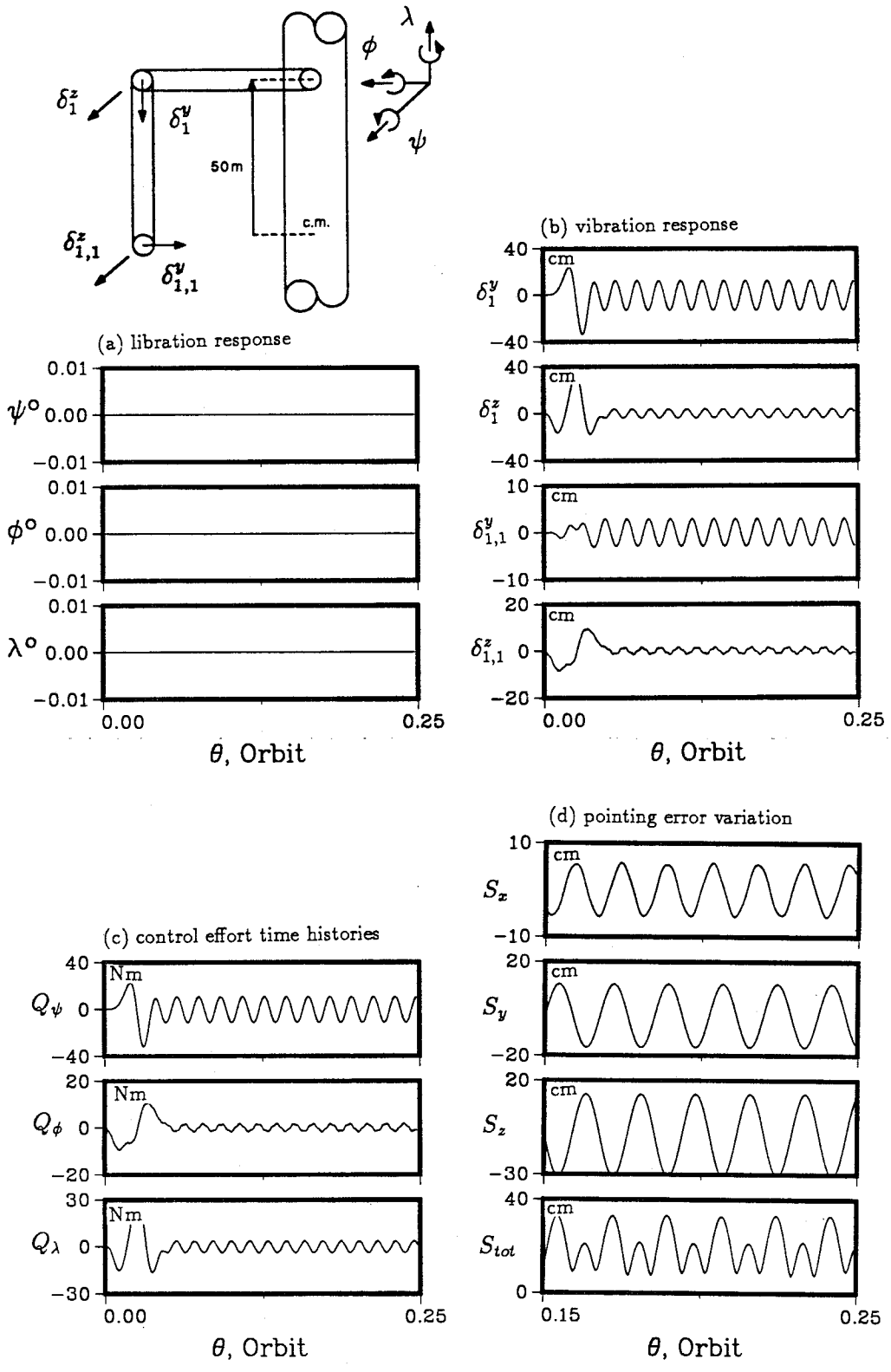

Figure 5-21 MSS performance in the presence of offset and undergoing a 5-minute OP maneuver with the controller implemented at the beginning of the slew: (a) libration response; (b) vibration response; (c) control effort time histories; (d) pointing error variation.

Table 5-3 Summary of the system performance for the controlled MSS with out-of-plane maneuver

Peak Control Effort (Nm)			Maximum Deflections (cm)		Pointing Error
Q_ψ	Q_ϕ	Q_λ	Upper Link	Lower Link	at 0.25 Orbit (cm)*
Control Implemented Half-way through the Maneuver					
5-minute maneuver					
−34.5	12.1	25.5	35.9	9.4	25.7 ± 4.9 (103.4)
10-minute maneuver					
−7.0	3.0	5.7	7.8	2.0	14.0 ± 1.6 (86.0)
5-minute maneuver & 50 m offset					
−74.3	−175.8	24.5	37.1	10.1	82.6 ± 8.3 (139.7)
10-minute maneuver & 50 m offset					
−22.6	−47.9	7.5	11.7	2.6	83.8 ± 1.2 (126.7)
Control Implemented at the Beginning of the Maneuver					
5-minute maneuver					
−31.8	10.7	32.1	36.1	9.5	18.9 ± 11.3 (103.4)
5-minute maneuver & 50 m offset					
−61.4	−213.0	31.5	37.3	9.5	81.7 ± 7.4 (139.7)

* Pointing error for the uncontrolled case are indicated in parentheses

the maneuver, the peak torque Q_ψ is now reduced to −61.4 Nm from −74.3 Nm. On the other hand, peak Q_ϕ and Q_λ increase by about 20% to −213 Nm and 31.5 Nm, respectively (Figure 5-21c).

The maximum control effort required and the pointing errors for the six cases studied are summarized in Table 5-3 .

5.6 Closing Comments

The FLT has been found to be effective in controlling the attitude motion of the rigid INSAT II. The performance with three sets of control gains is compared. With the satellite initially disturbed by 1° in pitch, roll, and yaw, the gains are found to

be adequate in reducing the attitude error to the design limit in about 2 minutes. In general, the rate of response is directly proportional to the magnitude of the control gains. With the inclusion of flexibility in the satellite model, the QCLC was found to be effective. Even in presence of relatively large initial attitude disturbances, the control scheme works remarkably well. The inclusion of thermal deformations of the array and beam does not adversely affect the controller's performance. As expected, although larger control torques are needed, the equilibrium attitude of the satellite is again restored in less than 2 minutes.

The QCLC is also effective in controlling the attitude of the space station and hence the accuracy of the MSS. Even with a 5-minute maneuver and an offset location of the manipulator (from c.m. of the station), the controller continues to be effective in damping the slew excited attitude motion. In turn, the pointing error of the arm diminishes significantly. Considering the large inertia of the space station, the control effort required is reasonable. In the presence of an offset, the controllers performance remains essentially unaffected except for larger control torques. In general, a longer the maneuver period results in smaller control effort and p-p amplitude of the arm vibration.

From practical considerations, it would be useful to study effectiveness of the controller subjected to constraints and system uncertainties. The gains and desired trajectory are selected arbitrarily in the present simulation. A more systematic approach in making these selections is needed. Also, as seen before, the control effort may oscillate at high frequencies implying a need for high bandwidth. Although the FLT is promising, these issues are among many which remain to be resolved.

6. CONCLUDING REMARKS

6.1 Conclusions

A relatively general Lagrangian formulation for studying the dynamics of spacecraft with interconnected flexible bodies forming a tree-type topology is presented. The formulation is applicable to a large class of systems negotiating arbitrary orbits and having any desired orientation in space. Each member is free to undergo transverse vibration, slewing maneuvers and thermal deformations. The governing equations are highly nonlinear, nonautonomous, and coupled. In general, implementation of these equations into a comprehensive computer code requires enormous amount of effort. This is minimized by defining three new operators. The computer program is structured in a modular form permitting assessment of the effects of shifting c.m., flexibility, thermal deformations, shape functions and higher modes. Validity of the computer program is established through extensive comparison with particular cases studied by Ng [90] and Chan [15]. Convergence of the beam shape functions has also been established.

Versatility of the formulation is then demonstrated through its application to four spacecraft models of contemporary interest: the First Element Launch (FEL) and Permanently Manned Configuration (PMC) of the proposed U.S. space station *Freedom*; Mobile Servicing System (MSS) under development by Canada; INSAT–II, a multipurpose communications satellites of India; and Japan's Space Flyer Unit (SFU). Simulation results provide insight into the interactions between librational and vibrational dynamics, slewing maneuvers, thermal deformations, orbit eccentricity, deployment and retrieval, etc. The focus is on results which help establish trends. The concept of nonlinear control using the Feedback Linearization Technique (FLT)

is discussed next. Effectiveness of the procedure to control rigid as well as flexible modes of the INSAT II is explored. Control of the satellite in the presence of thermal deformation is also demonstrated. The technique is then applied to the control of space station attitude during MSS maneuvers. Once again, the FLT has proved to be effective in controlling the attitude of the station. More important conclusions based on the parametric and control studies are summarized below:

(i) The FEL's nominal orientation is neither in equilibrium nor stable. Even with a very small initial pitch, roll, or yaw disturbance, a rigid FEL starts to tumble in less than 1 orbit. With the inclusion of member flexibility, the FEL's librational and vibrational responses become highly coupled. In general, even a small disturbance to a flexible member results in significant rigid body motion. Initial condition on the power boom is undesirable as it leads to pitch and roll responses with high amplitudes and frequencies. Furthermore, response results show the power boom and stinger dynamics to be quite sensitive to the disturbance direction.

(ii) As in the case of the FEL, the PMC of the space station is also in a nominally unstable orientation. Unlike the FEL, due to the relatively large inertia of the power boom, the system is less susceptible to disturbances from the arrays and radiators. However, even a small disturbance applied initially to the power boom can result in significant librational and vibrational motions.

(iii) In general, both eccentricity and thermal deformation of the PV arrays can affect the PMC pitch motion. Furthermore, thermal deformations influence flexible response of the system.

(iv) The study of the PMC's velocity and acceleration profiles indicate that in absence of any disturbance, the system velocity and microgravity distribution

stay within the design limits. However, even with a small disturbance in the local vertical or local horizontal direction, the design limits are easily violated. The presence of a small orbit eccentricity does not adversely affect the system performance; however, even small thermal deformation of the PV arrays result in velocity and acceleration beyond the acceptable values.

(v) As expected, the MSS study shows that longer the maneuver period, smaller the response amplitude both for rigid and flexible degrees of freedom. In general, an out-of-plane (OP) maneuver excites a smaller flexible motion than the corresponding inplane (IP) case. However, this advantage is offset by the 3 dimensional rigid body motion excited. Increasing the link stiffness results in only a small reduction in the librational response. On the other hand, the vibration response diminishes significantly. Offset of the MSS location from the system c.m. is detrimental to the spacecraft performance.

(vi) The excitation of roll and yaw responses during the OP maneuver results in a poor pointing accuracy. Even increasing the maneuver period or link stiffness does improve the situation significantly. The OP maneuver is feasible only if the system libration is controlled.

(vii) The SFU study shows that the spacecraft remains stable under both symmetric and asymmetric deployment of the Solar Array Pedals (SAPs) The parametric study also shows that the OP deployment has the advantage over the IP extension as the excitation is smaller.

(viii) The retrieval of the SAPs may pose some problems. The symmetric OP retrieval poses no difficulty. However, if only one SAP is retrieved, the spacecraft becomes unstable even when the retrieval time is increased. The SAP retrieval in the IP direction is found to be undesirable. Regardless of symme-

try and period of retrieval, the spacecraft starts to tumble in a short time.

(ix) Feedback Linearization Technique (FLT) for attitude control of highly non-linear systems appears promising. The method is straightforward and the control algorithm is simple. For the control of the rigid INSAT II, the effort required is minimal.

(x) For the control of flexible spacecraft, Quasi-Closed Loop Control (QCLC) based on FLT, performs well. In general, flexibility of the solar array and boom does not have significant influence on the control effort. Flexibility implies that controllers of higher bandwidth are needed especially for the roll and yaw control of the INSAT II. Even if appendages are thermally deformed, the controllers remain effective. In general, larger control torques are needed for the satellite with thermally deformed appendages.

(xi) The control of the space station during MSS maneuvers using the QCLC is again proved to be feasible. The controllers are effective in damping out attitude motion induced by OP maneuvers of the robotic arms. In turn, the pointing accuracy of the robotic arms improve significantly. Even the offset of robotic arms does not adversely affect the performance of the controllers except that larger control torques are required. In general, the longer the maneuver period implies smaller control effort required and p-p fluctuations of the pointing errors.

6.2 Recommendations for Future Work

The formulation presented in this thesis is relatively general; however, there is a scope for improvement. A few features that would enhance its general character and implementation efficiency include the following.

(i) As pointed out in Chapter 3, there are two areas in subroutine FCN which can be executed in parallel resulting in a substantial saving in computational time and cost. If parallel processing facility is available, the computer code should be modified to take its advantage.

(ii) The convergence of the beam shape functions is shown in Figure 3-11. It would be useful to study the convergence of the shape functions of cantilever plates. The formulation accounts for transverse vibration, thermal deformations, and slewing maneuvers of the members. Other possible member motion not accounted for includes longitudinal vibration, translational motion, and torsional oscillations. As pointed out in Chapter 4, the present formulation was tailored to facilitate the deployment/retrieval study of the SFU. A formulation that accounts for deployment/retrieval of arbitrary members would be useful.

(iii) As shown in Table 2-1, shape functions based on Warburton [94] are inadequate for modeling free-free plates. Incorporation of Gorman [96] shape functions in the general formulation is one alternative. Another option would be to use quasi-comparison functions put forward by Meirovitch and Kwak [88].

(iv) Thermal deformation of flexible members is the only environmental disturbance considered in the thesis. This is because it affects both high as well as low altitude spacecraft. However, for spacecraft at high altitude, solar radiation pressure effect may also be significant whereas at lower altitudes, aerodynamic drag may become significant. Inclusion of these two environmental disturbances would add to make the versatility of the formulation.

The dynamics and control studies of the five spacecraft configurations, though

comprehensive, are not complete. Obviously, there are numerous system parameters and countless possibilities for initial conditions (disturbances) that can be studied. Some of the simulations which are likely to be enlightening are indicated below.

(i) As the nominal orientations of the FEL and PMC are unstable, active control is necessary. It would be useful to investigate the feasibility of alternative orientations with respect to the control effort. The effect of slewing maneuvers of PV arrays on the dynamics of the FEL and PMC is likely to be of importance.

(ii) The study of the MSS presented in thesis is based on a gravity stabilized and rigid space station. Performance of the MSS under different orientations of the flexible space station is not easy to predict. Only a detailed investigation into orientation and flexibility effects can provide the insight needed.

(iii) The deployment/retrieval profile of the SFU assumed constant velocity. The stability study of the SFU under the influence of more efficient profiles would be a logical extension to the present study.

(iv) Control based on the FLT is promising; however, it needs to be further explored. In particular, a more systematic approach to select the controller gains and desired trajectory is needed. Furthermore, performance of the controller in the presence of logical constraints needs attention. The problems of robustness and bandwidth will have to be addressed. Investigations aimed at the FEL, PMC, and SFU would result in important and timely contributions to the field. It would be particularly useful to investigate performance of the QCLC algorithm in the presence of deploying or retrieving members.

BIBLIOGRAPHY

[1] Taylor, L., "The SCOLE Design Challenge – An Overview," *Proceedings of the 2nd Annual SCOLE Workshop*, Hampton, Virginia, December 1985, pp. 1–13.

[2] Singh, R.P., VanderVoort, R.J., and Likins, P.W., "Dynamics of Flexible Bodies in Tree-Topology – A Computer-Oriented Approach," *Journal of Guidance, Control and Dynamics*, Vol. 8, No. 5, September – October 1985, pp. 584–590.

[3] Ho, J.Y.L., and Herber, D.R., "Development of Dynamics and Control Simulation of Large Flexible Space Systems," *Journal of Guidance, Control and Dynamics*, Vol. 8, No. 3, May – June 1985, pp. 374–383.

[4] Ho, J.Y.L., Herber, D.R., Clapp, B.R., and Schultz, R.J., "ALLFLEX Program – Simulation Methodology," *Proceedings of the Workshop on Multibody Simulation*, Eds: G. Man and R. Laskin, April 1988, pp. 811–856.

[5] Ho, J.Y.L., "Direct Path Method for Flexible Multibody Spacecraft Dynamics," *Journal of Spacecraft and Rocket*, Vol. 14, No. 2, February 1977, pp. 102–110.

[6] Chun, H.M., Turner, J.D., and Frisch, H.P., "Experimental Validation of Order (N) DISCOS," *AAS/AIAA Astrodynamics Specialist Conference*, Stowe, Vermont, August 1989, Paper No. AAS–89–457.

[7] Likins, P., "Spacecraft Attitude Dynamics and Control – A Personal Perspective on Early Developments," *Journal of Guidance, Control and Dynamics*, Vol. 9, No. 2, March – April 1986, pp. 129–134.

[8] Modi, V.J., "Attitude Dynamics of Satellites with Flexible Appendages – A Brief Review," *Journal of Spacecraft and Rocket*, Vol. 11, No. 11, November 1974, pp. 743–751.

[9] Shrivastava, S.K., "Effects of Solar Radiation Pressure and Aerodynamic Forces on Satellite – Attitude Dynamics and Their Utilization for Control: A Survey," *Journal of the Indian Institute of Science*, Vol. 58, No. 9, September 1976, pp. 391–411.

[10] Shrivastava, S.K., Tschann, C., and Modi, V.J., "Librational Dynamics of Earth Oriented Satellites – A Brief Review," *Proceedings of 14th Congress on Theoretical and Applied Mechanics*, Kurukshetra, India, 1969, pp. 284–306.

[11] Roberson, R.E., "Two Decades of Spacecraft Attitude Control," *Journal of Guidance and Control*, Vol. 2, No. 1, January –February 1979, pp. 3–8.

[12] Markland, C.A., "A Review of the Attitude Control of Communications Satellites," *32nd Congress of the International Astronautical Federation*, Rome, Italy, 1981, Paper No. IAF–81–344.

[13] Lips, K.W., *Dynamics of a Large Class of Satellites with Deploying Flexible Appendage*, Ph.D. Thesis, The University of British Columbia, September 1980.

[14] Ibrahim, A.M., *Mathematical Modelling of Flexible Multibody Dynamics with Applications to Orbiting Systems*, Ph.D. Thesis, The University of British Columbia, April 1988.

[15] Chan, J.K., *Dynamics and Control of an Orbiting Space Platform Based Mobile Flexible Manipulator*, M.A.Sc. Thesis, The University of British Columbia, April 1990.

[16] Hooker, W.W., and Margulies, G., "The Dynamical Attitude Equations for an n-Body Satellite," *The Journal of the Astronautical Sciences*, Vol. 12, No. 4, 1965, pp. 123–128.

[17] Roberson, R.E., and Wittenburg, J., "A Dynamical Formalism for an Arbitrary Number of Interconnected Rigid Bodies, with Reference to the Problem of Satellite Attitude Control," *Proceedings of the 3rd International Federation on Automatic Control*, London, 1966, Paper No. 46D.

[18] Roberson, R.E., "A Form of the Translational Dynamical Equations for Relative Motion in Systems of Many Non-Rigid Bodies," *Acta Mechanica*, Vol. 14, 1972, pp. 297–308.

[19] Hooker, W.W., "Equations of Motion for Interconnected Rigid and Elastic Bodies: A Derivation Independent of Angular Momentum," *Celestial Mechanics*, Vol. 11, No. 1, 1975, pp. 337–359.

[20] Jerkovsky, W., "The Structure of Multibody Dynamics Equations," *Journal of Guidance and Control*, Vol. 1, No. 3, May –June 1978, pp. 173–182.

[21] Hooker, W.W., "A Set of r Dynamical Attitude Equations for an Arbitrary n-Body Satellite Having r Rotational Degrees of Freedom," *AIAA Journal*, Vol. 8, No. 7, July 1970, pp. 1205–1213.

[22] Hughes, P.C., "Dynamics of a Chain of Flexible Bodies," *The Journal of the Astronautical Sciences*, Vol. 27, No. 4, October – December 1979, pp. 359–380.

[23] Kane, T.R., and Levinson, D.A., "Formulation of Equations of Motion for Complex Spacecraft," *Journal of Guidance and Control*, Vol. 3, No. 2, March – April 1980, pp. 99–112.

[24] Modi, V.J., and Ibrahim, A.M., "A General Formulation for Librational Dynamics of Spacecraft with Deploying Appendages," *Journal of Guidance, Control and Dynamics*, Vol. 7, No. 5, September – October 1984, pp. 563–569.

[25] Meirovitch, L., and Quinn, R.D., "Equations of Motion for Maneuvring Flexible Spacecraft," *Journal of Guidance, Control and Dynamics*, Vol. 10, No. 5, September – October 1987, pp. 453–465.

[26] Vu-Quoc, L., and Simo, J.C., "Dynamics of Earth-Orbiting Flexible Satellites with Multibody Components," *Journal of Guidance, Control and Dynamics*, Vol. 10, No. 6, November – December 1987, pp. 549–558.

[27] Keat, J.E., "Multibody System Order n Dynamics Formulation Based on Velocity Transform Method," *Journal of Guidance, Control and Dynamics*, Vol. 13, No. 2, March – April 1990, pp. 207–212.

[28] Huston, R.L., "Multibody Dynamics Formulations Via Kane's Equations," *AIAA Dynamics Specialist Conference*, Long Beach, California, April 1990, Paper No. AIAA–90–1248–CP.

[29] Kurdila, A.J., "Multibody Dynamics Formulations Using Maggi's Approach," *AIAA Dynamics Specialist Conference*, Long Beach, California, April 1990, Paper No. AIAA–90–1248–CP.

[30] Balas, M.J., "Some Trends in Large Space Structure Control Theory: Fondest Hopes; Wildest Dreams," *Proceedings of the 1979 Joint Automatic Control*, Denver, Colorado, June 1979, pp. 42–53.

[31] Meirovitch, L., and Öz, H., "An Assessment of Methods for the Control of Large Space Structures," *Proceedings of the 1979 Joint Automatic Control*, Denver, Colorado, June 1979, pp. 34–41.

[32] Meirovitch, L., and Öz, H., "Modal-Space Control of Distributed Gyroscopic Systems," Ignorable Coordinates," *Journal of Guidance and Control*, Vol. 3, No. 2, March – April 1980, pp. 140–150.

[33] Meirovitch, L., and Öz, H., "Modal-Space Control of Large Flexible Spacecraft Possessing Ignorable Coordinates," *Journal of Guidance and Control*, Vol. 3, No. 6, November – December 1980, pp. 569–577.

[34] Meirovitch, L., Baruh, H., and Öz, H., "A Comparison of Control Techniques for Large Flexible Systems," *Journal of Guidance, Control and Dynamics*, Vol. 6, No. 4, July – August 1983, pp. 302–310.

[35] Öz, H., and Meirovitch, L., "Optimal Modal-Space Control of Flexible Gyroscopic Systems," *Journal of Guidance and Control*, Vol. 3, No. 3, May –June 1980, pp. 218–226.

[36] Balas, M.J., "Active Control of Flexible Systems," *Journal of Optimization Theory and Applications*, Vol. 25, No. 3, July 1978, pp. 415–436.

[37] Balas, M.J., "Feedback Control of Flexible Systems," *IEEE Transactions on Automatic Control*, Vol. AC–23, August 1978, pp. 673–679.

[38] Balas, M.J., "Modal Control of Certain Flexible Dynamic Systems," *SIAM Journal of Control and Optimization*, Vol. 16, May 1978, pp. 450–462.

[39] Balas, M.J., and Ginter, S., "Attitude Stabilization of Large Flexible Spacecraft," *Journal of Guidance and Control*, Vol. 4, No. 5, September – October 1981, pp. 561–564.

[40] Balas, M.J., "Direct Velocity Feedback Control of Large Space Structures," *Journal of Guidance and Control*, Vol. 2, No. 3, May – June 1979, pp. 252–253.

[41] Wie, B., and Bryson, A.E. Jr., "Pole-Zero Modeling of Flexible Space Structures," *Journal of Guidance, Control and Dynamics*, Vol. 11, No. 6, November – December 1988, pp. 554–561.

[42] Wie, B., "Active Vibration Control Synthesis for the Control of Flexible Structures Mast Flight System," *Journal of Guidance, Control and Dynamics*, Vol. 11, No. 3, May – June 1988, pp. 271–277.

[43] Chu, P.Y., Wie, B., Gretz, B., and Plescia, C., "Space Station Attitude Control: Modeling and Design," *AIAA Guidance, Navigation and Control Conference*, August 1988, Minneapolis, Minnesota, Paper No. AIAA–88–4133.

[44] Kida, T., Ohkami, Y., and Sambongi, S., "Poles and Transmission Zeros of Flexible Spacecraft Control Systems," *Journal of Guidance, Control and Dy-*

namics, Vol. 8, No. 2, March – April 1985, pp. 208–213.

[45] Goh, C.J., and Caughey, T.K., "A Quasi-Linear Vibration Suppression Technique for Large Space Structures via Stiffness Modification," *International Journal of Control*, Vol. 41, No. 3, 1985, pp. 803–811.

[46] Reddy, A.S.S.R., Bainum, P.M., Krishna, R., and Hamer, H.A., "Control of a Large Flexible Platform in Orbit," *Journal of Guidance and Control*, Vol. 4, No. 6, November – December 1981, pp. 642–649.

[47] Yedavalli, R.K., "Critical Parameter Selection in the Vibration Suppression of Large Space Structures," *Journal of Guidance, Control and Dynamics*, Vol. 7, No. 3, May – June 1984, pp. 274–278.

[48] Sundararajan, N., Joshi, S.M., and Armstrong, E.S., "Robust Controller Synthesis for a Large Flexible Space Antenna," *Journal of Guidance, Control and Dynamics*, Vol. 10, No. 2, March – April 1987, pp. 201–208.

[49] Modi, V.J., and Brereton, R.C., "Planar Librational Stability of a Flexible Satellites," *AIAA Journal*, Vol. 6, No. 3, March 1968, pp. 511–517.

[50] Modi, V.J., and Flanagan, R.C., "Effect of Environmental Forces on the Attitude of Gravity Oriented Satellites, Part I: High Altitude Orbits," *The Aeronautical Journal of the Royal Aeronautical Society*, Vol. 75, November 1971, pp. 783–793.

[51] Modi, V.J., and Flanagan, R.C., "Effect of Environmental Forces on the Attitude of Gravity Oriented Satellites, Part II: Intermediate Altitude Orbits Accounting for Earth Raidation," *The Aeronautical Journal of the Royal Aeronautical Society*, Vol. 75, December 1971, pp. 846–849.

[52] Flanagan, R.C., and Modi, V.J., "Effect of Environmental Forces on the Attitude Dynamics of Gravity Oriented Satellites, Part III: Close Earth Orbits Accounting for Aerodynamic Forces," *The Aeronautical Journal of the Royal Aeronautical Society*, Vol. 76, January 1972, pp. 34–40.

[53] Modi, V.J., and Flanagan, R.C., "Librational Damping of a Gravity Oriented System Using Solar Radiation Pressure," *The Aeronautical Journal of the Royal Aeronautical Society*, Vol. 75, August 1971, pp. 560–564.

[54] Modi, V.J., and Kumar, K., "Librational Dynamics of a Satellite with Thermally Flexed Appendages," *The Journal of the Astronautical Sciences*, Vol. 25, No. 1, January – March 1977, pp. 3–20.

[55] Beletsky, V.V., and Starostin, E.L., "Planar Librations of a Gravity Oriented Satellite Under the Influence of Solar Radiation Pressure," *38th Congress of the International Astronautical Federation*, Brighton, U.K., October 10–17, 1987, Paper No. IAF–87–352.

[56] Goldman, R.L., "Influence of Thermal Distortion on Gravity Gradient Stabilization," *Journal of Spacecraft and Rocket*, Vol. 12, No. 7, July 1975, pp. 406–413.

[57] Yu, Y.Y., "Thermally Induced Vibration and Flutter of a Flexible Boom," *Journal of Spacecraft and Rocket*, Vol. 6, No. 8, August 1969, pp. 902–910.

[58] Frisch, H.P., "Thermally Induced Vibrations of Long Thin-Walled Cylinders of Open Section," *Journal of Spacecraft and Rocket*, Vol. 7, No. 8, August 1970, pp. 897–905.

[59] Frisch, H.P., "Thermally Induced Response of Flexible Structures: A Method for Analysis," *Journal of Guidance and Control*, Vol. 3, No. 1, January – February 1980, pp. 92–94.

[60] Tsuchiya, K., "Thermally Induced Nutational Body Motion of a Spinning Spacecraft with Flexible Appendages," *AIAA Journal*, Vol. 13, No. 4, April 1975, pp. 448–453.

[61] Tsuchiya, K., "Thermally Induced Vibrations of a Flexible Appendage Attached to a Spacecraft," *AIAA Journal*, Vol. 15, No. 4, April 1977, pp. 505–510.

[62] Krishna, R., and Bainum, P.M., "Effect of Solar Radiation Disturbance on a Flexible Beam in Orbit," *AIAA 21st Aerospace Sciences Meeting*, Reno, Nevada, January 1981, Paper No. AIAA–83–0431.

[63] Bainum, P.M., and Krishna, R., "Control of an Orbiting Flexible Square Platform in the Presence of Solar Radiation," *14th International Symposium on Space Technology and Science*, Tokyo, Japan, May – June 1984, Paper No. i–2–1.

[64] Krishna, R., and Bainum, P.M., "Orientation and Shape Control of an Orbiting Flexible Beam under the Influence of Solar Radiation Pressure," *AAS/AIAA Astrodynamics Conference*, Lake Placid, N.Y., August 1983, Paper No. AAS–83–325.

[65] Krishna, R., and Bainum, P.M., "Environmental Effects on the Dynamics

and Control of an Orbiting Large Flexible Antenna System," *35th International Astronautical Congress*, Lausanne, Switzerland, October 1984, Paper No. IAF–84–358.

[66] Krishna, R., and Bainum, P.M., "Dynamics and Control of Orbiting Flexible Structures Exposed to Solar Radiation," *Journal of Guidance, Control and Dynamics*, Vol. 8, No. 5, September – October 1985, pp. 591–596.

[67] Jordan, P.F., "Comment on 'Thermally Induced Vibration and Flutter of Flexible Booms'," *Journal of Spacecraft and Rocket*, Vol. 8, No. 2, February 1971, pp. 204–205.

[68] Augusti, G., "Comment on 'Thermally Induced Vibration and Flutter of Flexible Booms'," *Journal of Spacecraft and Rocket*, Vol. 8, No. 2, February 1971, pp. 202–204.

[69] Sikka, S., Iqbal, M., and Aggarwala, B.D., "Temperature Distribution and Curvature Produced in Long Solid Cylinders in Space," *Journal of Spacecraft and Rocket*, Vol. 6, No. 8, August 1969, pp. 911–916.

[70] Lutz, J.D., Allen, D.H., and Haisler, W.E., "Finite Element Model for the Thermoelastic Analysis of Large Composite Space Structures," *Journal of Spacecraft and Rocket*, Vol. 24, No. 5, September – October 1987, pp. 430–436.

[71] Ng, A.C., *Dynamics of Gravity Oriented Axi-Symmetric Satellites with Thermally Flexed Appendages*, M.A.Sc. Thesis, The University of British Columbia, November 1986.

[72] Silver, W.M., "On the Equivalence of Lagrangian and Newton-Euler Dynamics for Manipulators," *The International Journal of Robotics*, Vol. 1, No. 2, 1982, pp. 60–70.

[73] Hurty, W.C., "Dynamic Analysis of Structural Systems Using Component Modes," *AIAA Journal*, Vol. 3, No. 4, 1965, pp. 678–685.

[74] Craig, R.R. Jr., and Bampton, M.C.C., "Coupling of Substructures for Dynamic Analysis," *AIAA Journal*, Vol. 6, No. 7, 1968, pp. 1313–1319.

[75] Benfield, W.A., and Hruda, R.F., "Vibration Analysis of Structures by Component Mode Substitution," *AIAA Journal*, Vol. 9, No. 7, 1971, pp. 1255–1261.

[76] MacNeal, R.H., "A Hybrid Method of Component Mode Synthesis," *Comput-*

ers and Structures, Vol. 1, No. 4, December 1971, pp. 581–601.

[77] Rubin, S., "Improved Component-Mode Representation for Structural Dynamic Analysis," *AIAA Journal*, Vol. 13, No. 8, 1975, pp. 995–1006.

[78] Hughes, P.C., "Dynamics of Flexible Space Vehicles with Active Attitude Control," *Celestial Mechanics*, Vol. 9, No. 1, 1974, pp. 22–39.

[79] Hughes, P.C., "Modal Identities for Elastic Bodies, with Application to Vehicle Dynamics and Control," *Transaction of ASME, Journal of Applied Mechanics*,, Vol. 47, No. 1, March 1980, pp. 177–184.

[80] Hablani, H.B., "Constrained and Unconstrained Modes: Some Modeling Aspects of Flexible Spacecraft," *Journal of Guidance and Control*, Vol. 5, No. 2, March – April 1982, pp. 164–173.

[81] Hughes, P.C., "Space Structure Vibration Modes: How Many Exist? Which Ones Are Important?" *IEEE Control Systems Magazine*,, Vol. 7, No. 1, February 1987, pp. 22–28.

[82] Hughes, P.C., and Skelton, R.E., "Modal Truncation for Flexible Spacecraft," *Journal of Guidance and Control*, Vol. 4, No. 3, May – June 1981, pp. 291–297.

[83] Gregory, C.Z. Jr., "Reduction of Large Flexible Spacecraft Models Using Internal Balancing Theory," *Journal of Guidance, Control and Dynamics*, Vol. 7, No. 6, November – December 1984, pp. 725–732.

[84] Moore, B.C., "Principal Component Analysis in Linear Systems: Controllability, Observability, and Model Reduction," *IEEE Transactions on Automatic Control*,, Vol. AC–26, No. 1, February 1981, pp. 17–32.

[85] Spanos, J.T., and Tsuha, W.S., "Selection of Component Modes for the Simulation of Flexible Multibody Spacecraft," *AAS/AIAA Astrodynamics Specialist Conference*, Stowe, Vermont, August 1989, Paper No. AAS–89–438.

[86] Hale, A.L., and Meirovitch, L., "A General Substructure Synthesis Method for the Dynamic Simulation of Complex Structures," *Journal of Sound and Vibration*, Vol. 69, No. 2, 1980, pp. 309–326.

[87] Meirovitch, L., and Hale, A.L., "On the Substructure Synthesis Method," *AIAA Journal*, Vol. 19, No. 7, 1981, pp. 940–947.

[88] Meirovitch, L., and Kwak, M.K., "On the Modeling of Flexible Multi-Body

Systems by the Rayleigh-Ritz Method," *AIAA Dynamics Specialist Conference*, Long Beach, California, April 1990, Paper No. AIAA–90–1245–CP.

[89] Johns, D.J., *Thermal Stress Analysis*, Pergamon Press, Oxford, U.K., 1965, pp. 48–55.

[90] Ng, A.C., and Modi, V.J., "Dynamics of Gravity Oriented Satellites with Thermally Flexed Appendages," *AAS/AIAA Astrodynamics Specialist Conference*, Kalispell, Montana, August 1987, Paper No. AAS–87–432.

[91] Blevins, R.D., *Formulas for Natural Frequencies and Mode Shapes*, Van Nostrand Reinhold Co., New York, N.Y., 1979, pp. 108–109.

[92] Timoshenko, S., and Woinowsky–Kreiger, S., *Theory of Plates and Shells*, McGraw–Hill Book Co., New York, N.Y., 1959, pp. 79–88.

[93] Leissa, A.W., "The Free Vibration of Rectangular Plates," *Journal of Sound and Vibration*, Vol. 31, No. 3, 1973, pp. 257–293.

[94] Warburton, G.B., "The Vibration of Rectangular Plates," *Proceedings of the Institution of Mechanical Engineers*, Vol. 168, No. 12, 1954, pp. 371–384.

[95] Gorman, D.J., and Sharma, R.K., "A Comprehensive Approach to the Free Vibration Analysis of Rectangular Plates by Use of the Method of Superposition," *Journal of Sound and Vibration*, Vol. 47, No. 1, 1976, pp. 126–128.

[96] Gorman, D.J., *Free Vibration Analysis of Rectangular Plates*, Elsevier North Holland, Inc., New York, New York, 1982, pp. 112–145.

[97] Hughes, P.C., *Spacecraft Attitude Dynamics*, John Wiley & Sons, New York, N.Y., 1986, pp. 18–22.

[98] Moran, J.P., "Effects of Planar Libration on the Orbital Motion of a Dumbbell Satellite," *ARS Journal*, Vol. 31, No. 8, August 1961, pp. 1089–1096.

[99] Yu, E.Y., "Long-term Coupling Effects Between the Librational and Orbital Motions of a Satellite," *AIAA Journal*, Vol. 2, No. 3, March 1964, pp. 553–555.

[100] *IMSL Library Reference Manual*, Vol. 1, IMSL Inc., Houston, Texas, June 1980, pp. DGEAR–1 – DGEAR 9.

[101] Gear, C.W., *Numerical Initial Value Problems in Ordinary Differential Equations*, Prentice–Hall, Englewood Cliffs, New Jersey, 1971, pp. 158–166.

[102] *Space Station Engineering Data Book*, NASA SSE-E-87-R1, NASA Space Station Program Office, November 1987.

[103] *Modal Analysis of Selected Space Station Configurations*, NASA SSE-E-88-R8, NASA Space Station Program Office, Washington D.C., June 1988.

[104] Kane, T.R., Likins, P.W., and Levinson, D.A., *Spacecraft Dynamics*, McGraw–Hill Book Co., New York, N.Y., 1983, pp. 199–211.

[105] Modi, V.J., and Ng, A.C., "Dynamics of Axisymmetric Satellite Under the Influence of Solar Radiation: Analytical and Numerical Approaches," *The Journal of the Astronautical Sciences*, Vol. 37, No. 1, January – March 1989, pp. 17–40.

[106] *Space Station Microgravity Environment Status*, NASA SSE-E-88-R12, NASA Space Station Program Office, Washington, D.C., June 1988.

[107] Small Space Platform Working Group, *Advanced Technology Experiment Onboard Space Flyer Unit (SFU)*, Institute of Space and Astronautical Science and Space Station Task Team, Japan, March 1986, pp. 115–202.

[107] Freund, E., "The Structure of Decoupled Nonlinear Systems," *International Journal of Control*, Vol. 21, No. 3, 1975, pp. 443–450.

[108] Freund, E., "Fast Nonlinear Control with Arbitrary Pole-Placement for Industrial Robots and Manipulators," *The International Journal of Robotics Research*, Vol. 1, No. 1, 1982, pp. 65–78.

[109] Slotine, J.E. and Sastry, S.S., "Tracking Control of Non-linear Systems using Sliding Surfaces with Application to Robot Manipulators," *International Journal of Control*, Vol. 38, No. 2, 1983, pp. 465–492.

[110] Slotine, J.E., "Sliding Controller Design for Non-linear Systems," *International Journal of Control*, Vol. 40, No. 2, 1984, pp. 421–434.

[111] Slotine, J.E., "The Robust Control of Robot Manipulators," *International Journal of Robotics Research*, Vol. 4, No. 2, 1985, pp. 49–64.

[112] Slotine, J.E., and Li, W., "On the Adaptive Control of Robot Manipulators," *International Journal of Robotics Research*, Vol. 6, No. 3, 1987, pp. 49–59.

[113] Beijczy, A.K., *Robot Arm Dynamics and Control*, JPL TM 33–669, California Institute of Technology, Pasadena, California, 1974.

[114] Singh, S.N., and Schy, A.A., "Invertibility and Robust Nonlinear Control of Robotic Systems," *Proceedings of 23rd Conference on Decision and Control*, Las Vegas, Nevada, December 1984, pp. 1058–1063.

[115] Spong, M.W., and Vidyasagar, M., "Robust Linear Compensator Design for Nonlinear Robotic Control," *Proceedings of IEEE Conference on Robotics and Automation*, St. Louis, Missouri, March 1985, pp. 954–959.

[116] Spong, M.W., and Vidyasagar, M., "Robust Nonlinear Control of Robot Manipulator," *Proceedings of the 24th IEEE Conference on Decision and Control*, Fort Lauderdale, Florida, December 1985, pp. 1767–1772.

[117] Spong, M.W., "Modelling and Control of Elastic Joint Robots," *Journal of Dynamic Systems, Measurement and Control*, Vol. 109, December 1987, pp. 310–319.

[118] Karray, F., Modi, V.J., and Chan, J.K., "Inverse Control of Flexible Orbiting Manipulators," *Proceedings of the American Control Conference*, Boston, Mass., June 1991, Editor: A.G. Ulsoy, pp. 1909–1912.

[119] Modi, V.J., Karray, F., and Chan, J.K., "On the Control of a Class of Flexible Manipulators Using Feedback Linearization Approach," *42nd Congress of the International Astronautical Federation*, October, 1991, Montreal, Canada, Paper No. IAF–91–324.

Appendix I: Details of T_{sys}, I_{sys}, and $\bar{H}_{sys}$

The details of the various components that make up T_{sys} of Eq. (2.35) are given below:

$$T_{orb} = \frac{1}{2} M \dot{\bar{R}}_{cm} \cdot \dot{\bar{R}}_{cm} \, ;$$

$$T_{cm} = -\frac{1}{2} M \dot{\bar{C}}_{cm} \cdot \dot{\bar{C}}_{cm} \, ;$$

$$T_h = \frac{1}{2} \sum_{i=1}^{N} \left[\int_{m_i} \dot{\bar{d}}_i \cdot \dot{\bar{d}}_i \, dm_i + \sum_{j=1}^{n_i} \int_{m_{i,j}} (\dot{\bar{d}}_i + \mathbf{C}_{\mathbf{i}}^{\mathbf{c}} \dot{\bar{d}}_{ij}) \cdot (\dot{\bar{d}}_i + \mathbf{C}_{\mathbf{i}}^{\mathbf{c}} \dot{\bar{d}}_{ij}) \, dm_{i,j} \right] ;$$

$$\begin{aligned} T_{jr} = \frac{1}{2} \sum_{i=1}^{N} \Bigg[& \int_{m_i} \dot{\mathbf{C}}_{\mathbf{i}}^{\mathbf{c}} (\bar{\rho}_i + \bar{\tau}_i + \bar{\delta}_i) \cdot \dot{\mathbf{C}}_{\mathbf{i}}^{\mathbf{c}} (\bar{\rho}_i + \bar{\tau}_i + \bar{\delta}_i) \, dm_i \\ & + \sum_{j=1}^{n_i} \int_{m_{i,j}} \left\{ \dot{\mathbf{C}}_{\mathbf{i}}^{\mathbf{c}} \bar{d}_{ij} + (\dot{\mathbf{C}}_{\mathbf{i,j}}^{\mathbf{c}} \mu_{\mathbf{i,j}} + \mathbf{C}_{\mathbf{i,j}}^{\mathbf{c}} \dot{\mu}_{\mathbf{i,j}}) (\bar{\rho}_{ij} + \bar{\tau}_{ij} + \bar{\delta}_{ij}) \right\} \cdot \\ & \left\{ \dot{\mathbf{C}}_{\mathbf{i}}^{\mathbf{c}} \bar{d}_{ij} + (\dot{\mathbf{C}}_{\mathbf{i,j}}^{\mathbf{c}} \mu_{\mathbf{i,j}} + \mathbf{C}_{\mathbf{i,j}}^{\mathbf{c}} \dot{\mu}_{\mathbf{i,j}}) (\bar{\rho}_{ij} + \bar{\tau}_{ij} + \bar{\delta}_{ij}) \right\} dm_{i,j} \Bigg] ; \end{aligned}$$

$$\begin{aligned} T_t = \frac{1}{2} \int_{m_c} \dot{\bar{\tau}}_c \cdot \dot{\bar{\tau}}_c \, dm_c + \frac{1}{2} \sum_{i=1}^{N} \Bigg[& \int_{m_i} (\mathbf{C}_{\mathbf{i}}^{\mathbf{c}} \dot{\bar{\tau}}_i) \cdot (\mathbf{C}_{\mathbf{i}}^{\mathbf{c}} \dot{\bar{\tau}}_i) \, dm_i \\ & + \sum_{j=1}^{n_i} \int_{m_{i,j}} (\mathbf{C}_{\mathbf{i,j}}^{\mathbf{c}} \mu_{\mathbf{i,j}} \dot{\bar{\tau}}_{ij}) \cdot (\mathbf{C}_{\mathbf{i,j}}^{\mathbf{c}} \mu_{\mathbf{i,j}} \dot{\bar{\tau}}_{ij}) \, dm_{i,j} \Bigg] ; \end{aligned}$$

$$\begin{aligned} T_v = \frac{1}{2} \int_{m_c} \dot{\bar{\delta}}_c \cdot \dot{\bar{\delta}}_c \, dm_c + \frac{1}{2} \sum_{i=1}^{N} \Bigg[& \int_{m_i} (\mathbf{C}_{\mathbf{i}}^{\mathbf{c}} \dot{\bar{\delta}}_i) \cdot (\mathbf{C}_{\mathbf{i}}^{\mathbf{c}} \dot{\bar{\delta}}_i) \, dm_i \\ & + \sum_{j=1}^{n_i} \int_{m_{i,j}} (\mathbf{C}_{\mathbf{i,j}}^{\mathbf{c}} \mu_{\mathbf{i,j}} \dot{\bar{\delta}}_{ij}) \cdot (\mathbf{C}_{\mathbf{i,j}}^{\mathbf{c}} \mu_{\mathbf{i,j}} \dot{\bar{\delta}}_{ij}) \, dm_{i,j} \Bigg] ; \end{aligned}$$

$$\begin{aligned} T_{h,jr} = \sum_{i=1}^{N} \Bigg[& \int_{m_i} \dot{\bar{d}}_i \cdot \dot{\mathbf{C}}_{\mathbf{i}}^{\mathbf{c}} (\bar{\rho}_i + \bar{\tau}_i + \bar{\delta}_i) \, dm_i + \sum_{j=1}^{n_i} \int_{m_{i,j}} \left\{ \dot{\bar{d}}_i + \mathbf{C}_{\mathbf{i}}^{\mathbf{c}} \dot{\bar{d}}_{ij} \right\} \cdot \\ & \left\{ \dot{\mathbf{C}}_{\mathbf{i}}^{\mathbf{c}} \bar{d}_{ij} + (\dot{\mathbf{C}}_{\mathbf{i,j}}^{\mathbf{c}} \mu_{\mathbf{i,j}} + \mathbf{C}_{\mathbf{i,j}}^{\mathbf{c}} \dot{\mu}_{\mathbf{i,j}}) (\bar{\rho}_{ij} + \bar{\tau}_{ij} + \bar{\delta}_{ij}) \right\} dm_{i,j} \Bigg] ; \end{aligned}$$

$$T_{h,t} = \sum_{i=1}^{N}\left[\int_{m_i} \dot{\bar{d}}_i \cdot (\mathbf{C}_{\mathbf{i}}^{\mathbf{c}}\dot{\bar{\tau}}_i)\, dm_i + \sum_{j=1}^{n_i}\int_{m_{i,j}} (\dot{\bar{d}}_i + \mathbf{C}_{\mathbf{i}}^{\mathbf{c}}\dot{\bar{d}}_{ij}) \cdot (\mathbf{C}_{\mathbf{i,j}}^{\mathbf{c}}\mu_{\mathbf{i,j}}\dot{\bar{\tau}}_{ij})\, dm_{i,j}\right];$$

$$T_{h,v} = \sum_{i=1}^{N}\left[\int_{m_i} \dot{\bar{d}}_i \cdot (\mathbf{C}_{\mathbf{i}}^{\mathbf{c}}\dot{\bar{\delta}}_i)\, dm_i + \sum_{j=1}^{n_i}\int_{m_{i,j}} (\dot{\bar{d}}_i + \mathbf{C}_{\mathbf{i}}^{\mathbf{c}}\dot{\bar{d}}_{ij}) \cdot (\mathbf{C}_{\mathbf{i,j}}^{\mathbf{c}}\mu_{\mathbf{i,j}}\dot{\bar{\delta}}_{ij})\, dm_{i,j}\right];$$

$$T_{jr,t} = \sum_{i=1}^{N}\left[\int_{m_i} \dot{\mathbf{C}}_{\mathbf{i}}^{\mathbf{c}}(\bar{\rho}_i + \bar{\tau}_i + \bar{\delta}_i) \cdot (\mathbf{C}_{\mathbf{i}}^{\mathbf{c}}\dot{\bar{\tau}}_i)\, dm_i + \sum_{j=1}^{n_i}\int_{m_{i,j}} \Big\{\dot{\mathbf{C}}_{\mathbf{i}}^{\mathbf{c}}\bar{d}_{ij} + (\dot{\mathbf{C}}_{\mathbf{i,j}}^{\mathbf{c}}\mu_{\mathbf{i,j}} + \mathbf{C}_{\mathbf{i,j}}^{\mathbf{c}}\dot{\mu}_{\mathbf{i,j}})(\bar{\rho}_{ij} + \bar{\tau}_{ij} + \bar{\delta}_{ij})\Big\} \cdot (\mathbf{C}_{\mathbf{i,j}}^{\mathbf{c}}\mu_{\mathbf{i,j}}\dot{\bar{\tau}}_{ij})\, dm_{i,j}\right];$$

$$T_{jr,v} = \sum_{i=1}^{N}\left[\int_{m_i} \dot{\mathbf{C}}_{\mathbf{i}}^{\mathbf{c}}(\bar{\rho}_i + \bar{\tau}_i + \bar{\delta}_i) \cdot (\mathbf{C}_{\mathbf{i}}^{\mathbf{c}}\dot{\bar{\delta}}_i)\, dm_i + \sum_{j=1}^{n_i}\int_{m_{i,j}} \Big\{\dot{\mathbf{C}}_{\mathbf{i}}^{\mathbf{c}}\bar{d}_{ij} + (\dot{\mathbf{C}}_{\mathbf{i,j}}^{\mathbf{c}}\mu_{\mathbf{i,j}} + \mathbf{C}_{\mathbf{i,j}}^{\mathbf{c}}\dot{\mu}_{\mathbf{i,j}})(\bar{\rho}_{ij} + \bar{\tau}_{ij} + \bar{\delta}_{ij})\Big\} \cdot (\mathbf{C}_{\mathbf{i,j}}^{\mathbf{c}}\mu_{\mathbf{i,j}}\dot{\bar{\delta}}_{ij})\, dm_{i,j}\right];$$

$$T_{t,v} = \int_{m_c} \dot{\bar{\tau}}_c \cdot \dot{\bar{\delta}}_c\, dm_c + \sum_{i=1}^{N}\left[\int_{m_i} (\mathbf{C}_{\mathbf{i}}^{\mathbf{c}}\dot{\bar{\tau}}_i) \cdot (\mathbf{C}_{\mathbf{i}}^{\mathbf{c}}\dot{\bar{\delta}}_i)\, dm_i + \sum_{j=1}^{n_i}\int_{m_{i,j}} (\mathbf{C}_{\mathbf{i,j}}^{\mathbf{c}}\mu_{\mathbf{i,j}}\dot{\bar{\tau}}_{ij}) \cdot (\mathbf{C}_{\mathbf{i,j}}^{\mathbf{c}}\mu_{\mathbf{i,j}}\dot{\bar{\delta}}_{ij})\, dm_{i,j}\right]. \qquad (\mathrm{I}-1)$$

The system inertia, $\mathbf{I}_{sys}$, is given by Eq. (2.36) and is the sum of the following components:

$$\mathbf{I}_{cm} = -M\left[\bar{C}_{cm} \cdot \bar{C}_{cm}\mathbf{U} - \bar{C}_{cm}\bar{C}_{cm}\right];$$

$$\mathbf{I}_h = \sum_{i=1}^{N}\left[\int_{m_i} \left\{\bar{d}_i \cdot \bar{d}_i\mathbf{U} - \bar{d}_i\bar{d}_i\right\} dm_i + \sum_{j=1}^{n_i}\int_{m_{i,j}} \Big\{(\bar{d}_i + \mathbf{C}_{\mathbf{i}}^{\mathbf{c}}\bar{d}_{ij}) \cdot (\bar{d}_i + \mathbf{C}_{\mathbf{i}}^{\mathbf{c}}\bar{d}_{ij})\mathbf{U} - (\bar{d}_i + \mathbf{C}_{\mathbf{i}}^{\mathbf{c}}\bar{d}_{ij})(\bar{d}_i + \mathbf{C}_{\mathbf{i}}^{\mathbf{c}}\bar{d}_{ij})\Big\} dm_{i,j}\right];$$

$$\mathbf{I}_r = \int_{m_c} \left\{\bar{\rho}_c \cdot \bar{\rho}_c\mathbf{U} - \bar{\rho}_c\bar{\rho}_c\right\} dm_c + \sum_{i=1}^{N}\left[\int_{m_i} \left\{(\mathbf{C}_{\mathbf{i}}^{\mathbf{c}}\bar{\rho}_i) \cdot (\mathbf{C}_{\mathbf{i}}^{\mathbf{c}}\bar{\rho}_i)\mathbf{U} - (\mathbf{C}_{\mathbf{i}}^{\mathbf{c}}\bar{\rho}_i)(\mathbf{C}_{\mathbf{i}}^{\mathbf{c}}\bar{\rho}_i)\right\} dm_i + \sum_{j=1}^{n_i}\int_{m_{i,j}} \left\{(\mathbf{C}_{\mathbf{i,j}}^{\mathbf{c}}\mu_{\mathbf{i,j}}\bar{\rho}_{ij}) \cdot (\mathbf{C}_{\mathbf{i,j}}^{\mathbf{c}}\mu_{\mathbf{i,j}}\bar{\rho}_{ij})\mathbf{U}\right.\right.$$

$$
\begin{aligned}
&\quad - (\mathbf{C}^{\mathbf{c}}_{\mathbf{i},\mathbf{j}}\mu_{\mathbf{i},\mathbf{j}}\bar{\rho}_{ij})(\mathbf{C}^{\mathbf{c}}_{\mathbf{i},\mathbf{j}}\mu_{\mathbf{i},\mathbf{j}}\bar{\rho}_{ij})\Big\}\, dm_{i,j}\Big]\,;\\
\mathbf{I}_t &= \int_{m_c}\Big\{\bar{\tau}_c\cdot\bar{\tau}_c\mathbf{U}-\bar{\tau}_c\bar{\tau}_c\Big\}\, dm_c\\
&\quad + \sum_{i=1}^{N}\Big[\int_{m_i}\Big\{(\mathbf{C}^{\mathbf{c}}_{\mathbf{i}}\bar{\tau}_i)\cdot(\mathbf{C}^{\mathbf{c}}_{\mathbf{i}}\bar{\tau}_i)\mathbf{U}-(\mathbf{C}^{\mathbf{c}}_{\mathbf{i}}\bar{\tau}_i)(\mathbf{C}^{\mathbf{c}}_{\mathbf{i}}\bar{\tau}_i)\Big\}\, dm_i\\
&\quad + \sum_{j=1}^{n_i}\int_{m_{i,j}}\Big\{(\mathbf{C}^{\mathbf{c}}_{\mathbf{i},\mathbf{j}}\mu_{\mathbf{i},\mathbf{j}}\bar{\tau}_{ij})\cdot(\mathbf{C}^{\mathbf{c}}_{\mathbf{i},\mathbf{j}}\mu_{\mathbf{i},\mathbf{j}}\bar{\tau}_{ij})\mathbf{U}\\
&\quad - (\mathbf{C}^{\mathbf{c}}_{\mathbf{i},\mathbf{j}}\mu_{\mathbf{i},\mathbf{j}}\bar{\tau}_{ij})(\mathbf{C}^{\mathbf{c}}_{\mathbf{i},\mathbf{j}}\mu_{\mathbf{i},\mathbf{j}}\bar{\tau}_{ij})\Big\}\, dm_{i,j}\Big]\,;\\
\mathbf{I}_v &= \int_{m_c}\Big\{\bar{\delta}_c\cdot\bar{\delta}_c\mathbf{U}-\bar{\delta}_c\bar{\delta}_c\Big\}\, dm_c\\
&\quad + \sum_{i=1}^{N}\Big[\int_{m_i}\Big\{(\mathbf{C}^{\mathbf{c}}_{\mathbf{i}}\bar{\delta}_i)\cdot(\mathbf{C}^{\mathbf{c}}_{\mathbf{i}}\bar{\delta}_i)\mathbf{U}-(\mathbf{C}^{\mathbf{c}}_{\mathbf{i}}\bar{\delta}_i)(\mathbf{C}^{\mathbf{c}}_{\mathbf{i}}\bar{\delta}_i)\Big\}\, dm_i\\
&\quad + \sum_{j=1}^{n_i}\int_{m_{i,j}}\Big\{(\mathbf{C}^{\mathbf{c}}_{\mathbf{i},\mathbf{j}}\mu_{\mathbf{i},\mathbf{j}}\bar{\delta}_{ij})\cdot(\mathbf{C}^{\mathbf{c}}_{\mathbf{i},\mathbf{j}}\mu_{\mathbf{i},\mathbf{j}}\bar{\delta}_{ij})\mathbf{U}\\
&\quad - (\mathbf{C}^{\mathbf{c}}_{\mathbf{i},\mathbf{j}}\mu_{\mathbf{i},\mathbf{j}}\bar{\delta}_{ij})(\mathbf{C}^{\mathbf{c}}_{\mathbf{i},\mathbf{j}}\mu_{\mathbf{i},\mathbf{j}}\bar{\delta}_{ij})\Big\}\, dm_{i,j}\Big]\,;\\
\mathbf{I}_{h,r} &= \sum_{i=1}^{N}\Big[\int_{m_i}\Big\{2\bar{d}_i\cdot(\mathbf{C}^{\mathbf{c}}_{\mathbf{i}}\bar{\rho}_i)\mathbf{U}-\bar{d}_i(\mathbf{C}^{\mathbf{c}}_{\mathbf{i}}\bar{\rho}_i)-(\mathbf{C}^{\mathbf{c}}_{\mathbf{i}}\bar{\rho}_i)\bar{d}_i\Big\}\, dm_i\\
&\quad + \sum_{j=1}^{n_i}\int_{m_{i,j}}\Big\{2(\bar{d}_i+\mathbf{C}^{\mathbf{c}}_{\mathbf{i}}\bar{d}_{ij})\cdot(\mathbf{C}^{\mathbf{c}}_{\mathbf{i},\mathbf{j}}\mu_{\mathbf{i},\mathbf{j}}\bar{\rho}_{ij})\mathbf{U}-(\bar{d}_i+\mathbf{C}^{\mathbf{c}}_{\mathbf{i}}\bar{d}_{ij})(\mathbf{C}^{\mathbf{c}}_{\mathbf{i},\mathbf{j}}\mu_{\mathbf{i},\mathbf{j}}\bar{\rho}_{ij})\\
&\quad - (\mathbf{C}^{\mathbf{c}}_{\mathbf{i},\mathbf{j}}\mu_{\mathbf{i},\mathbf{j}}\bar{\rho}_{ij})(\bar{d}_i+\mathbf{C}^{\mathbf{c}}_{\mathbf{i}}\bar{d}_{ij})\Big\}\, dm_{i,j}\Big]\,;\\
\mathbf{I}_{h,t} &= \sum_{i=1}^{N}\Big[\int_{m_i}\Big\{2\bar{d}_i\cdot(\mathbf{C}^{\mathbf{c}}_{\mathbf{i}}\bar{\tau}_i)\mathbf{U}-\bar{d}_i(\mathbf{C}^{\mathbf{c}}_{\mathbf{i}}\bar{\tau}_i)-(\mathbf{C}^{\mathbf{c}}_{\mathbf{i}}\bar{\tau}_i)\bar{d}_i\Big\}\, dm_i\\
&\quad + \sum_{j=1}^{n_i}\int_{m_{i,j}}\Big\{2(\bar{d}_i+\mathbf{C}^{\mathbf{c}}_{\mathbf{i}}\bar{d}_{ij})\cdot(\mathbf{C}^{\mathbf{c}}_{\mathbf{i},\mathbf{j}}\mu_{\mathbf{i},\mathbf{j}}\bar{\tau}_{ij})\mathbf{U}-(\bar{d}_i+\mathbf{C}^{\mathbf{c}}_{\mathbf{i}}\bar{d}_{ij})(\mathbf{C}^{\mathbf{c}}_{\mathbf{i},\mathbf{j}}\mu_{\mathbf{i},\mathbf{j}}\bar{\tau}_{ij})\\
&\quad - (\mathbf{C}^{\mathbf{c}}_{\mathbf{i},\mathbf{j}}\mu_{\mathbf{i},\mathbf{j}}\bar{\tau}_{ij})(\bar{d}_i+\mathbf{C}^{\mathbf{c}}_{\mathbf{i}}\bar{d}_{ij})\Big\}\, dm_{i,j}\Big]\,;\\
\mathbf{I}_{h,v} &= \sum_{i=1}^{N}\Big[\int_{m_i}\Big\{2\bar{d}_i\cdot(\mathbf{C}^{\mathbf{c}}_{\mathbf{i}}\bar{\delta}_i)\mathbf{U}-\bar{d}_i(\mathbf{C}^{\mathbf{c}}_{\mathbf{i}}\bar{\delta}_i)-(\mathbf{C}^{\mathbf{c}}_{\mathbf{i}}\bar{\delta}_i)\bar{d}_i\Big\}\, dm_i
\end{aligned}
$$

$$
\begin{aligned}
&+\sum_{j=1}^{n_i}\int_{m_{i,j}}\Big\{2(\bar{d}_i+\mathbf{C_i^c}\bar{d}_{ij})\cdot(\mathbf{C_{i,j}^c}\mu_{\mathbf{i,j}}\bar{\delta}_{ij})\mathbf{U}-(\bar{d}_i+\mathbf{C_i^c}\bar{d}_{ij})(\mathbf{C_{i,j}^c}\mu_{\mathbf{i,j}}\bar{\delta}_{ij})\\
&-(\mathbf{C_{i,j}^c}\mu_{\mathbf{i,j}}\bar{\delta}_{ij})(\bar{d}_i+\mathbf{C_i^c}\bar{d}_{ij})\Big\}\,dm_{i,j}\Big]\;;\\
\mathbf{I}_{r,t}=&\int_{m_c}\Big\{2\bar{\rho}_c\cdot\bar{\tau}_c\mathbf{U}-\bar{\rho}_c\bar{\tau}_c-\bar{\tau}_c\bar{\rho}_c\Big\}\,dm_c\\
&+\sum_{i=1}^{N}\Big[\int_{m_i}\Big\{2(\mathbf{C_i^c}\bar{\rho}_i)\cdot(\mathbf{C_i^c}\bar{\tau}_i)\mathbf{U}-(\mathbf{C_i^c}\bar{\rho}_i)(\mathbf{C_i^c}\bar{\tau}_i)-(\mathbf{C_i^c}\bar{\tau}_i)(\mathbf{C_i^c}\bar{\rho}_i)\Big\}\,dm_i\\
&+\sum_{j=1}^{n_i}\int_{m_{i,j}}\Big\{2(\mathbf{C_{i,j}^c}\mu_{\mathbf{i,j}}\bar{\rho}_{ij})\cdot(\mathbf{C_{i,j}^c}\mu_{\mathbf{i,j}}\bar{\tau}_{ij})\mathbf{U}-(\mathbf{C_{i,j}^c}\mu_{\mathbf{i,j}}\bar{\rho}_{ij})(\mathbf{C_{i,j}^c}\mu_{\mathbf{i,j}}\bar{\tau}_{ij})\\
&-(\mathbf{C_{i,j}^c}\mu_{\mathbf{i,j}}\bar{\tau}_{ij})(\mathbf{C_{i,j}^c}\mu_{\mathbf{i,j}}\bar{\rho}_{ij})\Big\}\,dm_{i,j}\Big]\;;\\
\mathbf{I}_{r,v}=&\int_{m_c}\Big\{2\bar{\rho}_c\cdot\bar{\delta}_c\mathbf{U}-\bar{\rho}_c\bar{\delta}_c-\bar{\delta}_c\bar{\rho}_c\Big\}\,dm_c\\
&+\sum_{i=1}^{N}\Big[\int_{m_i}\Big\{2(\mathbf{C_i^c}\bar{\rho}_i)\cdot(\mathbf{C_i^c}\bar{\delta}_i)\mathbf{U}-(\mathbf{C_i^c}\bar{\rho}_i)(\mathbf{C_i^c}\bar{\delta}_i)-(\mathbf{C_i^c}\bar{\delta}_i)(\mathbf{C_i^c}\bar{\rho}_i)\Big\}\,dm_i\\
&+\sum_{j=1}^{n_i}\int_{m_{i,j}}\Big\{2(\mathbf{C_{i,j}^c}\mu_{\mathbf{i,j}}\bar{\rho}_{ij})\cdot(\mathbf{C_{i,j}^c}\mu_{\mathbf{i,j}}\bar{\delta}_{ij})\mathbf{U}-(\mathbf{C_{i,j}^c}\mu_{\mathbf{i,j}}\bar{\rho}_{ij})(\mathbf{C_{i,j}^c}\mu_{\mathbf{i,j}}\bar{\delta}_{ij})\\
&-(\mathbf{C_{i,j}^c}\mu_{\mathbf{i,j}}\bar{\delta}_{ij})(\mathbf{C_{i,j}^c}\mu_{\mathbf{i,j}}\bar{\rho}_{ij})\Big\}\,dm_{i,j}\Big]\;;\\
\mathbf{I}_{t,v}=&\int_{m_c}\Big\{2\bar{\tau}_c\cdot\bar{\delta}_c\mathbf{U}-\bar{\tau}_c\bar{\delta}_c-\bar{\delta}_c\bar{\tau}_c\Big\}\,dm_c\\
&+\sum_{i=1}^{N}\Big[\int_{m_i}\Big\{2(\mathbf{C_i^c}\bar{\tau}_i)\cdot(\mathbf{C_i^c}\bar{\delta}_i)\mathbf{U}-(\mathbf{C_i^c}\bar{\tau}_i)(\mathbf{C_i^c}\bar{\delta}_i)-(\mathbf{C_i^c}\bar{\delta}_i)(\mathbf{C_i^c}\bar{\tau}_i)\Big\}\,dm_i\\
&+\sum_{j=1}^{n_i}\int_{m_{i,j}}\Big\{2(\mathbf{C_{i,j}^c}\mu_{\mathbf{i,j}}\bar{\tau}_{ij})\cdot(\mathbf{C_{i,j}^c}\mu_{\mathbf{i,j}}\bar{\delta}_{ij})\mathbf{U}-(\mathbf{C_{i,j}^c}\mu_{\mathbf{i,j}}\bar{\tau}_{ij})(\mathbf{C_{i,j}^c}\mu_{\mathbf{i,j}}\bar{\delta}_{ij})\\
&-(\mathbf{C_{i,j}^c}\mu_{\mathbf{i,j}}\bar{\delta}_{ij})(\mathbf{C_{i,j}^c}\mu_{\mathbf{i,j}}\bar{\tau}_{ij})\Big\}\,dm_{i,j}\Big]\,. \qquad (\mathrm{I}-2)
\end{aligned}
$$

Here $\mathbf{U}$ is the unit matrix.

The components that contribute to $\bar{H}_{sys}$, the system angular momentum vector,

are shown in Eq. (2.37) and their details are as follows:

$$\bar{H}_{cm} = -M\left[\bar{C}_{cm} \times \dot{\bar{C}}_{cm}\right];$$

$$\bar{H}_h = \sum_{i=1}^{N}\left[\int_{m_i} (\bar{d}_i \times \dot{\bar{d}}_i)\, dm_i + \sum_{j=1}^{n_i}\int_{m_{i,j}} (\bar{d}_i + \mathbf{C}^{\mathbf{c}}_{\mathbf{i}}\bar{d}_{ij}) \times (\dot{\bar{d}}_i + \mathbf{C}^{\mathbf{c}}_{\mathbf{i}}\dot{\bar{d}}_{ij})\, dm_{i,j}\right];$$

$$\begin{aligned}\bar{H}_{jr} = \sum_{i=1}^{N}\Bigg[&\int_{m_i} \mathbf{C}^{\mathbf{c}}_{\mathbf{i}}(\bar{\rho}_i + \bar{\tau}_i + \bar{\delta}_i) \times \dot{\mathbf{C}}^{\mathbf{c}}_{\mathbf{i}}(\bar{\rho}_i + \bar{\tau}_i + \bar{\delta}_i)\, dm_i \\ &+ \sum_{j=1}^{n_i}\int_{m_{i,j}} \left\{\mathbf{C}^{\mathbf{c}}_{\mathbf{i}}\bar{d}_{ij} + \mathbf{C}^{\mathbf{c}}_{\mathbf{i,j}}\mu_{\mathbf{i,j}}(\bar{\rho}_{ij} + \bar{\tau}_{ij} + \bar{\delta}_{ij})\right\} \\ &\times \left\{\dot{\mathbf{C}}^{\mathbf{c}}_{\mathbf{i}}\bar{d}_{ij} + (\dot{\mathbf{C}}^{\mathbf{c}}_{\mathbf{i,j}}\mu_{\mathbf{i,j}} + \mathbf{C}^{\mathbf{c}}_{\mathbf{i,j}}\dot{\mu}_{\mathbf{i,j}})(\bar{\rho}_{ij} + \bar{\tau}_{ij} + \bar{\delta}_{ij})\right\} dm_{i,j}\Bigg];\end{aligned}$$

$$\begin{aligned}\bar{H}_t = &\int_{m_c} (\bar{\tau}_c \times \dot{\bar{\tau}}_c)\, dm_c + \sum_{i=1}^{N}\Bigg[\int_{m_i} (\mathbf{C}^{\mathbf{c}}_{\mathbf{i}}\bar{\tau}_i \times \mathbf{C}^{\mathbf{c}}_{\mathbf{i}}\dot{\bar{\tau}}_i)\, dm_i \\ &+ \sum_{j=1}^{n_i}\int_{m_{i,j}} (\mathbf{C}^{\mathbf{c}}_{\mathbf{i,j}}\mu_{\mathbf{i,j}}\bar{\tau}_{ij} \times \mathbf{C}^{\mathbf{c}}_{\mathbf{i,j}}\mu_{\mathbf{i,j}}\dot{\bar{\tau}}_{ij})\, dm_{i,j}\Bigg];\end{aligned}$$

$$\begin{aligned}\bar{H}_v = &\int_{m_c} (\bar{\delta}_c \times \dot{\bar{\delta}}_c)\, dm_c + \sum_{i=1}^{N}\Bigg[\int_{m_i} (\mathbf{C}^{\mathbf{c}}_{\mathbf{i}}\bar{\delta}_i \times \mathbf{C}^{\mathbf{c}}_{\mathbf{i}}\dot{\bar{\delta}}_i)\, dm_i \\ &+ \sum_{j=1}^{n_i}\int_{m_{i,j}} (\mathbf{C}^{\mathbf{c}}_{\mathbf{i,j}}\mu_{\mathbf{i,j}}\bar{\delta}_{ij} \times \mathbf{C}^{\mathbf{c}}_{\mathbf{i,j}}\mu_{\mathbf{i,j}}\dot{\bar{\delta}}_{ij})\, dm_{i,j}\Bigg];\end{aligned}$$

$$\begin{aligned}\bar{H}_{h,jr} = \sum_{i=1}^{N}\Bigg[&\int_{m_i} \bar{d}_i \times \dot{\mathbf{C}}^{\mathbf{c}}_{\mathbf{i}}(\bar{\rho}_i + \bar{\tau}_i + \bar{\delta}_i)\, dm_i \\ &+ \sum_{j=1}^{n_i}\int_{m_{i,j}} \bar{d}_i \times \left\{\dot{\mathbf{C}}^{\mathbf{c}}_{\mathbf{i}}\bar{d}_{ij} + (\dot{\mathbf{C}}^{\mathbf{c}}_{\mathbf{i,j}}\mu_{\mathbf{i,j}} + \mathbf{C}^{\mathbf{c}}_{\mathbf{i,j}}\dot{\mu}_{\mathbf{i,j}})(\bar{\rho}_{ij} + \bar{\tau}_{ij} + \bar{\delta}_{ij})\right\} dm_{i,j}\Bigg];\end{aligned}$$

$$\bar{H}_{h,r} = \sum_{i=1}^{N}\left[\int_{m_i} (\mathbf{C}^{\mathbf{c}}_{\mathbf{i}}\bar{\rho}_i \times \dot{\bar{d}}_i)\, dm_i + \sum_{j=1}^{n_i}\int_{m_{i,j}} \left\{\mathbf{C}^{\mathbf{c}}_{\mathbf{i,j}}\mu_{\mathbf{i,j}}\bar{\rho}_{ij} \times (\dot{\bar{d}}_i + \mathbf{C}^{\mathbf{c}}_{\mathbf{i}}\dot{\bar{d}}_{ij})\right\} dm_{i,j}\right];$$

$$\begin{aligned}\bar{H}_{h,t} = \sum_{i=1}^{N}\Bigg[&\int_{m_i} (\mathbf{C}^{\mathbf{c}}_{\mathbf{i}}\bar{\tau}_i \times \dot{\bar{d}}_i + \bar{d}_i \times \mathbf{C}^{\mathbf{c}}_{\mathbf{i}}\dot{\bar{\tau}}_i)\, dm_i \\ &+ \sum_{j=1}^{n_i}\int_{m_{i,j}} \left\{\mathbf{C}^{\mathbf{c}}_{\mathbf{i,j}}\mu_{\mathbf{i,j}}\bar{\tau}_{ij} \times (\dot{\bar{d}}_i + \mathbf{C}^{\mathbf{c}}_{\mathbf{i}}\dot{\bar{d}}_{ij})\right.\end{aligned}$$

$$+ (\bar{d}_i + \mathbf{C}_{\mathbf{i}}^{\mathbf{c}} \bar{d}_{ij}) \times (\mathbf{C}_{\mathbf{i},\mathbf{j}}^{\mathbf{c}} \mu_{\mathbf{i},\mathbf{j}} \dot{\bar{\tau}}_{ij}) \Big\} \, dm_{i,j} \Big] \; ;$$

$$\bar{H}_{h,v} = \sum_{i=1}^{N} \Big[\int_{m_i} (\mathbf{C}_{\mathbf{i}}^{\mathbf{c}} \bar{\delta}_i \times \dot{\bar{d}}_i + \bar{d}_i \times \mathbf{C}_{\mathbf{i}}^{\mathbf{c}} \dot{\bar{\delta}}_i) \, dm_i$$
$$+ \sum_{j=1}^{n_i} \int_{m_{i,j}} \Big\{ \mathbf{C}_{\mathbf{i},\mathbf{j}}^{\mathbf{c}} \mu_{\mathbf{i},\mathbf{j}} \bar{\delta}_{ij} \times (\dot{\bar{d}}_i + \mathbf{C}_{\mathbf{i}}^{\mathbf{c}} \dot{\bar{d}}_{ij})$$
$$+ (\bar{d}_i + \mathbf{C}_{\mathbf{i}}^{\mathbf{c}} \bar{d}_{ij}) \times (\mathbf{C}_{\mathbf{i},\mathbf{j}}^{\mathbf{c}} \mu_{\mathbf{i},\mathbf{j}} \dot{\bar{\delta}}_{ij}) \Big\} \, dm_{i,j} \Big] \; ;$$

$$\bar{H}_{r,t} = \int_{m_c} (\bar{\rho}_c \times \dot{\bar{\tau}}_c) \, dm_c + \sum_{i=1}^{N} \Big[\int_{m_i} (\mathbf{C}_{\mathbf{i}}^{\mathbf{c}} \bar{\rho}_i \times \mathbf{C}_{\mathbf{i}}^{\mathbf{c}} \dot{\bar{\tau}}_i) \, dm_i$$
$$+ \sum_{j=1}^{n_i} \int_{m_{i,j}} (\mathbf{C}_{\mathbf{i},\mathbf{j}}^{\mathbf{c}} \mu_{\mathbf{i},\mathbf{j}} \bar{\rho}_{ij} \times \mathbf{C}_{\mathbf{i},\mathbf{j}}^{\mathbf{c}} \mu_{\mathbf{i},\mathbf{j}} \dot{\bar{\tau}}_{ij}) \, dm_{i,j} \Big] \; ;$$

$$\bar{H}_{r,v} = \int_{m_c} (\bar{\rho}_c \times \dot{\bar{\delta}}_c) \, dm_c + \sum_{i=1}^{N} \Big[\int_{m_i} (\mathbf{C}_{\mathbf{i}}^{\mathbf{c}} \bar{\rho}_i \times \mathbf{C}_{\mathbf{i}}^{\mathbf{c}} \dot{\bar{\delta}}_i) \, dm_i$$
$$+ \sum_{j=1}^{n_i} \int_{m_{i,j}} (\mathbf{C}_{\mathbf{i},\mathbf{j}}^{\mathbf{c}} \mu_{\mathbf{i},\mathbf{j}} \bar{\rho}_{ij} \times \mathbf{C}_{\mathbf{i},\mathbf{j}}^{\mathbf{c}} \mu_{\mathbf{i},\mathbf{j}} \dot{\bar{\delta}}_{ij}) \, dm_{i,j} \Big] \; ;$$

$$\bar{H}_{t,v} = \int_{m_c} (\bar{\tau}_c \times \dot{\bar{\delta}}_c + \bar{\delta}_c \times \dot{\bar{\tau}}_c) \, dm_c + \sum_{i=1}^{N} \Big[\int_{m_i} (\mathbf{C}_{\mathbf{i}}^{\mathbf{c}} \bar{\tau}_i \times \mathbf{C}_{\mathbf{i}}^{\mathbf{c}} \dot{\bar{\delta}}_i + \mathbf{C}_{\mathbf{i}}^{\mathbf{c}} \bar{\delta}_i \times \mathbf{C}_{\mathbf{i}}^{\mathbf{c}} \dot{\bar{\tau}}_i) \, dm_i$$
$$+ \sum_{j=1}^{n_i} \int_{m_{i,j}} \Big\{ \mathbf{C}_{\mathbf{i},\mathbf{j}}^{\mathbf{c}} \mu_{\mathbf{i},\mathbf{j}} \bar{\tau}_{ij} \times (\mathbf{C}_{\mathbf{i},\mathbf{j}}^{\mathbf{c}} \mu_{\mathbf{i},\mathbf{j}} \dot{\bar{\delta}}_{ij})$$
$$+ \mathbf{C}_{\mathbf{i},\mathbf{j}}^{\mathbf{c}} \mu_{\mathbf{i},\mathbf{j}} \bar{\delta}_{ij} \times (\mathbf{C}_{\mathbf{i},\mathbf{j}}^{\mathbf{c}} \mu_{\mathbf{i},\mathbf{j}} \dot{\bar{\tau}}_{ij}) \Big\} \, dm_{i,j} \Big] \; . \qquad (\mathrm{I}-3)$$

Appendix II: Representation of T_{sys}, $\mathbf{I}_{sys}$, and $\bar{H}_{sys}$ in terms of the New Operators

In terms of operators Υ and Θ, the components of T_{sys} in Eq. (I–1) can be written as follows:

$$T_{cm} = -\frac{1}{2} M \Upsilon(\mathbf{U},\mathbf{U}) \circ \Theta(\bar{C}'_{cm}, \bar{C}'_{cm})\,;$$

$$\begin{aligned} T_h = \frac{1}{2}\sum_{i=1}^{N}\Bigg[& \int_{m_i} \Upsilon(\mathbf{U},\mathbf{U}) \circ \Theta(\bar{d}'_i, \bar{d}'_i)\, dm_i \\ & + \sum_{j=1}^{n_i} \int_{m_{i,j}} \Big\{ \Upsilon(\mathbf{U},\mathbf{U}) \circ \Theta(\bar{d}'_i, \bar{d}'_i) + 2\Upsilon(\mathbf{U}, \mathbf{C}^{\mathbf{c}}_{\mathbf{i}}) \circ \Theta(\bar{d}'_i, \bar{d}'_{ij}) \\ & + \Upsilon(\mathbf{C}^{\mathbf{c}}_{\mathbf{i}}, \mathbf{C}^{\mathbf{c}}_{\mathbf{i}}) \circ \Theta(\bar{d}'_{ij}, \bar{d}'_{ij}) \Big\}\, dm_{i,j} \Bigg]\,; \end{aligned}$$

$$\begin{aligned} T_{jr} = \frac{1}{2}\sum_{i=1}^{N}\Bigg[& \int_{m_i} \Upsilon(\mathbf{C}^{\mathbf{c}\prime}_{\mathbf{i}}, \mathbf{C}^{\mathbf{c}\prime}_{\mathbf{i}}) \circ \Theta((\bar{\rho}_i + \bar{\tau}_i + \bar{\delta}_i), (\bar{\rho}_i + \bar{\tau}_i + \bar{\delta}_i))\, dm_i \\ & + \sum_{j=1}^{n_i} \int_{m_{i,j}} \Big\{ \Upsilon(\mathbf{C}^{\mathbf{c}\prime}_{\mathbf{i}}, \mathbf{C}^{\mathbf{c}\prime}_{\mathbf{i}}) \circ \Theta(\bar{d}_{ij}, \bar{d}_{ij}) \\ & + 2\Upsilon(\mathbf{C}^{\mathbf{c}\prime}_{\mathbf{i}}, (\mathbf{C}^{\mathbf{c}}_{\mathbf{i},\mathbf{j}}\mu_{\mathbf{i},\mathbf{j}})') \circ \Theta(\bar{d}_{ij}, (\bar{\rho}_{ij} + \bar{\tau}_{ij} + \bar{\delta}_{ij})) \\ & + \Upsilon((\mathbf{C}^{\mathbf{c}}_{\mathbf{i},\mathbf{j}}\mu_{\mathbf{i},\mathbf{j}})', (\mathbf{C}^{\mathbf{c}}_{\mathbf{i},\mathbf{j}}\mu_{\mathbf{i},\mathbf{j}})') \circ \Theta((\bar{\rho}_{ij} + \bar{\tau}_{ij} + \bar{\delta}_{ij}), (\bar{\rho}_{ij} + \bar{\tau}_{ij} + \bar{\delta}_{ij})) \Big\}\, dm_{i,j} \Bigg]\,; \end{aligned}$$

$$\begin{aligned} T_t = \frac{1}{2}\int_{m_c} \Upsilon(\mathbf{U},\mathbf{U}) \circ \Theta(\bar{\tau}'_c, \bar{\tau}'_c)\, dm_c + \frac{1}{2}\sum_{i=1}^{N}\Bigg[& \int_{m_i} \Upsilon(\mathbf{C}^{\mathbf{c}}_{\mathbf{i}}, \mathbf{C}^{\mathbf{c}}_{\mathbf{i}}) \circ \Theta(\bar{\tau}'_i, \bar{\tau}'_i)\, dm_i \\ & + \sum_{j=1}^{n_i} \int_{m_{i,j}} \Upsilon(\mathbf{C}^{\mathbf{c}}_{\mathbf{i},\mathbf{j}}\mu_{\mathbf{i},\mathbf{j}}, \mathbf{C}^{\mathbf{c}}_{\mathbf{i},\mathbf{j}}\mu_{\mathbf{i},\mathbf{j}}) \circ \Theta(\bar{\tau}'_{ij}, \bar{\tau}'_{ij})\, dm_{i,j} \Bigg]\,; \end{aligned}$$

$$\begin{aligned} T_v = \frac{1}{2}\int_{m_c} \Upsilon(\mathbf{U},\mathbf{U}) \circ \Theta(\bar{\delta}'_c, \bar{\delta}'_c)\, dm_c + \frac{1}{2}\sum_{i=1}^{N}\Bigg[& \int_{m_i} \Upsilon(\mathbf{C}^{\mathbf{c}}_{\mathbf{i}}, \mathbf{C}^{\mathbf{c}}_{\mathbf{i}}) \circ \Theta(\bar{\delta}'_i, \bar{\delta}'_i)\, dm_i \\ & + \sum_{j=1}^{n_i} \int_{m_{i,j}} \Upsilon(\mathbf{C}^{\mathbf{c}}_{\mathbf{i},\mathbf{j}}\mu_{\mathbf{i},\mathbf{j}}, \mathbf{C}^{\mathbf{c}}_{\mathbf{i},\mathbf{j}}\mu_{\mathbf{i},\mathbf{j}}) \circ \Theta(\bar{\delta}'_{ij}, \bar{\delta}'_{ij})\, dm_{i,j} \Bigg]\,; \end{aligned}$$

$$T_{h,jr} = \sum_{i=1}^{N} \Bigg[\int_{m_i} \Upsilon(\mathbf{U}, \mathbf{C_i^{c\prime}}) \circ \Theta(\bar{d}_i', (\bar{\rho}_i + \bar{\tau}_i + \bar{\delta}_i))\, dm_i$$
$$+ \sum_{j=1}^{n_i} \int_{m_{i,j}} \Big\{ \Upsilon(\mathbf{U}, \mathbf{C_i^{c\prime}}) \circ \Theta(\bar{d}_i', \bar{d}_{ij})$$
$$+ \Upsilon(\mathbf{U}, (\mathbf{C_{i,j}^{c}}\mu_{\mathbf{i,j}})') \circ \Theta(\bar{d}_i', (\bar{\rho}_{ij} + \bar{\tau}_{ij} + \bar{\delta}_{ij}))$$
$$+ \Upsilon(\mathbf{C_i^{c}}, \mathbf{C_i^{c\prime}}) \circ \Theta(\bar{d}_{ij}', (\bar{\rho}_{ij} + \bar{\tau}_{ij} + \bar{\delta}_{ij})) \Big\}\, dm_{i,j} \Bigg];$$

$$T_{h,t} = \sum_{i=1}^{N} \Bigg[\int_{m_i} \Upsilon(\mathbf{U}, \mathbf{C_i^{c}}) \circ \Theta(\bar{d}_i', \bar{\tau}_i')\, dm_i$$
$$+ \sum_{j=1}^{n_i} \int_{m_{i,j}} \Big\{ \Upsilon(\mathbf{U}, \mathbf{C_{i,j}^{c}}\mu_{\mathbf{i,j}}) \circ \Theta(\bar{d}_i', \bar{\tau}_{ij}')$$
$$+ \Upsilon(\mathbf{C_i^{c}}, \mathbf{C_{i,j}^{c}}\mu_{\mathbf{i,j}}) \circ \Theta(\bar{d}_{ij}', \bar{\tau}_{ij}') \Big\}\, dm_{i,j} \Bigg];$$

$$T_{h,v} = \sum_{i=1}^{N} \Bigg[\int_{m_i} \Upsilon(\mathbf{U}, \mathbf{C_i^{c}}) \circ \Theta(\bar{d}_i', \bar{\delta}_i')\, dm_i$$
$$+ \sum_{j=1}^{n_i} \int_{m_{i,j}} \Big\{ \Upsilon(\mathbf{U}, \mathbf{C_{i,j}^{c}}\mu_{\mathbf{i,j}}) \circ \Theta(\bar{d}_i', \bar{\delta}_{ij}')$$
$$+ \Upsilon(\mathbf{C_i^{c}}, \mathbf{C_{i,j}^{c}}\mu_{\mathbf{i,j}}) \circ \Theta(\bar{d}_{ij}', \bar{\delta}_{ij}') \Big\}\, dm_{i,j} \Bigg];$$

$$T_{jr,t} = \sum_{i=1}^{N} \Bigg[\int_{m_i} \Upsilon(\mathbf{C_i^{c\prime}}, \mathbf{C_i^{c}}) \circ \Theta((\bar{\rho}_i + \bar{\tau}_i + \bar{\delta}_i), \bar{\tau}_i')\, dm_i$$
$$+ \sum_{j=1}^{n_i} \int_{m_{i,j}} \Big\{ \Upsilon(\mathbf{C_i^{c\prime}}, \mathbf{C_{i,j}^{c}}\mu_{\mathbf{i,j}}) \circ \Theta(\bar{d}_{ij}, \bar{\tau}_{ij}')$$
$$+ \Upsilon((\mathbf{C_{i,j}^{c}}\mu_{\mathbf{i,j}})', \mathbf{C_{i,j}^{c}}\mu_{\mathbf{i,j}}) \circ \Theta((\bar{\rho}_{ij} + \bar{\tau}_{ij} + \bar{\delta}_{ij}), \bar{\tau}_{ij}') \Big\}\, dm_{i,j} \Bigg];$$

$$T_{jr,v} = \sum_{i=1}^{N} \Bigg[\int_{m_i} \Upsilon(\mathbf{C_i^{c\prime}}, \mathbf{C_i^{c}}) \circ \Theta((\bar{\rho}_i + \bar{\tau}_i + \bar{\delta}_i), \bar{\delta}_i')\, dm_i$$
$$+ \sum_{j=1}^{n_i} \int_{m_{i,j}} \Big\{ \Upsilon(\mathbf{C_i^{c\prime}}, \mathbf{C_{i,j}^{c}}\mu_{\mathbf{i,j}}) \circ \Theta(\bar{d}_{ij}, \bar{\delta}_{ij}')$$

$$+ \Upsilon((\mathbf{C}^{\mathbf{c}}_{\mathbf{i,j}}\mu_{\mathbf{i,j}})', \mathbf{C}^{\mathbf{c}}_{\mathbf{i,j}}\mu_{\mathbf{i,j}}) \circ \Theta((\bar{\rho}_{ij} + \bar{\tau}_{ij} + \bar{\delta}_{ij}), \bar{\delta}'_{ij}) \Big\} \, dm_{i,j} \Big] ;$$

$$T_{t,v} = \int_{m_c} \Upsilon(\mathbf{U},\mathbf{U}) \circ \Theta(\bar{\tau}'_c, \bar{\delta}'_c) \, dm_c + \sum_{i=1}^{N} \Big[\int_{m_i} \Upsilon(\mathbf{C}^{\mathbf{c}}_{\mathbf{i}}, \mathbf{C}^{\mathbf{c}}_{\mathbf{i}}) \circ \Theta(\bar{\tau}'_i, \bar{\delta}'_i) \, dm_i$$
$$+ \sum_{j=1}^{n_i} \int_{m_{i,j}} \Upsilon(\mathbf{C}^{\mathbf{c}}_{\mathbf{i,j}}\mu_{\mathbf{i,j}}, \mathbf{C}^{\mathbf{c}}_{\mathbf{i,j}}\mu_{\mathbf{i,j}}) \circ \Theta(\bar{\tau}'_{ij}, \bar{\delta}'_{ij}) \, dm_{i,j} \Big] . \qquad (\mathrm{II}-1)$$

The components of inertia $\mathbf{I}_{sys}$ in Eq. (I–2) can be written in terms of the operators Υ, Γ, and Θ:

$$\mathbf{I}_{cm} = -M \Big[\Upsilon(\mathbf{U},\mathbf{U}) \circ \Theta(\bar{C}_{cm}, \bar{C}_{cm})\mathbf{U}$$
$$- \Gamma(\mathbf{U},\mathbf{U}) \circ \Theta(\bar{C}_{cm}, \bar{C}_{cm}) \Big] ;$$

$$\mathbf{I}_h = \sum_{i=1}^{N} \Big[\int_{m_i} \Big\{ \Upsilon(\mathbf{U},\mathbf{U}) \circ \Theta(\bar{d}_i, \bar{d}_i)\mathbf{U} - \Gamma(\mathbf{U},\mathbf{U}) \circ \Theta(\bar{d}_i, \bar{d}_i) \Big\} \, dm_i$$
$$+ \sum_{j=1}^{n_i} \Big[\int_{m_{i,j}} \Big\{ \Big[\Upsilon(\mathbf{U},\mathbf{U}) \circ \Theta(\bar{d}_i, \bar{d}_i) + 2\Upsilon(\mathbf{U}, \mathbf{C}^{\mathbf{c}}_{\mathbf{i}}) \circ \Theta(\bar{d}_i, \bar{d}_{ij})$$
$$+ \Upsilon(\mathbf{C}^{\mathbf{c}}_{\mathbf{i}}, \mathbf{C}^{\mathbf{c}}_{\mathbf{i}}) \circ \Theta(\bar{d}_{ij}, \bar{d}_{ij}) \Big]\mathbf{U} - \Big[\Gamma(\mathbf{U},\mathbf{U}) \circ \Theta(\bar{d}_i, \bar{d}_i)$$
$$+ 2\Gamma(\mathbf{U}, \mathbf{C}^{\mathbf{c}}_{\mathbf{i}}) \circ \Theta(\bar{d}_i, \bar{d}_{ij}) + \Gamma(\mathbf{C}^{\mathbf{c}}_{\mathbf{i}}, \mathbf{C}^{\mathbf{c}}_{\mathbf{i}}) \circ \Theta(\bar{d}_{ij}, \bar{d}_{ij}) \Big] \Big\} \, dm_{i,j} \Big] ;$$

$$\mathbf{I}_r = \int_{m_c} \Big\{ \Upsilon(\mathbf{U},\mathbf{U}) \circ \Theta(\bar{\rho}_c, \bar{\rho}_c)\mathbf{U} - \Gamma(\mathbf{U},\mathbf{U}) \circ \Theta(\bar{\rho}_c, \bar{\rho}_c) \Big\} \, dm_c$$
$$+ \sum_{i=1}^{N} \Big[\int_{m_i} \Big\{ \Upsilon(\mathbf{C}^{\mathbf{c}}_{\mathbf{i}}, \mathbf{C}^{\mathbf{c}}_{\mathbf{i}}) \circ \Theta(\bar{\rho}_i, \bar{\rho}_i)\mathbf{U} - \Gamma(\mathbf{C}^{\mathbf{c}}_{\mathbf{i}}, \mathbf{C}^{\mathbf{c}}_{\mathbf{i}}) \circ \Theta(\bar{\rho}_i, \bar{\rho}_i) \Big\} \, dm_i$$
$$+ \sum_{j=1}^{n_i} \int_{m_{i,j}} \Big\{ \Upsilon(\mathbf{C}^{\mathbf{c}}_{\mathbf{i,j}}\mu_{\mathbf{i,j}}, \mathbf{C}^{\mathbf{c}}_{\mathbf{i,j}}\mu_{\mathbf{i,j}}) \circ \Theta(\bar{\rho}_{ij}, \bar{\rho}_{ij})\mathbf{U}$$
$$- \Gamma(\mathbf{C}^{\mathbf{c}}_{\mathbf{i,j}}\mu_{\mathbf{i,j}}, \mathbf{C}^{\mathbf{c}}_{\mathbf{i,j}}\mu_{\mathbf{i,j}}) \circ \Theta(\bar{\rho}_{ij}, \bar{\rho}_{ij}) \Big\} \, dm_{i,j} \Big] ;$$

$$\mathbf{I}_t = \int_{m_c} \Big\{ \Upsilon(\mathbf{U},\mathbf{U}) \circ \Theta(\bar{\tau}_c, \bar{\tau}_c)\mathbf{U} - \Gamma(\mathbf{U},\mathbf{U}) \circ \Theta(\bar{\tau}_c, \bar{\tau}_c) \Big\} \, dm_c$$
$$+ \sum_{i=1}^{N} \Big[\int_{m_i} \Big\{ \Upsilon(\mathbf{C}^{\mathbf{c}}_{\mathbf{i}}, \mathbf{C}^{\mathbf{c}}_{\mathbf{i}}) \circ \Theta(\bar{\tau}_i, \bar{\tau}_i)\mathbf{U} - \Gamma(\mathbf{C}^{\mathbf{c}}_{\mathbf{i}}, \mathbf{C}^{\mathbf{c}}_{\mathbf{i}}) \circ \Theta(\bar{\tau}_i, \bar{\tau}_i) \Big\} \, dm_i$$

$$
\begin{aligned}
&+\sum_{j=1}^{n_i}\int_{m_{i,j}}\Big\{\Upsilon(\mathbf{C}^{\mathbf{c}}_{\mathbf{i},\mathbf{j}}\mu_{\mathbf{i},\mathbf{j}},\mathbf{C}^{\mathbf{c}}_{\mathbf{i},\mathbf{j}}\mu_{\mathbf{i},\mathbf{j}})\circ\Theta(\bar{\tau}_{ij},\bar{\tau}_{ij})\mathbf{U}\\
&-\Gamma(\mathbf{C}^{\mathbf{c}}_{\mathbf{i},\mathbf{j}}\mu_{\mathbf{i},\mathbf{j}},\mathbf{C}^{\mathbf{c}}_{\mathbf{i},\mathbf{j}}\mu_{\mathbf{i},\mathbf{j}})\circ\Theta(\bar{\tau}_{ij},\bar{\tau}_{ij})\Big\}\,dm_{i,j}\Big];\\
\mathbf{I}_v=&\int_{m_c}\Big\{\Upsilon(\mathbf{U},\mathbf{U})\circ\Theta(\bar{\delta}_c,\bar{\delta}_c)\mathbf{U}-\Gamma(\mathbf{U},\mathbf{U})\circ\Theta(\bar{\delta}_c,\bar{\delta}_c)\Big\}\,dm_c\\
&+\sum_{i=1}^{N}\Big[\int_{m_i}\Big\{\Upsilon(\mathbf{C}^{\mathbf{c}}_{\mathbf{i}},\mathbf{C}^{\mathbf{c}}_{\mathbf{i}})\circ\Theta(\bar{\delta}_i,\bar{\delta}_i)\mathbf{U}-\Gamma(\mathbf{C}^{\mathbf{c}}_{\mathbf{i}},\mathbf{C}^{\mathbf{c}}_{\mathbf{i}})\circ\Theta(\bar{\delta}_i,\bar{\delta}_i)\Big\}\,dm_i\\
&+\sum_{j=1}^{n_i}\int_{m_{i,j}}\Big\{\Upsilon(\mathbf{C}^{\mathbf{c}}_{\mathbf{i},\mathbf{j}}\mu_{\mathbf{i},\mathbf{j}},\mathbf{C}^{\mathbf{c}}_{\mathbf{i},\mathbf{j}}\mu_{\mathbf{i},\mathbf{j}})\circ\Theta(\bar{\delta}_{ij},\bar{\delta}_{ij})\mathbf{U}\\
&-\Gamma(\mathbf{C}^{\mathbf{c}}_{\mathbf{i},\mathbf{j}}\mu_{\mathbf{i},\mathbf{j}},\mathbf{C}^{\mathbf{c}}_{\mathbf{i},\mathbf{j}}\mu_{\mathbf{i},\mathbf{j}})\circ\Theta(\bar{\delta}_{ij},\bar{\delta}_{ij})\Big\}\,dm_{i,j}\Big];\\
\mathbf{I}_{h,r}=&\sum_{i=1}^{N}\Big[\int_{m_i}\Big\{2\Upsilon(\mathbf{U},\mathbf{C}^{\mathbf{c}}_{\mathbf{i}})\circ\Theta(\bar{d}_i,\bar{\rho}_i)\mathbf{U}\\
&-\big[\Gamma(\mathbf{U},\mathbf{C}^{\mathbf{c}}_{\mathbf{i}})\circ\Theta(\bar{d}_i,\bar{\rho}_i)+\Gamma(\mathbf{C}^{\mathbf{c}}_{\mathbf{i}},\mathbf{U})\circ\Theta(\bar{\rho}_i,\bar{d}_i)\big]\Big\}\,dm_i\\
&+\sum_{j=1}^{n_i}\int_{m_{i,j}}\Big\{2\big[\Upsilon(\mathbf{U},\mathbf{C}^{\mathbf{c}}_{\mathbf{i},\mathbf{j}}\mu_{\mathbf{i},\mathbf{j}})\circ\Theta(\bar{d}_i,\bar{\rho}_{ij})+\Upsilon(\mathbf{C}^{\mathbf{c}}_{\mathbf{i}},\mathbf{C}^{\mathbf{c}}_{\mathbf{i},\mathbf{j}}\mu_{\mathbf{i},\mathbf{j}})\circ\Theta(\bar{d}_{ij},\bar{\rho}_{ij})\big]\mathbf{U}\\
&-\big[\Gamma(\mathbf{U},\mathbf{C}^{\mathbf{c}}_{\mathbf{i},\mathbf{j}}\mu_{\mathbf{i},\mathbf{j}})\circ\Theta(\bar{d}_i,\bar{\rho}_{ij})+\Gamma(\mathbf{C}^{\mathbf{c}}_{\mathbf{i}},\mathbf{C}^{\mathbf{c}}_{\mathbf{i},\mathbf{j}}\mu_{\mathbf{i},\mathbf{j}})\circ\Theta(\bar{d}_{ij},\bar{\rho}_{ij})\\
&+\Gamma(\mathbf{C}^{\mathbf{c}}_{\mathbf{i},\mathbf{j}}\mu_{\mathbf{i},\mathbf{j}},\mathbf{U})\circ\Theta(\bar{\rho}_{ij},\bar{d}_i)+\Gamma(\mathbf{C}^{\mathbf{c}}_{\mathbf{i},\mathbf{j}}\mu_{\mathbf{i},\mathbf{j}},\mathbf{C}^{\mathbf{c}}_{\mathbf{i}})\circ\Theta(\bar{\rho}_{ij},\bar{d}_{ij})\big]\Big\}\,dm_{i,j}\Big];\\
\mathbf{I}_{h,t}=&\sum_{i=1}^{N}\Big[\int_{m_i}\Big\{2\Upsilon(\mathbf{U},\mathbf{C}^{\mathbf{c}}_{\mathbf{i}})\circ\Theta(\bar{d}_i,\bar{\tau}_i)\mathbf{U}\\
&-\big[\Gamma(\mathbf{U},\mathbf{C}^{\mathbf{c}}_{\mathbf{i}})\circ\Theta(\bar{d}_i,\bar{\tau}_i)+\Gamma(\mathbf{C}^{\mathbf{c}}_{\mathbf{i}},\mathbf{U})\circ\Theta(\bar{\tau}_i,\bar{d}_i)\big]\Big\}\,dm_i\\
&+\sum_{j=1}^{n_i}\int_{m_{i,j}}\Big\{2\big[\Upsilon(\mathbf{U},\mathbf{C}^{\mathbf{c}}_{\mathbf{i},\mathbf{j}}\mu_{\mathbf{i},\mathbf{j}})\circ\Theta(\bar{d}_i,\bar{\tau}_{ij})+\Upsilon(\mathbf{C}^{\mathbf{c}}_{\mathbf{i}},\mathbf{C}^{\mathbf{c}}_{\mathbf{i},\mathbf{j}}\mu_{\mathbf{i},\mathbf{j}})\circ\Theta(\bar{d}_{ij},\bar{\tau}_{ij})\big]\mathbf{U}\\
&-\big[\Gamma(\mathbf{U},\mathbf{C}^{\mathbf{c}}_{\mathbf{i},\mathbf{j}}\mu_{\mathbf{i},\mathbf{j}})\circ\Theta(\bar{d}_i,\bar{\tau}_{ij})+\Gamma(\mathbf{C}^{\mathbf{c}}_{\mathbf{i}},\mathbf{C}^{\mathbf{c}}_{\mathbf{i},\mathbf{j}}\mu_{\mathbf{i},\mathbf{j}})\circ\Theta(\bar{d}_{ij},\bar{\tau}_{ij})\\
&+\Gamma(\mathbf{C}^{\mathbf{c}}_{\mathbf{i},\mathbf{j}}\mu_{\mathbf{i},\mathbf{j}},\mathbf{U})\circ\Theta(\bar{\tau}_{ij},\bar{d}_i)+\Gamma(\mathbf{C}^{\mathbf{c}}_{\mathbf{i},\mathbf{j}}\mu_{\mathbf{i},\mathbf{j}},\mathbf{C}^{\mathbf{c}}_{\mathbf{i}})\circ\Theta(\bar{\tau}_{ij},\bar{d}_{ij})\big]\Big\}\,dm_{i,j}\Big];\\
\mathbf{I}_{h,v}=&\sum_{i=1}^{N}\Big[\int_{m_i}\Big\{2\Upsilon(\mathbf{U},\mathbf{C}^{\mathbf{c}}_{\mathbf{i}})\circ\Theta(\bar{d}_i,\bar{\delta}_i)\mathbf{U}\\
&-\big[\Gamma(\mathbf{U},\mathbf{C}^{\mathbf{c}}_{\mathbf{i}})\circ\Theta(\bar{d}_i,\bar{\delta}_i)+\Gamma(\mathbf{C}^{\mathbf{c}}_{\mathbf{i}},\mathbf{U})\circ\Theta(\bar{\delta}_i,\bar{d}_i)\big]\Big\}\,dm_i
\end{aligned}
$$

$$
\begin{aligned}
&+\sum_{j=1}^{n_i}\int_{m_{i,j}}\Big\{2\big[\Upsilon(\mathbf{U},\mathbf{C}^{\mathbf{c}}_{\mathbf{i},\mathbf{j}}\mu_{\mathbf{i},\mathbf{j}})\circ\Theta(\bar{d}_i,\bar{\delta}_{ij})+\Upsilon(\mathbf{C}^{\mathbf{c}}_{\mathbf{i}},\mathbf{C}^{\mathbf{c}}_{\mathbf{i},\mathbf{j}}\mu_{\mathbf{i},\mathbf{j}})\circ\Theta(\bar{d}_{ij},\bar{\delta}_{ij})\big]\mathbf{U}\\
&-\big[\Gamma(\mathbf{U},\mathbf{C}^{\mathbf{c}}_{\mathbf{i},\mathbf{j}}\mu_{\mathbf{i},\mathbf{j}})\circ\Theta(\bar{d}_i,\bar{\delta}_{ij})+\Gamma(\mathbf{C}^{\mathbf{c}}_{\mathbf{i}},\mathbf{C}^{\mathbf{c}}_{\mathbf{i},\mathbf{j}}\mu_{\mathbf{i},\mathbf{j}})\circ\Theta(\bar{d}_{ij},\bar{\delta}_{ij})\\
&+\Gamma(\mathbf{C}^{\mathbf{c}}_{\mathbf{i},\mathbf{j}}\mu_{\mathbf{i},\mathbf{j}},\mathbf{U})\circ\Theta(\bar{\delta}_{ij},\bar{d}_i)+\Gamma(\mathbf{C}^{\mathbf{c}}_{\mathbf{i},\mathbf{j}}\mu_{\mathbf{i},\mathbf{j}},\mathbf{C}^{\mathbf{c}}_{\mathbf{i}})\circ\Theta(\bar{\delta}_{ij},\bar{d}_{ij})\big]\Big\}\,dm_{i,j}\Big]\;;\\
\mathbf{I}_{r,t}=&\int_{m_c}\Big\{2\Upsilon(\mathbf{U},\mathbf{U})\circ\Theta(\bar{\rho}_c,\bar{\tau}_c)\mathbf{U}-\Gamma(\mathbf{U},\mathbf{U})\circ\big[\Theta(\bar{\rho}_c,\bar{\tau}_c)+\Theta(\bar{\tau}_c,\bar{\rho}_c)\big]\Big\}\,dm_c\\
&+\sum_{i=1}^{N}\Big[\int_{m_i}\Big\{2\Upsilon(\mathbf{C}^{\mathbf{c}}_{\mathbf{i}},\mathbf{C}^{\mathbf{c}}_{\mathbf{i}})\circ\Theta(\bar{\rho}_i,\bar{\tau}_i)\mathbf{U}\\
&-\Gamma(\mathbf{C}^{\mathbf{c}}_{\mathbf{i}},\mathbf{C}^{\mathbf{c}}_{\mathbf{i}})\circ\big[\Theta(\bar{\rho}_i,\bar{\tau}_i)+\Theta(\bar{\tau}_i,\bar{\rho}_i)\big]\Big\}\,dm_i\\
&+\sum_{j=1}^{n_i}\int_{m_{i,j}}\Big\{2\Upsilon(\mathbf{C}^{\mathbf{c}}_{\mathbf{i},\mathbf{j}}\mu_{\mathbf{i},\mathbf{j}},\mathbf{C}^{\mathbf{c}}_{\mathbf{i},\mathbf{j}}\mu_{\mathbf{i},\mathbf{j}})\circ\Theta(\bar{\rho}_{ij},\bar{\tau}_{ij})\mathbf{U}\\
&-\Gamma(\mathbf{C}^{\mathbf{c}}_{\mathbf{i},\mathbf{j}}\mu_{\mathbf{i},\mathbf{j}},\mathbf{C}^{\mathbf{c}}_{\mathbf{i},\mathbf{j}}\mu_{\mathbf{i},\mathbf{j}})\circ\Big[\Theta(\bar{\rho}_{ij},\bar{\tau}_{ij})+\Theta(\bar{\tau}_{ij},\bar{\rho}_{ij})\Big]\Big\}\,dm_{i,j}\Big]\;;\\
\mathbf{I}_{r,v}=&\int_{m_c}\Big\{2\Upsilon(\mathbf{U},\mathbf{U})\circ\Theta(\bar{\rho}_c,\bar{\delta}_c)\mathbf{U}-\Gamma(\mathbf{U},\mathbf{U})\circ\Big[\Theta(\bar{\rho}_c,\bar{\delta}_c)+\Theta(\bar{\delta}_c,\bar{\rho}_c)\Big]\Big\}\,dm_c\\
&+\sum_{i=1}^{N}\Big[\int_{m_i}\Big\{2\Upsilon(\mathbf{C}^{\mathbf{c}}_{\mathbf{i}},\mathbf{C}^{\mathbf{c}}_{\mathbf{i}})\circ\Theta(\bar{\rho}_i,\bar{\delta}_i)\mathbf{U}\\
&-\Gamma(\mathbf{C}^{\mathbf{c}}_{\mathbf{i}},\mathbf{C}^{\mathbf{c}}_{\mathbf{i}})\circ\Big[\Theta(\bar{\rho}_i,\bar{\delta}_i)+\Theta(\bar{\delta}_i,\bar{\rho}_i)\Big]\Big\}\,dm_i\\
&+\sum_{j=1}^{n_i}\int_{m_{i,j}}\Big\{2\Upsilon(\mathbf{C}^{\mathbf{c}}_{\mathbf{i},\mathbf{j}}\mu_{\mathbf{i},\mathbf{j}},\mathbf{C}^{\mathbf{c}}_{\mathbf{i},\mathbf{j}}\mu_{\mathbf{i},\mathbf{j}})\circ\Theta(\bar{\rho}_{ij},\bar{\delta}_{ij})\mathbf{U}\\
&-\Gamma(\mathbf{C}^{\mathbf{c}}_{\mathbf{i},\mathbf{j}}\mu_{\mathbf{i},\mathbf{j}},\mathbf{C}^{\mathbf{c}}_{\mathbf{i},\mathbf{j}}\mu_{\mathbf{i},\mathbf{j}})\circ\Big[\Theta(\bar{\rho}_{ij},\bar{\delta}_{ij})+\Theta(\bar{\delta}_{ij},\bar{\rho}_{ij})\Big]\Big\}\,dm_{i,j}\Big]\;;\\
\mathbf{I}_{t,v}=&\int_{m_c}\Big\{2\Upsilon(\mathbf{U},\mathbf{U})\circ\Theta(\bar{\tau}_c,\bar{\delta}_c)\mathbf{U}-\Gamma(\mathbf{U},\mathbf{U})\circ\Big[\Theta(\bar{\tau}_c,\bar{\delta}_c)+\Theta(\bar{\delta}_c,\bar{\tau}_c)\Big]\Big\}\,dm_c\\
&+\sum_{i=1}^{N}\Big[\int_{m_i}\Big\{2\Upsilon(\mathbf{C}^{\mathbf{c}}_{\mathbf{i}},\mathbf{C}^{\mathbf{c}}_{\mathbf{i}})\circ\Theta(\bar{\tau}_i,\bar{\delta}_i)\mathbf{U}\\
&-\Gamma(\mathbf{C}^{\mathbf{c}}_{\mathbf{i}},\mathbf{C}^{\mathbf{c}}_{\mathbf{i}})\circ\Big[\Theta(\bar{\tau}_i,\bar{\delta}_i)+\Theta(\bar{\delta}_i,\bar{\tau}_i)\Big]\Big\}\,dm_i\\
&+\sum_{j=1}^{n_i}\int_{m_{i,j}}\Big\{2\Upsilon(\mathbf{C}^{\mathbf{c}}_{\mathbf{i},\mathbf{j}}\mu_{\mathbf{i},\mathbf{j}},\mathbf{C}^{\mathbf{c}}_{\mathbf{i},\mathbf{j}}\mu_{\mathbf{i},\mathbf{j}})\circ\Theta(\bar{\tau}_{ij},\bar{\delta}_{ij})\mathbf{U}
\end{aligned}
$$

$$- \Gamma(\mathbf{C^c_{i,j}}\mu_{\mathbf{i,j}}, \mathbf{C^c_{i,j}}\mu_{\mathbf{i,j}}) \circ \Big[\Theta(\bar{\tau}_{ij}, \bar{\delta}_{ij}) + \Theta(\bar{\delta}_{ij}, \bar{\tau}_{ij})\Big]\Big\}\, dm_{i,j}\Bigg]. \qquad (\mathrm{II}-2)$$

Similarly, the angular momentum components of $\bar{H}_{sys}$ as given in Eq (I–3) can be represented by using operators Λ and Θ:

$$\bar{H}_{cm} = -M\Big[\Lambda(\mathbf{U},\mathbf{U}) \circ \Theta(\bar{C}_{cm}, \bar{C}'_{cm})\Big];$$

$$\begin{aligned}
\bar{H}_h = \sum_{i=1}^{N}\Bigg[&\int_{m_i} \Lambda(\mathbf{U},\mathbf{U}) \circ \Theta(\bar{d}_i, \bar{d}'_i)\, dm_i \\
&+ \sum_{j=1}^{n_i} \int_{m_{i,j}} \Big\{\Lambda(\mathbf{U},\mathbf{U}) \circ \Theta(\bar{d}_i, \bar{d}'_i) + \Lambda(\mathbf{U},\mathbf{C^c_i}) \circ \Theta(\bar{d}_i, \bar{d}'_{ij}) \\
&+ \Lambda(\mathbf{C^c_i},\mathbf{U}) \circ \Theta(\bar{d}_{ij}, \bar{d}'_i) + \Lambda(\mathbf{C^c_i},\mathbf{C^c_i}) \circ \Theta(\bar{d}_{ij}, \bar{d}'_{ij})\Big\}\, dm_{i,j}\Bigg];
\end{aligned}$$

$$\begin{aligned}
\bar{H}_{jr} = \sum_{i=1}^{N}\Bigg[&\int_{m_i} \Lambda(\mathbf{C^c_i},\mathbf{C^{c\prime}_i}) \circ \Theta((\bar{\rho}_i + \bar{\tau}_i + \bar{\delta}_i), (\bar{\rho}_i + \bar{\tau}_i + \bar{\delta}_i))\, dm_i \\
&+ \sum_{j=1}^{n_i} \int_{m_{i,j}} \Big\{\Lambda(\mathbf{C^c_i},\mathbf{C^{c\prime}_i}) \circ \Theta(\bar{d}_{ij}, \bar{d}_{ij}) \\
&+ \Lambda(\mathbf{C^c_{i,j}}\mu_{\mathbf{i,j}},\mathbf{C^{c\prime}_i}) \circ \Theta((\bar{\rho}_{ij} + \bar{\tau}_{ij} + \bar{\delta}_{ij}), \bar{d}_{ij}) \\
&+ \Lambda(\mathbf{C^c_i},(\mathbf{C^c_{i,j}}\mu_{\mathbf{i,j}})') \circ \Theta(\bar{d}_{ij}, (\bar{\rho}_{ij} + \bar{\tau}_{ij} + \bar{\delta}_{ij})) \\
&+ \Lambda(\mathbf{C^c_{i,j}}\mu_{\mathbf{i,j}},(\mathbf{C^c_{i,j}}\mu_{\mathbf{i,j}})') \circ \Theta((\bar{\rho}_{ij} + \bar{\tau}_{ij} + \bar{\delta}_{ij}), (\bar{\rho}_{ij} + \bar{\tau}_{ij} + \bar{\delta}_{ij}))\Big\}\, dm_{i,j}\Bigg];
\end{aligned}$$

$$\begin{aligned}
\bar{H}_t = &\int_{m_c} \Lambda(\mathbf{U},\mathbf{U}) \circ \Theta(\bar{\tau}_c, \bar{\tau}'_c)\, dm_c \\
&+ \sum_{i=1}^{N}\Bigg[\int_{m_i} \Lambda(\mathbf{C^c_i},\mathbf{C^c_i}) \circ \Theta(\bar{\tau}_i, \bar{\tau}'_i)\, dm_i \\
&+ \sum_{j=1}^{n_i} \int_{m_{i,j}} \Lambda(\mathbf{C^c_{i,j}}\mu_{\mathbf{i,j}},\mathbf{C^c_{i,j}}\mu_{\mathbf{i,j}}) \circ \Theta(\bar{\tau}_{ij}, \bar{\tau}'_{ij})\, dm_{i,j}\Bigg];
\end{aligned}$$

$$\begin{aligned}
\bar{H}_v = &\int_{m_c} \Lambda(\mathbf{U},\mathbf{U}) \circ \Theta(\bar{\delta}_c, \bar{\delta}'_c)\, dm_c \\
&+ \sum_{i=1}^{N}\Bigg[\int_{m_i} \Lambda(\mathbf{C^c_i},\mathbf{C^c_i}) \circ \Theta(\bar{\delta}_i, \bar{\delta}'_i)\, dm_i
\end{aligned}$$

$$+\sum_{j=1}^{n_i}\int_{m_{i,j}}\Lambda(\mathbf{C^c_{i,j}}\mu_{\mathbf{i,j}},\mathbf{C^c_{i,j}}\mu_{\mathbf{i,j}})\circ\Theta(\bar{\delta}_{ij},\bar{\delta}'_{ij})\,dm_{i,j}\Bigg];$$

$$\bar{H}_{h,jr}=\sum_{i=1}^{N}\Bigg[\int_{m_i}\Lambda(\mathbf{U},\mathbf{C_i^{c\prime}})\circ\Theta(\bar{d}_i,(\bar{\rho}_i+\bar{\tau}_i+\bar{\delta}_i))\,dm_i$$
$$+\sum_{j=1}^{n_i}\int_{m_{i,j}}\Big\{\Lambda(\mathbf{U},\mathbf{C_i^{c\prime}})\circ\Theta(\bar{d}_i,(\bar{\rho}_i+\bar{\tau}_i+\bar{\delta}_i))\,dm_i$$
$$+\Lambda(\mathbf{U},(\mathbf{C^c_{i,j}}\mu_{\mathbf{i,j}})')\circ\Theta(\bar{d}_i,(\bar{\rho}_{ij}+\bar{\tau}_{ij}+\bar{\delta}_{ij}))\Big\}\,dm_{i,j}\Bigg];$$

$$\bar{H}_{h,r}=\sum_{i=1}^{N}\Bigg[\int_{m_i}\Lambda(\mathbf{C_i^c},\mathbf{U})\circ\Theta(\bar{\rho}_i,\bar{d}'_i)\,dm_i$$
$$+\sum_{j=1}^{n_i}\int_{m_{i,j}}\Big\{\Lambda(\mathbf{C^c_{i,j}}\mu_{\mathbf{i,j}},\mathbf{U})\circ\Theta(\bar{\rho}_{ij},\bar{d}'_i)$$
$$+\Lambda(\mathbf{C^c_{i,j}}\mu_{\mathbf{i,j}},\mathbf{C_i^c})\circ\Theta(\bar{\rho}_{ij},\bar{d}'_{ij})\Big\}\,dm_{i,j}\Bigg];$$

$$\bar{H}_{h,t}=\sum_{i=1}^{N}\Bigg[\int_{m_i}\Big\{\Lambda(\mathbf{C_i^c},\mathbf{U})\circ\Theta(\bar{\tau}_i,\bar{d}'_i)+\Lambda(\mathbf{U},\mathbf{C_i^c})\circ\Theta(\bar{d}_i,\bar{\tau}'_i)\Big\}\,dm_i$$
$$+\sum_{j=1}^{n_i}\int_{m_{i,j}}\Big\{\Lambda(\mathbf{C^c_{i,j}}\mu_{\mathbf{i,j}},\mathbf{U})\circ\Theta(\bar{\tau}_{ij},\bar{d}'_i)+\Lambda(\mathbf{C^c_{i,j}}\mu_{\mathbf{i,j}},\mathbf{C_i^c})\circ\Theta(\bar{\tau}_{ij},\bar{d}'_{ij})$$
$$+\Lambda(\mathbf{U},\mathbf{C^c_{i,j}}\mu_{\mathbf{i,j}})\circ\Theta(\bar{d}_i,\bar{\tau}'_{ij})+\Lambda(\mathbf{C_i^c},\mathbf{C^c_{i,j}}\mu_{\mathbf{i,j}})\circ\Theta(\bar{d}_{ij},\bar{\tau}'_{ij})\Big\}\,dm_{i,j}\Bigg];$$

$$\bar{H}_{h,v}=\sum_{i=1}^{N}\Bigg[\int_{m_i}\Big\{\Lambda(\mathbf{C_i^c},\mathbf{U})\circ\Theta(\bar{\rho}_i,\bar{d}'_i)+\Lambda(\mathbf{U},\mathbf{C_i^c})\circ\Theta(\bar{d}_i,\bar{\delta}'_i)\Big\}\,dm_i$$
$$+\sum_{j=1}^{n_i}\int_{m_{i,j}}\Big\{\Lambda(\mathbf{C^c_{i,j}}\mu_{\mathbf{i,j}},\mathbf{U})\circ\Theta(\bar{\delta}_{ij},\bar{d}'_i)+\Lambda(\mathbf{C^c_{i,j}}\mu_{\mathbf{i,j}},\mathbf{C_i^c})\circ\Theta(\bar{\delta}_{ij},\bar{d}'_{ij})$$
$$+\Lambda(\mathbf{U},\mathbf{C^c_{i,j}}\mu_{\mathbf{i,j}})\circ\Theta(\bar{d}_i,\bar{\delta}'_{ij})+\Lambda(\mathbf{C_i^c},\mathbf{C^c_{i,j}}\mu_{\mathbf{i,j}})\circ\Theta(\bar{d}_{ij},\bar{\delta}'_{ij})\Big\}\,dm_{i,j}\Bigg];$$

$$\bar{H}_{r,t}=\int_{m_C}\Lambda(\mathbf{U},\mathbf{U})\circ\Theta(\bar{\rho}_c,\bar{\tau}'_c)\,dm_c+\sum_{i=1}^{N}\Bigg[\int_{m_i}\Lambda(\mathbf{C_i^c},\mathbf{C_i^c})\circ\Theta(\bar{\rho}_i,\bar{\tau}'_i)\,dm_i$$
$$+\sum_{j=1}^{n_i}\int_{m_{i,j}}\Lambda(\mathbf{C^c_{i,j}}\mu_{\mathbf{i,j}},\mathbf{C^c_{i,j}}\mu_{\mathbf{i,j}})\circ\Theta(\bar{\rho}_{ij},\bar{\tau}'_{ij})\,dm_{i,j}\Bigg];$$

$$
\begin{aligned}
\bar{H}_{r,v} = & \int_{m_c} \Lambda(\mathbf{U},\mathbf{U}) \circ \Theta(\bar{\rho}_c, \bar{\delta}'_c)\, dm_c + \sum_{i=1}^{N} \Bigg[\int_{m_i} \Lambda(\mathbf{C}^{\mathbf{c}}_{\mathbf{i}}, \mathbf{C}^{\mathbf{c}}_{\mathbf{i}}) \circ \Theta(\bar{\rho}_i, \bar{\delta}'_i)\, dm_i \\
& + \sum_{j=1}^{n_i} \int_{m_{i,j}} \Lambda(\mathbf{C}^{\mathbf{c}}_{\mathbf{i},\mathbf{j}} \mu_{\mathbf{i},\mathbf{j}}, \mathbf{C}^{\mathbf{c}}_{\mathbf{i},\mathbf{j}} \mu_{\mathbf{i},\mathbf{j}}) \circ \Theta(\bar{\rho}_{ij}, \bar{\delta}'_{ij})\, dm_{i,j} \Bigg] ; \\
\bar{H}_{t,v} = & \int_{m_c} \Lambda(\mathbf{U},\mathbf{U}) \circ \left[\Theta(\bar{\tau}_c, \bar{\delta}'_c) + \Theta(\bar{\delta}_c, \bar{\tau}'_c) \right] dm_c \\
& + \sum_{i=1}^{N} \Bigg[\int_{m_i} \Lambda(\mathbf{C}^{\mathbf{c}}_{\mathbf{i}}, \mathbf{C}^{\mathbf{c}}_{\mathbf{i}}) \circ \left[\Theta(\bar{\tau}_i, \bar{\delta}'_i) + \Theta(\bar{\delta}_i, \bar{\tau}'_i) \right] dm_i \\
& + \sum_{j=1}^{n_i} \int_{m_{i,j}} \Lambda(\mathbf{C}^{\mathbf{c}}_{\mathbf{i},\mathbf{j}} \mu_{\mathbf{i},\mathbf{j}}, \mathbf{C}^{\mathbf{c}}_{\mathbf{i},\mathbf{j}} \mu_{\mathbf{i},\mathbf{j}}) \circ \left[\Theta(\bar{\tau}_{ij}, \bar{\delta}'_{ij}) + \Theta(\bar{\delta}_{ij}, \bar{\tau}'_{ij}) \right] dm_{i,j} \Bigg] .
\end{aligned}
\tag{II - 3}
$$

Appendix III: A Sample of the Computer Program for the Evaluation of $\partial T_{sys}/\partial q$, $\mathbf{I}_{sys}$ and $\bar{H}_{sys}$

It is impractical to list the whole computer program here as it is over 5,000 lines. Instead, the objective is to illustrate simple algorithms required to assemble $\partial T_{sys}/\partial q$, $\mathbf{I}_{sys}$ and $\bar{H}_{sys}$. In so doing, only arrays that are used are declared in the DIMENSION statements. The actual program would require additional arrays to accomodate the evaluation of other derivatives of T_{sys}, $\mathbf{I}_{sys}$ and $\bar{H}_{sys}$. The array names are the same as those in Tables 3-1 and 3-2. A few points that may help understand the notations used are as follows:

(i) The $R91$, $R99$, and $R93$ arrays have the following structures:

$R99$: $R99c(m,n,p)$, $R99i(m,n,p,i)$, $R99ij(m,n,p,j)$,$R99j(m,n,p,j)$;

$R93$: $R93c(m,n,p)$, $R93i(m,n,p,i)$, $R93ij(m,n,p,j)$,$R93j(m,n,p,j)$;

where m (for $R91$) and m,n (for $R99$ and $R93$) refer to ν_m, $\gamma_{m,n}$, and $\lambda_{m,n}$, respectively, in Eq. (3.4); p is the subscript of Υ, Γ, and Λ in Table 3-1; i and j denote body B_i and $B_{i,j}$, respectively.

(ii) In order to save the array space, each $B_{i,j}$ body is identified by the numbers k and $Jcon(k)$. For instance, consider a system with two B_i bodies (B_1 and B_2) such that B_1 has three $B_{i,j}$ bodies attached ($B_{1,1}$, $B_{1,2}$, and $B_{1,3}$) while B_2 has only $B_{2,1}$ attached. Without any identification numbers, the minimum array size for, say $R91j$, would be $R91j(9,5,2,3)$ where the third and fourth dimensions are for identifying B_i and its associated $B_{i,j}$. Using the identification number so that $k = 1,2,3,4$ for $B_{1,1}$, $B_{1,2}$, $B_{1,3}$, and $B_{1,4}$, respectively; $Jcon(1) = Jcon(2) = Jcon(3) = 1$ and $Jcon(4) = 2$, each $B_{i,j}$ remains unambiguously identified but the minimum array for $R91j$ would be

$R91j(9,5,4)$ resulting in a saving in the array size.

(iii) The arrays for Θ operation have the similar structure as Υ operation. Using DH as an example,

DH: $DHi(m,p,i)$; $DHij(m,p,j)$; $DHj(m,p,j)$;

where m identifies θ_m of Eq. (3.4d); p is the subscript of Θ in Table 3-2; i and j denote body B_i and $B_{i,j}$, respectively.

(iv) The generalized coordinates, q, are each assigned a number m_q ($m_q = 1, \ldots, Nq$). The first three, $m_q = 1, 2, 3$, are for the librational degrees of freedom, ψ, ϕ, and λ, respectively. The rest ($m_q = 4, \ldots, Nq$) are for vibrational degrees of freedom.

(v) The prefix Q in the array name represents the $(\partial/\partial q)$ of the array; hence, one more dimension is required to identify the differentiation with respect to the generalized coordinate q_{m_q}. For instance, $QR91i(m,3,i,m_q)$ refers to $\partial v_m/\partial q_{m_q}$ of $\Upsilon_3(\mathbf{C_i^{c\prime}}, \mathbf{C_i^c})$.

(vi) It should be pointed out that, for simplicity, derivative arrays have the additional dimension of length N_q in the sample program here. This length can be shortened by recognizing the fact that not all arrays are functions of all generalized coordinates.

Sample subroutine to calculate $\partial T_{sys}/\partial q$

```
C
C     The array QKe represents the T{sys} derivative
C
      Subroutine KINENE(QKe)
      Implicit Real*8(a-h,o-z)
C
C     First declare the common blocks
C
      Common /No/    N, Nj, Nq, Jcon(Nj)
C
C     Rmc, Rmi, Rmj are the masses of body Bc, Bi, and Bij,
C     respectively
C
      Common /Ratio/ Rmi(N), Rmj(Nj)
C
      Common /CM/ CMc(9,4),     QCMc(9,4,Nq)
C
      Common /DD/ DDi(9,4,N),   QDDi(9,4,Nq,N),
     2            DDij(9,4,Nj), QDDij(9,4,Nq,Nj),
     3            DDj(9,4,Nj),  QDDj(9,4,Nq,Nj)
C
      Common /DF/ DFi(9,2,N),   QDFi(9,2,Nq,N),
     2            DFij(9,2,Nj), QDFij(9,2,Nq,Nj),
     3            DFj(9,2,Nj),  QDFj(9,2,Nq,Nj)
C
      Common /DG/ DGi(9,4,N),   QDGi(9,4,Nq,N),
     2            DGij(9,4,Nj), QDGij(9,4,Nq,Nj),
     3            DGj(9,4,Nj),  QDGj(9,4,Nq,Nj)
C
      Common /DH/ DHi(9,4,N),   QDHi(9,4,Nq,N),
     2            DHij(9,4,Nj), QDHij(9,4,Nq,Nj),
     3            DHj(9,4,Nj),  QDHj(9,4,Nq,Nj)
C
      Common /RR/ RRc(9,1),
     2            RRi(9,1,6),
```

```
     3            RRj(9,1,4)
C
      Common /RT/ RTc(9,3),     QRTc(9,3,Nq),
     2            RTi(9,3,N),   QRTi(9,3,Nq,N),
     3            RTj(9,3,Nj),  QRTj(9,3,Nq,Nj)
C
      Common /RV/ RVc(9,3),     QRVc(9,3,Nq),
     2            RVi(9,3,N),   QRVi(9,3,Nq,N),
     3            RVj(9,3,Nj),  QRVj(9,3,Nq,Nj)
C
      Common /TT/ TTc(9,4),     QTTc(9,4,Nq),
     2            TTi(9,4,N),   QTTi(9,4,Nq,N),
     3            TTj(9,4,Nj),  QTTj(9,4,Nq,Nj)
C
      Common /VV/ VVc(9,4),     QVVc(9,4,Nq),
     2            VVi(9,4,N),   QVVi(9,4,Nq,N),
     3            VVj(9,4,Nj),  QVVj(9,4,Nq,Nj)
C
      Common /TV/ TVc(9,4),     QTVc(9,4,Nq),
     2            TVi(9,4,N),   QTVi(9,4,Nq,N),
     3            TVj(9,4,Nj),  QTVj(9,4,Nq,Nj)
C
      Common /R91/ R91c(9),
     2             R91i(9,5,N),   QR91i(9,5,Nq,N),
     3             R91ij(9,4,Nj), QR91ij(9,4,Nq,Nj),
     4             R91j(9,5,Nj),  QR91j(9,5,Nq,Nj)
C
C     Declare matrices QKe and the temporary matrices QK
C     QK(m,n) (m=1,...11; n=1,Nq), refers to the m-th term
C     derivative in Eq. (I-1)
C     For instance, QK(1,iq) for T{cm}', QK(2,iq) for T{h}',
C     and so on
C
      Real*8 QKe(Nq), QK(11,Nq)
C
      Data Hf/0.5d0/
```

```
C
C     Initialize the arrays QKe and QK
C
      Do 7010 iq=1,Nq
      QKe(iq)=0.d0
 7010 Continue
C
      Do 7012 iq=1,Nq
      Do 7012 in=1,11
      QK(in,iq)=0.d0
 7012 Continue
C
C     Evaluate all terms for body Bc
C
      Do 710 iq=1,Mqi
      Do 710 i1=1,9
      QK(1,iq) =QK(1,iq)-Hf*R91c(i1)*QCMc(i1,1,iq)
      QK(4,iq) =QK(4,iq)+Hf*R91c(i1)*QTTc(i1,1,iq)
      QK(11,iq)=QK(11,iq)+Hf*R91c(i1)*QTVc(i1,1,iq)
 710  Continue
C
      Do 714 i =1,N
      Do 714 iq=1,Nq
      Do 714 i1=1,9
C
C     Proceed to Bi bodies
C
      QK(2,iq) =QK(2,iq)+Hf*R91c(i1)*QDDi(i1,1,iq,i)
      QK(3,iq) =QK(3,iq)+Hf*QR91i(i1,1,iq,i)*(RRi(i1,1,i)
     2         +RTi(i1,3,i)+RVi(i1,3,i)
     3         +TTi(i1,4,i)+VVi(i1,4,i)+TVi(i1,4,i))
     4         +Hf*R91i(i1,1,i)*(QRTi(i1,3,iq,i)
     5         +QRVi(i1,3,iq,i)+QTTi(i1,4,iq,i)
     6         +QVVi(i1,4,iq,i)+QTVi(i1,4,iq,i))
      QK(4,iq) =QK(4,iq)+Hf*(QR91i(i1,4,iq,i)*TTi(i1,1,i)
     2         +R91i(i1,4,i)*QTTi(i1,1,iq,i))
```

```
      QK(5,iq) =QK(5,iq)+Hf*QR91i(i1,4,iq,i)*VVi(i1,1,i)
      QK(6,iq) =QK(6,iq)+QR91i(i1,3,iq,i)*(
     2          DFi(i1,1,i)+DGi(i1,2,i)+DHi(i1,2,i))
     3         +R91i(i1,3,i)*(QDFi(i1,1,iq,i)
     4         +QDGi(i1,2,iq,i)+QDHi(i1,2,iq,i))
      QK(7,iq) =QK(7,iq)+QR91i(i1,5,iq,i)*DGi(i1,1,i)
     2         +R91i(i1,5,i)*QDGi(i1,1,iq,i)
      QK(8,iq) =QK(8,iq)+QR91i(i1,5,iq,i)*DHi(i1,1,i)
     2         +R91i(i1,5,i)*QDHi(i1,1,iq,i)
      QK(9,iq)=QK(9,iq)+QR91i(i1,2,iq,i)*(
     2          RTi(i1,1,i)+TTi(i1,3,i)+TVi(i1,3,i))
     3         +R91i(i1,2,i)*(QRTi(i1,1,iq,i)
     4         +QTTi(i1,3,iq,i)+QTVi(i1,3,iq,i))
      QK(10,iq)=QK(10,iq)+QR91i(i1,2,iq,i)*(RVi(i1,1,i)+VVi(i1,3,i))
     2         +R91i(i1,2,i)*QVVi(i1,3,iq,i)
      QK(11,iq)=QK(11,iq)+Hf*(QR91i(i1,4,iq,i)*TVi(i1,1,i)
     2         +R91i(i1,4,i)*QTVi(i1,1,iq,i))
  714 Continue
C
C     QKe for all the generalized coordinates are evaluated if Bij
C     body does not exist
C
      Do 718 iq=1,Nq
      Do 718 in=1,11
  718 QKe(iq)=QKe(iq)+QK(in,iq)
C
C     Now execute the same procedures for Bij bodies provided
C     they exist
C
      If(Nj .eq. 0)Go to 810
C
C     Initialize the temporary arrays
C
      Do 8020 jq=1,Nq
      Do 8020 jn=1,11
      QK(jn,jq)=0.d0
```

```
 8020 Continue
C
      Do 822 j =1,Nj
      Do 822 jq=1,Nq
      Do 822 j1=1,9
C
      i=Jcon(j)
      QK(2,jq) =QK(2,jq)+Hf*(
     2          (Rmj(j)/Rmi(i))*R91c(j1)*QDDi(j1,1,jq,i)
     3         +2.d0*(QR91i(j1,5,jq,i)*DDij(j1,1,j)
     4         +R91i(j1,5,i)*QDDij(j1,1,jq,j))
     5         +QR91i(j1,4,jq,i)*DDj(j1,1,j)
     6         +R91i(j1,4,i)*QDDj(j1,1,jq,j))
      QK(3,jq) =QK(3,jq)+Hf*(QR91i(j1,1,jq,i)*DDj(j1,4,j)
     2         +R91i(j1,1,i)*QDDj(j1,4,jq,j)
     3         +2.d0*(QR91ij(j1,1,jq,j)*(DFj(j1,2,j)
     4         +DGj(j1,4,j)+DHj(j1,4,j))
     5         +R91ij(j1,1,j)*(QDFj(j1,2,jq,j)
     6         +QDGj(j1,4,jq,j)+QDHj(j1,4,jq,j)))
     7         +QR91j(j1,1,jq,j)*(
     8          RRj(j1,1,j)+RTj(j1,3,j)+RVj(j1,3,j)
     9         +TTj(j1,4,j)+VVj(j1,4,j)+TVj(j1,4,j))
     +         +R91j(j1,1,j)*(QRTj(j1,3,jq,j)+QRVj(j1,3,jq,j)
     1         +QTTj(j1,4,jq,j)+QVVj(j1,4,jq,j)+QTVj(j1,4,jq,j)))
      QK(4,jq) =QK(4,jq)+Hf*(QR91j(j1,4,jq,j)*TTj(j1,1,j)
     2         +R91j(j1,4,j)*QTTj(j1,1,jq,j))
      QK(5,jq) =QK(5,jq)+Hf*(QR91j(j1,4,jq,j)*VVj(j1,1,j)
     2         +R91j(j1,4,j)*QVVj(j1,1,jq,j))
      QK(6,jq) =QK(6,jq)+QR91i(j1,3,jq,i)*DDij(j1,2,j)
     2         +R91i(j1,3,i)*QDDij(j1,2,jq,j)
     3         +QR91j(j1,3,jq,j)*(DFij(j1,1,j)
     4         +DGij(j1,2,j)+DHij(j1,2,j))
     5         +R91j(j1,3,j)*(QDFij(j1,1,jq,j)
     6         +QDGij(j1,2,jq,j)+QDHij(j1,2,jq,j))
     7         +QR91i(j1,2,jq,i)*DDj(j1,3,j)
     8         +R91i(j1,2,j)*QDDj(j1,3,jq,j)
```

```
     9          +QR91ij(j1,3,jq,j)*(
     +           DFj(j1,1,j)+DGj(j1,2,j)+DHj(j1,2,j))
     1          +R91ij(j1,3,j)*(QDFj(j1,1,jq,j)
     2          +QDGj(j1,2,jq,j)+QDHj(j1,2,jq,j))
      QK(7,jq) =QK(7,jq)+QR91j(j1,5,jq,j)*DGij(j1,1,j)
     2          +R91j(j1,5,j)*QDGij(j1,1,jq,j)
     3          +QR91ij(j1,4,jq,j)*DGj(j1,1,j)
     4          +R91ij(j1,4,j)*QDGj(j1,1,jq,j)
      QK(8,jq) =QK(8,jq)+QR91j(j1,5,jq,j)*DHij(j1,1,j)
     2          +R91j(j1,5,j)*QDHij(j1,1,jq,j)
     3          +QR91ij(j1,4,jq,j)*DHj(j1,1,j)
     4          +R91ij(j1,4,j)*QDHj(j1,1,jq,j)
      QK(9,jq) =QK(9,jq)+QR91ij(j1,2,jq,j)*DGj(j1,3,j)
     2          +R91ij(j1,2,j)*QDGj(j1,3,jq,j)
     3          +QR91j(j1,2,jq,j)*(
     4           RTj(j1,1,j)+TTj(j1,3,j)+TVj(j1,3,j))
     5          +R91j(j1,2,j)*(QRTj(j1,1,jq,j)
     6          +QTTj(j1,3,jq,j)+QTVj(j1,3,jq,j))
      QK(10,jq)=QK(10,jq)+QR91ij(j1,2,jq,j)*DHj(j1,3,j)
     2          +R91ij(j1,2,j)*QDHj(j1,3,jq,j)
     3          +QR91j(j1,2,jq,j)*(RVj(j1,1,j)+VVj(j1,3,j))
     4          +R91j(j1,2,j)*QVVj(j1,3,jq,j)
      QK(11,jq)=QK(11,jq)+Hf*(QR91j(j1,4,jq,j)*TVj(j1,1,j)
     2          +R91j(j1,4,j)*QTVj(j1,1,jq,j))
  822 Continue
C
C     Hence QKe for all the generalized coordinates are evaluated
C
      Do 828 jq=1,Nq
      Do 828 jn=1,11
  828 QKe(jq)=QKe(jq)+QK(jn,jq)
C
  810 Continue
      Stop
      End
```

Subroutine to calculate the I_{sys} of the system

```
C
C     The I{sys} of the system is denoted by the 3X3 array Imat
C     The common blocks, except for R99,  are the same as KINENE
C     and are omitted here
C
      Subroutine INEMAT(Imat)
      Implicit Real*8(a-h, o-z)
C
C     Common /R99/ R99c(9,9),       R99i(9,9,2,N),
     2             R99ij(9,9,1,Nj), R99j(9,9,2,Nj)
C
      Real*8    Imat(3,3)
C
C     Set up the temporary matrices
C     In Eq. (I-2), each component has two terms
C     The first one is a scalar product times the unit matrix
C     The second one is the product of two 3X3 matrices
C     The scalar product is stored in Sc(m)
C     (m=1,...,11) for the m-th term in Eq. (I-2)
C     Am(m,n,p)=Sc(m)X the unit matrix
C     Bm(m,n,p) is the second term of each component
C     Dm(m,n,p) (m=1,...,4) are the dummy matrices
C
      Real*8 Am(11,3,3), Bm(11,3,3), Dm(4,3,3), Sc(11)
C
C     First, initialize the matrices
C
      Do 5000 i1=1,11
 5000 Sc(i1,1)=0.d0
C
      Do 5002 i2=1,3
      Do 5002 i1=1,3
 5002 Imat(i1,i2)=0.d0
C
      Do 5004 i2=1,3
```

```
      Do 5004 i1=1,3
      Do 5004 in=1,11
      Am(in,i1,i2)=0.d0
 5004 Bm(in,i1,i2)=0.d0
C
      Do 5006 i2=1,3
      Do 5006 i1=1,3
      Do 5006 in=1,3
 5006 Dm(in,i1,i2)=0.d0
C
C     First start with body Bc to calculate the first term
C
      Do 500 i1=1,9
C
      Sc(1) =Sc(1)-R91c(i1)*CMc(i1,4)
      Sc(3) =Sc(3)+R91c(i1)*RRc(i1,1)
      Sc(4) =Sc(4)+R91c(i1)*TTc(i1,4)
      Sc(5) =Sc(5)+R91c(i1)*VVc(i1,4)
      Sc(9) =Sc(9)+R91c(i1)*RTc(i1,3)
      Sc(10)=Sc(10)+R91c(i1)*RVc(i1,3)
      Sc(11)=Sc(11)+R91c(i1)*TVc(i1,4)
 500  Continue
C
C     Now proceed the calculation for Bi bodies
C
      Do 502 i =1,Ni
      Do 502 i1=1,9
C
      Sc(2) =Sc(2)+R91c(i1)*DDi(i1,4,i)
      Sc(3) =Sc(3)+R91i(i1,4,i)*RRi(i1,1,i)
      Sc(4) =Sc(4)+R91i(i1,4,i)*TTi(i1,4,i)
      Sc(5) =Sc(5)+R91i(i1,4,i)*VVi(i1,4,i)
      Sc(6) =Sc(6)+2.d0*R91i(i1,5,i)*DFi(i1,2,i)
      Sc(7) =Sc(7)+2.d0*R91i(i1,5,i)*DGi(i1,4,i)
      Sc(8) =Sc(8)+2.d0*R91i(i1,5,i)*DHi(i1,4,i)
      Sc(9) =Sc(9)+R91i(i1,4,i)*RTi(i1,3,i)
```

```
      Sc(10)=Sc(10)+R91i(i1,4,i)*RVi(i1,3,i)
      Sc(11)=Sc(11)+R91i(i1,4,i)*TVi(i1,4,i)
 502  Continue
C
      Do 504 i1=1,3
      Do 504 in=1,11
 504  Am(in,i1,i1)=Sc(in)
C
C     Second, the calculation of the second term for Bc
C
      Do 506 i2=1,3
      Do 506 i1=1,3
      Do 506 i3=1,9
C
      ia=(i1-1)*3+i2
      Bm(1,i1,i2) =Bm(1,i1,i2)-R99c(ia,i3)*CMc(i3,4)
      Bm(3,i1,i2) =Bm(3,i1,i2)+R99c(ia,i3)*RRc(i3,1)
      Bm(4,i1,i2) =Bm(4,i1,i2)+R99c(ia,i3)*TTc(i3,4)
      Bm(5,i1,i2) =Bm(5,i1,i2)+R99c(ia,i3)*VVc(i3,4)
      Bm(9,i1,i2) =Bm(9,i1,i2)+R99c(ia,i3)*RTc(i3,3)
      Bm(10,i1,i2)=Bm(10,i1,i2)+R99c(ia,i3)*RVc(i3,3)
      Bm(11,i1,i2)=Bm(11,i1,i2)+R99c(ia,i3)*TVc(i3,4)
 506  Continue
C
C     Repeat the calculation of the second term for Bi
C
      Do 508 i =1,N
      Do 508 i2=1,3
      Do 508 i1=1,3
      Do 508 i3=1,9
C
      ia=(i1-1)*3+i2
      Bm(2,i1,i2) =Bm(2,i1,i2)+R99c(ia,i3)*DDi(i3,4,i)
      Bm(3,i1,i2) =Bm(3,i1,i2)+R99i(ia,i3,1,i)*RRi(i3,1,i)
      Bm(4,i1,i2) =Bm(4,i1,i2)+R99i(ia,i3,1,i)*TTi(i3,4,i)
      Bm(5,i1,i2) =Bm(5,i1,i2)+R99i(ia,i3,1,i)*VVi(i3,4,i)
```

```
      Dm(1,i1,i2) =Dm(1,i1,i2)+R99i(ia,i3,2,i)*DFi(i3,2,i)
      Dm(2,i1,i2) =Dm(2,i1,i2)+R99i(ia,i3,2,i)*DGi(i3,4,i)
      Dm(3,i1,i2) =Dm(3,i1,i2)+R99i(ia,i3,2,i)*DHi(i3,4,i)
      Bm(9,i1,i2) =Bm(9,i1,i2)+R99i(ia,i3,1,i)*RTi(i3,3,i)
      Bm(10,i1,i2)=Bm(10,i1,i2)+R99i(ia,i3,1,i)*RVi(i3,3,i)
      Bm(11,i1,i2)=Bm(11,i1,i2)+R99i(ia,i3,1,i)*TVi(i3,4,i)
 508  Continue
C
      Do 510 i =1,N
      Do 510 i2=1,3
      Do 510 i1=1,3
C
      Bm(6,i1,i2)=Dm(1,i1,i2)+Dm(1,i2,i1)
      Bm(7,i1,i2)=Dm(2,i1,i2)+Dm(2,i2,i1)
      Bm(8,i1,i2)=Dm(3,i1,i2)+Dm(3,i2,i1)
 510  Continue
C
C     Evaluate I{sys} for the system Bc and Bi bodies
C
      Do 512 i2=1,3
      Do 512 i1=1,3
      Do 512 in=1,11
      Imat(i1,i2)=Imat(i1,i2)+Am(in,i1,i2)-Bm(in,i1,i2)
 512  Continue
C
C     Proceed if Bij is not zero
C
      If(Nj .eq. 0)Go to 600
C
C     Initialize the matrices
C
      Do 6000 j1=1,11
 6000 Sc(j1)=0.d0
C
      Do 6002 j2=1,3
      Do 6002 j1=1,3
```

```
      Do 6002 jn=1,11
      Am(jn,j1,j2)=0.d0
      Bm(jn,j1,j2)=0.d0
 6002 Continue
C
      Do 6004 j2=1,3
      Do 6004 j1=1,3
      Do 6004 jn=1,4
 6004 Dm(jn,j1,j2)=0.d0
C
C     Begin the first term calculation for Bij bodies
C
      Do 602 j =1,Nj
      Do 602 j1=1,9
C
      i=Jcon(j)
      Sc(2) =Sc(2)+(Rmj(j)/Rmi(i))*R91c(j1)*DDi(j1,4,i)
     2      +2.d0*R91i(j1,5,i)*DDij(j1,4,j)
     3      +R91i(j1,4,i)*DDj(j1,4,j)
      Sc(3) =Sc(3)+R91j(j1,4,j)*RRj(j1,1,j)
      Sc(4) =Sc(4)+R91j(j1,4,j)*TTj(j1,4,j)
      Sc(5) =Sc(5)+R91j(j1,4,j)*VVj(j1,4,j)
      Sc(6) =Sc(6)+2.d0*(R91j(j1,5,j)*DFij(j1,2,j)
     2      +R91ij(j1,4,j)*DFj(j1,2,j))
      Sc(7) =Sc(7)+2.d0*(R91j(j1,5,j)*DGij(j1,4,j)
     2      +R91ij(j1,4,j)*DGj(j1,4,j))
      Sc(8) =Sc(8)+2.d0*(R91j(j1,5,j)*DHij(j1,4,j)
     2      +R91ij(j1,4,j)*DHj(j1,4,j))
      Sc(9) =Sc(9)+R91j(j1,4,j)*RTj(j1,3,j)
      Sc(10)=Sc(10)+R91j(j1,4,j)*RVj(j1,3,j)
      Sc(11)=Sc(11)+R91j(j1,4,j)*TVj(j1,4,j)
 602  Continue
C
      Do 604 j1=1,3
      Do 604 jn=1,11
 604  Am(jn,j1,j1)=Sc(jn)
```

```
C
C     Then, calculate the second term for Bij
C
      Do 606 j =1,Nj
      Do 606 j2=1,3
      Do 606 j1=1,3
      Do 606 j3=1,9
C
      i =Jcon(j)
      ja=(j1-1)*3+j2
      Bm(2,j1,j2) =Bm(2,j1,j2)
     2            +(Rmj(j)/Rmi(i))*R99c(ja,j3)*DDi(j3,4,i)
     3            +R99i(ja,j3,1,i)*DDj(j3,4,j)
      Dm(1,j1,j2) =Dm(1,j1,j2)+R99i(ja,j3,2,i)*DDij(j3,4,j)
      Bm(3,j1,j2) =Bm(3,j1,j2)+R99j(ja,j3,1,j)*RRj(j3,1,j)
      Bm(4,j1,j2) =Bm(4,j1,j2)+R99j(ja,j3,1,j)*TTj(j3,4,j)
      Bm(5,j1,j2) =Bm(5,j1,j2)+R99j(ja,j3,1,j)*VVj(j3,4,j)
      Dm(2,j1,j2) =Dm(2,j1,j2)+R99j(ja,j3,2,j)*DFij(j3,2,j)
     2            +R99ij(ja,j3,1,j)*DFj(j3,2,j)
      Dm(3,j1,j2) =Dm(3,j1,j2)+R99j(ja,j3,2,j)*DGij(j3,4,j)
     2            +R99ij(ja,j3,1,j)*DGj(j3,4,j)
      Dm(4,j1,j2) =Dm(4,j1,j2)+R99j(ja,j3,2,j)*DHij(j3,4,j)
     2            +R99ij(ja,j3,1,j)*DHj(j3,4,j)
      Bm(9,j1,j2) =Bm(9,j1,j2)+R99j(ja,j3,1,j)*RTj(j3,3,j)
      Bm(10,j1,j2)=Bm(10,j1,j2)+R99j(ja,j3,1,j)*RVj(j3,3,j)
      Bm(11,j1,j2)=Bm(11,j1,j2)+R99j(ja,j3,1,j)*TVj(j3,4,j)
 606  Continue
C
      Do 608 j2=1,3
      Do 608 j1=1,3
C
      Bm(2,j1,j2)=Bm(2,j1,j2)+Dm(1,j1,j2)+Dm(1,j2,j1)
      Bm(6,j1,j2)=Dm(2,j1,j2)+Dm(2,j2,j1)
      Bm(7,j1,j2)=Dm(3,j1,j2)+Dm(3,j2,j1)
      Bm(8,j1,j2)=Dm(4,j1,j2)+Dm(4,j2,j1)
 608  Continue
```

```
C
C     Hence, the matrix Imat is calculated
C
      Do 610 j2=1,3
      Do 610 j1=1,3
      Do 610 jn=1,11
      Imat(j1,j2)=Imat(j1,j2)+Am(jn,j1,j2)-Bm(jn,j1,j2)
 610  Continue
C
 600  Continue
      Stop
      End
```

Sample subroutine to calculate H_{sys} of the system

```
C
C     The  H{sys} of the system is represented by the array Hvec
C     The common blocks, except for R93, are the same as KINENE
C     and are omitted here
C
      Subroutine ANGMOM(Hvec)
      Implicit Real*8(a-h, o-z)
C
      Common /R93/ R93c(3,9),       R93i(3,9,5,N),
     2             R93ij(3,9,4,Nj), R93j(3,9,5,Nj)
C
C     Set up the matrix Hvec and temporary matrix Hv
C     Hvec(n) (n=1,2,3) refer to the X, Y, and Z components,
C     respectively
C     Hv(m,n) (m=1,...,12; n=1,3) refers to the contribution
C     from the m-th term in Eq. (I-3)
C     For instance, Hv(1,n) for H{cm}, Hv(2,n) for H{h} and so on
C
      Real*8 Hvec(3), Hv(12,3)
C
C     Initialize the matrices
C
      Do 3000 i1=1,3
      Hvec(i1)=0.d0
 3000 Continue
C
      Do 3002 i1=1,3
      Do 3002 in=1,12
      Hv(in,i1)=0.d0
 3002 Continue
C
C     Start with Body Bc
C
      Do 300 i2=1,9
      Do 300 i1=1,3
```

```
C
      Hv(1,i1) =Hv(1,i1)-R39c(i1,i2)*CMc(i2,3)
      Hv(4,i1) =Hv(4,i1)+R39c(i1,i2)*TTc(i2,3)
      Hv(5,i1) =Hv(5,i1)+R39c(i1,i2)*VVc(i2,3)
      Hv(10,i1)=Hv(10,i1)+R39c(i1,i2)*RTc(i2,1)
      Hv(11,i1)=Hv(11,i1)+R39c(i1,i2)*RVc(i2,1)
      Hv(12,i1)=Hv(12,i1)+R39c(i1,i2)*TVc(i2,3)
 300  Continue
C
C     Proceed to the Bi bodies
C
      Do 302 i =1,N
      Do 302 i2=1,9
      Do 302 i1=1,3
C
      Hv(2,i1) =Hv(2,i1)+R39c(i1,i2)*DDi(i2,3,i)
      Hv(3,i1) =Hv(3,i1)-R39i(i1,i2,2,i)*(RRi(i2,1,i)
     2         +RTi(i2,3,i)+RVi(i2,3,i)
     3         +TTi(i2,4,i)+VVi(i2,4,i)+TVi(i2,4,i))
      Hv(4,i1) =Hv(4,i1)+R39i(i1,i2,4,i)*TTi(i2,3,i)
      Hv(5,i1) =Hv(5,i1)+R39i(i1,i2,4,i)*VVi(i2,3,i)
      Hv(6,i1) =Hv(6,i1)+R39i(i1,i2,3,i)*(
     2          DFi(i2,2,i)+DGi(i2,4,i)+DHi(i2,4,i))
      Hv(7,i1) =Hv(7,i1)-R39i(i1,i2,5,i)*DFi(i2,1,i)
      Hv(8,i1) =Hv(8,i1)+R39i(i1,i2,5,i)*(-DGi(i2,2,i)+DGi(i2,3,i))
      Hv(9,i1) =Hv(9,i1)+R39i(i1,i2,5,i)*(-DHi(i2,2,i)+DHi(i2,3,i))
      Hv(10,i1)=Hv(10,i1)+R39i(i1,i2,4,i)*RTi(i2,1,i)
      Hv(11,i1)=Hv(11,i1)+R39i(i1,i2,4,i)*RVi(i2,1,i)
      Hv(12,i1)=Hv(12,i1)+R39i(i1,i2,4,i)*TVi(i2,3,i)
 302  Continue
C
C     Hvec calculated if Bij does not exist
C
      Do 304 i1=1,3
      Do 304 in=1,12
      Hvec(i1)=Hvec(i1)+Hv(in,i1)
```

```
 304  Continue
C
C     Proceed if Nj is not zero
C
      If(Nj .eq. 0)Go to 400
C
      Do 4000 in=1,12
      Do 4000 i1=1,3
 4000 Hv(in,i1)=0.d0
C
      Do 402 j =1,Nj
      Do 402 j2=1,9
      Do 402 j1=1,3
C
      i=Jcon(j)
      Hv(2,j1) =Hv(2,j1)+R39c(j1,j2)*(Rmj(j)/Rmi(i))*DDi(j2,3,i)
     2         +R39i(j1,j2,5,i)*(DDij(j2,3,j)-DDij(j2,2,j))
     3         +R39i(j1,j2,4,i)*DDj(j2,3,j)
      Hv(3,j1) =Hv(3,j1)-R39i(j1,j2,2,i)*DDj(j2,4,j)
     2         +(R39ij(j1,j2,3,j)-R39ij(j1,j2,2,j))*(
     3          DFj(j2,2,j)+DGj(j2,4,j)+DHj(j2,4,j))
     4         -R39j(j1,j2,2,j)*(RRj(j2,1,j)+RTj(j2,3,j)+RVj(j2,3,j)
     5         +TTj(j2,4,j)+VVj(j2,4,j)+TVj(j2,4,j))
      Hv(4,j1) =Hv(4,j1)+R39j(j1,j2,4,j)*TTj(j2,3,j)
      Hv(5,j1) =Hv(5,j1)+R39j(j1,j2,4,j)*VVj(j2,3,j)
      Hv(6,j1) =Hv(6,j1)+R39i(j1,j2,3,i)*DDij(j2,4,j)
     2         +R39j(j1,j2,3,j)*(
     3          DFij(j2,2,j)+DGij(j2,4,j)+DHij(j2,4,j))
      Hv(7,j1) =Hv(7,j1)-R39j(j1,j2,5,j)*DFij(j2,1,j)
     2         -R39ij(j1,j2,4,j)*DFj(j2,1,j)
      Hv(8,j1) =Hv(8,j1)+R39j(j1,j2,5,j)*(DGij(j2,3,j)-DGij(j2,2,j))
     2         +R39ij(j1,j2,4,j)*(DGj(j2,3,j)-DGj(j2,2,j))
      Hv(9,j1) =Hv(9,j1)+R39j(j1,j2,5,j)*(DHij(j2,3,j)-DHij(j2,2,j))
     2         +R39ij(j1,j2,4,j)*(DHj(j2,3,j)-DHj(j2,2,j))
      Hv(10,j1)=Hv(10,j1)+R39j(j1,j2,4,j)*RTj(j2,1,j)
      Hv(11,j1)=Hv(11,j1)+R39j(j1,j2,4,j)*RVj(j2,1,j)
```

```
      Hv(12,j1)=Hv(12,j1)+R39j(j1,j2,4,j)*TVj(j2,3,j)
 402  Continue
C
C     Calculate Hvec for the whole system
C
      Do 404 j1=1,3
      Do 404 jn=1,12
      Hvec(j1)=Hvec(j1)+Hv(jn,j1)
 404  Continue
C
 400  Continue
      Stop
      End
```